University of California
Santa Barbara

First-principles study of ion ordering and diffusion in layered oxides for Na- and K-ion batteries

A dissertation submitted in partial satisfaction
of the requirements for the degree

Doctor of Philosophy
in
Materials

by

Jonas Leif Kaufman

Committee in charge:

Professor Anton Van der Ven, Chair
Professor Ram Seshadri
Professor Raphaële Clément
Professor M. Scott Shell

June 2022

The Dissertation of Jonas Leif Kaufman is approved.

Professor Ram Seshadri

Professor Raphaële Clément

Professor M. Scott Shell

Professor Anton Van der Ven, Committee Chair

May 2022

First-principles study of ion ordering and diffusion in layered oxides for Na- and K-ion batteries

by

Jonas Leif Kaufman

Acknowledgements

I am immensely grateful to my advisor, Prof. Anton Van der Ven. He is an exceptional teacher who emphasizes both scientific rigor and effective communication. Over the course of my PhD, I have enjoyed and appreciated his trust, guidance, and endless supply of creative research ideas.

I would like to thank the entire Van der Ven Group for all the engaging discussions and fun times inside and outside of the office. I am particularly indebted to Drs. Max Radin, Julija Vinckevičiūtė, Sanjeev Kolli, John Goiri, and Harsha Gunda for welcoming me so warmly into the group and helping me get started. I also thank Dr. John Thomas, Dr. Daniil Kitchaev, and Prof. Anirudh Natarajan for assisting me in various ways.

I am grateful for the fruitful collaborations I have been a part of through the DOE SCALAR EFRC, and all the wonderful researchers who made these possible. Working directly alongside experimentalists has been one of the most energizing and rewarding research experiences for me.

I appreciate the amazing teachers I have had during graduate school, particularly Profs. Ram Seshadri, Raphaële Clément, and Stephen Wilson, for their dedication inside and outside of the classroom. I would also like to thank my entire committee for their time, support, and thoughtful feedback on my research.

Thank you to all of the Materials Department staff, in particular Jocelyn Guzman, for helping me with various administrative issues over the course of my PhD. I also deeply appreciate everyone at the Krell Institute, especially Lindsey Eilts, for facilitating my wonderful experience as part of the DOE Computational Science Graduate Fellowship.

I would not be where I am today without my amazing advisors and mentors from my time at Harvey Mudd College, particularly Profs. Lori Bassman and Aurora Pribram-Jones, who helped me traverse unfamiliar subjects in materials science and taught me

how to be an effective researcher. I also appreciate Dr. Brandon Wood and everyone at Lawrence Livermore National Laboratory who helped make my summer there a great experience.

I am lucky to have made some truly incredible friends before and during my time in Santa Barbara. To Sam Teicher, Julia Zuo, Caroline Reilly, and Peter McWilliams (and, of course, Argos), thank you for all the food, alcohol, banter, gossip, and memes, and especially for the company and countless fun diversions during the early days of the pandemic. John Goiri, thank you for being a fantastic friend and mentor, and for always being down to watch something together. To all my friends from Mudd, thank you for being there for me over the years, and a special shout-out to the Wolfpack for staying in touch so closely. I look forward to many more reunions, celebrations, and travels together.

Finally, I am extremely thankful for all of my family across the U.S. and Iceland. I hope to be able to see more of you in the coming years. To my brother Jacob and to my parents, thank you for instilling in me an enthusiasm for learning, and for all your love and support.

Curriculum Vitæ

Jonas Leif Kaufman

Education

May 2022 Ph.D. in Materials (Expected), University of California, Santa Barbara.

May 2017 B.S. in Physics, Harvey Mudd College.

Publications

8. J. L. Kaufman and Anton Van der Ven, First-principles investigation of phase stability in layered Na_xCrO_2, Submitted.
7. K. E. Wyckoff, J. L. Kaufman, S. W. Baek, C. Dolle, J. J. Zak, J. Bienz, L. Kautzsch, R. C. Vincent, A. Zohar, K. A. See, Y. M. Eggeler, L. Pilon, A. Van der Ven, and R. Seshadri, Metal-metal bonding as an electrode design principle in the low-strain cluster compound $LiScMo_3O_8$, *Journal of the American Chemical Society* **144** (2022) 5841–5854. DOI: 10.1021/jacs.1c12070
6. J. L. Kaufman and A. Van der Ven, Cation diffusion facilitated by antiphase boundaries in layered intercalation compounds, *Chemistry of Materials* **34** (2022) 1889–1896. DOI: 10.1021/acs.chemmater.1c04152
5. J. L. Kaufman and A. Van der Ven, Antiphase boundary migration as a diffusion mechanism in a P3 sodium layered oxide, *Physical Review Materials* **5** (2021) 055401, Editors' Suggestion. DOI: 10.1103/PhysRevMaterials.5.055401
4. J. L. Kaufman and A. Van der Ven, Ordering and structural transformations in layered K_xCrO_2 for K-ion batteries, *Chemistry of Materials* **32** (2020) 6392–6400. DOI: 10.1021/acs.chemmater.0c01460
3. J. L. Kaufman, J. Vinckevičiūtė, S. K. Kolli, J. G. Goiri, and A. Van der Ven, Understanding intercalation compounds for sodium-ion batteries and beyond, *Philosophical Transactions of the Royal Society A* **377** (2019) 20190020. DOI: 10.1098/rsta.2019.0020
2. M. Y. Toriyama, J. L. Kaufman, and A. Van der Ven, Potassium ordering and structural phase stability in layered K_xCoO_2, *ACS Applied Energy Materials* **2** (2019) 2629–2636. DOI: 10.1021/acsaem.8b02238
1. J. L. Kaufman and A. Van der Ven, Na_xCoO_2 phase stability and hierarchical orderings in the O3/P3 structure family, *Physical Review Materials* **3** (2019) 015402. DOI: 10.1103/PhysRevMaterials.3.015402

Abstract

First-principles study of ion ordering and diffusion in layered oxides for Na- and K-ion batteries

by

Jonas Leif Kaufman

Electrochemical energy storage technology must continue to improve in order to meet increasing demand across sectors, while balancing performance with cost and resource constraints. For large-scale stationary applications such as grid storage of renewable energy, Na- and K-ion batteries have received attention as potential alternatives to Li-ion batteries mainly due to the far greater abundance of those elements. Research efforts for these "beyond Li-ion" technologies include developing robust electrode materials that can undergo many cycles without degrading. One promising class of candidate materials are layered oxide intercalation compounds, which have been widely adopted in positive electrodes for commercial Li-ion batteries. However, when intercalated with the larger Na^+ and K^+ ions, these materials often exhibit additional structural phase transitions and ion-vacancy orderings that are not encountered with Li^+. These effects have important implications for the voltage profile, degradation mechanisms, and rate capability.

In this dissertation, we study thermodynamic and kinetic properties of layered oxides for Na- and K-ion battery electrodes using first-principles techniques. Density functional theory calculations provide energies and relaxed geometries of ordered configurations at varying Na/K concentration (corresponding to different states of charge), as well as barriers for ion migration. Statistical mechanics methods, namely cluster expansion effective Hamiltonians and Monte Carlo simulations, are employed to efficiently model finite-temperature behavior and predict ground state configurations.

In the Na_xCoO_2, Na_xCrO_2, and K_xCrO_2 systems ($0 \leq x \leq 1$), we examine phase stability among layered structures that host Na/K in octahedral or prismatic coordination, as well as ion-vacancy orderings within them. We establish a comprehensive description of ordering in these systems, in which most of the stable ordered phases belong to families that are each based on a particular motif. At intermediate x, we identify orderings with Na/K in prismatic coordination that accommodate variations in composition as antiphase boundaries. We demonstrate how the composition can be changed essentially continuously by adjusting the average spacing between boundaries, leading to "Devil's staircase" behavior that agrees well with experimental observations. We predict a similar family of orderings at high x in K_xCrO_2 that host both prismatically and octahedrally coordinated K within the same intercalation layer, which we find to be a plausible explanation of the experimentally reported structural evolution during cycling. In Na_xCrO_2, we also confirm a preference for Cr migration to the intercalation layers at low x, which is a key degradation mechanism observed in this material.

Using Na_xCoO_2 as a model system, we explore Na diffusion within the orderings identified near $x = 1/2$. While Na mobility is found to be highly restricted, we uncover a mechanism that enables the collective motion of antiphase boundaries through the intercalation layers, the limiting migration barriers for which are relatively low. We simulate the macroscopic diffusion behavior arising from this mechanism using a kinetic Monte Carlo model. Our simulations show that antiphase boundary migration, though quite distinct from textbook atomistic diffusion mechanisms, follows normal Fickian diffusion in one dimension, but with strong composition dependence of the diffusion coefficient. These results lay important groundwork for understanding the effects of ordering and engineering improved battery materials that might take advantage of unconventional diffusion mechanisms in ordered phases.

Contents

Curriculum Vitae vi

Abstract vii

1 Introduction 1
- 1.1 Moving beyond Li for batteries . . . 1
- 1.2 Ordering phenomena in electrode materials . . . 2
- 1.3 Overview . . . 3
- 1.4 Permissions and attributions . . . 4

2 Computational methods 6
- 2.1 Electronic structure calculations . . . 6
- 2.2 Cluster expansion effective Hamiltonians . . . 13
- 2.3 Monte Carlo simulations . . . 17
- 2.4 Details . . . 21

3 Structure and chemistry of intercalation compounds 23
- 3.1 Introduction . . . 23
- 3.2 Thermodynamics . . . 25
- 3.3 Crystallography . . . 27
- 3.4 Chemistry . . . 29
- 3.5 Trends in phase stability . . . 32
- 3.6 Intercalant orderings . . . 38
- 3.7 Stacking sequence changes . . . 40
- 3.8 Conclusion . . . 46

4 Ordering and phase stability in layered Na_xCoO_2 48
- 4.1 Introduction . . . 48
- 4.2 Methods . . . 51
- 4.3 Results . . . 52
- 4.4 Discussion . . . 64
- 4.5 Conclusion . . . 68

5 Ordering and phase stability in layered Na_xCrO_2 69
5.1 Introduction . . . 69
5.2 Methods . . . 73
5.3 Results . . . 74
5.4 Discussion . . . 87
5.5 Conclusion . . . 91

6 Ordering and phase stability in layered K_xCrO_2 92
6.1 Introduction . . . 92
6.2 Methods . . . 95
6.3 Results . . . 96
6.4 Discussion . . . 108
6.5 Conclusion . . . 111

7 Atomistic diffusion involving antiphase boundaries 113
7.1 Introduction . . . 113
7.2 Background . . . 116
7.3 Methods . . . 118
7.4 Results . . . 119
7.5 Discussion . . . 130
7.6 Conclusion . . . 133

8 Macroscopic diffusion facilitated by antiphase boundaries 135
8.1 Introduction . . . 135
8.2 Background . . . 138
8.3 Methods . . . 140
8.4 Results . . . 143
8.5 Discussion . . . 149
8.6 Conclusion . . . 151

9 Conclusion 153

A Orbital occupation matrices 156

B Calculation details for Chapter 3 159

C Details of hierarchical orderings in Na_xCoO_2 160
C.1 The θ orderings in O3 . . . 160
C.2 The ζ^- and ζ^+ orderings in P3 . . . 162
C.3 The η^+ orderings in P3 . . . 162

D Supporting information for Chapter 5 **164**
D.1 Cluster expansions 164
D.2 Monte Carlo simulations 165
D.3 Additional figures 165

E Kinetic model of antiphase boundary migration **172**
E.1 Simulation grid 172
E.2 Kinetic events 174
E.3 Total energy 182
E.4 Simulator code 182

Bibliography **183**

Chapter 1

Introduction

1.1 Moving beyond Li for batteries

The development of the rechargeable Li-ion battery revolutionized energy storage, enabling advances in many applications, including portable electronics, electric vehicles, and grid energy storage [1]. While commercial Li-ion batteries are being continually optimized, design constraints related to factors such as cost, energy density, power density, cycle life, and safety have spurred interest in various "beyond Li-ion" battery technologies. In particular, lower-cost solutions are needed to support grid storage of energy generated from intermittent renewable sources such as solar and wind [2], an important part of the greater transition toward a more sustainable future. For these grid storage applications, where energy density is of far less importance than cost, Na- and K-ion batteries have received renewed attention as possible alternatives to Li-ion batteries. The most obvious and significant advantage of Na and K is their greater supply (and subsequently lower cost): Both elements are about three orders of magnitude more abundant than Li in the Earth's crust and are geographically ubiquitous [3]. While their chemical similarity to Li has allowed for the transfer of many insights from the Li-ion domain, there are some

additional challenges for developing suitable Na- and K-ion battery materials.

A great amount of research has been devoted to active materials for battery electrodes, particularly for positive electrodes. These are typically intercalation compounds, "hosts" which allow for insertion and removal of the "guest" charge-carrying ions with minimal change to their crystal structure [4]. It is critical that these materials be able to shuttle the intercalating guest ions reversibly, to prolong cycle life, and rapidly, to provide high rate capability. In the case of Na- and K-ion battery electrode materials, the larger size of Na^+ and K^+ ions (compared to Li^+) generally leads to more ion orderings and structural rearrangements of the host during cycling, which can adversely affect battery performance. Strategies for improving the properties of electrode materials range from doping to nanostructuring, and rely on understanding the materials' intrinsic thermodynamic and kinetic behavior [5].

1.2 Ordering phenomena in electrode materials

A central aspect of the behavior of intercalation compounds for battery electrodes is the presence of and interplay between different ordering phenomena. For instance, a typical transition-metal oxide material may exhibit various ion-vacancy orderings on the guest ion sublattice over the range of concentrations accessed during battery cycling. The transition-metal sublattice of the host may contain a (dis)ordered mixture of metal ions, which themselves could carry unpaired spins that order magnetically. Additionally, transition-metal ions undergoing redox may adopt charge-ordered configurations and/or orbital orderings (e.g. cooperative Jahn-Teller distortions) depending on their oxidation state [6]. It is convenient to assume that these various degrees of freedom can be decoupled, but this is not true in general. And even in materials where long-range order is limited to low temperatures, short-range order can still be relevant to electrode per-

formance. Ion-vacancy ordering is of particular importance in Na- and K-ion systems, as it is often intimately related to structural phase transitions and diffusion mechanisms [7,8]. It is worth noting that many oxide materials studied as battery electrodes also display interesting electronically ordered phases, which could have unrealized applications in which these phases are tuned electrochemically [9].

Ordering phenomena and their effect on processes such as diffusion are often quite difficult to directly observe in experiments. Computational techniques therefore offer an invaluable source of insights, and may be used in both explanatory and predictive capacities. Atomistic properties can be calculated in a rigorous and efficient fashion using first-principles electronic structure methods, while statistical mechanics approaches provide ways to search large configuration spaces for possible ground states and predict thermodynamic and kinetic properties at finite temperature [4, 10].

1.3 Overview

The following chapters explore the application of first-principles techniques to electrode materials for Na- and K-ion batteries. Chapter 2 describes the main computational methods used throughout. We specifically focus on layered oxide intercalation compounds, which are reviewed broadly in Chapter 3 from an atomistic perspective, along with some discussion of mesoscale considerations. Chapters 4, 5, and 6 describe detailed studies of intercalant ion ordering and structural phase stability in Na_xCoO_2, Na_xCrO_2, and K_xCrO_2, which serve as model systems through which we may understand the effects of changing alkali- and transition-metal cation identity. These studies provide a unified picture of ion-vacancy ordering across systems, in which most orderings are found to belong to families that are each based on a common motif. Though not as relevant for battery applications, some aspects of magnetic ordering in the Cr sys-

tems are addressed as well. Chapters 7 and 8 build on the thermodynamic results from Chapter 4 and present an unconventional Na diffusion mechanism in ordered phases of Na_xCoO_2 that relies on extended defects, namely antiphase boundaries. The atomistic details of this mechanism are introduced in Chapter 7, while Chapter 8 examines the resulting macroscopic diffusion behavior using a kinetic model. Chapter 9 summarizes the preceding studies and discusses some of their broader implications.

1.4 Permissions and attributions

1. The content of Chapter 3 has previously appeared in Reference [11]: J. L. Kaufman, J. Vinckevičiūtė, S. K. Kolli, J. G. Goiri, and A. Van der Ven, Understanding intercalation compounds for sodium-ion batteries and beyond, *Phil. Trans. R. Soc. A* **377** (2019) 20190020. DOI: 10.1098/rsta.2019.0020. Section 3.4 features contributions from Julija Vinckevičiūtė.

2. The content of Chapter 4 has previously appeared in Reference [12]: J. L. Kaufman and A. Van der Ven, Na_xCoO_2 phase stability and hierarchical orderings in the O3/P3 structure family, *Phys. Rev. Mater.* **3** (2019) 015402.
   DOI: 10.1103/PhysRevMaterials.3.015402. Copyright © 2019 American Physical Society.

3. The content of Chapter 6 has previously appeared in Reference [13]: Reprinted with permission from *Chem. Mater.* 2020, 32, 15, 6392–6400.
   DOI: 10.1021/acs.chemmater.0c01460. Copyright © 2020 American Chemical Society.

4. The content of Chapter 7 has previously appeared in Reference [14]: J. L. Kaufman and A. Van der Ven, Antiphase boundary migration as a diffusion mechanism in a

P3 sodium layered oxide, *Phys. Rev. Mater.* **5** (2021) 055401.
DOI: 10.1103/PhysRevMaterials.5.055401.

5. The content of Chapter 8 has previously appeared in Reference [15]: Reprinted with permission from *Chem. Mater.* 2022, 34, 4, 1889–1896.
DOI: 10.1021/acs.chemmater.1c04152.

6. This work was supported by the U.S. Department of Energy through the Computational Science Graduate Fellowship (DOE CSGF) under Grant No. DE-FG02-97ER25308 and as part of the Center for Synthetic Control Across Length-scales for Advancing Rechargeables (SCALAR), an Energy Frontier Research Center funded by the U.S. Department of Energy, Office of Science, Basic Energy Sciences under Award No. DE-SC0019381.

7. Use was made of computational facilities purchased with funds from the National Science Foundation (CNS-1725797) and administered by the Center for Scientific Computing (CSC). The CSC is supported by the California NanoSystems Institute and the Materials Research Science and Engineering Center (MRSEC; NSF DMR 1720256) at UC Santa Barbara. This research used resources of the National Energy Research Scientific Computing Center (NERSC), a U.S. Department of Energy Office of Science User Facility operated under Contract No. DE-AC02-05CH11231.

Chapter 2

Computational methods

2.1 Electronic structure calculations

The primary goal of computational chemistry and materials science is to describe systems from first principles, i.e. the basic laws of quantum mechanics, without reliance on empirical data. A monumental leap toward this goal came with the development of density functional theory (DFT) by Kohn, Sham, and Hohenberg in the 1960s [16, 17], for which Kohn won the 1998 Nobel Prize in Chemistry. DFT has since become the workhorse for electronic structure calculations across many research areas. This section motivates and summarizes DFT, mostly following *Electronic Structure: Basic Theory and Practical Methods* by Martin [18]. Other potentially helpful resources for further reading include *The ABC of DFT* by Burke [19], *Density Functional Theory: A Practical Introduction* by Sholl and Steckel [20], and Kohn's Nobel lecture [21].

2.1.1 Schrödinger equation

At the heart of the quantum mechanical treatment of matter lies the Schrödinger equation [22]. The time-independent Schrödinger equation may be written generally as

$$\hat{H}\Psi = E\Psi, \tag{2.1}$$

where $\hat{H}$ is the Hamiltonian operator, E is an energy eigenvalue of the system, and Ψ is the corresponding eigenfunction known as a wave function. The wave function depends on the degrees of freedom of the system and encodes the probability amplitude of the system taking on particular values of those degrees of freedom, such that $|\Psi|^2$ gives the observable probability density.

More concretely, for a collection of electrons and nuclei (e.g. comprising a molecule or solid), Ψ is a function of the spatial coordinates of the electrons, $\mathbf{r}_i$, and those of the nuceli, $\mathbf{R}_I$. The corresponding (non-relativistic) many-body Hamiltonian is

$$\hat{H} = -\frac{\hbar^2}{2m_e}\sum_i \nabla_i^2 - \sum_{i,I}\frac{Z_I e^2}{|\mathbf{r}_i - \mathbf{R}_I|} + \frac{1}{2}\sum_{i\neq j}\frac{e^2}{|\mathbf{r}_i - \mathbf{r}_j|} - \sum_I \frac{\hbar^2}{2M_I}\nabla_I^2 + \frac{1}{2}\sum_{I\neq J}\frac{Z_I Z_J e^2}{|\mathbf{R}_I - \mathbf{R}_J|}, \tag{2.2}$$

where $\hbar$ is the reduced Planck constant, e is the elementary charge, m_e is the electron mass, and Z_I and M_I are the atomic numbers and masses, respectively, of each nucleus. The terms, in order, account for kinetic energy of the electrons, Coulomb interaction between the electrons and the nuclei, Coulomb interaction between the electrons, kinetic energy of the nuclei, and Coulomb interaction between the nuclei. It is often acceptable to ignore the fourth term and treat the nuclei as stationary, given that they are much heavier than electrons. This is known as the Born-Oppenheimer approximation [23]. The fifth term, while not insignificant, depends only on the nuclear coordinates and thus may be evaluated separately.

With these simplifications, we can write the electronic Hamiltonian (which we will now call $\hat{H}$) as

$$\begin{aligned}\hat{H} &= -\frac{\hbar^2}{2m_e}\sum_i \nabla_i^2 + \frac{1}{2}\sum_{i\neq j}\frac{e^2}{|\mathbf{r}_i - \mathbf{r}_j|} + \sum_i V_{\text{ext}}(\mathbf{r}_i) \\ &= \hat{T} + \hat{V}_{\text{int}} + \hat{V}_{\text{ext}},\end{aligned} \tag{2.3}$$

where the third term has been generalized to include any external potentials (e.g. due to electric fields) in addition to the potential imposed by the nuclei. The corresponding wave function is $\Psi(\mathbf{r}_1, \mathbf{r}_2, \ldots, \mathbf{r}_N)$ for N electrons. Note that this function depends on $3N$ coordinates, which presents a critical challenge for solving the many-body Schrödinger equation. Obtaining or even evaluating reasonable approximate solutions quickly becomes computationally intractable, as the cost scales as exponentially with N (dubbed the "exponential wall" by Kohn [21]). Thus a fundamental reimagining of the problem is necessary in order to efficiently treat many-electron systems.

2.1.2 Density functional theory

An important insight is that the N-electron wave function $\Psi(\mathbf{r}_1, \mathbf{r}_2, \ldots, \mathbf{r}_N)$ is not itself physically meaningful. Labelling of the electrons is generally not achievable or valuable in experiments, and probability amplitudes are not observable [20]. What can actually be observed are quantities derived from Ψ, such as the electron density

$$n(\mathbf{r}) = N\int \mathrm{d}\mathbf{r}_2 \ldots \int \mathrm{d}\mathbf{r}_N \Psi^*(\mathbf{r}, \mathbf{r}_2, \ldots, \mathbf{r}_N)\Psi(\mathbf{r}, \mathbf{r}_2, \ldots, \mathbf{r}_N). \tag{2.4}$$

This function encapsulates the essential information of a system's electronic structure and is only a function of three coordinates. Working with the electron density rather than the wave function is the essence of density functional theory (DFT).

DFT relies on two foundational theorems known as the Hohenberg-Kohn theorems [16], which may be stated like so:

1. The external potential, which uniquely determines all properties of the system, is uniquely determined (up to an arbitrary constant) by the ground-state electron density $n(\mathbf{r})$, such that the energy is a unique functional of $n(\mathbf{r})$: $E = E[n(\mathbf{r})]$.

2. The energy functional $E[n(\mathbf{r})]$ is minimized if and only if $n(\mathbf{r})$ is the exact ground-state electron density.

These statements allow us to recast the contributions to the energy from Equation 2.3 in terms of the electron density:

$$E[n(\mathbf{r})] = T[n(\mathbf{r})] + E_{\text{int}}[n(\mathbf{r})] + E_{\text{ext}}[n(\mathbf{r})]. \tag{2.5}$$

If the forms of these functionals were known, it would be possible to arrive at the ground-state energy by variational minimization with respect to the electron density.

In DFT, this variational problem is handled through the Kohn-Sham approach, which considers an auxiliary system of non-interacting electrons that is defined to have the same ground-state density as the true, interacting system of electrons [17]. The Kohn-Sham wave function is constructed as a Slater determinant of single-electron wave functions ψ_i, with density given by

$$n(\mathbf{r}) = \sum_i |\psi_i(\mathbf{r})|^2. \tag{2.6}$$

We can rewrite the energy of the system as

$$E[n(\mathbf{r})] = T_s[n(\mathbf{r})] + E_{\text{ext}}[n(\mathbf{r})] + E_{\text{Hartree}}[n(\mathbf{r})] + E_{\text{xc}}[n(\mathbf{r})], \tag{2.7}$$

where

$$T_s\left[n(\mathbf{r})\right] = -\frac{\hbar^2}{2m_e}\sum_i \int \mathrm{d}\mathbf{r}\psi_i^*(\mathbf{r})\nabla^2\psi_i(\mathbf{r}) \tag{2.8}$$

is the single-electron kinetic energy,

$$E_{\mathrm{ext}}\left[n(\mathbf{r})\right] = \int \mathrm{d}\mathbf{r}V_{\mathrm{ext}}(\mathbf{r})n(\mathbf{r}) \tag{2.9}$$

is the energy due to the external potential, and

$$E_{\mathrm{Hartree}}\left[n(\mathbf{r})\right] = \frac{e^2}{2}\int \mathrm{d}\mathbf{r}\int \mathrm{d}\mathbf{r}'\frac{n(\mathbf{r})n(\mathbf{r}')}{|\mathbf{r}-\mathbf{r}'|} \tag{2.10}$$

is the Hartree energy, the Coulomb interaction of the electron density with itself (note that this is not the same as E_{int}). Equation 2.7 is made equal to Equation 2.5 by lumping any discrepancy into the final term, known as the exchange-correlation energy:

$$E_{\mathrm{xc}}\left[n(\mathbf{r})\right] = T\left[n(\mathbf{r})\right] - T_s\left[n(\mathbf{r})\right] + E_{\mathrm{int}}\left[n(\mathbf{r})\right] - E_{\mathrm{Hartree}}\left[n(\mathbf{r})\right]. \tag{2.11}$$

This term can also be expressed as

$$E_{\mathrm{xc}}\left[n\right] = \int \mathrm{d}\mathbf{r}n(\mathbf{r})\epsilon_{\mathrm{xc}}\left(\left[n\right],\mathbf{r}\right), \tag{2.12}$$

where $\epsilon_{\mathrm{xc}}\left(\left[n\right],\mathbf{r}\right)$ is an energy density at $\mathbf{r}$ that depends on the electron density in some vicinity of $\mathbf{r}$.

Minimizing Equation 2.7 with respect to the Kohn-Sham orbitals yields a set of Kohn-Sham equations

$$\left(-\frac{\hbar^2}{2m_e}\nabla^2 + V_{\mathrm{KS}}(\mathbf{r})\right)\psi_i = \varepsilon_i\psi_i, \tag{2.13}$$

which describe non-interacting electrons under an effective potential

$$\begin{aligned} V_{\mathrm{KS}}(\mathbf{r}) &= V_{\mathrm{ext}}(\mathbf{r}) + V_{\mathrm{Hartree}}(\mathbf{r}) + V_{\mathrm{xc}}(\mathbf{r}) \\ &= V_{\mathrm{ext}}(\mathbf{r}) + e^2 \int \mathrm{d}\mathbf{r}' \frac{n(\mathbf{r}')}{|\mathbf{r} - \mathbf{r}'|} + \frac{\delta E_{\mathrm{xc}}\left[n(\mathbf{r})\right]}{\delta n(\mathbf{r})}. \end{aligned} \tag{2.14}$$

While the Kohn-Sham equations equations can seemingly be solved independently, the dependence of V_{Hartree} and V_{xc} on the electron density (which in turn depends on the ψ_i) means that they must be solved in an iterative (self-consistent) fashion, starting from an initial guess and ending when convergence is reached.

DFT as described thus far is an exact theory, in that the Kohn-Sham system by definition reproduces the exact ground state energy and density of the true system. Unfortunately, however, the exact form of the exchange-correlation functional E_{xc} is unknown, so calculations must instead rely on some approximation of it. Various approximations have been developed, beginning with the local density approximation (LDA), in which the local exchange-correlation energy density ϵ_{xc} depends only on the local electron density n [17]. Improvements upon LDA include the generalized-gradient approximation (GGA), which depends also on the gradient (first derivative) of n [24–26], as well as meta-GGA approximations that incorporate the Laplacian (second derivative) of either n or the Kohn-Sham orbitals (the latter representing the non-interacting kinetic energy density) [27–31]. These semi-local approaches can offer a reasonable balance of accuracy and computational efficiency. There is a so-called "ladder" of functionals with roughly increasing accuracy, each rung of which contains numerous functionals designed with certain constraints or target systems in mind, or to capture certain phenomena such as long-range van der Waals interactions [32, 33]. Note that many functionals do introduce empirical parameterizations into this otherwise first-principles approach [34]. There are also popular approaches that augment DFT, such as DFT+U, which adds a Hubbard

U term to the Hamiltonian to penalize non-integer occupation of orbitals and encourage electron localization [35]. While not detailed here, DFT is easily generalized to account for electron spin, within what is known as spin-DFT [36, 37].

2.1.3 Practical considerations

Beyond the formalism of DFT, there are many practical considerations for its application to periodic systems [20]. Periodicity implies that the single-electron eigenstates are Bloch states, which themselves can be expanded in a basis of plane waves. The plane-wave basis may be truncated at some cutoff (typically specified by an energy) which determines the shortest achievable real-space modulations of the wave function in the unit cell. A key obstacle in this approach is that an unreasonably large basis of plane waves is usually needed to accurately describe the highly oscillatory wave functions of core electrons located close to the nuclei. However, the behavior of core electrons is generally less important than that of valence electrons, as they do not participate significantly in chemical bonding. This enables a pseudopotential approach, in which the true potential of each nucleus is approximated by an effective potential acting only on the valence electrons that behaves more smoothly close to the nucleus while reproducing the all-electron energies and wave functions beyond some cutoff radius [38–42]. The use of pseudopotentials can greatly reduce the size of the plane-wave basis required in a DFT calculation. Much of the computation needed to solve the Kohn-Sham equations for a periodic system involves integrals over reciprocal space, which can be evaluated numerically by sampling a grid of "**k**-points" in the first Brillouin zone [43]. The density of this grid along with the cutoff of the plane-wave basis represent two primary sources of numerical error in periodic DFT calculations, and must be chosen carefully based on convergence testing.

2.2 Cluster expansion effective Hamiltonians

While DFT offers a computationally tractable method for calculating the properties of crystals, some applications require much faster evaluations of the energy (or other properties). In these cases, a surrogate model (or effective Hamiltonian, if approximating the energy) can be constructed and trained using data from DFT. One such model is the cluster expansion. This section describes the configurational cluster expansion introduced by Sanchez et al. [44,45], but the technique is readily extended to crystals with arbitrary degrees of freedom [10], as well as off-lattice systems [46, 47]. A key feature of these models is that they are constructed to obey the symmetries of the system, e.g. the space group of the parent crystal. Symmetry is also considered when enumerating distinct configurations to use as training data. While transformations under symmetry operations are straightforward for isotropic degrees of freedom (such as site occupation), greater care must be taken when dealing with anisotropic degrees of freedom. The treatment of one such degree of freedom, orbital occupation, is described in Appendix A.

2.2.1 Site basis functions

Local degrees of freedom on crystallographic sites may be represented by a collection of site variables. Consider the simple case of a crystal of N sites, each of which may be occupied by one of two species, A or B. These species could, for instance, correspond to two different metals in an alloy, or Na and vacancies in a battery electrode material. Each site n may be assigned an occupation variable σ_n whose value is mapped to the site's occupant, e.g. $\sigma_n = 1$ for A and $\sigma_n = -1$ for B. The occupation variables of all sites are stored as a configuration vector $\boldsymbol{\sigma} = (\sigma_1, \sigma_2, \ldots, \sigma_N)$.

Any local function at a site n that depends only on the occupation σ_n may be written in terms of site basis functions $\phi_m^n(\sigma_n)$, where $m = 0, \ldots, M-1$ for M possible occupants.

In the case of the binary A-B crystal, $M = 2$ and a complete set of site basis functions is given by $\phi_0^n(\sigma_n) = 1$ and $\phi_1^n(\sigma_n) = \sigma_n$. These site basis functions are orthonormal based on the scalar product defined by Sanchez et al., who also provide a general procedure for generating site basis functions of an M-component system [44]. Note that depending on the particular mapping of the M species to values of σ_n and the form of the $\phi_m^n(\sigma_n)$, the site basis functions may not be orthonormal. For instance, assigning σ_n to 1 for A and 0 for B, while maintaining the forms of $\phi_0^n(\sigma_n)$ and $\phi_1^n(\sigma_n)$ given above, results in a basis that is complete, but not orthonormal.

2.2.2 Crystal basis functions

Now we construct a set of crystal basis functions $\Phi_{\mathbf{m}}(\boldsymbol{\sigma})$ to represent any function of the crystal that depends only on the configuration $\boldsymbol{\sigma}$. This is done by taking a tensor product of all the site basis functions

$$\Phi_{\mathbf{m}}(\boldsymbol{\sigma}) = \prod_{n=1}^{N} \phi_{m_n}^n(\sigma_n), \tag{2.15}$$

where the vector $\mathbf{m} = (m_1, m_2, \ldots, m_N)$ denotes which site basis functions comprise each crystal basis function. This procedure generates M^N crystal basis functions which are complete (and orthonormal) provided the site basis functions used to construct them are complete (and orthonormal).

Careful inspection of the cluster basis functions reveals a more meaningful way to label them. Because $\phi_0^n(\sigma_n) = 1$, each σ_n only appears in select basis functions. In the binary case, we can write the basis functions as

$$\Phi_\alpha(\boldsymbol{\sigma}) = \prod_{i \in \alpha} \sigma_i, \tag{2.16}$$

where α denotes a particular set or cluster of sites (comprised of anywhere from zero to N sites). Any property that depends only on $\boldsymbol{\sigma}$, such as the relaxed energy E, can be written as a "cluster expansion"

$$E(\boldsymbol{\sigma}) = V_0 + \sum_{\alpha} V_\alpha \Phi_\alpha(\boldsymbol{\sigma}), \tag{2.17}$$

where the coefficients V_α are referred to as effective cluster interactions (ECIs). Note we have separated V_0, the ECI of the zero-site or null cluster, from the rest of the sum. It is crucial that the cluster expansion be invariant under the symmetry of the parent (undecorated) crystal. To enforce this, we group the basis functions into orbits of symmetrically equivalent clusters and allow one unique ECI per orbit:

$$E(\boldsymbol{\sigma}) = V_0 + \sum_{\alpha} V_\alpha \sum_{\beta \in \Omega_\alpha} \Phi_\beta(\boldsymbol{\sigma}), \tag{2.18}$$

where each orbit of clusters Ω_α is represented by a single distinct cluster α.

It is also convenient to normalize the cluster expansion by the number of primitive cells of the parent crystal, taken here to equal N, which gives

$$\begin{aligned} \frac{E(\boldsymbol{\sigma})}{N} &= \frac{V_0}{N} + \sum_{\alpha} V_\alpha m_\alpha \left(\frac{\sum_{\beta \in \Omega_\alpha} \Phi_\beta(\boldsymbol{\sigma})}{m_\alpha N} \right) \\ &= v_0 + \sum_{\alpha} V_\alpha m_\alpha \xi_\alpha(\boldsymbol{\sigma}). \end{aligned} \tag{2.19}$$

In this equation, m_α is the multiplicity of the cluster α in the primitive cell, while

$$\xi_\alpha(\boldsymbol{\sigma}) = \langle \Phi_\alpha(\boldsymbol{\sigma}) \rangle = \frac{1}{|\Omega_\alpha|} \sum_{\beta \in \Omega_\alpha} \Phi_\beta(\boldsymbol{\sigma}) \tag{2.20}$$

is the corresponding correlation function, or average value of the cluster function. The

correlation functions (or simply, "correlations") for a particular set of clusters enable us to describe orderings across different supercells in a consistent manner. Note that the cluster multiplicities m_α may be absorbed into either the ECIs or the correlations for compactness. This form of the cluster expansion can exactly represent properties of the infinite crystal, albeit with an infinite number of clusters. In practice, the cluster expansion is truncated to a finite number of terms.

2.2.3 Fitting

Determining the ECIs for a truncated cluster expansion requires first generating a set of training data, consisting of a vector of calculated energies $\mathbf{y}$ (e.g. calculated from DFT) and a matrix of correlations X (obtained directly from the ideal crystal geometry) for a set of distinct configurations. We may then consider the linear regression model

$$\mathbf{y} = X\mathbf{v} + \boldsymbol{\varepsilon}, \tag{2.21}$$

where $\mathbf{v}$ is the ECIs and $\boldsymbol{\varepsilon}$ is the error term. This model can be fit using any number of statistical learning techniques. These typically rely on a (generalized) least squares loss function

$$(\mathbf{y} - X\mathbf{v})^\top M (\mathbf{y} - X\mathbf{v}), \tag{2.22}$$

where M is a symmetric, positive-definite "weight matrix," or equivalently, the inverse of the covariance matrix of $\boldsymbol{\varepsilon}$ given X. Common special cases are when M is identity, known as ordinary least squares, and when M is diagonal, known as weighted least squares. M can be chosen to introduce some statistical or physical intuition into the fitting problem. For instance, one may use diagonal weights to assign more importance to configurations that lie closer to the convex hull in energy-composition space, as those

are thermodynamically more important at low temperatures.

It is typical to consider a large pool of clusters in the truncated expansion, such that the number of correlation functions exceeds the number of configurations (energies). The regression model in this case is underdetermined, meaning there may be infinitely many solutions with $\boldsymbol{\varepsilon} = 0$. To remedy this, one can employ regularization techniques, in which the loss function is augmented by some penalty term that forces a unique solution (e.g. ridge [48] or LASSO [49] regression). Another approach is to explicitly select a set of features (correlation functions) to include prior to fitting (e.g. by genetic algorithm [50] or Monte Carlo approaches [51]). Some techniques, such as LASSO, perform regularization and feature selection simultaneously. Cross-validation scores may be used to optimize fits with respect to any hyperparameters or choice of feature set. Note that while the truncated cluster expansion is generally expected to be sparse (i.e. few nonzero ECIs), there is no inherent reason that it should be [10]. Nevertheless, sparsity is desirable to limit the complexity of the model and avoid unphysical predictions due to overfitting.

2.3 Monte Carlo simulations

The methods described thus far enable the prediction of microscopic properties from first principles. The microscopic behavior of systems is linked to their macroscopic thermodynamic properties, i.e. those observed experimentally, by statistical mechanics. Within this framework, Monte Carlo methods offer a way to efficiently approximate thermodynamic quantities of interest through random sampling.

2.3.1 Thermodynamic averages

The average value of any thermodynamic variable X can be calculated by

$$\overline{X} = \sum_s X(s)\mathcal{P}(s), \tag{2.23}$$

where $X(s)$ is the value of X in microstate s and $\mathcal{P}(s)$ is the probability that the system at equilibrium is in that particular microstate. This probability is given by

$$\mathcal{P}(s) = \frac{1}{Z} e^{-\beta\Phi(s)}, \tag{2.24}$$

where $\beta = 1/k_{\mathrm{B}}T$ for temperature T and Boltzmann constant k_{B}, $\Phi(s)$ is an energy of the microstate s, and Z is the partition function, given by

$$Z = \sum_s e^{-\beta\Phi(s)}. \tag{2.25}$$

The form of $\Phi(s)$ depends on which thermodynamic variables are held fixed (i.e. the particular ensemble). For example, in the canonical ensemble (fixed number of particles N, volume V, and T), $\Phi(s) = E(s)$, the energy itself. In the grand canonical ensemble (fixed chemical potential μ, V, and T), $\Phi(s) = E(s) - \mu N(s)$.

All thermodynamic properties of a system can be derived from its partition function Z. However, the required summation over all possible microstates is generally not feasible, even when equipped with a method to rapidly evaluate the energy of each microstate (such as a cluster expansion). Instead we turn to Monte Carlo methods, namely the Metropolis-Hastings algorithm [52,53], which generates a Markov chain of microstates sampled from the probability distribution $\mathcal{P}(s)$. Following an initial equilibration period, thermodynamic properties can be calculated via a simple average (rather than a weighted

average) over the sampled microstates.

2.3.2 Thermodynamic integration

After performing a set of Monte Carlo simulations, it is usually necessary to calculate the free energy (or characteristic potential), which determines equilibrium for a particular ensemble. In the grand canonical ensemble, the relevant free energy is the grand potential

$$\Omega = E - TS - \mu N. \tag{2.26}$$

Note that for simplicity we have assumed a single chemical species. While average values of E and N are readily obtained from Monte Carlo simulations, the entropy S is not. However, S, and therefore Ω, can be obtained by thermodynamic integration of Monte Carlo data over a grid of T and μ values [54]. At constant T, we can integrate across chemical potential from μ_0 to μ

$$\Omega(\mu) = \Omega_0 - \int_{\mu_0}^{\mu} \mathrm{d}\mu' N\left(\mu'\right), \tag{2.27}$$

where $\Omega_0 = \Omega(\mu_0)$. At constant μ, we can integrate across inverse temperature from β_0 to β

$$\Omega(\beta) = \frac{1}{\beta}\left(\beta_0\Omega_0 + \int_{\beta_0}^{\beta} \mathrm{d}\beta'\Phi\left(\beta'\right)\right), \tag{2.28}$$

where $\Omega_0 = \Omega(\beta_0)$ and, as before, $\Phi = E - \mu N$. In each case, this approach requires careful selection of suitable reference states to obtain values of Ω_0. Typically these are taken to be states with nearly zero entropy, e.g. at extreme values of μ or close to zero temperature, such that $\Omega \approx \Phi$. The result of one integration may also be used as the reference of a subseqeuent integration.

Once Ω has been calculated, it is trivial to obtain other properties based on S, such as

the Helmholtz free energy $F = E - TS$ or the Gibbs free energy $G = E - TS + pV$, where p is the pressure and V is the volume (note that $F = G$ when $p = 0$). It is often necessary to transform values of Ω to values of G, e.g. for the construction of temperature-composition phase diagrams. However, in some cases, such as the construction of equilibrium voltage-composition curves at fixed T, it is simpler to work with Ω directly, as the phase with the lowest value of Ω will be preferred at each value of μ.

2.3.3 Kinetic Monte Carlo

In addition to calculating thermodynamic averages, Monte Carlo simulations can also be used model processes occurring over time within the kinetic Monte Carlo (KMC) method. Consider a system in state k that may undergo a transition to a state i with transition rate $\Gamma_{k,i}$. For example, this could correspond to a single atom hopping from one lattice site to a neighboring one, with a rate given by

$$\Gamma_{k,i} = \nu^* e^{-\beta E_{k,i}}, \tag{2.29}$$

where ν^* is the vibrational prefactor of the hop [55] and $E_{k,i}$ is its energy barrier. Such barriers can be calculated from DFT using the nudged elastic band method [56], and can also be approximated using local cluster expansion methods that account for the dependence of the barrier on the hop's local environment [57].

If the transition rates to all possible states i from the initial state k are known, the system's evolution can be modeled using KMC. A single transition, or event, is selected with probability

$$\mathcal{P}_{k,i} = \frac{\Gamma_{k,i}}{Q_k}, \tag{2.30}$$

where

$$Q_k = \sum_i \Gamma_{k,i} \tag{2.31}$$

is the total rate for exiting state k. The event is then carried out and the time is incremented by

$$\Delta t = -\frac{\ln(u)}{Q_k}, \tag{2.32}$$

where u is uniform random number on $(0, 1]$. The process can then be repeated starting from state i. This method is known as rejection-free KMC (because no candidate events are rejected), or the Bortz-Kalos-Lebowitz algorithm [58]. Its application to a particular model system and an exploration of the resulting kinetic properties are described in Chapter 8.

2.4 Details

All DFT calculations described in the subsequent chapters were performed using the Vienna *Ab initio* Simulation Package (VASP) version 5.4.4 [59–62]. Projector augmented-wave (PAW) method pseudopotentials [41,42] were used, with the following valence configuration labels: Li, Na_pv, K_sv, Ti_sv, Cr_pv, Co, O, S. Brillouin zone sampling was performed using Γ-centered Monkhorst-Pack **k**-meshes [43]. The chosen plane-wave energy cutoff and **k**-mesh density vary by chapter. Spin-polarization was enabled, with all magnetic moments initialized ferromagnetically unless otherwise noted. Structures were relaxed until the forces were smaller than 0.02 eV/Å, prior to performing final static calculations using the linear tetrahedron method [63]. Different exchange-correlation functionals were employed, primarily the optB86b-vdW van der Waals functional [64–67] and the SCAN meta-GGA functional [30,31].

The Clusters Approach to Statistical Mechanics (CASM) software package [10,68–70],

was used throughout to enumerate symmetrically distinct configurations and kinetic hops, construct and fit cluster expansion effective Hamiltonians, and perform grand canonical Monte Carlo simulations. This work was performed using development branches of CASM version 0.2.X/0.3.X.

All crystal structure visualizations were created using VESTA [71].

Chapter 3

Structure and chemistry of intercalation compounds

3.1 Introduction

Rechargeable Li-ion batteries have been tremendously successful in industrial and consumer applications, and continue to attract attention from the research community in order to find ways of further improving battery performance [1, 72]. Efforts are also being made to move beyond Li-ion for low-cost solutions to large-scale energy storage problems. This includes a renewed interest in Na-ion batteries [73] and other less traditional chemistries for batteries that shuttle K [74] and multivalent cations [75, 76]. The success of such technologies hinges on the development of new electrolyte and electrode materials that can withstand the extreme chemical and structural changes that often accompany each charge and discharge cycle of a battery.

Many intercalation compounds, particularly layered ones, have been studied as electrode materials for rechargeable batteries. The canonical layered $LiCoO_2$ [77] and related Ni-Mn-Co (NMC) and Ni-Co-Al (NCA) compounds are used as cathodes in many Li-ion

battery applications [1,78]. Layered intercalation compounds are similarly the subject of great interest for Na- and K-ion battery electrodes [74,79], though there is some question of how they will compete with the current state-of-the-art polyanionic compound $Na_3V_2(PO_4)_2F_3$ for Na-ion battery cathodes [80]. A main obstacle is the prevalence of structural phase transitions involving stacking sequence changes of the layers [81–83], which often lead to mechanical degradation and poor cyclability [80,84]. Many of these materials also exhibit strong cation-vacancy ordering tendencies [81,85,86], which result in large jumps in voltage and sluggish diffusion at particular compositions [87,88]. Turning to other host structures such as spinel may offer benefits of better structural stability and high rate capability [89–92]. Though we will primarily discuss intercalation compounds used as cathode materials, all of these considerations apply to anode materials as well.

In exploring various candidate electrode materials for beyond Li-ion batteries, it is critical to understand their fundamental thermodynamic behavior. Structural phase stability and ordering phenomena have large impacts on many aspects of battery performance including the voltage profile, diffusion rates, and degradation mechanisms. Key thermodynamic properties that may be difficult to access experimentally can be readily probed using first-principles statistical mechanics techniques [10,68–70], which can also be used to examine nonequilibrium kinetic processes [5,57,93–95]. Detailed atomic and mesoscale studies of battery electrode materials based on first-principles techniques may offer more clues as to how to avoid unfavorable phase transitions, or alleviate their effects.

Na-ion batteries provide a lens through which to examine some effects not typically seen in the more well-studied Li-ion systems, including, in particular, ordering phenomena and structural phase transitions in the electrode materials. Certain underlying trends observed here may extend to other more novel chemistries, such as K-ion batteries, and help explain observations in those largely unexplored composition spaces. Recent progress

on beyond Li-ion battery technology, including Na-ion, has been extensively reviewed [3, 73–75, 79, 96–103]. Here, we aim to summarize some insights we have gleaned from computational work into the fundamental behavior of intercalation compounds, with a focus on ordering and stacking sequence changes in layered systems.

3.2 Thermodynamics

First-principles thermodynamic studies of battery materials begin with a calculation of free energies of the relevant phases. Free energies at zero temperature can be calculated using quantum mechanical techniques such as density functional theory (DFT) [17], while free energies at finite temperature can be calculated with statistical mechanical techniques that build on the ground state results using effective Hamiltonians [10, 44]. Figure 3.1(a) shows the free energy of the layered Na_yTiS_2 intercalation compound, calculated at 300 K [8]. The envelope of equilibrium free energies over the different phases as determined with the common tangent construction delineates the single- and two-phase regions as a function of composition.

The free energies of the electrode materials also embed information about the voltage of a battery. Indeed, the battery voltage is determined by the difference in chemical potential of the intercalating species A between the two electrodes according to

$$V(y) = -\frac{\mu_A(y) - \mu_A^\circ}{ne} \tag{3.1}$$

where $\mu_A(y)$ is the chemical potential of A in the cathode at composition y, μ_A° is the chemical potential of A in the reference electrode, n is the number of electrons transferred per A ion, and e is the elementary charge. Note that for reversible electrochemical cells, the positive (negative) electrode is technically only defined as the cathode (anode) upon

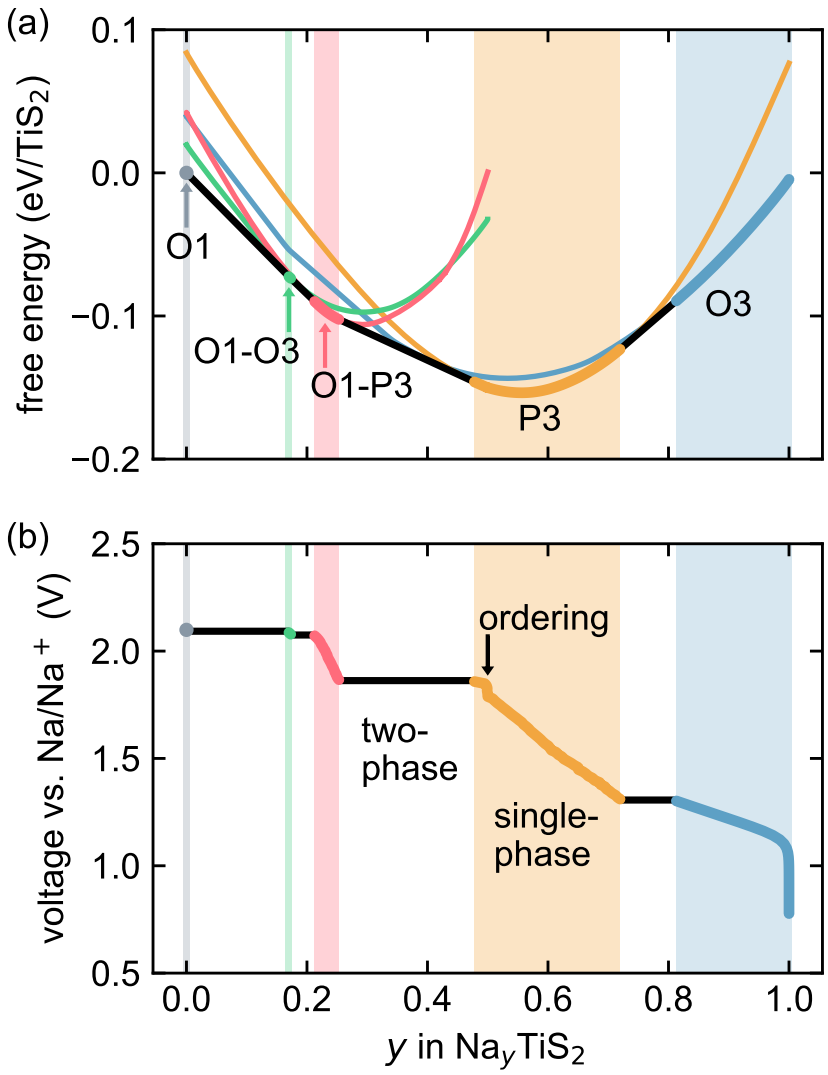

Figure 3.1: (a) Calculated free energy curves of Na_yTiS_2 in different layered host structures at 300 K. The global convex hull of free energies is show with black lines connecting the curves of each stable phase. (b) Voltage curve derived from the free energy at 300 K. Colored rectangles in the background represent single-phase regions, while black lines correspond to two-phase equilibria. The step at $y = 1/2$ corresponds to a stable ordering of Na ions in P3. Data is from Reference [8].

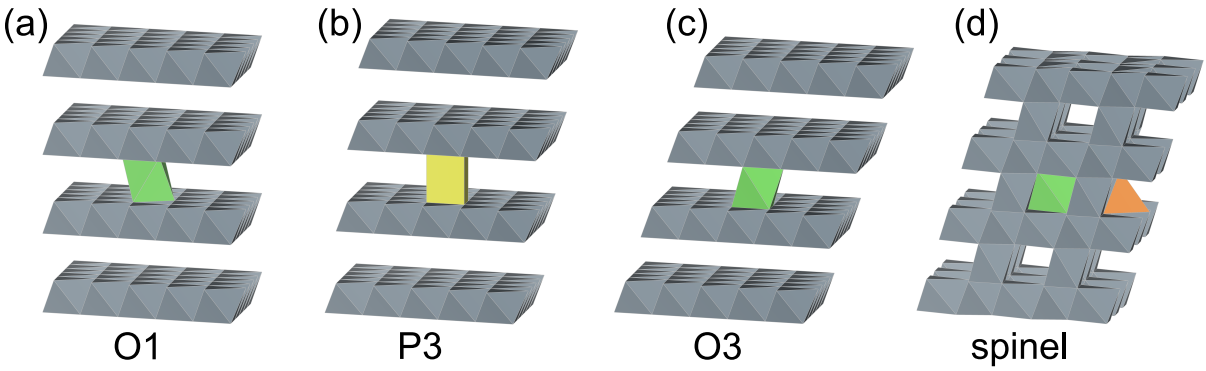

Figure 3.2: The layered (a) O1, (b) P3, and (c) O3 host structures, in addition to (d) the spinel host structure. Gray octahedra represent M cations with X anions at the corners. Green, yellow, and orange are used to show A cations in octahedral, trigonal prismatic, and tetrahedral coordination, respectively.

discharge, while the opposite is true upon charge. However, we will continue to use these terms, consistent with much of the literature. With a constant chemical potential in the reference electrode, the voltage is simply related to the chemical potential of the intercalating species in the cathode, which is the slope of free energy versus composition. Through this connection, the meaning of certain features in the voltage profile become clear, as illustrated in Figure 3.1(b). Plateaus correspond to two-phase regions, where the chemical potential is constant, while steps correspond to ordered phases at fixed composition, where the concavity (the energetic strength) of the ordering determines the magnitude of its step. Sloping regions usually correspond to solid solutions. Note that kinetic effects, chemical participation from the electrolyte, and other extraneous factors can significantly alter the voltage curve, but the equilibrium voltage curve is an essential starting point for understanding battery performance.

3.3 Crystallography

We will discuss compounds of the formula A_yMX_2 $(0 \leq y \leq 1)$, where A is an alkali or alkaline earth metal, M is a transition metal, and X is oxygen or sulfur. Four key

host structures that we will examine are shown in Figure 3.2. The layered (O1, P3, O3) and spinel structures are all based on stacked triangular lattices of X. In the layered compounds (Figure 3.2(a-c)), triangular M layers lie between every other pair of X layers, forming slabs of edge-sharing MX_6 octahedra separated by van der Waals gaps. The intercalant A is inserted into these gaps, and its site topology is determined by the X stacking sequence: A can occupy octahedral sites in O1 and O3 or trigonal prismatic sites in P3, with the available sites sharing faces with two, one, and zero M in O1, P3, and O3, respectively. Hybrid structures that switch between different stackings, such as O1-O3, are also seen, and are often "staged," meaning that the A concentration is not the same in every layer [104, 105].

Closely related to the layered phases is the spinel structure (Figure 3.2(d)). Spinels are normally represented by the formula AM_2X_4, but with vacancies incorporated on the A sites and allowing for octahedral occupancy of the A cations, this may also be expressed as A_yMX_2. Spinel shares the face-centered cubic X framework of O3, but with one quarter of the M moved from the M layers into the gaps. This M ordering results in a three-dimensional interconnected network of MX_6 octahedra in which A can occupy tetrahedral or octahedral sites, neither of which share faces with M.

The commonality of the anion (X) sub lattices of spinel and O3 make phase transitions between the two kinetically facile. The irreversible transition from O3 to spinel, for example, simply requires the migration of one out of every four M from the metal layer to the A layers. There is typically a significant driving force for this transition in partially deintercalated $\mathrm{Li}_y MO_2$ (around $y = 1/2$), although it tends to occur quite gradually due to kinetic limitations [78, 106]. Such a driving force is notably absent in $\mathrm{Na}_{1/2}MO_2$, which has been attributed to the larger size of Na^+ [107]. Note that in the completely deintercalated state ($y = 0$) all layered intercalation compounds tend to be susceptible to decomposition into other phases.

In contrast to the O3-spinel transition, transitions between different layered structures within the O3 family (O3, P3, O1, and their hybrids) are generally reversible and facilitated through the shearing of MX_2 slabs [108]. Though we focus on the O3 family here, there is another family of layered structures based on a distinct set of stackings called the O2/P2 family [109]. Any transition between the two families requires a stacking sequence change of the layers within a single MX_2 slab and is therefore prohibited at room temperature by the energetic cost of breaking M-X bonds. P2 compounds have received great interest as Na-ion battery electrodes [73,87], but higher capacities are generally achievable with the O3 family because P2 hosts are often not fully intercalated in order to avoid the transition to O2 [110]. O3-type compounds also yield higher voltages since the NaMX_2 end member is usually most stable in the O3 structure [111, 112].

3.4 Chemistry

The chemical properties of the intercalant A are important in determining its behavior within an intercalation compound. Consider the intercalants Li, Na, K, Mg, and Ca. These exhibit a range of ionic radii, with $Mg^{2+} \approx Li^{+} < Ca^{2+} \approx Na^{+} < K^{+}$ (based on the Shannon crystal radii [113] for six-coordination). The ionic radius influences the preferred coordination for each species, as well its migration barriers and the distortions it induces when inserted into a host structure. The difference in valence between monovalent cations (Li^{+}, Na^{+}, K^{+}) and divalent cations (Mg^{2+}, Ca^{2+}) is important not only in setting the battery capacity and voltage but also in scaling the strength of electrostatic interactions within the electrode material. The other key factor for electrostatics is electropositivity, for which Mg < Ca and Li < Na < K. More electropositive species tend to give up more of their electrons, resulting in stronger electrostatic interactions.

The chemistry of the host MX_2 plays a key role in its electronic structure. Electronic

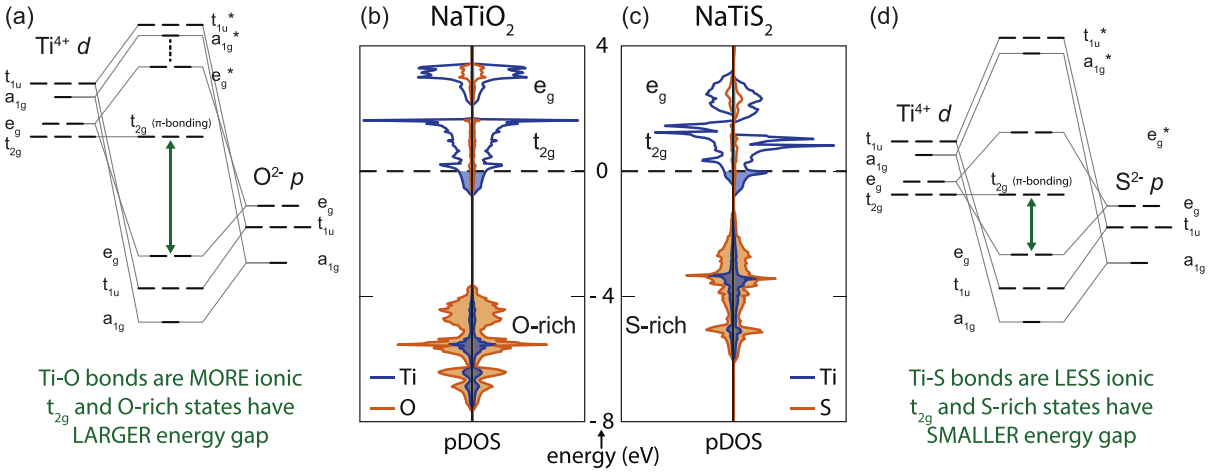

Figure 3.3: Molecular orbital diagrams for isolated (a) TiO_6 and (d) TiS_6 octahedra alongside the partial density of states of layered (b) $NaTiO_2$ and (c) $NaTiS_2$ in the O3 structure. Na density of states is shown in gray, but is negligible in this energy range.

structure is often analyzed by looking at density of states (DOS) diagrams (or partial DOS (pDOS) where the density is broken up by contributing species), which indicate the density of electrons at specific energy levels. As a simplified model, consider an isolated octahedron of a transition metal such as Ti surrounded by six ligand species (e.g. O or S). The degeneracy of the transition-metal d orbitals is split by the ligand field according to the O_h symmetry group in a perfect octahedron [114, 115]. The octahedra in real compounds are often distorted such that the degeneracy of the orbitals is reduced further (for example, the octahedral transition-metal environments in the layered structures are typically trigonally compressed along the stacking direction, lowering their symmetry to D_{3d}).

The d orbitals of the transition metal and the p orbitals of the ligand readily interact to form hybridized states. Molecular orbital diagrams depicting the hybridization between these species are shown in Figures 3.3(a) and (d) for perfect TiO_6 and TiS_6 octahedra, respectively. We have shown only σ-bonding (no π-bonding) in these simplified diagrams. The states within each species' orbitals can be assigned to a symmetry group

representation, and only states with the same representation can hybridize. Note, for instance, that there are no available t_{2g} O or S states to σ-bond with the available t_{2g} Ti states (though it turns out they can hybridize via π-bonds). When states hybridize, they split into low-energy bonding and high-energy antibonding (indicated by an asterisk) hybridized states. Electrons fill lowest energy states first (i.e. from the bottom of the diagram up), filling up to around the t_{2g} states for materials discussed in this work. The bonding states (e.g. t_{1u} and a_{1g}) are below the energy of the isolated ligand p states, are filled first, and have mainly ligand character; the antibonding states (e_g^*, a_{1g}^*, and t_{1u}^*) are above their respective Ti states and therefore have largely transition-metal character.

The available states in TiO_6 are identical to those in TiS_6 and it is only the relative energy of the states that differs between the two chemistries. The more ionic the M-ligand pair (i.e. the greater their electronegativity difference), the further apart in energy the hybridized states will reside, which can be seen in comparing the pDOS of layered $NaTiO_2$ and $NaTiS_2$ crystals (Figures 3.3(b) and (c)). The intercalant (in this case, Na) serves largely as an electron donor and is generally not considered to hybridize with the transition metals or ligands. However, increased intercalant concentration does raise the Fermi level as more electronic states are filled. For instance, Ti^{4+} in TiX_2 has a d^0 electronic configuration while Ti^{3+} in $NaTiX_2$ results in d^1, corresponding to one electron beginning to fill the t_{2g} states.

When an octahedron is in a crystal, the localized states spread out into bands and new, more complicated symmetries are introduced. However, we can approximate the regions in the pDOS diagram as ligand-rich states, t_{2g}-like states, and e_g-like states. The dashed line at the top of the filled states indicates the Fermi level, which is conventionally set to 0 eV. We see that the decrease in ionicity between Ti and S (as compared to O) results in a considerable decrease in the energy gap between the S-rich states and the e_g and t_{2g} states. Since electronic structure plays a role in conductivity, magnetization,

and even structural changes, understanding the effects of different transition metal and ligand pairings is instrumental in material design. Oxides tend to be more ionic than sulfides due to the high electronegativity of O. The transition metal identity can also have a significant effect. We have focused on the TiS_2 and CoO_2 hosts, as the itinerant nature of their valence electrons and absence of Jahn-Teller activity makes these good model systems for examining fundamental behavior.

3.5 Trends in phase stability

A high-throughput study of layered A_yTiS_2 and A_yCoO_2 (A = Li, Na, K, Mg, Ca) identified key trends in phase stability and the energetic factors underlying them [7]. Three important factors are depicted in Figure 3.4 and can be explained in terms of size considerations and varying strengths of competing electrostatic interactions between different cations. The strength of these electrostatic effects depends significantly on the ionicity of the compound [7]. This simplified picture does not include purely steric effects or highly covalent bonding, but nonetheless accounts for much of the observed behavior.

The relative stability between prismatic and octahedral A coordination is strongly influenced by X-X interactions. Prismatic coordination leads to a shorter interlayer X-X distance than octahedral coordination for fixed A and X ionic radii (Figure 3.4(a)). Smaller intercalants such as Li are therefore unstable in prismatic coordination because the X anions are too close together, while larger intercalants such as Na and K do not penalize the host when it adopts a P3 or P2 structure.

Face-sharing between AX_6 polyhedra and MX_6 octahedra also influences the stability of different layered structures due to the repulsive nature of the short-range A-M interactions (Figure 3.4(b)). In P3 each A site shares a face with one MX_6 octahedron, while in O3 there is no face-sharing. More ionic compounds therefore tend to adopt O3 at

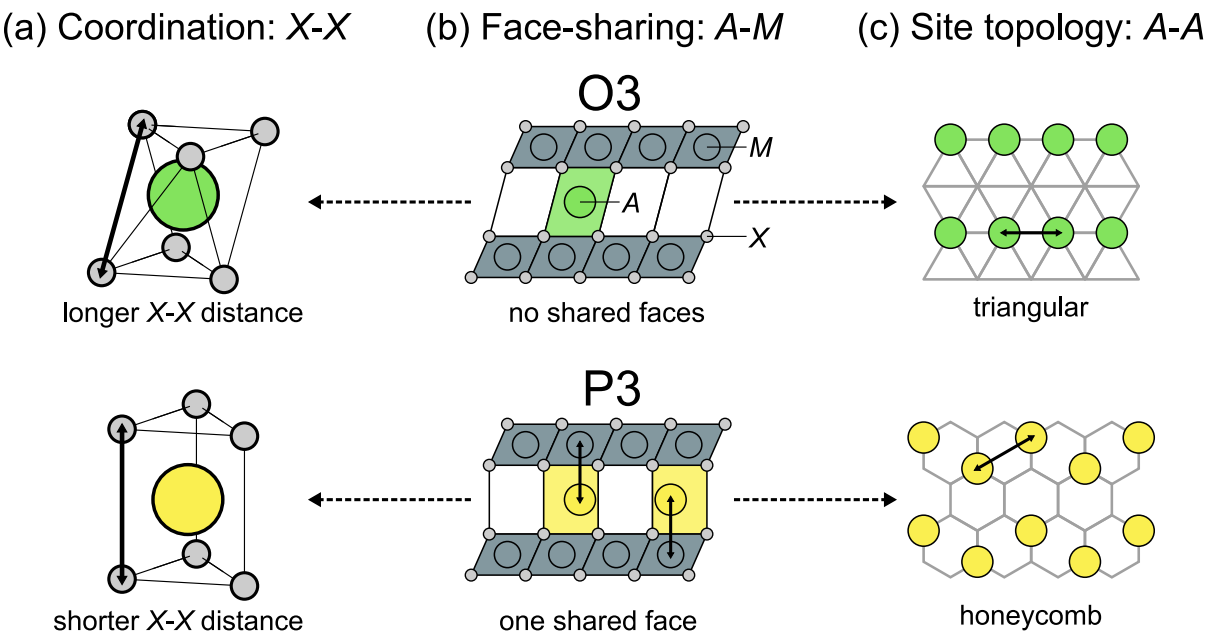

Figure 3.4: Important electrostatic interactions that determine phase stability in AMX_2 layered intercalation compounds, illustrated using O3 and P3 as examples. (a) Interlayer X-X distances determine whether prismatically coordinated A are stable. (b) Face-sharing results in energetically unfavorable A-M interactions (c) The sites available to intercalants determine the possible orderings that limit A-A interactions.

high compositions to avoid the electrostatic repulsion of face-sharing sites. The octahedral sites of O1 share faces with both neighboring MX_6 octahedra, making O1 unstable for any intercalant concentration in more ionic compounds. More covalent compounds, however, tend to adopt O1 over the full composition range, which has been ascribed to a diminished repulsion between X p orbitals in the gap between layers [116].

The topology of the A sites within each host plays an important role in determining the type of ordered phases that are possible at intermediate intercalant compositions. In more ionic compounds, repulsive electrostatic interactions will strive to separate the A cations as far apart from each other as possible within each intercalant layer. In P3, the available prismatic A sites form a honeycomb network, which allows for A-A distances that are not available on the triangular lattice of octahedral A sites in O3 (Figure 3.4(c)). This tends to stabilize P3 at intermediate concentrations when the benefit of maximizing A-A distances on the honeycomb network outweighs the penalty for face-sharing. Repulsive interactions on the honeycomb network can lead to intricate A orderings which will be discussed later.

A systematic study of spinel A_yTiS_2 and A_yCoO_2 (A = Li, Na, Mg) revealed similar trends in these compounds [117]. Here the host structure is fixed and intercalants may occupy either octahedral or tetrahedral sites, the relative stability of which is determined by two competing factors: Larger cations favor the octahedral sites because they offer more space, while tetrahedral sites allow A cations to lie further away from neighboring M cations and limit A-M interactions. The latter is more important in more ionic hosts, much like the face-sharing penalty in the layered structures.

In the layered and spinel structures, phase stability is greatly influenced by the identities of both the host and the intercalant. Electrostatic interactions are stronger in more ionic hosts such as CoO_2 compared to more covalent hosts such as TiS_2. Furthermore, intercalation of a more electropositive species, such as Na compared to Li, results in

stronger A-A and A-M repulsions. Ion size plays a similar role in the layered structures, as larger ions such as Na and K result in larger interlayer spacing and reduced screening from the X anions [105]. Divalent intercalant cations such as Mg and Ca tend to create stronger electrostatic interactions than monovalent ones from the same period, as their charge is doubled [117, 118].

To examine some of the trends in phase stability more closely, we turn to voltage profiles and phase diagrams obtained from first-principles studies [8, 12, 92, 93]. Figure 3.5 shows calculated room temperature voltage profiles and phase diagrams of Li_yTiS_2, Na_yTiS_2, and Na_yCoO_2 in the layered (O3-type) and spinel structures. The agreement with available experimental voltage curves, which are shown in red, is quite good. Recall that plateaus correspond to two-phase regions, while steps correspond to ordered phases. The steepness of each curve is related to the strength of A-A repulsion, which reflects the ionicity of the compound: The Na_yCoO_2 voltage curves in Figure 3.5(c,f) are noticeably steeper than their respective Na_yTiS_2 counterparts in Figure 3.5(b,e). The particular characteristics of the transition metal, such as on-site electron repulsion, can also affect the slope and average value of the voltage. For oxides, a systematic underprediction of the voltage is not uncommon when using DFT (without additional corrections such as a Hubbard U) [123].

Layered Li_yTiS_2 is quite covalent and remains O1 at all Li concentrations (Figure 3.5(a)). Mg_yTiS_2 (not shown) behaves quite similarly [118]. Na_yTiS_2, conversely, stabilizes O3 at high Na concentrations and P3 at intermediate concentrations (Figure 3.5(b)). O1 is stable only at $y = 0$, while staged hybrid O1-P3 and O1-O3 phases are predicted to be stable at low Na concentrations. Na_yCoO_2 stabilizes similar phases as those adopted by Na_yTiS_2 but there are some important differences which reflect the increased ionicity of Na_yCoO_2. The Na_yCoO_2 voltage curve is steeper and contains more steps (the curve shown was actually calculated at zero temperature because none of the ground states

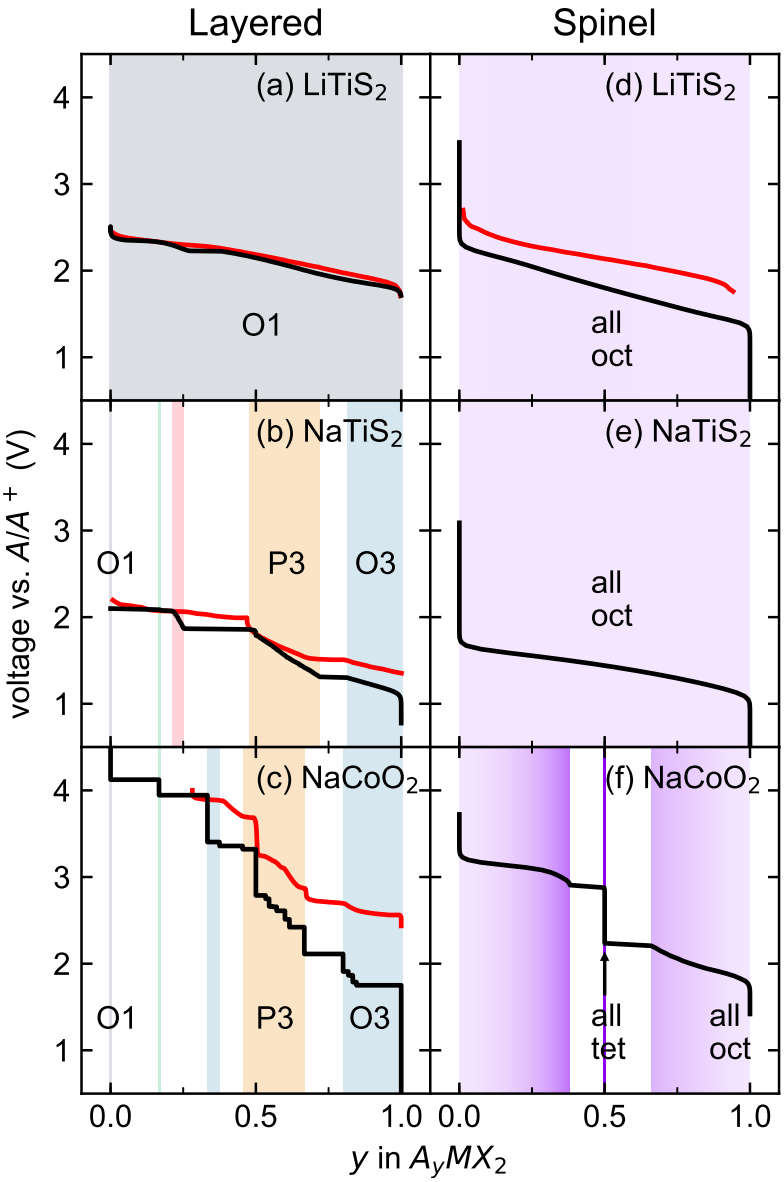

Figure 3.5: Calculated equilibrium voltage profiles (black) for various layered (a [93], b [8], c [12]) and spinel (d,e,f) [92] intercalation compounds at 300 K. Available experimental curves (red) are shown for comparison in (a [119], b [120], c [121], d [122]). Colored rectangles in the background of (a,b,c) indicate regions in which each layered host structure was found to be stable. Background color in (d,e,f) indicates the fraction of A occupying tetrahedral sites (versus octahedral sites) in the spinel host structure.

were found to disorder at room temperature [12]), with a much larger step at $y = 1/2$ compared to that of $Na_{1/2}TiS_2$ (Figure 3.5(c)). The ordering that produces this step will be discussed in Section 3.6. A significant step near $y = 1/2$ has also been observed in some K intercalation compounds [124,125], which likely corresponds to a similar ordering [126]. P3 is stable up to $y = 2/3$ in Na_yCoO_2 versus $y \approx 0.72$ in Na_yTiS_2, indicating that the face-sharing penalty begins to destabilize P3 sooner in the more ionic Na_yCoO_2. The even more ionic Na_yTiO_2 (not shown) remains O3 throughout cycling [127, 128], as face-sharing in P3 is likely even more unfavorable.

In the spinel host, Li_yTiS_2 and Na_yTiS_2 display similar solid solution behavior resulting in smooth voltage profiles (Figure 3.5(d,e)). The intercalants in these compounds occupy only octahedral sites. In the more ionic Na_yCoO_2, occupancy of tetrahedral and octahedral sites were found to be essentially degenerate, with the energy penalty of the smaller tetrahedral sites being balanced by reduced A-M interactions [92]. This results in solid solution behavior with mixed octahedral and tetrahedral occupancy at high and low Na concentrations. However, at $y = 1/2$ the compound orders with Na filling all the tetrahedral sites, thereby maximizing the distances between Na cations. This ordering produces a significant step in the voltage curve, with two-phase regions on either side (Figure 3.5(f)). Mg, being a divalent cation, produces stronger electrostatic interactions than Na, stabilizing some tetrahedral occupancy in Mg_yTiS_2 and multiple ordered phases in Mg_yCoO_2 (not shown) [92, 117].

In the following sections, we focus on ordering and structural changes that can occur in layered intercalation compounds. First we present the rich intercalant orderings that appear in more ionic compounds and then we discuss the mechanisms for structural phase transitions between layered structures.

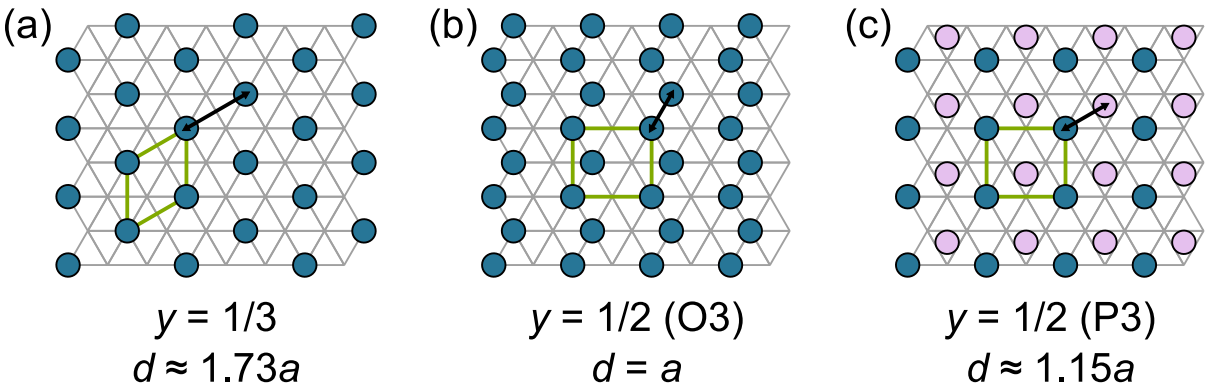

Figure 3.6: Typical low-energy A orderings predicted at (a) $y = 1/3$ in O3 and P3, (b) $y = 1/2$ in O3, and (c) $y = 1/2$ in P3. a is the lattice parameter and d is the shortest A-A distance. Dark blue and light purple are used to distinguish between the two different triangular sublattices.

3.6 Intercalant orderings

Larger intercalants such as Na and K tend to form ordered phases in more ionic hosts, which manifest themselves as steps in the voltage profiles. Both the O3 and P3 structures favor the hexagonal ground state ordering at $y = 1/3$, shown in Figure 3.6(a) [8,12,126]. This ordering maximizes the distance between A cations where the shortest A-A distance is $d = \sqrt{3}a \approx 1.73a$ (a being the lattice parameter). At $y = 1/2$, however, it is not possible to arrange the A ions on a single triangular sublattice without occupying adjacent nearest-neighbor sites with separation $d = a$ (Figure 3.6(b)). Orderings at $y = 1/2$ in O3 are therefore frustrated in the sense that they must include this electrostatically unfavorable interaction [7]. However, if a second triangular sublattice is available, as in P3, the A ions can spread out slightly further to achieve a separation of $d = \frac{2}{\sqrt{3}}a \approx 1.15a$. This is realized in the zig-zag row ordering at $y = 1/2$ shown in Figure 3.6(c), which is observed in many Na intercalation compounds in both the P3 and P2 structures [97,121,129–131].

The honeycomb network of A sites in P3 yields many more possible orderings than O3, which can result in very complex ground states at intermediate intercalant concentrations. However, a unifying picture of these orderings is revealed by considering them as regions

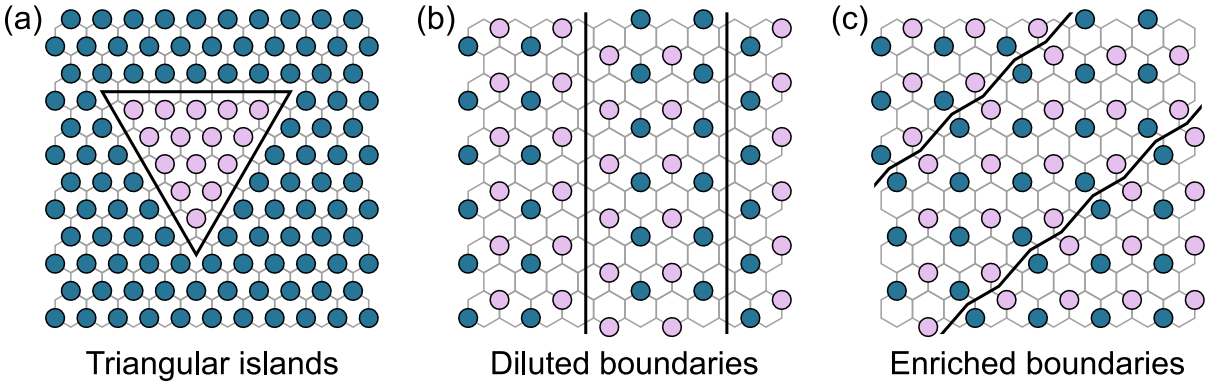

Figure 3.7: Different types of antiphase boundaries predicted to appear on the honeycomb network in P3. (a) Vacancies congregate along boundaries to form triangular island domains at high compositions. At intermediate compositions, two type of boundaries incorporate (b) additional vacancies or (c) additional A ions between regions of the $y = 1/2$ ordering from Figure 3.6(c). Dark blue and light purple are used to distinguish between the two different triangular sublattices.

of one ordering separated by antiphase boundaries (APBs). For example, in Na_yTiS_2, the P3 orderings at room temperature are predicted to consist of triangular islands of Na occupying a single sublattice, as shown in Figure 3.7(a) [8]. The APBs formed along the edges of the triangular domains introduce vacancies into the structures. The total length of APBs therefore determines the composition. Another example is in Na_yCoO_2, where the zig-zag row ordering at $y = 1/2$ is much stronger than in Na_yTiS_2. As such, the orderings immediately above and below $y = 1/2$ preserve this ordering locally, but include APBs to accommodate changes in Na composition. There are two types of boundaries that introduce either more vacancies ("diluted") or more Na ("enriched"), as shown in Figure 3.7(b,c) [12]. More complicated orderings are predicted between $y = 4/7$ and $y = 2/3$ that are based on the $y = 4/7$ ground state periodically separated by another type of "enriched" APB. More details about the precise orderings are reported in Reference [12]. The same intercalant ordering preferences have been predicted for K_yCoO_2 in the P3 structure [126].

In both Na_yTiS_2 and Na_yCoO_2, stable ordered superstructures are predicted at nearly

arbitrary composition (within some range) and formed by incorporating a certain density of APBs. This produces sloping regions in the voltage profile that correspond to sequences of ordered structures rather than solid solutions. Similar ordering phenomena may very well occur in other systems that stabilize the P3 structure. The occurrence of such orderings may also give rise to more exotic diffusion mechanisms than are usually considered. For example, diffusion could occur exclusively along "diluted" APBs [8], resulting in reduced dimensionality of transport, or by creation/annihilation of APBs in waves throughout the crystal. Detailed kinetic studies are required to resolve these mechanisms exactly.

3.7 Stacking sequence changes

Stacking sequence changes in layered intercalation compounds can be accomplished by a simple shearing of the MX_2 slabs. These transitions tend to be more prevalent in intercalation compounds containing larger ions such as Na and K since they can stabilize prismatic coordination. O3 typically transitions to P3 toward the beginning of charge (deintercalation), while empty layers take on O1 stacking toward the end of charge to form hybrid structures (consisting of a mix of O1 and O3 or O1 and P3 layers) and eventually purely O1. These stacking sequence changes are accompanied by a collective reordering of the intercalant within the layers as the composition changes. Such transitions are critical to battery performance and can lead to mechanical degradation of electrode materials.

Despite the prevalence and importance of stacking sequence changes, the finer details of these processes are not well understood. First-principles techniques can be used to gain some insights into these transitions that may be difficult to probe experimentally. A fundamental property of interest here is the generalized stacking fault energy or γ-surface, which gives the energy per unit area of shearing half of a crystal relative to the

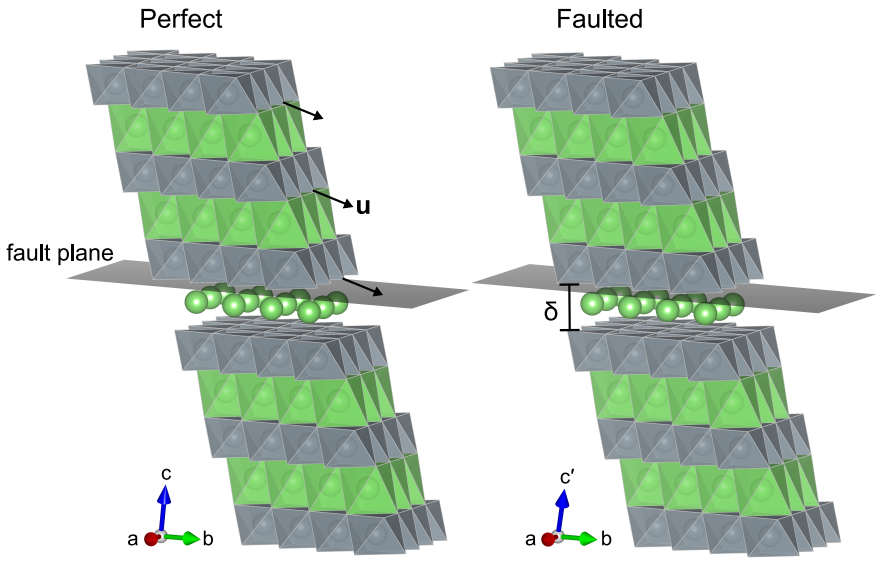

Figure 3.8: Stacking of an O3 AMX_2 supercell before and after shearing by $\mathbf{u} = \frac{\mathbf{a}}{2} + \frac{\mathbf{b}}{2}$. The displacement vector $\mathbf{u}$ has been scaled up by a factor of three for better visibility. M and A ions are shown as gray and green, respectively, with X anions at the corners of all octahedra. The fault plane is shown in gray.

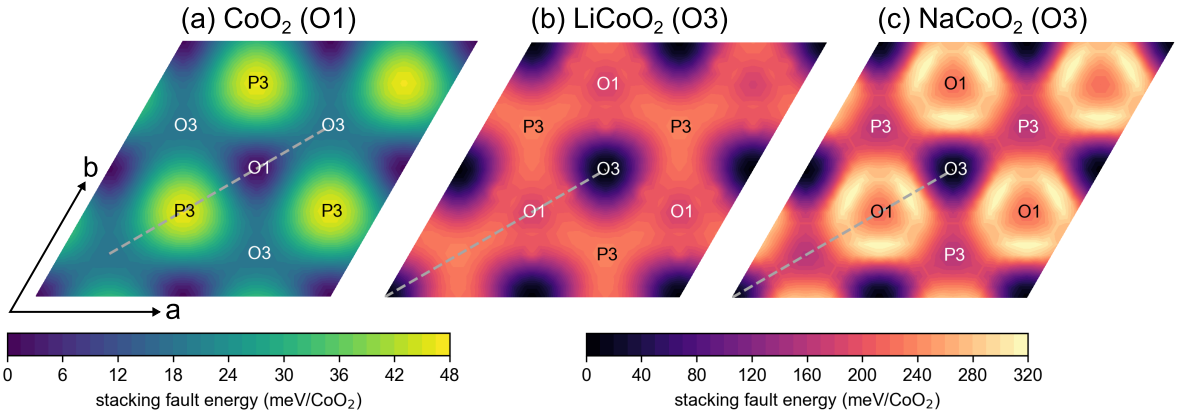

Figure 3.9: Calculated γ-surfaces of (a) O1 CoO_2, (b) O3 $LiCoO_2$, and (c) O3 $NaCoO_2$. Special points on the surface are annotated with the local stacking.

other half [132, 133]. This has long been recognized as a key property that influences deformation behavior in metallic alloys [134–137]. The stable points corresponding to local minima of the γ-surface represent allowed stackings, while the unstable points, which are experimentally inaccessible, give the barriers between those stackings. This information provides a starting point for understanding stacking sequence changes as well as key parameters for multiscale modeling efforts.

Figure 3.8 illustrates the methodology of our γ-surface calculations. Supercells with three MX_2 slabs are used to isolate faults from their periodic images. A displacement $\mathbf{u}$ within the **a**-**b** plane is introduced by adjusting the $\mathbf{c}$ lattice vector ($\mathbf{c}' = \mathbf{c} + \mathbf{u}$), which changes the stacking between each periodic supercell and the next. For each displacement $\mathbf{u}$, we optimize the interlayer spacing δ around the fault plane as well as the position of the intercalant ion nearest to the fault plane. More details about the calculations are described in Appendix B. Figure 3.9 shows calculated γ-surfaces of CoO_2 in the O1 structure and $LiCoO_2$ and $NaCoO_2$ in the O3 structure. Each point on these surfaces corresponds to a particular displacement vector $\mathbf{u}$, with the color representing the stacking fault energy. Special points are labeled with the *local stacking* of the oxygen layers around the fault plane (O1, O3, or P3) although the remaining layers retain their original stacking, as illustrated in Figure 3.8. Note the difference in energy scales between the three compositions: the highest point for $LiCoO_2$ is about five times that of CoO_2, while the highest point for $NaCoO_2$ is about 30% higher than that of $LiCoO_2$. The energy landscape is relatively flat in CoO_2 because the interlayer interactions are mainly limited to van der Waals forces. The presence of an intercalant raises the energy through A-O and A-Co interactions, which are more significant with the larger and more electropositive Na than Li. Another important detail is the three-fold symmetry of the crystal, which is reflected in the γ-surfaces. With this underlying symmetry there are three equivalent directions for a given stacking sequence transition to occur, so it may not proceed in

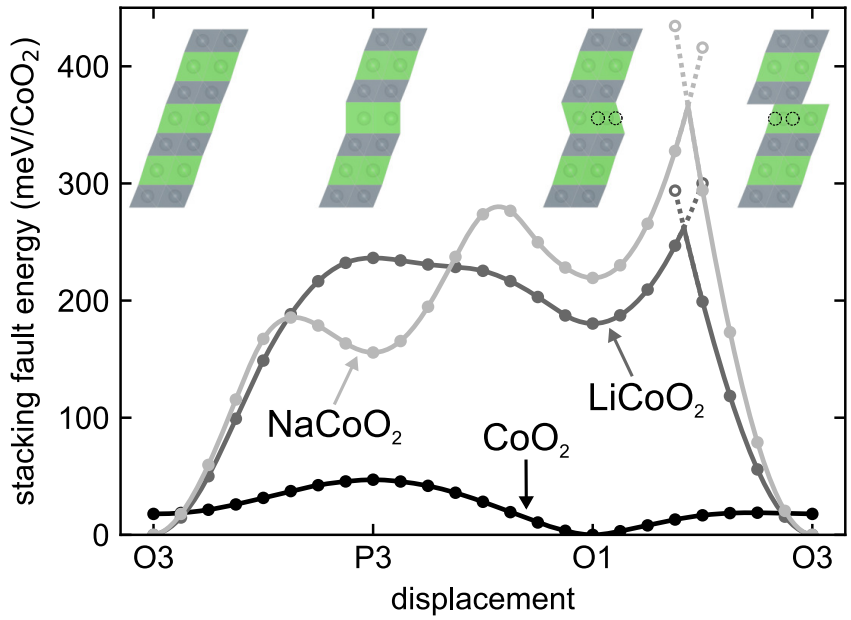

Figure 3.10: Stacking fault energy along the [110] direction (gray dashed lines in Figure 3.9) for CoO_2, $LiCoO_2$, and $NaCoO_2$. Circles indicate calculated points. Filled circles and solid lines represent equilibrium fault energies, while open circles and dotted lines represent metastable fault energies. Inset supercells show the most stable local A coordination within the O3 structure for $LiCoO_2$ and $NaCoO_2$ at each special point on the γ-surface. Black dotted circles in the insets identify vacant tetrahedral A sites within the structures.

the same crystallographic direction going forward and backward even if it is completely reversible. This entropic effect can lead to "electrochemical creep" after many cycles, resulting in roughening of the electrode particles [84].

To compare the γ-surfaces from Figure 3.9 more closely, we examine the energy along the dotted line connecting O3 to P3 to O1 to O3, shown in Figure 3.10. The preferred coordination of the intercalant in the fault plane at each special point is also shown. For both $LiCoO_2$ and $NaCoO_2$, the intercalant favors prismatic coordination in a local P3 stacking and octahedral (as opposed to tetrahedral) coordination in a local O1 stacking. However, the relative stabilities of each local stacking are different. In $NaCoO_2$, local P3 stacking is more favorable than O1, and both are local minima. In $LiCoO_2$, the situation

is reversed, and P3 is actually an unstable maximum. This confirms the established fact that Li is too small to stabilize prismatic coordination. The CoO_2 curve has its lowest value in O1, has a local minimum in a local O3 stacking, and has a maximum for a local P3 stacking, with smooth transitions in between. In contrast, the curves for $LiCoO_2$ and $NaCoO_2$ are mostly smooth but both contain a sharp cusp between the O1 and O3 minima that corresponds to an abrupt change in the intercalant position as the structure is sheared. The smooth transitions (O3 $\leftrightarrow$ P3 and P3 $\leftrightarrow$ O1) require the intercalant to travel along with either the top or bottom layer as the crystal is sheared. However, for the O1 $\leftrightarrow$ O3 transition, if the intercalant travels continuously along with either the top or bottom layer it moves toward a tetrahedral site (black dotted circles in the insets of Figure 3.10), which is higher in energy than the preferred octahedral site. The presence of this cusp feature highlights an important subtlety of γ-surfaces in layered intercalation compounds in that careful consideration of intercalant site preference must be accounted for when calculating them.

The γ-surfaces of Figure 3.9 collect the energies associated with a homogeneous shear of adjacent MX_2 slabs in layered intercalation compounds. However, these materials do not undergo stacking sequence changes via the macroscopic collective shearing of an entire particle. Much like in metallic alloys, the transitions are instead likely mediated by dislocation motion, which requires less energy [133, 138, 139]. Dislocations have also been observed in intercalation compounds [104, 139–145]. The details of their behavior, however, are still largely a mystery, so we will simply present some underlying concepts.

Figure 3.11 schematically illustrates an electrode particle as it transitions from O3 to P3 upon deintercalation of Na. During the transition the two phases coexist within the same particle and are separated by a moving front at which a stacking sequence change from O3 to P3 must occur. These local changes in the stacking sequence is likely to be mediated by a periodic array of dislocations as schematically represented by right

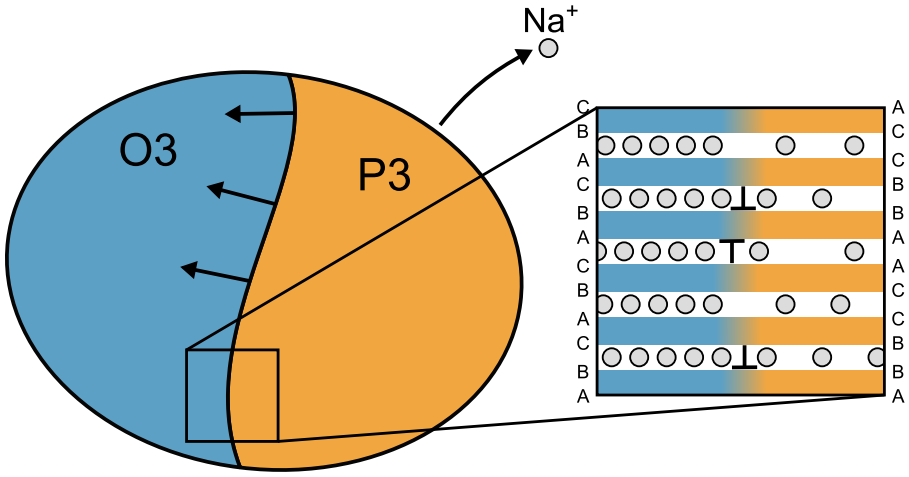

Figure 3.11: Depiction of an electrode particle undergoing a first-order transition from O3 to P3 upon deintercalation of Na. Inset shows a suggested dislocation structure at the interface.

side up and upside down "T"s. By simply considering the X anion stacking sequences of the two structures (AB CA BC for O3 versus AB BC CA for P3), we arrive at the dislocation structure shown in the inset of Figure 3.11. Because O3 and P3 have the same stacking periodicity, every third layer is continuous, while pairs of dislocations must be introduced along the phase boundary to accommodate the change in stacking. Another important detail is the depletion of Na locally within the P3 phase. A severe gradient in composition may result in a large interlayer spacing mismatch along the boundary and lead to cracking.

In Figure 3.12, we show what the dislocation structure along the phase front may look like within the X layers. The X layer below the intercalant layer is shown in dark gray, while the layer above is shown in blue or orange, depending on the stacking. Dislocation lines may change directions or form kinks throughout the particle. The dislocation structure may also consist of a sudden change between the two stackings or a more continuous transition. The former would result in large local strain of the layers but a lower stacking fault energy (Figure 3.12(a)), while the latter would result in smaller strain and higher stacking fault energy (Figure 3.12(b)). The competition

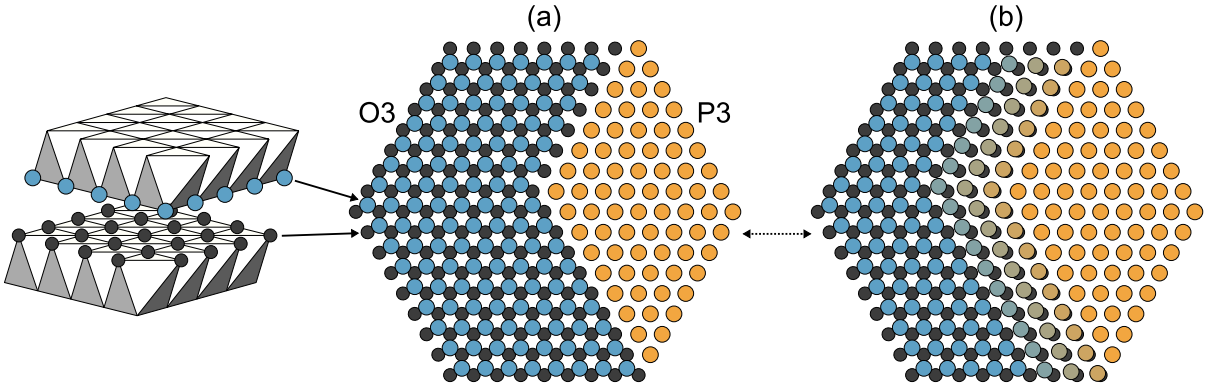

Figure 3.12: Dislocation structure of an O3/P3 two-phase region viewed along the stacking direction, showing only the two X anion layers nearest to the fault plane. The layer below is shown in dark gray, while the layer above is shown in blue or orange for O3 or P3, respectively. In (a) the change in stacking is abrupt, while in (b) it is more continuous, as reflected by the color gradient.

between strain and stacking fault energies should therefore determine how spread out the dislocation is. A clearer picture of these dislocations and their motion will provide a better understanding of stacking sequence changes, and perhaps how to mitigate them.

3.8 Conclusion

As battery research pushes beyond Li-ion technology into less well-explored territory, a fundamental understanding of materials in these composition spaces must be developed. We have illustrated the utility of first-principles techniques to predict detailed behavior of electrode materials. In both layered and spinel host structures, simple size and electrostatic effects can explain thermodynamic trends with varying host and intercalant identities. These include site preferences in spinel, as well as the relative stability of various layered phases and intercalant orderings.

We have highlighted two phenomena that are more prevalent in layered Na intercalation compounds than their Li counterparts: complex Na-vacancy orderings and phase transitions involving shearing of the host layers. Staircases of ordered superstructures

that incorporate composition changes through antiphase boundaries likely have profound implications for Na diffusion, while stacking sequence changes can cause increased susceptibility to mechanical degradation.

Our examination of stacking sequence changes suggests potential strategies that could be developed to avoid them. These transitions may be prevented or delayed thermodynamically through tuning of the host chemistry and ionicity [146], or kinetically penalized by achieving a high dislocation energy. If they cannot be avoided, then they could perhaps be managed so that they are not as harmful, for instance by matching lattice parameters of the two endpoint phases [80]. The challenges inherent to intercalating Na and other less traditional cations can hopefully be overcome through a combination of experimental efforts and computational insights in order to develop next-generation electrode materials.

Chapter 4

Ordering and phase stability in layered Na_xCoO_2

4.1 Introduction

Na-ion batteries offer a promising alternative to Li-ion for applications in which weight is not critical. Layered intercalation compounds have received widespread attention as positive electrodes for both technologies since the 1980s [79,97,109]. Layered Na intercalation compounds typically undergo more structural phase transformations upon cycling compared to their Li counterparts [73,81–84,112,128,130,147–156] due to the stability of both octahedral and prismatic Na coordination [78,157]. Furthermore, host structures that offer prismatic sites to Na allow for more complex Na-vacancy orderings than are possible in hosts with octahedral sites. Structural phase transitions and Na orderings are both important in determining the voltage profile, susceptibility to degradation, and diffusion mechanisms of electrode materials.

Many layered transition-metal oxide and sulfide Na intercalation compounds have been investigated experimentally [97] and computationally [7,8,158,159]. Two distinct

types of phases are synthesized: P2 and O3, with the latter converting to P3 upon deintercalation through the gliding of transition-metal oxide/sulfide slabs. O3-type Na_xCoO_2 ($0 \leq x \leq 1$) is among the oldest [108] and one of the most studied layered Na intercalation compounds [97], but the details of Na ordering as the compound is deintercalated are not well-understood. Experimental voltage profiles suggest rich ordering phenomena in the P3 phase for intermediate Na content, but so far no comprehensive picture of these orderings has been established.

An overview of the O3-type Na_xCoO_2 host structures considered in this study is shown in Figure 4.1. Each consists of stacked triangular lattices of O alternated by layers of Co and Na/vacancies. The Co and O layers form sheets of edge-sharing CoO_6 octahedra, and the stacking sequence of the O layers determines the coordination of the Na sites. In O1 stacking (AB), each Na site is octahedrally coordinated by O and shares faces with the two neighboring CoO_6 octahedra. In O3 stacking (AB CA BC), the Na sites are also octahedrally coordinated but do not share faces with CoO_6 octahedra. In P3 stacking (AB BC CA), each Na site is prismatically coordinated and shares a face with a single CoO_6 octahedron, either above or below. While the Na sites in O1 and O3 belong to a single triangular lattice, those in P3 lie on one of two distinct triangular lattices that together form a honeycomb network. This allows for Na-Na pair distances in P3 that are not available in O1 or O3, expanding the possible orderings that Na may take on to minimize electrostatic interactions [7]. Phase transformations within this set of structures are accomplished by gliding of CoO_2 sheets, without the need to break strong bonds. In addition to the pure structures O1, O3, and P3, hybrid structures such as O1-O3 (also known as H1-3) and O1-P3 are also possible. The labels O′3 or P′3 are commonly used to indicate a distortion of the O3 or P3 parent structure [108].

In this study, we use first-principles techniques to predict phase stability and ground state Na orderings within the various host structures that can be derived from O3-type

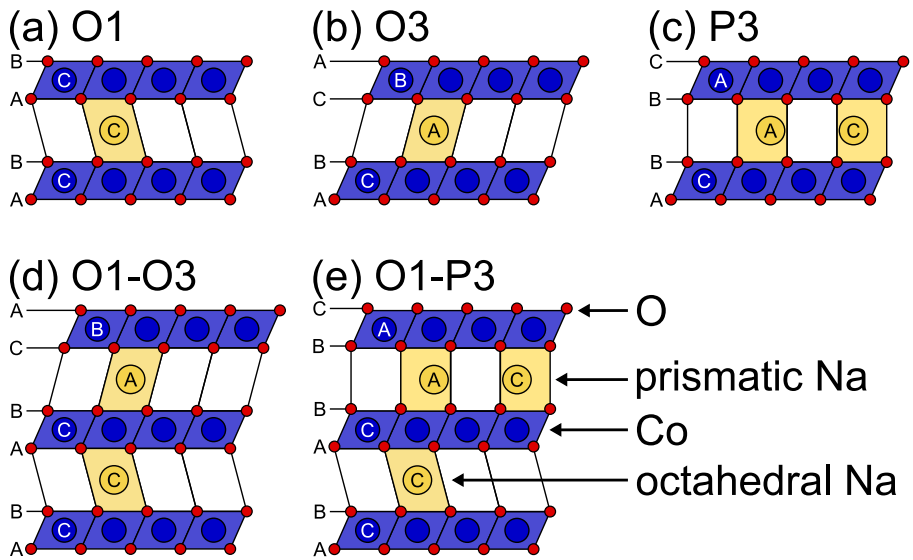

Figure 4.1: Stacking sequences of the (a) O1, (b) O3, and (c) P3 structures and the hybrid structures (d) O1-O3 and (e) O1-P3. Polyhedra are shown as parallelograms with O (red circles) at the corners. Co (blue circles) occupy octahedral sites while Na (yellow circles) occupy either octahedral sites on a single triangular sublattice or prismatic sites on two distinct triangular sublattices.

Na_xCoO_2 through a simple shearing of the CoO_2 sheets. P3 is found to be stable at intermediate compositions, in agreement with experiment, as well as O3 and a hybrid O1-O3 phase at lower compositions. We identify several families of hierarchical orderings in O3 and P3 that result in staircases of stable periodic ground states. These are predicted to remain ordered at room temperature and together produce a sloping voltage profile consisting of many small steps and plateaus similar to that observed experimentally. We find that the zig-zag row motif found at $x = 1/2$ forms the basis of all ground state orderings in P3 Na_xCoO_2. We discuss the likelihood of the same orderings appearing in other layered intercalation compounds.

4.2 Methods

DFT calculations were performed using VASP [59–62] with a plane-wave energy cutoff of 700 eV and **k**-point meshes of density of 38 Å along each reciprocal lattice vector. The optB86b-vdW exchange-correlation functional [64] was used to account for van der Waals interactions, which are necessary to accurately describe the interlayer cohesion near complete deintercalation [118, 123]. Although the addition of a Hubbard U correction can produce average voltages in better agreement with experiments [123], this method was not used because it has been shown to yield some unphysical results in layered cobalt oxide systems. Specifically, a typical U value of 3 eV or greater inverts the phase stability between O1 and O3 in CoO_2 [123] and leads to incorrect ordering tendencies in P2-Na_xCoO_2 [160]. DFT without U, conversely, has been used to accurately predict phase stability in Li_xCoO_2 [105, 161]. A hybrid functional such as HSE was not used in this study due to the computational cost, inability to capture van der Waals effects in CoO_2 [162], and demonstrated overprediction of voltages in Li_xCoO_2 [123, 162].

CASM [10,68–70] was used to enumerate symmetrically distinct configurations within each host structure across the composition range of Na_xCoO_2. DFT energies were calculated for 22 O1 configurations, 339 O3 configurations, 365 P3 configurations, 34 O1-O3 configurations, and 60 O1-P3 configurations. For hybrid structures, only those configurations containing zero Na in the O1 layers were enumerated because O1 was found to be unstable for $x > 0$, in agreement with previous studies [7, 111]. Cluster expansion effective Hamiltonians were fit for each host structure (except O1) and used iteratively to predict new near ground state configurations for which to calculate DFT energies. The cluster expansions made it feasible to traverse the configuration space at large supercell volumes. Monte Carlo heating and cooling runs were performed for a grid of temperatures and chemical potentials. For further details of the cluster expansions and Monte

Carlo simulations, we refer the reader to the Supporting Information [163]. Free energy integration of our Monte Carlo results showed that at room temperature (300 K), the ordered ground states are more stable than the disordered phases resulting from cooling runs, and that the ground states do not disorder appreciably until above 400 K. For this reason all phases were treated as line compounds, i.e. the free energies at room temperature were taken to be the zero temperature formation energies obtained from DFT. Unless otherwise noted, all reported energies and structures are DFT predictions.

The cathode voltage is related to the Na chemical potential μ_{Na} by

$$V = -\frac{\mu_{\mathrm{Na}} - \mu^{\circ}_{\mathrm{Na}}}{e} \tag{4.1}$$

where $\mu^{\circ}_{\mathrm{Na}}$ is the Na chemical potential in the reference anode and e is the elementary charge. Hexagonal close-packed Na metal was chosen as the reference.

4.3 Results

4.3.1 Phase stability

Figure 4.2(a) shows the calculated formation energies and the convex hull for each host structure. As reference states, we use O1 CoO_2 and O3 $NaCoO_2$. The global convex hull is outlined in black. O1 is predicted to be globally stable only at $x = 0$ and is not shown for other compositions. O3 is globally stable both for $1/3 \leq x \leq 3/8$ and $4/5 \leq x \leq 1$, while P3 is stable for intermediate Na concentration, $5/11 \leq x \leq 2/3$. The width of the two-phase region between O3 at $x = 3/8$ and P3 at $x = 5/11$ may be smaller than is shown, as there are several P3 ground states in this region that are above the global convex hull by less than 1 meV/CoO_2, which is well within numerical error of the DFT calculations. For the hybrid structures, O1-P3 is not found to be globally stable,

while O1-O3 is stable at $x = 1/6$. The predicted phase stability agrees with experimental studies by Lei et al. [112] and Kubota et al. [121] for $x \geq 1/2$. The characterization of structure for lower compositions has proven difficult experimentally [121], so we cannot compare our results for $x < 1/2$ as closely.

The slope of the formation energy is related to the chemical potential of Na, which is used to calculate the equilibrium voltage curve in Figure 4.2(b). Each plateau corresponds to a two-phase region, while each step corresponds to a ground state ordering. We have identified four families of hierarchical ground state orderings, whose predicted composition ranges are indicated in Figure 4.2(b) along with important orderings at their endpoints. The ζ^- and ζ^+ orderings in P3 can be generated by combining translational variants of the $x = 1/2$ ground state ordering (ζ) separated by antiphase boundaries (APBs). Similarly, the η^+ orderings can be generated from the orientational variants of the $x = 4/7$ ground state (η) separated by APBs. The θ orderings in O3 consist of fully sodiated regions separated by rows of vacancies. We will examine these families of orderings in detail along with the other ground states.

The calculated equilibrium voltage curve in Figure 4.2(b) is compared to the experimental curve from Kubota et al. [121] The relative jaggedness of the calculated curve is in part due to a finite sampling of the large number of possible orderings in each family of ground states. Our voltage underpredicts experiment by about 0.5 V, which is consistent with systematic errors inherent to approximations to DFT when comparing energies of metals and oxides. The voltage of the O3 region for $x \geq 4/5$ is predicted to be lower still. We attribute this underprediction to an inability of DFT approaches in accurately describing charge localization in the vicinity of the metal-insulator transition in cobalt oxide compounds at high intercalant concentrations [105]. Despite these issues, the overall qualitative agreement with experiment is good. We predict a large step of about 0.5 V at $x = 1/2$ and a smaller one at $x = 2/3$, with a sloping region rich in small

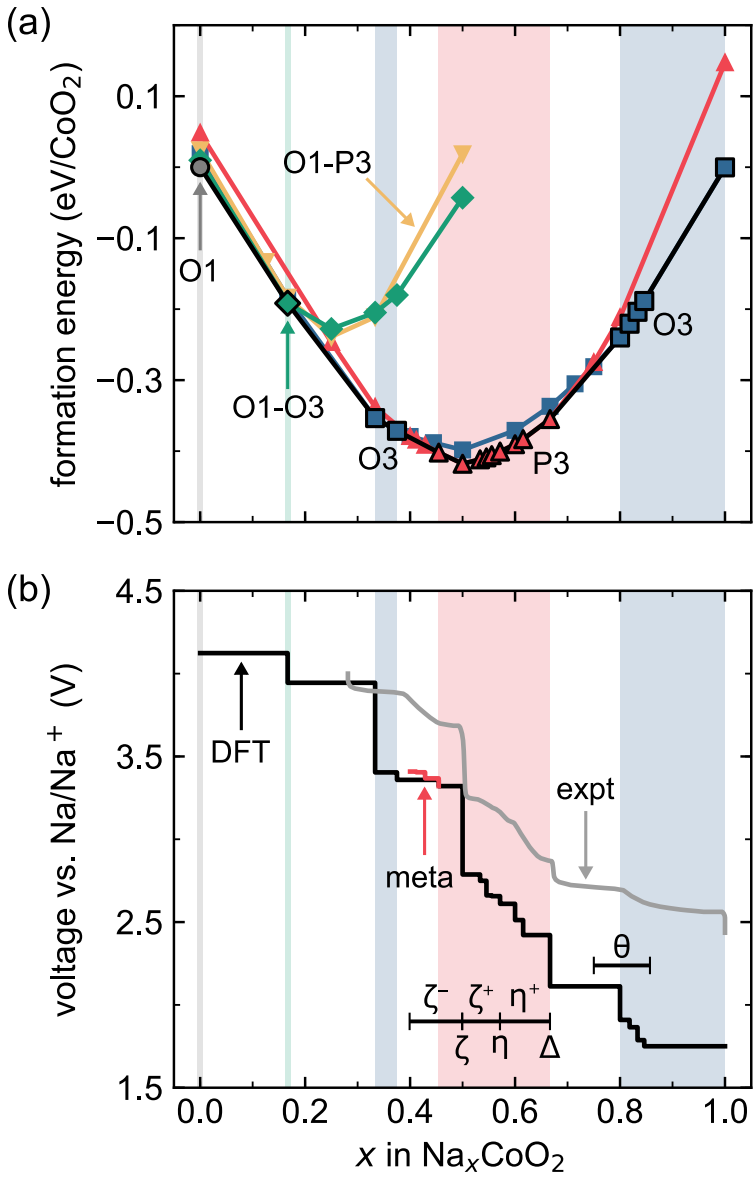

Figure 4.2: (a) Calculated formation energies versus composition for configurations on the local convex hull of each host structure. The global convex hull is shown in black. Single phase regions are highlighted in the background. (b) Calculated zero temperature equilibrium voltage curve (black) compared to experiment from Kubota et al. [121] (gray). A section of the metastable P3 voltage curve is shown in red. The composition ranges for various families of orderings in P3 and O3 are indicated.

steps and plateaus between the steps at $x = 1/2$ and $2/3$. The metastable P3 voltage curve corresponding to the ζ^- family of orderings is shown in red, and may be the path followed experimentally as the equilibrium path requires a two-phase reaction from P3 to O3.

4.3.2 O3 orderings

At $x = 1$ there is only one ordering possible in O3 as all Na sites are then filled. For $3/4 \leq x \leq 6/7$ we find that the O3 ground states all consist of different arrangements of rows of vacancies as shown in Figure 4.3. There are an infinite number of orderings in this family with different sequences of spacings between vacant rows, resulting in a "Devil's staircase" [164,165] of stable ground states at almost arbitrary composition. We refer to this family of orderings as θ and present a naming convention and composition formula for specific orderings in the Appendix C.

The θ orderings bring about significant distortions of the O3 host, as shown in Figure 4.4. Na directly adjacent to the vacancy rows are displaced from the centers of their octahedral sites toward the vacancies, and the interlayer spacing tends to expand around the vacancies, resulting in undulating CoO_2 layers. Configurations in which vacancy rows are not stacked immediately on top of each other seem to be energetically preferred, though we did not probe this exhaustively. The strong distortions made it difficult to parameterize an accurate cluster expansion, so we were unable to perform reliable Monte Carlo simulations to determine if the θ orderings remain ordered at room temperature. We expect, however, that the rows are "locked in" such that breaking them is energetically unfavorable. To test this, we calculated the energies of perturbed structures in which every fourth Na in a row adjacent to a vacant row was moved into the vacant row itself. This was found to increase the energy by 283 and 384 meV for θ_3 and θ_4 (Figure 4.3(a,b)),

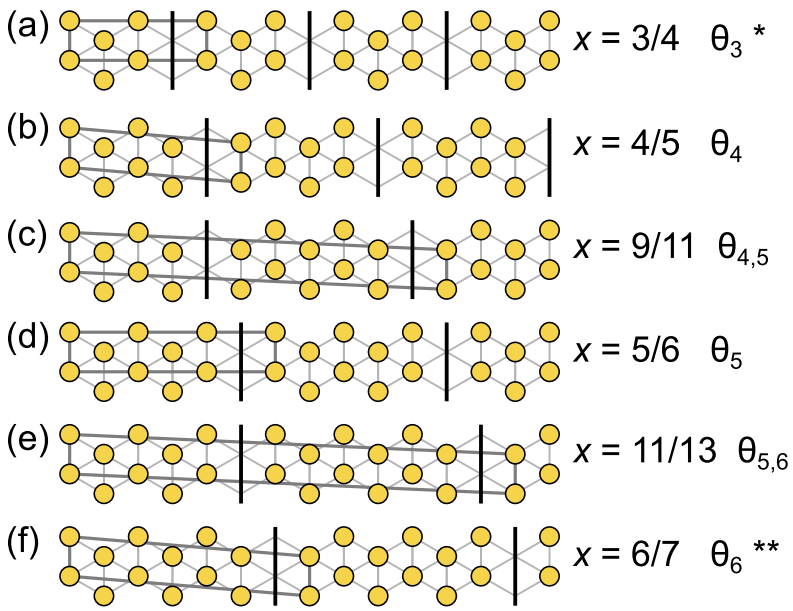

Figure 4.3: Orderings belonging to the θ family on the local convex hull of O3. Yellow circles represent Na and black lines indicate vacancy rows between fully sodiated regions. Unit cells are shown in dark gray. Single asterisks indicate that the ordering is above the global hull and double asterisks indicate that the ordering is also above the local hull but by less than 0.5 meV/CoO_2.

respectively. These are large energy increases, and we, therefore, expect that the θ ground states will remain ordered at room temperature.

Experimental studies report a stable O′3 phase, described as O3 with a monoclinic distortion, from $x = 0.8$ or 0.83 to around 0.86 or 0.88, followed by a two-phase region between O′3 and hexagonal O3 at $x = 1$ [112, 121]. This composition range is similar to that where the θ family is found to be stable. The predicted two-phase region between fully sodiated O3 and $\theta_{5,6}$ at $x = 11/13$ coincides with the experimental two-phase region. Other θ orderings having Na concentrations that are slightly higher than $x = 11/13$, such as θ_6, θ_7 and θ_8, were predicted to be only 1-2 meV/CoO_2 above the global convex hull.

As is evident in Figure 4.2(a), the O3 host is not only stable at high Na concentrations, but also at concentrations around $x = 1/3$. Figure 4.5 shows ground state orderings in O3 for $1/3 \leq x \leq 1/2$. The $x = 1/3$ ordering in Figure 4.5(a) is the typical $\sqrt{3}a \times \sqrt{3}a$

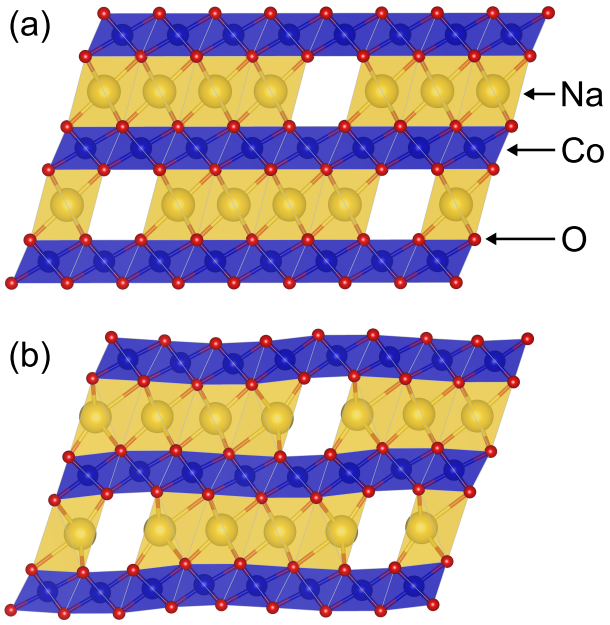

Figure 4.4: Structure of the θ_4 ground state at $x = 4/5$ (a) before and (b) after relaxation.

ordering on a triangular lattice, where a is the lattice parameter. The orderings at $x = 3/8$ and $x = 2/5$ (Figure 4.5(b,c)) can be viewed as consisting of different translational variants of the $x = 1/3$ ordering separated by APBs. This suggests that there could be another family of O3 ground state orderings in this composition range with different spacings of APBs, but we have not pursued this further. At $x = 1/6$, the O3 ground state is a staged structure with layers of the $x = 1/3$ ordering alternated by vacant layers. Its energy is lowered by 8 meV/CoO_2 if the O3 stacking sequence of the vacant layers are changed to an O1 stacking sequence, thereby producing the globally stable O1-O3 hybrid at $x = 1/6$ (also known as H1-3 [105]). This suggests that there are possible higher order hybrids with the same $x = 1/3$ O3 ordering between vacant O1 layers at even lower compositions, e.g. O1-O1-O3 at $x = 1/9$.

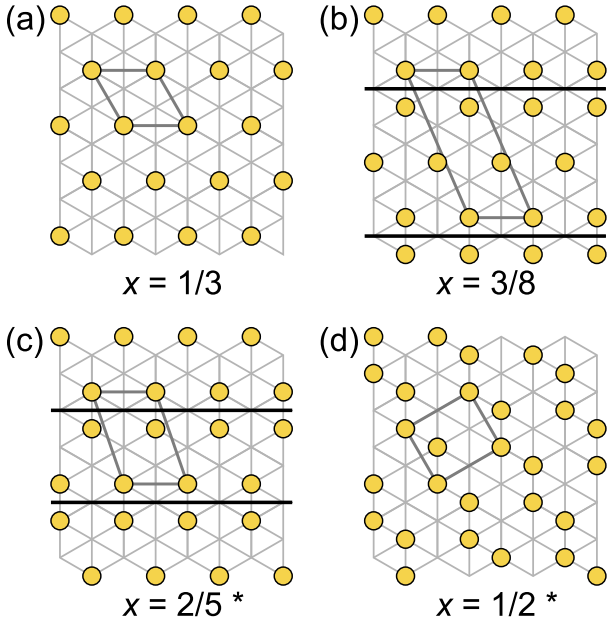

Figure 4.5: Orderings on the local convex hull of O3 for $1/3 \leq x \leq 1/2$. Yellow circles represent Na and black lines indicate APBs between translational variants of the $x = 1/3$ ordering. Unit cells are shown in dark gray. Asterisks indicate that the ordering is above the global hull.

4.3.3 P3 orderings

Figure 4.2(a) shows that the P3 host is stable at intermediate Na concentrations. The two triangular sublattices of Na sites in P3 form a honeycomb network, and we distinguish Na occupancy of the different sublattices with light and dark circles, as in Figure 4.6. At $x = 1/2$, the P3 ground state is a zig-zag row ordering with Na occupying third-nearest-neighbor sites on the honeycomb network, as shown in Figure 4.6(a)(i). The same ordering has been observed experimentally [121] and predicted computationally [8, 111] in several transition-metal oxides and sulfides intercalated with Na. We denote this ordering by ζ, and it forms the foundation of all the hierarchical orderings we identified in P3. We found that the relative stacking of orderings in P3 tends not to affect the energy significantly (within ~ 2 meV/CoO_2), but we did not test this exhaustively. We also confirmed that occupation of nearest-neighbor sites results in a large energy penalty

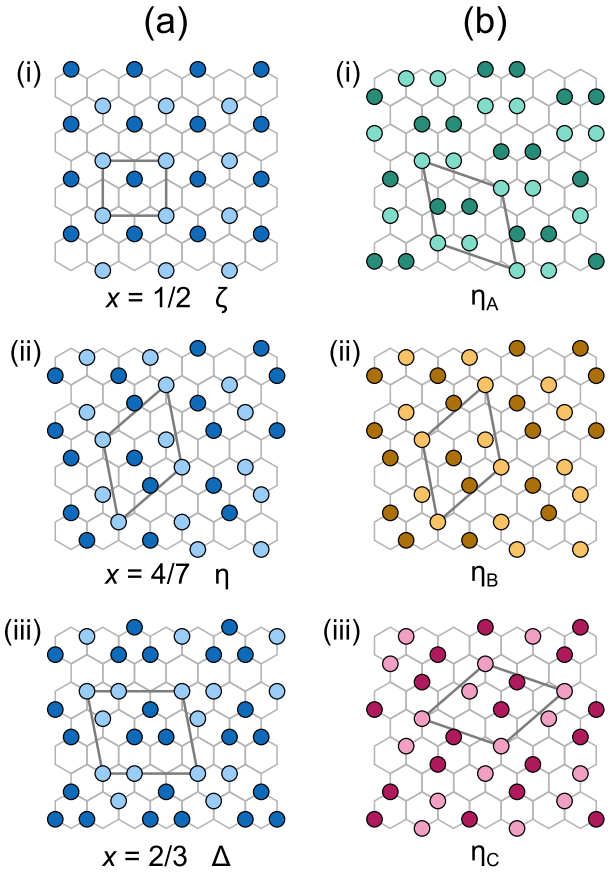

Figure 4.6: (a) Important P3 ground state orderings ζ, η, and Δ, with Na shown in blue. (b) The three orientational variants of the η ordering from (a)(ii), shown in green, orange, and magenta. Unit cells are shown in dark gray. Light and dark circles distinguish Na occupancy of the two distinct triangular sublattices.

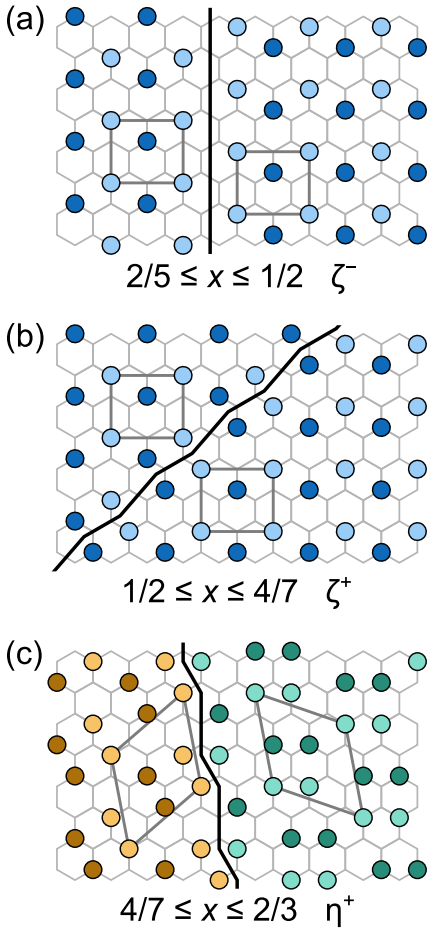

Figure 4.7: APBs (black lines) that make up the (a) ζ^-, (b) ζ^+, and (c) η^+ families of hierarchical orderings, separating (a,b) translational variants of the ζ ordering (blue), or (c) orientational variants of the η ordering (orange and green). Unit cells of each variant are shown in dark gray. Light and dark circles distinguish Na occupancy of the two distinct triangular sublattices.

(> 1 eV/Na-Na pair) due to steric repulsion.

We identified three families of hierarchical orderings in P3. Endpoints of these families correspond to important orderings at $x = 1/2$, $x = 4/7$, and $x = 2/3$ (Figure 4.6(a)) that we have labeled ζ, η, and Δ, respectively. The Δ ordering can be generated from the η ordering, which itself can be generated from the ζ ordering. This is achieved by introducing different kinds of APBs, which are shown in Figure 4.7. We describe each family of orderings next, with naming conventions, composition formulas, and specific ground state orderings given in Appendix C.

The ζ^- and ζ^+ orderings in P3

The P3 ground states for $2/5 \leq x \leq 1/2$ consist of translational variants of ζ separated by APBs, as shown in Figure 4.7(a). This type of APB introduces more vacancies compared to ζ. The infinite possible sequences of APB spacings result in another Devil's staircase of hierarchical ground state orderings. We label this family of orderings as ζ^- and introduce a notation to label them specifically that is similar to that used to describe the θ family (see the Appendix Section C.2 for details).

For $1/2 \leq x \leq 4/7$, we observe ground states with a different type of APB between translational variants of ζ, as shown in Figure 4.7(b). In this type, Na are condensed along the APB, with adjacent third-nearest-neighbor pairs forming quadruplet clusters. As with the ζ^- orderings, one can choose an arbitrarily complex sequence of APB spacings, leading to another family of ground state orderings which we call ζ^+. Within both the ζ^- and ζ^+ families, multiple structures can have the same composition and are likely degenerate in energy, as discussed in the Appendix Section C.2.

The η^+ orderings in P3

The $x = 4/7$ ordering (labeled ζ_4^+) shown in Figure 4.6(a)(ii) is of particular importance, and is denoted separately as the η ordering. This is the endpoint of the ζ^+ family, as smaller APB spacings (higher x) do not produce stable orderings. It consists entirely of the quadruplet clusters formed along the ζ^+-type APBs. The η ordering resides in a $\sqrt{7}a \times \sqrt{7}a$ supercell and has three orientational variants η_A, η_B, and η_C related by a three-fold rotation, shown as green, orange, and magenta in Figure 4.6(b). The three variants are commensurate with the same unit cell, though we have chosen to show the unit cell rotated along with the ordering.

Sections of the two variants η_A and η_B separated by the type of APB shown in Figure 4.7(c) form another family of ground state orderings for $4/7 \leq x \leq 2/3$ which we refer to as η^+. For a specific naming convention and composition formula, see the Appendix Section C.3. The η^+ orderings are fundamentally different from the ζ^- and ζ^+ orderings in that they alternate between two orientational variants and as such, every η^+ ordering contains an even number of APBs in its unit cell.

Two examples of the η^+ orderings are shown in Figure 4.8. The $x = 8/13$ ordering $\eta_{4,4}^+$ consists of equal portions of the two η variants (Figure 4.8(a)), while in the $x = 2/3$ ordering, $\eta_{2,4}^+$ or Δ, the η_A regions are half as wide (Figure 4.8(b)). Along the APBs there are triplet clusters of Na on the same triangular sublattice, shown as light or dark circles, and at $x = 2/3$ the structure is made up entirely of such clusters, as shown in Figures 4.6(a)(iii) and 4.8(b) (note that these are the exact same ordering Δ viewed in different ways).

A hexagonal P3 phase has been reported experimentally around $x = 0.56$, with regions of monoclinic P$'3$ above and below it in composition [112]. Because $x = 4/7 \approx 0.57$ is close to this composition, we suggest that the experimental phase may correspond to the

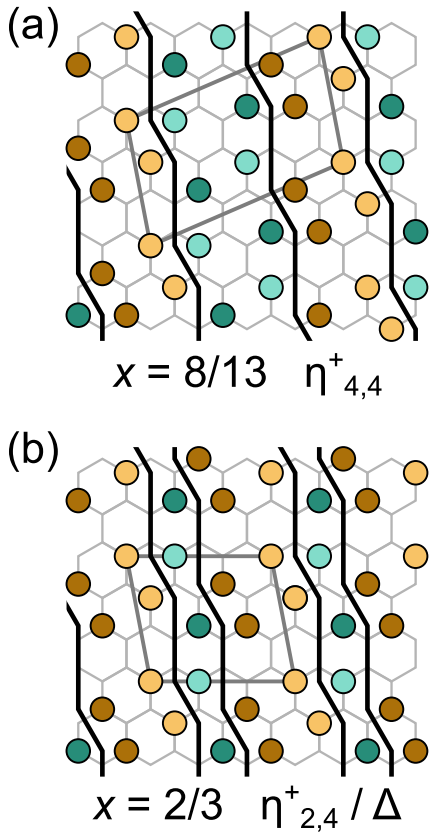

Figure 4.8: Example ground state orderings belonging to the η^+ family in P3, composed of regions of the η_A (green) and η_B (orange) orientational variants separated by APBs (black lines). Unit cells are shown in dark gray. Light and dark circles distinguish Na occupancy of the two distinct triangular sublattices.

η ordering, which is described by a hexagonal supercell. Lei et al. also speculate that the two regions of P′3 above and below $x = 0.56$ may be distinct ordered superstructures [112], which could correspond to the ζ^+ and η^+ families identified here. In addition to being the endpoint of the η^+ orderings, the Δ ordering at $x = 2/3$ is representative of the low-energy P3 orderings at higher compositions, beyond where P3 is globally stable. These orderings consist of triangular islands of Na on a single sublattice separated by APBs, like those found computationally in Na_xCoO_2 [111, 166] and Na_xTiS_2 [8]. Some illustrative snapshots from our Monte Carlo cooling simulations are shown in Figure 4.9, with Na on either sublattice indicated with light and dark blue.

4.4 Discussion

Our first-principles study of Na_xCoO_2 has revealed several families of stable hierarchical Na orderings that span wide composition ranges. The predicted phase stability follows the experimentally observed O3 → O′3 → P′3 → P3 → P′3 transitions upon deintercalation of $NaCoO_2$, matching both the single-phase composition ranges and the shape of the voltage profile. In addition to the well-known ordering at $x = 1/2$ (ζ), we have identified important orderings in P3 at $x = 4/7$ (η) and $x = 2/3$ (Δ) that may assist experimental studies in resolving structure at these compositions.

We predict a staged hybrid phase for more dilute Na, below compositions that have been accessed experimentally. It is curious that we find a globally stable O1-O3 hybrid at $x = 1/6$ but not a globally stable O1-P3 hybrid at $x = 1/4$, as is the case in Na_xTiS_2 [8]. The O1-P3 hybrid groundstate in Na_xTiS_2 consists of layers of the P3 ζ ordering at $x = 1/2$ alternating with vacant O1 layers. Not only does this configuration lie above the common tangent between O3 and O1-O3 for Na_xCoO_2, but it has a higher formation energy than the P3 ground state at $x = 1/4$, which is not staged. This suggests a

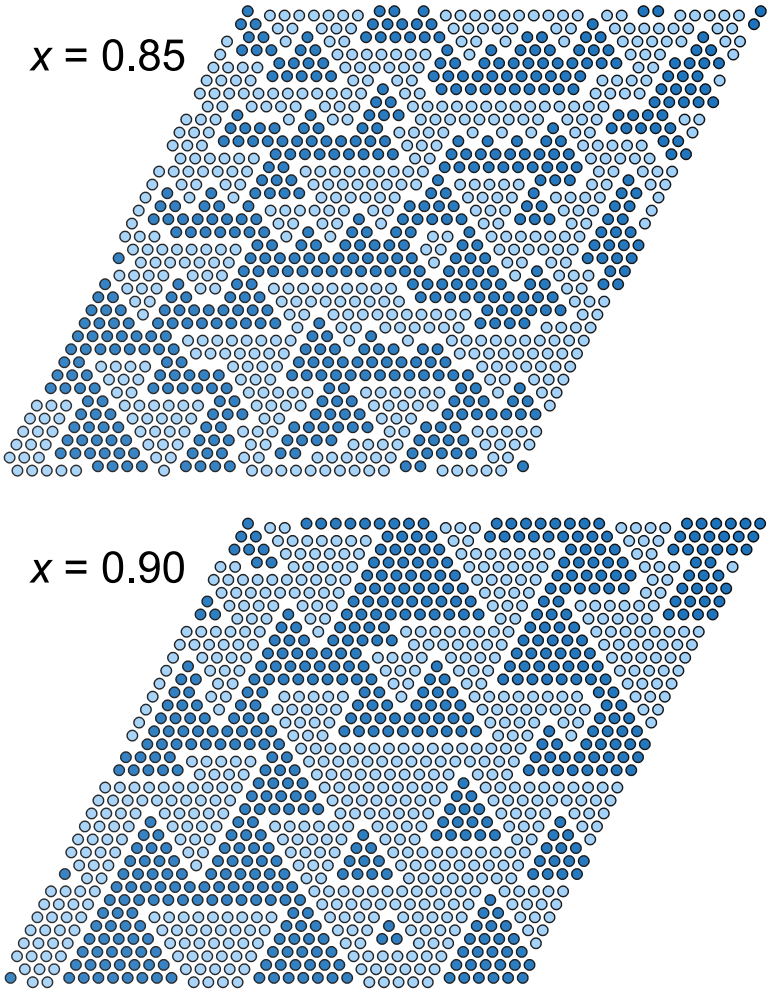

Figure 4.9: Representative snapshots from P3 Monte Carlo cooling runs at 300 K (cooled from 1000 K). Light and dark blue circles distinguish Na occupancy of the two distinct triangular sublattices.

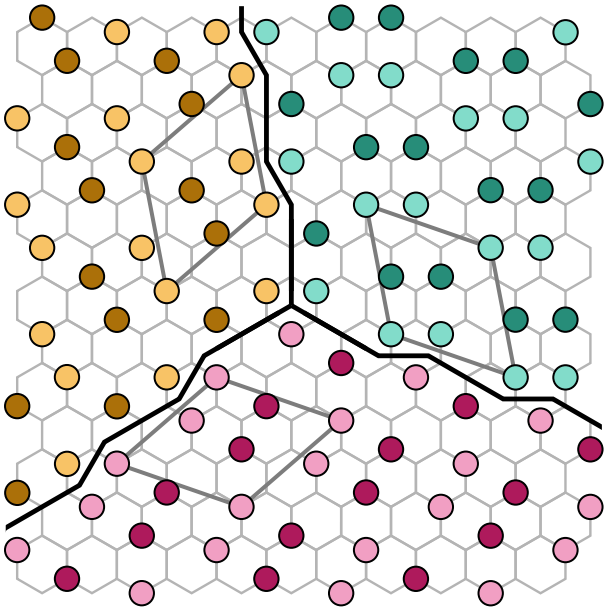

Figure 4.10: A hypothetical triple junction between the three orientational variants of the η ordering (green, orange, magenta). Black lines indicate APBs and unit cells of each variant are shown as dark gray boxes. Light and dark circles distinguish Na occupancy of the two distinct triangular sublattices.

preference in P3 for Na to spread out within each layer, rather than limiting interlayer interactions by staging.

This study highlights the importance of hierarchical orderings in layered Na intercalation compounds. In each family, orderings consist of regions of favorable local ordering, such as the zig-zag rows of the ζ ordering in P3, separated by a particular kind of APB to accommodate changes in composition. Orientational variants occupying the same commensurate supercell offer a convenient way of stitching them together, as is the case with the η ordering. The ordering tendencies described here could lead to even more intricate superstructures. For example, the η ordering could potentially support triple junctions between all three orientational variants separated by the same kind of APB discussed earlier, as illustrated in Figure 4.10. We leave the energetics of such structures to be explored in a later study.

Infinite staircases of orderings can be difficult to treat with a cluster expansion ap-

proach, as they often require long-range interactions to capture a sufficient number of the ground states. It can also be difficult to find such orderings by brute force enumeration, as even relatively simple hierarchical orderings often require large supercells. Monte Carlo approaches will fail to predict specific orderings if the chosen supercell is not of commensurate shape (even if it is large enough), but may be useful in revealing preferred local ordering phenomena. Also of note is that there is likely a large degeneracy of orderings within a given family. While it is convenient to model simpler ones, experimentally we would expect to see larger superstructrures with different spacings between APBs. Such Devil's staircases are common in other types of compounds as well, including metallic alloys [167–169].

The Na ordering of a phase has implications for diffusion and the kinetics of Na insertion and removal. Diffusion in layered intercalation compounds is intimately tied to cation ordering [57, 93, 95] and happens differently in P3 compared to O3 [88, 170, 171]. Diffusion may occur more readily along APBs, as has been proposed for the orderings of triangular islands for high Na content [8], but likely only along APBs that contain more vacancies compared to the rest of the structure, as in the ζ^- orderings. The insertion and removal of Na in P3 will likely require non-local rearrangements of the Na ions. Since the composition of the hierarchical orderings are determined by the density of APBs, any change in composition will require the creation or annihilation of APBs that is simultaneously coupled with a readjustment of the spacing between existing APBs. We leave a detailed examination of these non-local diffusion processes for a future study.

Similar families of orderings may be stable in other intercalation compounds that adopt the P3 structure, particularly oxides, where electrostatic effects are strong due to ionicity [7]. This may be the case in alloyed transition-metal oxides like $Na_xFe_{1/2}Co_{1/2}O_2$, which also exhibits the ζ ordering at $x = 1/2$ and undergoes similar structural transformations during cycling [121]. It is possible that the intercalation of K instead of Na

may yield the same orderings unless they are somehow destabilized by the larger ionic radius of K^+. Intercalating into different transition-metal oxides like MnO_2 or NiO_2 may see these ordering tendencies competing or coupling with Jahn-Teller distortions, which are critical to understanding the energetics of these systems [85, 172]. The Jahn-Teller distortions themselves can take on distinctive orbital orderings within the lattice, such as collinear and zig-zag arrangements [6]. The interaction of these with Na orderings is potentially rich but not well-explored.

4.5 Conclusion

In this study we have examined phase stability in Na_xCoO_2 between O3, P3, O1, and staged hybrid structures. The calculated voltage profile agrees qualitatively with experiment. We find that a family of vacancy row orderings are stable in O3 at high Na concentrations, which may correspond to the O′3 phase seen experimentally. At intermediate composition, we have discovered several families of ground state Na orderings on the honeycomb network in P3 and a unifying picture of their construction. An infinite number of hierarchical orderings are obtained by combining regions of the zig-zag row ordering at $x = 1/2$ separated by different types of antiphase boundaries. These orderings are likely to be common among other P3 intercalation compounds.

Chapter 5

Ordering and phase stability in layered Na_xCrO_2

5.1 Introduction

There is a growing effort to develop "beyond Li-ion" battery technologies that could address the world's energy storage needs at lower cost and using more widely available resources [2, 101]. Na-ion batteries are one such technology that hold promise for applications such as stationary energy storage due to the far greater abundance of Na compared to Li [3]. Much research has been devoted to developing suitable materials for Na-ion batteries, particularly cathode materials [73, 97]. One of the most popular classes of candidate Na-ion cathode materials are layered transition-metal oxides intercalation compounds, which generally exhibit high energy density and rate capability, and share many similarities with their well-studied Li-ion counterparts [78, 79].

Various layered oxide compounds with the formula Na_xMO_2 (M = Ti, V, Cr, Mn, Fe, Co, Ni, or some combination) have been explored as electrode materials [108, 121, 127, 128, 147, 148, 173–182]. Among these, Na_xCrO_2 is of particular interest as a high-rate

cathode material [183]. It is also considered to be inherently safe due to its exceptional thermal stability in contact with an electrolyte [184]. Despite these advantages, Na_xCrO_2 does display certain structural phase transitions and Na-vacancy ordering effects that are common to many Na layered oxide systems and generally considered detrimental [8, 11, 80]. Beyond battery applications, layered $NaCrO_2$ has also received attention from the solid-state physics community as a frustrated magnetic system [185–190].

The fully sodiated $NaCrO_2$ adopts the O3 structure, depicted in Figure 5.1(a). This structure is made up of stacked sheets of edge-sharing CrO_6 octahedra, which host Na in octahedral sites in the intercalation layers between them. The Na sites form triangular lattices and do not share faces with the CrO_6 octahedra. There are also tetrahedral sites in the intercalation layers that share faces with the CrO_6 octahedra. While these sites are generally too small for Na occupation, they are able to accommodate Cr that can migrate via the shared faces. Like many O3-Na_xMO_2 materials, O3-$NaCrO_2$ transforms to a P3 structure, depicted in Figure 5.1(b), upon desodiation [7, 8, 84, 97]. This structure is obtained from O3 by a change in the stacking sequence of the CrO_2 sheets [108]. The Na sites form honeycomb networks, with each site sharing one face with a CrO_6 octahedron. While there is an energy penalty associated with the Na-Cr face-sharing in P3, the honeycomb network allows for unique Na-vacancy orderings that lower the electrostatic energy contribution of Na-Na interactions relative to O3 [7, 11].

The phase stability between O3 and P3 in Na_xCrO_2 has been examined in various experimental studies. Figure 5.2 shows several reported phase diagrams for $x > 0.5$ obtained from *ex situ* [82] or *in situ* [191–193] X-ray diffraction (XRD). These follow the same general picture of phase evolution with desodiation: The O3 structure near $x = 1$ undergoes a first-order transition to a O′3 phase near $x = 0.8$, which eventually undergoes a first-order transition to a P′3 phase at lower x. The primed phases here indicate a monoclinic distortion of the hexagonal O3 or P3 parent structure. Beyond these general

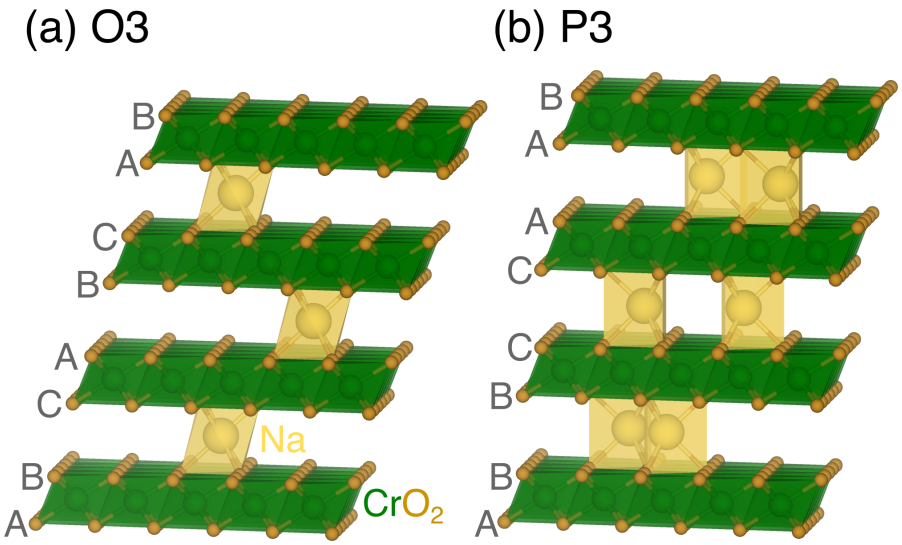

Figure 5.1: The (a) O3 and (b) P3 layered structures of Na_xCrO_2, which host Na on octahedral and trigonal prismatic sites, respectively. Letters (A, B, C) indicate the oxygen stacking sequence of each structure.

similarities, there are some key discrepancies between the various experimental phase diagrams. The boundaries of each single-phase region differ significantly across studies, and Jakobsen et al. recently reported the appearance of an extra O′3 phase (dubbed O′3-E) near $x = 0.7$ [193]. The details of Na ordering within each phase are also not well understood. Some orderings have been reported in the P′3 phase [131, 194], but no comprehensive picture of ordering across composition in the O3 and P3 structures has been established. For $x < 0.5$, Na_xCrO_2 has been found to undergo an irreversible phase transition to an O3 phase involving charge disproportionation and migration of the Cr to tetrahedral sites in the intercalation layers, although there is some disagreement over its exact nature [82, 192].

The Na_xCrO_2 system displays an interesting assortment of behavior for $0 \leq x \leq 1$. While some specific aspects have been studied using first-principles techniques [82, 159, 192], questions remain regarding the true equilibrium phase stability between O3 and

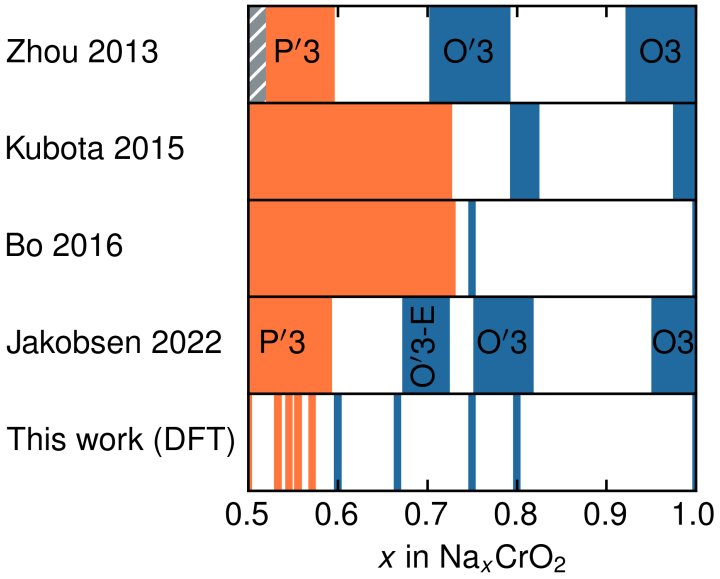

Figure 5.2: Reported phase diagrams from several experimental studies [82,191–193]. Solid-colored and white blocks indicate single- and two-phase regions, respectively, while the hatched region indicates that no data was reported there. The predicted ground states from this work, drawn as line compounds, are shown for comparison.

P3, as well as the nature of Na ordering and Cr migration. Here we report on a first-principles study of phase stability between various Na-vacancy orderings in the O3 and P3 structures of Na_xCrO_2. We predict O3 to be stable at high x, with the preferred orderings forming families based on the common motif of rows of vacancies that separate fully sodiated regions. Some of these orderings are also found to couple to favorable magnetic orderings. At intermediate x, we predict P3 to be stable and identify families of (near) ground state orderings containing antiphase boundaries between regions of the $x = 1/2$ ordering. We also confirm a preference for Cr migration to tetrahedral sites in O3 at $x = 0$, along with charge disproportionation. Our predicted phase stability and voltage profile are compared to experimental reports, and we discuss possible sources of discrepancy as well as similarities to other layered oxide systems.

5.2 Methods

Density functional theory calculations were performed using VASP [59–62]. The plane-wave energy cutoff was chosen to be 600 eV, and the Brillouin zone was sampled with **k**-meshes of density 34 Å along each reciprocal lattice vector (increased to 40 Å for calculating density of states). All calculations were spin-polarized and initialized in the ferromagnetic (FM) state, unless otherwise noted. The SCAN meta-GGA exchange-correlation functional [30, 31] was used because it has been shown to provide accurate predictions of voltage, structural parameters, and phase stability in related layered oxide systems [13, 195–200]. Some calculations were also run with PBE [26] and PBE+U [35] (with $U = 3.5$ eV for Cr) for comparison. Unless otherwise noted, all reported properties and structures are from calculations using the SCAN functional.

Symmetrically distinct Na-vacancy orderings in the O3 and P3 host structures of Na_xCrO_2 were enumerated using the Clusters Approach to Statistical Mechanics (CASM) software package [10,68–70]. DFT energies were calculated for 228 O3 configurations and 273 P3 configurations. Energies were calculated for an additional 37 configurations of O3-CrO_2 in which one third of the Cr have been moved to tetrahedral sites in the intercalation layers (all such structures in supercells of volume up to six times the primitive cell volume). We also enumerated and calculated DFT energies for collinear magnetic orderings of the Cr spins within the predicted O3 and P3 ground states at select compositions.

CASM was used to construct cluster expansion effective Hamiltonians for the O3 and P3 structures (not considering magnetic ordering or Cr migration), which we employed to iteratively predict candidate ground state structures whose energies were subsequently calculated with DFT. Details of the cluster expansions are provided in Appendix Section D.1. These cluster expansions were also used to run Monte Carlo simulations of finite-

temperature phase stability, the details of which are provided in Appendix Section D.2.

Voltages were calculated using the Nernst equation [4]

$$V = -\frac{\mu_{\mathrm{Na}} - \mu^{\circ}_{\mathrm{Na}}}{e} \tag{5.1}$$

where μ_{Na} is the chemical potential of Na in Na_xCrO_2, $\mu^{\circ}_{\mathrm{Na}}$ is the chemical potential of the reference anode (taken to be body-centered cubic Na metal [201]), and e is the elementary charge.

5.3 Results

5.3.1 Phase stability

Figure 5.3(a) shows the calculated zero-temperature formation energies of Na_xCrO_2 configurations in the O3 and P3 structures, referenced to O3-CrO_2 and O3-$NaCrO_2$ (FM). Also included are energies of the most favorable magnetic orderings found in O3 at $x = 1$, $x = 4/5$, and $x = 3/4$, as well as O3 configurations at $x = 0$ with one third of the Cr migrated to tetrahedral sites in the intercalation layers. Note that we generally do not distinguish between parent and distorted host structures (e.g. O3 vs O′3) in our results. The global formation energy convex hull determines the zero-temperature phase stability. To more easily compare energies of configurations close to the hull, distances above the hull (excluding the Cr migration configurations) are also plotted in Figure D.3 of Appendix D. We predict O3 to be stable for $3/5 \leq x \leq 1$, and P3 to be stable for $1/2 \leq x \leq 4/7$. At $x = 0$ an O3 configuration with tetrahedral Cr is predicted to have the lowest energy. Our predicted phase stability for $x \geq 1/2$ is generally in good agreement with experimental studies (Figure 5.2), which report O3-type phases appearing around $x = 0.8$ upon desodiation and P3-type phases appearing at or just

below $x = 0.6$ (according to Zhou et al. [191] and Jakobsen et al. [193]). We do predict a narrower two-phase region between P3 and O3 than has been reported experimentally, with O3 predicted to be stable down to $x = 3/5$. The results of our grand canonical Monte Carlo simulations (summarized in Appendix Section D.2) also suggest that the O3 regime extends to even lower x with increasing temperature, while the P3 regime becomes narrower.

While we performed most calculations with FM alignment of the Cr spins, we did explore non-FM magnetic configurations at select compositions in O3 and P3, the energies and net magnetic moments of which are shown in Figure D.4 of Appendix D. At $x = 1$ in both O3 and P3, an antiferromagnetic (AFM) in-layer ordering (Figure D.5, Appendix D) is predicted to be most stable. This configuration is 31 meV/CrO_2 and 43 meV/CrO_2 lower in energy than the FM configuration in O3 and P3, respectively. The predicted preference for AFM ordering at $x = 1$ is consistent with experimental reports of the magnetic behavior of $NaCrO_2$, which displays AFM direct exchange interactions resulting from overlap of the Cr t_{2g} orbitals [186]. The collinear AFM ordering we identify is almost certainly not the true ground state, however, as $NaCrO_2$ is a known triangular Heisenberg antiferromagnet with more exotic low-temperature magnetic behavior [186–188]. In O3, we find non-FM configurations are also preferred at $x = 4/5$ (10 meV/CrO_2 below FM) and $x = 3/4$ (6 meV/CrO_2 below FM), while no such preference is found in P3 at $x = 2/3$ or $x = 1/2$. It is somewhat intuitive that the preference for AFM ordering would diminish with decreasing x. As Na is removed and Cr is oxidized from 3+ (d^3) toward 4+ (d^2), the hopping of aligned spins between t_{2g} orbitals of neighboring Cr ions would no longer be completely suppressed due the Pauli exclusion principle [115]. We emphasize that we expect the material to be paramagnetic at room temperature, as the reported Néel temperature of $NaCrO_2$ is 41 K [186].

Figure 5.3(b) shows the equilibrium voltage derived from the calculated zero-temper-

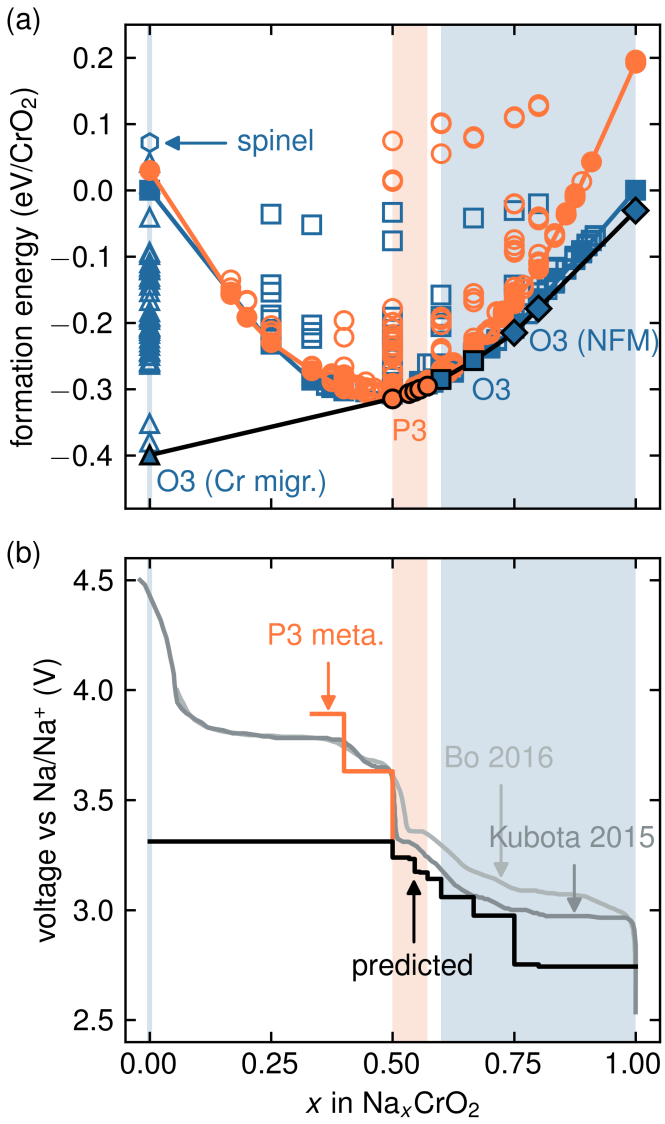

Figure 5.3: (a) Calculated formation energies of O3 and P3 configurations versus composition. For O3, FM configurations are marked by squares while non-FM configurations are marked by diamonds, and configurations with Cr migrated to tetrahedral sites are marked by triangles. Filled markers with lines connecting them indicate configurations on the local convex hull of each host structure (not accounting for magnetic ordering or Cr migration). The global convex hull is outlined in black. Shaded regions indicate where each host structure is globally stable. (b) Predicted voltage curve from DFT (black) compared to experimental voltage curves from first charge reported by Bo et al. [192] and Kubota et al. [82] (light and dark gray). The composition of the voltage curve from Kubota et al. has been transformed as $x \to 1.09x - 0.09$. Part of the predicted metastable P3 voltage curve is also shown (orange).

ature formation energies in Figure 5.3(a). The multitude of steps in the predicted voltage curve correspond to Na-vacancy orderings in O3 and P3, which we examine in detail in Section 5.3.2. The O3-CrO_2 configuration with tetrahedral Cr produces a large two-phase voltage plateau at around 3.3 V, however, following the convex hull of metastable configurations in P3 (which is observed down to $x \approx 0.4$ experimentally [82,192]) instead reveals a large voltage step at $x = 1/2$. Experimentally measured first-charge voltage curves reported by Kubota et al. [82] and Bo et al. [192] are also shown in Figure 5.3(b) for comparison. For $x > 1/2$, the agreement between the predicted and experimental voltage curves is quite close, with the many steps in the predicted curve matching the sloped section measured experimentally. At high x, we expect that magnetic entropy would lower the free energy of the O3 phases at room temperature and raise the corresponding voltage to be closer to the experimental value. At low x, we predict a lower voltage for Cr migration to tetrahedral sites than the 3.8 V plateau observed experimentally. We address this discrepancy and present further details of the Cr migration mechanism in Section 5.3.3. The predicted metastable voltage curve of P3, however, provides excellent correspondence with experiment, reproducing the observed step at $x = 1/2$.

5.3.2 Ground state orderings

As shown in Figure 5.3, there are numerous (near) ground state configurations predicted in the O3 and P3 structures. By closely examining these Na-vacancy orderings, we are able to identify overarching patterns that connect them.

O3 orderings

Key orderings in the O3 structure are shown in Figure 5.4. The ground state orderings immediately below $x = 1$, at $x = 4/5$ and $x = 3/4$, contain straight rows of vacancies

between fully sodiated regions (Figure 5.4(a,b)). As previously mentioned, both of these configurations prefer non-FM orderings of the Cr spins, which are shown in Figure 5.5. These magnetic orderings are coupled to distortions of the CrO_2 sheets caused by the Na orderings, such that the distance between neighboring Cr ions is smaller when their spins are antialigned than it is when they are aligned. We also identify an ordering at $x = 7/9$ (not shown) that interpolates the $x = 3/4$ and $x = 4/5$ orderings, alternating between three and four rows of Na between vacant rows. It is predicted to lie just 0.1 meV/CrO_2 above the FM convex hull. This suggests that there could be a "Devil's staircase" of many orderings with varying average spacing between vacant rows, as was previously predicted to be stable in O3-Na_xCoO_2 and labeled the θ family [12]. Like in that system, these orderings could correspond to the monoclinically distorted O′3 phases observed experimentally at high x (around 0.75–0.8) in Na_xCrO_2 (Figure 5.2).

At lower compositions in O3, the preferred orderings also consist of rows of vacancies between fully sodiated regions, however, the rows are no longer completely straight. The $x = 7/10$ ordering shown in Figure 5.4(c), which lies on the hull of FM configurations in O3, contains periodic kinks in the vacant rows. In the ground states at $x = 2/3$ and $x = 3/5$ (Figure 5.4(d,e)), the kinks are as closely spaced as possible, and these orderings only differ in the spacing between the rows of vacancies. As with the θ family at higher compositions, there could potentially be a staircase of orderings in this composition regime with varying spacing of vacant rows and/or varying density of kinks along the vacant rows. Thus we identify two qualitatively distinct families of orderings in O3 above $x = 1/2$, based on either straight or corrugated rows of vacancies. The latter could possibly explain the second O′3 phase around $x = 0.7$ recently reported by Jakobsen et al. [193] (Figure 5.2).

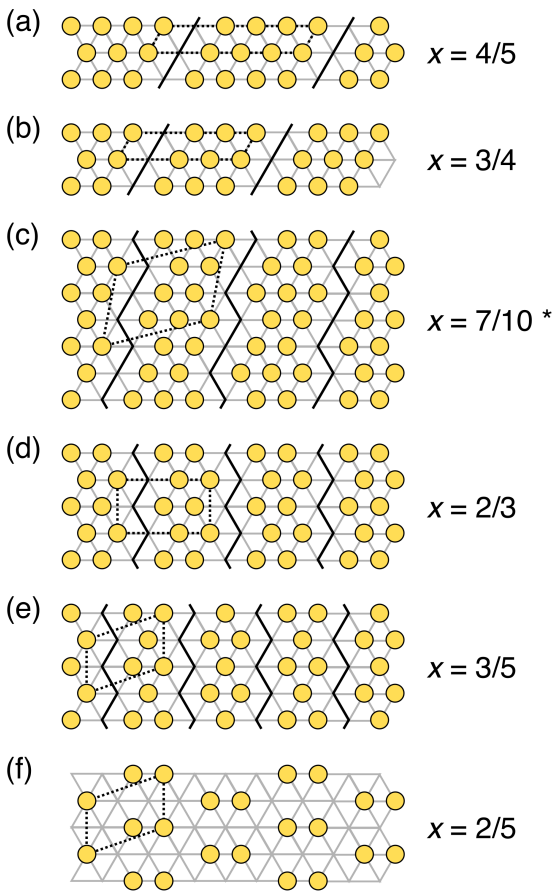

Figure 5.4: Select predicted ground state Na orderings on the triangular lattice in O3. Dotted black lines indicate the unit cells and solid black lines indicate rows of vacancies between fully sodiated regions. Asterisk indicates that the ordering is on the hull of FM configurations, but is displaced from the hull when accounting for non-FM configurations

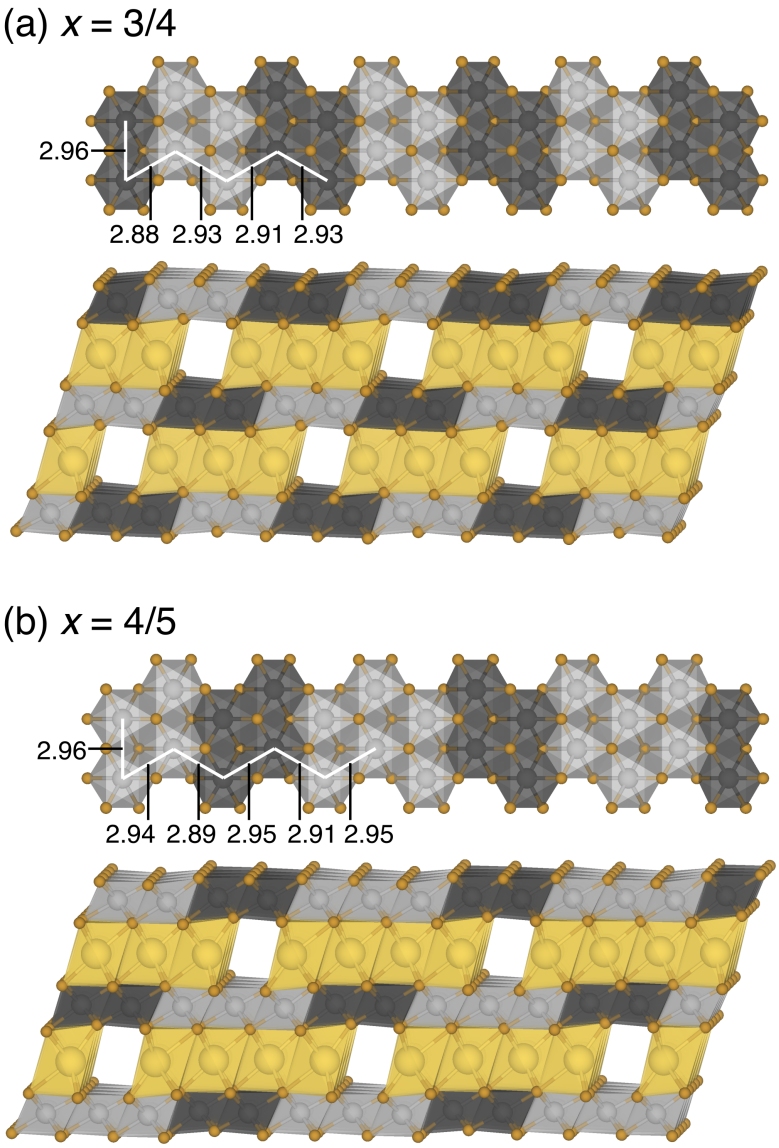

Figure 5.5: Relaxed structures of the lowest energy non-FM configurations found in O3 for (a) $x = 3/4$ and (b) $x = 4/5$. Spin up/down Cr are shown as light/dark gray. The unique nearest-neighbor Cr-Cr pair distances for each structure (in Å) are labeled.

P3 orderings

Figure 5.6 shows important orderings predicted in the P3 structure. The ground state at $x = 1/2$ (Figure 5.6(a)) is particularly stable, as demonstrated by the large step it produces in the P3 voltage curve (Figure 5.3(b)) This ordering, which we refer to as ζ, is also favored by several other layered Na and K intercalation compounds in the P3 and P2 structures [13, 97, 121, 126, 129–131]. Its stability is attributed to increased Na-Na distances relative to alternate arrangements, which minimize the electrostatic repulsion between the ions. Yabuuchi et al. confirmed the ζ ordering experimentally in P′3-$Na_{0.5}CrO_2$ via synchrotron XRD, and also found that it undergoes a disordering transition upon heating at 150–200 °C [131]. We estimate from our Monte Carlo simulations that the ζ ordering disorders at around 475 K (202 °C) (Figure D.2, Appendix D), which is in close agreement with the experimentally determined transition temperature.

Above $x = 1/2$ in P3, we predict that the highly favorable ζ ordering is preserved locally, and that additional Na are accommodated along antiphase boundaries (APBs). The ground state ordering at $x = 6/11$, shown in Figure 5.6(d), illustrates this motif. There are also predicted ground states at $x = 8/15$ and $x = 5/9$ (not shown) that differ only in the average spacing between APBs. The ground state at $x = 4/7$, which we refer to as the η ordering, has the smallest separation of APBs that was found to be stable (Figure 5.6(e)). As with the vacancy row orderings identified in O3, these APB-based orderings allow for essentially arbitrary variation in composition controlled by the average density of APBs. This particular staircase of orderings was also predicted in P3-Na_xCoO_2 and labeled the ζ^+ family [12]. Above $x = 4/7$, we also find ground states at $x = 8/13$ and $x = 2/3$ (not shown) that are common to P3-Na_xCoO_2 and belong to a staircase of orderings containing APBs between variants of the η ordering, referred to as the η^+ family [12]. However, these are not found to be globally stable here. Chen

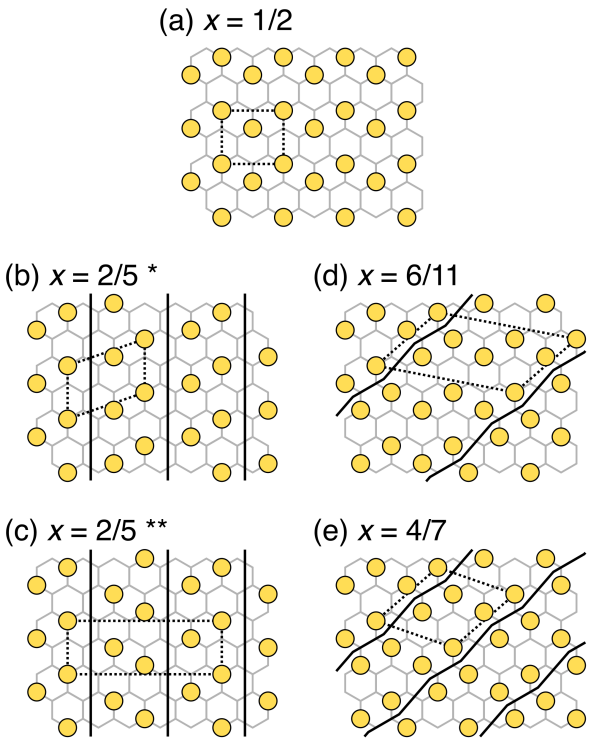

Figure 5.6: Select predicted (near) ground state Na orderings on the honeycomb network in P3. Dotted black lines indicate the unit cells and solid black lines antiphase boundaries between regions of the $x = 1/2$ ordering (a). A single asterisk indicates that the ordering is above the global hull, while a double asterisk indicates that the ordering is also above the P3 hull.

et al. recently reported similar APB-based orderings for $1/2 \leq x \leq 2/3$ in Na_xCrO_2 determined from *in situ* XRD [194]. They identified superstructures consisting of regions of the ζ ordering separated different APBs from those presented here. Though not an exhaustive comparison, we calculated the energies of two such alternative orderings from Chen et al. at $x = 5/9$ and $x = 2/3$ to lie 7 meV/CrO_2 and 8 meV/CrO_2 above the hull, respectively.

Below $x = 1/2$, we predict one ground state ordering in P3 at $x = 2/5$, shown in Figure 5.6(b). Like the P3 orderings above $x = 1/2$, this ordering can be viewed as regions of the ζ ordering separated by APBs, however, this type of APB accommodates vacancies rather than additional Na. This again suggests that there could be numerous (near) ground states between $x = 1/2$ and $x = 2/5$ with varying average densities of APBs. For instance, there is one ordering at $x = 4/9$ with more widely spaced APBs (not shown) that has a calculated energy just 0.5 meV/CrO_2 above the P3 convex hull. Interestingly, these orderings are slightly different from those predicted in P3-Na_xCoO_2, which are based on a different type of APB and form a staircase of orderings below $x = 1/2$ labeled the ζ^- family. This other APB type is shown in the alternative $x = 2/5$ ordering in Figure 5.6(c). In Na_xCrO_2, we calculate the energy of this ordering to lie 6 meV/CrO_2 above that of the preferred ordering in Figure 5.6(b). We note, however, that the energy of the latter is 3 meV/CrO_2 above that of the O3 ground state at $x = 2/5$ (Figure 5.4(f)), which contradicts experimental observations of a P3-type phase down to $x \approx 0.4$ [192]. While this may signify an incorrect prediction of the SCAN functional, the predicted difference in energy between P3 and O3 is very small and there is undoubtedly a sizeable kinetic barrier for the stacking sequence transformation from P3 to O3.

One subtlety we have disregarded in presenting these two-dimensional orderings is their stacking within the three-dimensional crystal. The influence of stacking on the energy of O3 orderings in various Na transition metal oxides was studied by Toumar et

al., who determined that, while it is generally less important than intralayer Na ordering, the effect of stacking is not necessarily negligible [159]. To investigate this effect for our predicted P3 orderings, we calculated the energies of all distinct single-layer stackings of key P3 ground states at $x = 2/5$, $x = 1/2$, $x = 4/7$, and $x = 2/3$ (Figure D.6, Appendix D). The energy range of different stackings is less than 10 meV/CrO_2 at $x = 1/2$, $x = 4/7$, and $x = 2/3$, but is 20 meV/CrO_2 at $x = 2/5$. These results suggest that stacking does indeed have a significant effect, which should be considered in more detailed studies involving the orderings we have identified here.

5.3.3 Cr migration

As shown in Figure 5.3(a), interlayer Cr migration to tetrahedral sites is predicted to be favorable in O3-CrO_2. The corresponding predicted ground state structure is shown in Figure 5.7. In this structure, one third of the Cr have migrated to the intercalation layers, forming rows of tetrahedral Cr sites. Examining the calculated partial densities of states (Figure 5.8), we find that the tetrahedral Cr contribute minimally to the Cr d states immediately below the Fermi energy, consistent with an oxidation state of 6+ (d^0). These states represent a total of two electrons per CrO_2, or three electrons per octahedral Cr, in line with an oxidation state close to 3+ (d^3) for the octahedral Cr. Thus our results agree with the expected disproportionation of $Cr^{4+} \rightarrow \frac{2}{3}Cr^{3+} + \frac{1}{3}Cr^{6+}$.

Although the structure in Figure 5.7 has the lowest energy among those at $x = 0$ considered in this work, it is unlikely that it is accessed during the electrochemical extraction of Na. Bo et al. observed that the plateau at 3.8 V corresponds to the formation of an O3-$Na_\delta CrO_2$ phase with hexagonal ($R\bar{3}m$) symmetry, one third of the Cr migrated to tetrahedral sites, and a small amount of residual Na ($\delta = 0.04$) [192]. While the structure in Figure 5.7 is consistent with the observed charge disproportionation and

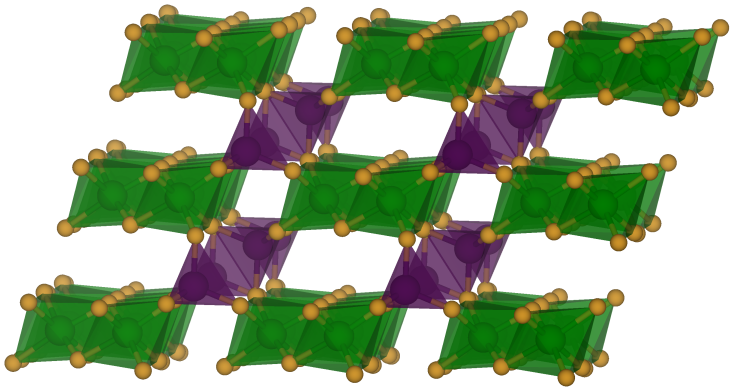

Figure 5.7: Relaxed structure of the predicted ground state O3-CrO_2 configuration with one third of the Cr occupying tetrahedral sites in the intercalation layers.

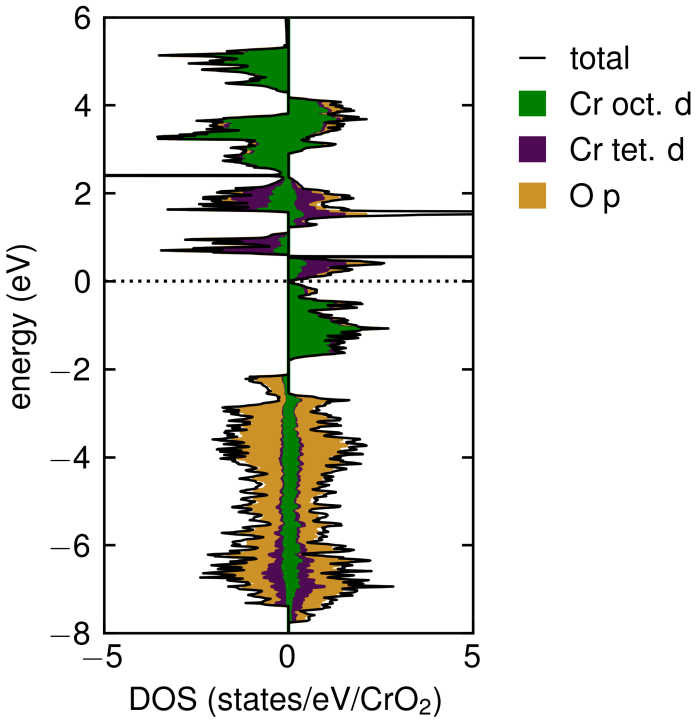

Figure 5.8: Total and partial densities of states for predicted ground state O3-CrO_2 structure with Cr migration to tetrahedral sites.

migration of Cr, the row ordering of tetrahedral sites (Figure 5.7) clearly breaks the $R\bar{3}m$ symmetry. The true structure formed experimentally likely contains a disordered arrangement of tetrahedral Cr sites.

There are also kinetic effects that would hinder the complete extraction of Na. In O3, Na hops between octahedral sites via the intermediate tetrahedral sites, but if a significant number of those sites are occupied by Cr then some Na could become trapped in the structure. However, with 1/3 of the Cr in tetrahedral sites, 5/6 of the tetrahedral sites in the intercalation layer would still be vacant, suggesting that Na diffusion channels would not be completely blocked. The more relevant effect is likely the contraction of the interlayer spacing near $x = 0$, which is known to inhibit diffusion by significantly increasing ion migration barriers [57, 93, 95, 202]. The structure shown in Figure 5.7 has an average interlayer spacing (between the oxygen above and below the intercalation layer) of 2.49 Å, compared to 3.16 Å for O3-$NaCrO_2$. This is also smaller than the interlayer spacing of O3-CrO_2 without Cr migration (2.58 Å), indicating that the presence of tetrahedral Cr contributes to an even more severe contraction. While these effects are often acknowledged as preventing ion reinsertion [82, 127, 173, 179, 192], they may also explain why a small amount of Na remains. If the kinetically accessible $Na_\delta CrO_2$ phase has a significantly higher formation energy than the CrO_2 phase we have identified, then it would raise the voltage of the two-phase plateau closer to the value measured experimentally.

Bo et al. reported that the O3-$Na_\delta CrO_2$ phase serves as an intermediate for a transition to a rocksalt CrO_2 phase (with Cr occupying half of the available octahedral sites) [192]. This differs from an earlier experimental report by Kubota et al., who described a single O3-$Na_\delta CrO_2$ phase (with $\delta = 0.06$) containing both tetrahedral and octahedral Cr in the intercalation layers, rather than a two-phase mixture with rocksalt [82]. To address this discrepancy, we considered a rocksalt-derived structure with stoichiometry CrO_2 in

which Cr adopts the same ordering as Mn in spinel $LiMn_2O_4$ (shown in Figure D.7, Appendix D). This spinel-like structure can be viewed as a particular one-half vacancy ordering on the rocksalt parent structure. As shown in Figure 5.3(a), we find that the formation of the spinel-like structure is unfavorable, with its energy lying 72 meV/CrO_2 above that of O3-CrO_2. Other Cr-vacancy arrangements would need to be considered to determine definitively if there is a more stable (dis)ordered rocksalt phase of CrO_2. However, disordered rocksalt structures are qualitatively different from ones containing tetrahedral Cr, and we find that the energetic driving force for charge disproportionation and migration to tetrahedral sites is quite significant.

5.4 Discussion

In this first-principles study, we have examined phase stability among various ion orderings in the O3 and P3 layered host structures of Na_xCrO_2 ($0 \leq x \leq 1$). O3 is found to be stable at high Na concentrations while P3 appears at intermediate ones. We identify many low-energy Na-vacancy orderings which can be organized into families, each based on a specific motif. In O3 the orderings contain rows of vacancies that serve as boundaries between fully sodiated regions, and in P3 the orderings contain APBs between regions of the particularly favorable $x = 1/2$ ordering (ζ). In each case, variations in the boundary density produce variations in the overall composition. The predicted phase stability regions and voltage are mostly consistent with experimental reports. We also confirm a preference for AFM ordering at high x and for Cr migration to tetrahedral sites in the intercalation layers of O3 at low x.

The main discrepancy between our predictions and experimental reports is in precisely where the transition from O3- to P3-type stacking occurs upon desodiation (see Figure 5.2). At zero temperature, we predict that O3 is stable down to $x = 3/5 = 0.6$, which

marks the start of a two-phase region with P3 at $x = 4/7 \approx 0.57$. Some experimental studies, however, report a P3 phase at compositions as high as $x \approx 0.7$ [82, 192]. There are also reports of P3 not appearing until $x \approx 0.6$ [191, 193], but with a significantly wider two-phase region with O3 than we predict. While it is possible that we could have missed important configurations in P3, we did verify that there were no new ground state orderings predicted by our cluster expansion for $3/8 \leq x \leq 3/4$ in supercells of volume 10 times the primitive cell volume or less. It is therefore unlikely that any dramatically more stable configurations were omitted. Furthermore, previous DFT studies similarly found O3 to be more stable than P3 at $x = 2/3$ [192] and $x = 3/5$ [82]. We also see no evidence that magnetic ordering lowers the energies of P3 configurations for intermediate x (Figure D.4, Appendix D).

There are several possible explanations for the discrepancy between the predicted phase boundaries of P3 and those inferred from experimental observations. One possibility is that P3 is further stabilized by entropy at finite temperature. Our Monte Carlo simulation results, however, show that configurational entropy actually serves to stabilize O3 even more (Figure D.1, Appendix D), though we do caution that the cluster expansion and Monte Carlo approach may not be able to capture collective excitations in the ordered phases of P3, such as rearrangements of APBs [14]. We have not considered vibrational entropy, which could potentially be relevant. Yabuuchi et al. reported the somewhat unusual decomposition of P′3-$Na_{0.5}CrO_2$ into Na-rich and Na-free P3 phases upon heating, which could indicate the importance of phonons at high (and low) x [131].

In assessing our predictions, it is also informative to examine their sensitivity to the particular DFT method used. We took the FM ground states from each structure as determined by SCAN and recalculated their energies using PBE and PBE+U, with $U = 3.5$ eV for Cr (the value typically chosen in the literature [82, 192, 194]). The resulting formation energies and voltage curves are shown in Figure D.8 of Appendix D,

compared to our SCAN results. While we acknowledge that a more rigorous comparison would involve a recalculation of the energies of many/all configurations with each DFT method, our analysis still provides some useful insights. Compared to SCAN, PBE yields a wider stability region for the P3 structure that extends up to $x = 8/13$ (versus $x = 4/7$ with SCAN). O3 is still predicted to be more stable than P3 at $x = 2/5$, but by a mere 0.1 meV/CrO_2 (versus 3 meV/CrO_2 with SCAN). The predicted voltage from PBE is about 1 V lower than the SCAN voltage, which is consistent with benchmarking results for transition-metal oxides intercalated with Li [196]. The O3-CrO_2 structure containing tetrahedral Cr is less stable with PBE, producing a higher cutoff voltage (relative to the rest of the voltage curve) than with SCAN. With PBE+U, we find that many of the SCAN ground states are displaced from the formation energy convex hull, and that the P3 stability region is even narrower (Figure D.8(c), Appendix D). This produces a voltage curve that is quite different in shape from the SCAN and PBE curves, even though it is close in value to the voltages from SCAN and experiment. It is known that the addition of a U term can significantly alter ground state predictions by inducing charge ordering [160]. Our comparison highlights the advantage of SCAN: It seems to provide reliable predictions of both phase stability and average voltage without requiring an empirical parameter such as U.

We find that Na_xCrO_2 displays many similarities to related layered oxide systems, as well as some key differences. The APB-based P3 orderings predicted here are largely the same as those predicted by first-principles studies of Na_xCoO_2, K_xCoO_2, and K_xCrO_2 [12,13,126]. This suggests that their stability arises from simple electrostatic interactions rather than specific chemical effects. The vacancy row orderings we identify in O3 are also the same as those predicted in Na_xCoO_2 [12]. In the analogous K systems, however, these structures relax to "M" phases containing a mixture of octahedral and prismatic K in the same intercalation layer [13,126], which has been attributed to the increased electrostatic

repulsion between K^+ ions compared to Na^+. A key distinction of the Na_xCrO_2 system is the relatively lower stability of P3 relative to O3 at intermediate x. Here we predict P3 to be stable up to $x = 4/7$, while it is found to be stable up to $x = 2/3$ in the Co and K analogues [12, 13, 126]. This behavior can be explained by considering the competing electrostatic repulsions that serve to (de)stabilize P3. While the intercalant ions in P3 share faces with transition-metal ions in the neighboring layers (which they do not in O3), this penalty is balanced by a reduction of intralayer repulsions between intercalant ions by their arrangement on the honeycomb networks [7]. In the case of K_xCoO_2 and K_xCrO_2, the repulsions between K^+ ions are strong enough that changing the transition-metal identify does not noticeably alter the stability of P3. In the case of Na_xCoO_2 and Na_xCrO_2, however, the larger ionic radius of Cr compared to Co in the same oxidation state [195] yields larger distances between intercalation sites, making the the effects of intralayer Na-Na repulsions, and thus the stability of P3, less pronounced.

The ordering patterns we have identified likely have significant consequences for ion diffusion. Highly ordered phases tend to lead to a significant reduction in the diffusion coefficient [57], however, this may not be true of the APB-based orderings in P3 predicted here. In P3-Na_xCoO_2, APBs have been theorized to facilitate diffusion via their collective motion through the intercalation layers [14]. The simulated diffusion was found to be Fickian, with a strong dependence of the diffusion coefficient on the Na concentration (corresponding to the APB density) [15]. The orderings we predict for $x > 1/2$ in Na_xCrO_2 are identical to those predicted in Na_xCoO_2, and although we predict a slightly different type of APB for $x < 1/2$, we believe that a similar diffusion mechanism based on APB migration may play a key role in both regimes in this system. Comparable mechanisms may also be relevant in the vacancy row orderings found in O3 at Na high concentrations. We do acknowledge that the orderings in Na_xCrO_2 are likely more tolerant to defects than those in Na_xCoO_2 due to the increased in-layer lattice parameter,

which may enable additional diffusion mechanisms.

5.5 Conclusion

In this study, we investigated phase stability between the O3 and P3 structures of layered Na_xCrO_2 and the nature of Na ordering within them. We identified several families of low-energy orderings: Some in O3 at high x containing rows of vacancies and some in P3 at intermediate x containing antiphase boundaries, which both enable smooth variations in composition. Similar orderings have been predicted in related Na and K intercalation compounds, and have important consequences for Na diffusion. In O3, we considered migration of Cr to tetrahedral sites in the intercalation layers at $x = 0$ and found a strong energetic preference tied to charge disproportionation. We have discussed how our findings may clarify discrepancies in the literature, specifically regarding the O3 $\rightarrow$ P3 transition upon desodiation and the Cr migration mechanism at low x. These results serve as fundamental groundwork for future computational and experimental studies of this promising electrode material.

Chapter 6

Ordering and phase stability in layered K_xCrO_2

6.1 Introduction

There is a consensus that deep decarbonization efforts must include extensive electrification across industries [203], which in turn will require reliable and cost-effective options for grid energy storage. Rechargeable Li-ion batteries are well suited for short-duration storage needs, but alternative technologies are highly desirable to avoid supply problems related to Li and other constituents [204]. Na- and K-ion batteries have emerged as potential replacements for Li-ion batteries in such applications, mostly due to the far greater abundance of those elements [3, 73, 205]. Compared to Na, K offers several additional advantages: Its lower redox potential can yield higher voltages and it can reversibly intercalate into graphite anodes [3, 206].

Several classes of materials have been investigated as cathodes for K-ion batteries, including the familiar layered transition-metal oxides used in Li- and Na-ion batteries [205, 207, 208]. The layered oxides generally promise high theoretical energy density

and rate capability [79, 208]. However, almost all of the layered oxide K intercalation compounds investigated thus far, such as K_xMnO_2 and K_xCoO_2, have only been synthesized and cycled at intermediate K concentration x, limiting their practical capacities [124, 209–218]. An important exception is layered $KCrO_2$, first synthesized by Delmas et al. [219,220], which is stable in the fully potassiated limit. In a key breakthrough, Kim et al. recently showed that this stability is unique to Cr (among redox-active $3d$ transition metals), and demonstrated the cyclability of layered $KCrO_2$ in electrochemical cells over a wide range of K concentrations [195]. Other studies have examined K-deficient K_xCrO_2 starting materials [125, 221], which display different cycling behavior. This variation in experimental observations necessitates an understanding of the equilibrium thermodynamics of this system.

While $KCrO_2$ is a viable candidate cathode material for K-ion batteries, questions remain about its structural evolution during cycling, which directly impacts battery performance. As observed by Kim et al., the system displays a multitude of different phases upon deintercalation, which produce a complex, stepwise voltage profile not unlike those of many layered Na intercalation compounds [195]. Phase transitions occur between the layered O3 and P3 structures (O/P denote octahedral/prismatic K coordination), shown in Figure 6.1, as well as O′3 and P′3 (primes indicate monoclinic distortions of the hexagonal parent structures [108]). Such transitions are accommodated by the facile sliding of CrO_2 layers [8, 11]. The details of structural phase stability and K ordering preferences are currently unknown for K_xCrO_2. Kim et al. [195] found that a significant fraction of the capacity is lost after the first charge, which may be related to the irreversibility of certain transitions. Elucidating the nature of structural changes and K-ordering transitions will assist the engineering of Cr-based cathodes for next-generation K-ion batteries.

Here we describe the results of a comprehensive first-principles study of phase stability

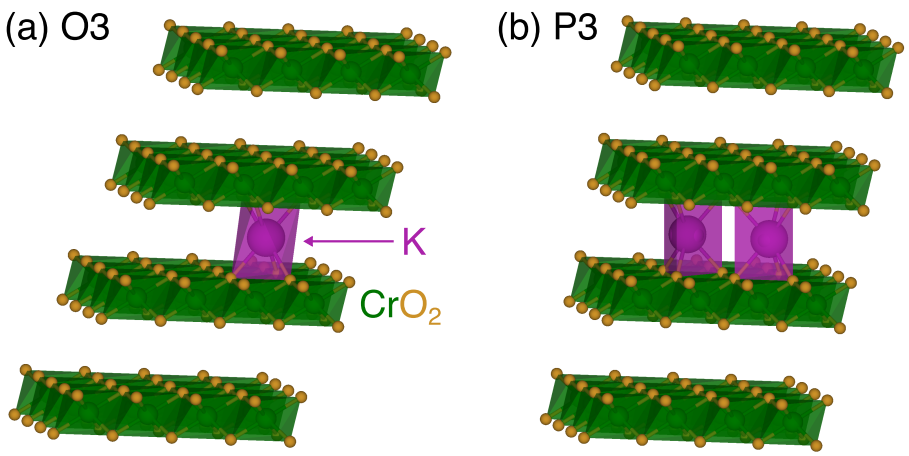

Figure 6.1: The (a) O3 and (b) P3 host structures of K_xCrO_2, which alternate between slabs of edge-sharing CrO_6 octahedra and K intercalation layers. The O3 structure allows K to lie on octahedral sites on a single triangular lattice, while the P3 structure allows K to lie on prismatic sites on either of two triangular lattices.

of K_xCrO_2 as a function of x ($0 \leq x \leq 1$). We predict a myriad of ground state and low energy orderings in P3 at intermediate K concentrations that belong to several families of hierarchical phases. These phases consist of periodic arrays of antiphase boundaries that separate well-ordered domains. We also predict the stability of a family of undulating phases with a mixture of octahedral and prismatic coordination within the same K intercalation layer at high K concentrations. The undulating phases are referred to as M phases as they host *mixed* K coordination. An analysis of simulated diffraction patterns of the M phases suggests that they may have already been observed experimentally, being mistaken for O′3. We argue that the large elastic deformations that are required to form the M phases may explain experimentally observed capacity losses at high K concentrations.

6.2 Methods

Total energies were calculated from DFT using VASP [59–62]. Calculations used a plane-wave energy cutoff of 600 eV, which, during testing, was found to be sufficient for convergence of energy differences to within 0.6 meV/CrO_2. **k**-point meshes were automatically generated with a density of 34 Å, which, during testing, was found to be sufficient for convergence of total energies to within 0.1 meV/CrO_2. The SCAN meta-GGA functional [30, 31] was employed to approximate the exchange-correlation energy, as it has been found to produce an improved description of layered oxides compared to GGA(+U) [195–198].

Symmetrically distinct K/vacancy-ordered configurations within periodic supercells of the O3 and P3 host structures were enumerated using CASM [10, 68–70]. Energies were calculated for 219 O3 configurations, 258 P3 configurations, and 39 M configurations. The M structures relaxed from certain O3 configurations, and were identified visually and by the deformation scores calculated by CASM. The majority of P3 configurations considered in this study were limited to those that do not contain a nearest-neighbor (NN) K-K pair, as configurations with such pairs were found to be highly unstable due to steric repulsion. Some non-ferromagnetic orderings of Cr spins were considered for the O3-$KCrO_2$ and P3-$K_{1/2}CrO_2$ ground state structures. Cluster expansion effective Hamiltonians for the O3 and P3 structures were fit iteratively in order to predict low-energy configurations and to run grand canonical Monte Carlo simulations of finite-temperature phase stability. For P3, the effective cluster interaction of the NN pair was manually set to a large value (5 eV/pair) to ensure no simultaneous occupation of those sites in our cluster expansion predictions. Details of the cluster expansions and Monte Carlo simulations can be found in Sections S1 and S2 of the Supporting Information [222], respectively.

Voltage was calculated using the Nernst equation [4]

$$V = -\frac{\mu_K - \mu_K^\circ}{e} \tag{6.1}$$

where μ_K is the K chemical potential of K_xCrO_2, μ_K° is the reference chemical potential of K metal in the body-centered cubic structure, and e is the elementary charge.

6.3 Results

6.3.1 Phase stability and voltage

Figure 6.2(a) shows the calculated zero-temperature formation energies of configurations within each host structure (O3, P3, or M). Formation energies were calculated relative to CrO_2 and $KCrO_2$ in the O3 structure. The convex hulls are shown for each host individually, along with the global convex hull of ground states over all host structures. O3 is predicted to be stable for $0 \leq x \leq 1/6$, $x = 1/3$, and $x = 1$, P3 is predicted to be stable for $1/5 \leq x \leq 1/4$ and $2/5 \leq x \leq 2/3$, and M is predicted to be stable for $3/4 \leq x \leq 7/8$. The set of high-energy (near zero formation energy) configurations in O3 and P3 at intermediate concentrations correspond to staged structures in which all layers are either completely empty or completely filled. Figure S2 of the Supporting Information [222] plots the distance of each formation energy to the global hull in order to more clearly reveal structures that are close to the global hull. A high degree of degeneracy is predicted among different host structures and ordered K-vacancy configurations. For example, the energy difference between the O3 and P3 ground states at $x = 1/5$ and $x = 1/4$ is less than 2.5 meV/CrO_2, indicating that the two host structures are nearly degenerate at these compositions considering the accuracy of the DFT calculations. We did not exhaustively explore phase stability below $x = 1/3$, given that this region is above

the voltage interval that has been reversibly accessed experimentally [195]. Fully deintercalated layered oxides often prefer the O1 structure [7, 105], however, we calculated the energy of O1-CrO_2 to be 1.0 meV/CrO_2 higher than that of O3-CrO_2. We therefore did not consider any staged hybrid structures with alternating O1- and O3-type stacking at low x.

All formation energies plotted in Figure 6.2(a), with the exception of O3 $KCrO_2$, were calculated with a ferromagnetic (FM) configuration. The O3 ground state at $x = 1$ (indicated by a diamond in Figure 6.2(a)) has an antiferromagnetic (AFM) in-layer ordering of the Cr spins (Figure S3a, Supporting Information [222]). This ordering is 14 meV/CrO_2 lower in energy than the FM configuration of $KCrO_2$. A preference for AFM ordering is consistent with the low-temperature magnetic behavior observed experimentally in $KCrO_2$ [223, 224]. The P3 ground state at $x = 1/2$, in contrast, prefers a FM in-layer ordering, with negligible magnetic interactions between adjacent CrO_2 layers (Figure S3b, Supporting Information [222]). The FM $x = 1/2$ ground state was predicted to be 17 meV/CrO_2 more stable than the closest non-FM in-layer ordering considered in this study. We therefore performed all other calculations ferromagnetically.

Figure 6.2(b) shows the zero-temperature equilibrium voltage curve obtained by calculating the K chemical potential using the global hull formation energies of Figure 6.2(a). The numerous ground state orderings in P3 produce a series of small steps in the voltage curve, along with larger steps at $x = 1/2$, 6/11, and 2/3. The M ground states yield another staircase of steps at higher composition, while the O3 ground state at $x = 1/3$ produces a large step. Generally, plateaus in the equilibrium voltage profile signify the occurrence of first-order phase transitions, as they correspond to a discontinuous jump in composition at a constant K chemical potential. In the case of the ordered phases that we describe in Section 6.3.2, computational constraints limit us to examining a finite number of orderings, which results in a stepped voltage profile. However, an actual material

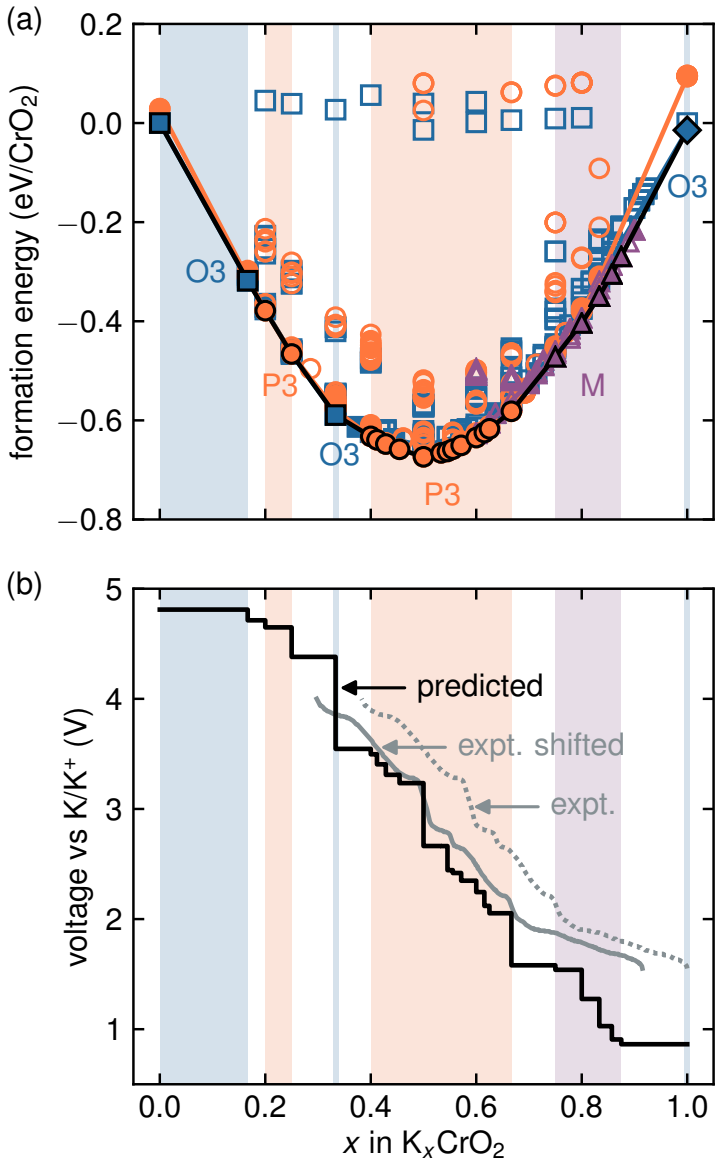

Figure 6.2: (a) Formation energy vs composition for calculated configurations. Filled symbols denote configurations on the local hull of each host structure. The global hull is outlined in black. Colored regions in the background indicate where each host structure is globally stable. The diamond at $x = 1$ indicates an antiferromagnetic ordering in O3. All other configurations shown are ferromagnetic. (b) Voltage vs composition as predicted by DFT (black) compared to an experimentally measured first charge curve from Kim et al. (gray, taken from Figure 3a of Reference [195]). The original experimental curve is shown as a dotted line, while the solid line is shifted in composition by $\Delta x = -0.085$.

will have the flexibility to sample a much larger number of phases that are separated by much smaller composition intervals, thereby giving the impression of a smoother, sloping voltage profile.

A first-charge voltage curve measured by Kim et al. [195] is also plotted in Figure 6.2(b). The reported capacity for the experimental voltage curve was converted to composition based on the theoretical capacity of $KCrO_2$. Figure 6.2(b) also shows the same experimental voltage curve shifted by $\Delta x = -0.085$, such that the largest step coincides with the $x = 1/2$ ordering in P3. Such a shift is appropriate, as Kim et al. [195] observed that some K is extracted from the stoichiometric $KCrO_2$ starting material before cycling. They attributed this to interaction with the carbon that was added to the electrode. A rigid shift in composition is the only adjustment we can include in our comparison without making assumptions about other factors such as side reactions. We also note that the chemical potential gradients present in real systems typically introduce polarization, whereby the measured voltage lies above and below the equilibrium voltage on charge and discharge, respectively [78], though we have not considered this in our comparison. After accounting for the shift in composition, the quantitative and qualitative agreement between our predicted voltage curve and experiment is quite good. In particular, the three major steps in the experimental curve match those predicted at $x = 1/2$, $6/11$, and $2/3$, with sloping regions in between that are consistent with many smaller steps.

Our grand canonical Monte Carlo simulations (described in Section S2, Supporting Information [222]) suggest that the O3 and P3 ground states for $x \geq 1/3$ do not disorder at 300 K (Figure S1, Supporting Information [222]). The cluster expansion and Monte Carlo approach can overestimate order-disorder transition temperatures, however we also saw no significant disordering of the ground states up to around 500 K (Figure S1, Supporting Information [222]). This is consistent with the strong ordering preferences displayed by related systems such as Na_xCoO_2 [12]. The highly distorted nature of the

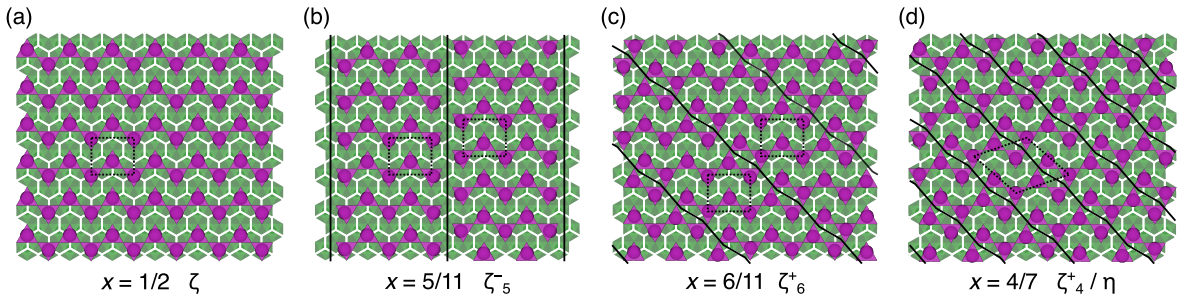

Figure 6.3: Relaxed in-plane K orderings of the (a) $x = 1/2$, (b) $x = 5/11$, (c) $x = 6/11$, and (d) $x = 4/7$ ground states in P3. The honeycomb network of available prismatic sites is shown in white. Black solid lines indicate antiphase boundaries. Black dotted lines indicated the in-layer unit cells of the ζ ordering (abc) and the η ordering (d).

M phases (see Section 6.3.2) makes them difficult to model with a configurational cluster expansion approach, but the coupling of K ordering to periodic undulations of the host layers likely limits the ability of the M phases to accommodate disorder. It is, therefore, reasonable to treat each M phase as a line compound with their free energy approximated by their DFT formation energy.

6.3.2 Ground state orderings

As shown in Figure 6.2, many ordered phases appear over a wide range of compositions in K_xCrO_2. We focus on the P3 and M ground states, as these appear in the experimentally accessed composition interval. The ground state orderings found in P3 (for $2/5 \leq x \leq 2/3$) belong to several families of hierarchical orderings first identified in Na_xCoO_2 and later predicted for K_xCoO_2 [12, 126]. These phases consist of regions of a single in-layer ordering separated by antiphase boundaries (APBs) that accommodate additional K or vacancies, thereby allowing for smooth variations in composition. This is illustrated in Figure 6.3. The $x = 1/2$ ordering (Figure 6.3(a)), which has been labeled ζ [12], corresponds to the familiar zig-zag row ordering on the honeycomb network that has been observed in several Na systems with the P3 structure [121, 131]. Below $x = 1/2$,

the ζ ordering is maintained locally while vacancies accumulate along periodically spaced APBs as shown in Figure 6.3(b). Above $x = 1/2$, the excess K concentrate along the APBs shown in Figure 6.3(c). We have labeled the families of orderings immediately below and above $x = 1/2$ as the ζ^- and ζ^+ phases, respectively [12]. At $x = 4/7$ we predict an important ζ^+ ground state having the maximum possible density of APBs (Figure 6.3(d)). This ordering has been labeled η to distinguish it from the other ζ^+ phases. It forms the basis of a third family of orderings (η^+) for $4/7 < x \leq 2/3$ that consist of η domains separated by APBs that introduce additional K. A complete description of the ζ^-, ζ^+, and η^+ orderings can be found in Reference [12].

The hierarchy of ground state orderings in P3 have the flexibility to vary their K concentration almost continuously without significantly disrupting strong local ordering preferences. This is achieved by varying the density of APBs. Orderings within the hierarchy can, therefore, be enumerated algorithmically by varying the periodicity with which APBs occur. This was done to systematically enumerate 3387 hierarchical orderings in an automated fashion. We generated all in-layer ζ^-, ζ^+, and η^+ orderings in supercells of volume 36 times the primitive cell volume or less, as well as all symmetrically distinct stackings of those orderings. We subsequently approximated their energies using the cluster expansion developed for the P3 host. There is typically a large number of these orderings at a given composition because different spacings of APBs can yield the same composition [12], as do different stackings of the same in-layer ordering. To summarize, all 3387 configurations enumerated belong to one of the three families of APB-based orderings, allowing us to assess the energetics of these orderings across many more compositions than we investigated with DFT. As shown in Figure 6.4, the cluster-expanded energies of these configurations all lie within 12 meV/CrO_2 of the hull, with many of them less than 1 meV/CrO_2 above the hull. For comparison, the weighted root-mean-square error of our P3 cluster expansion is 6.0 meV/CrO_2 (Section S1, Sup-

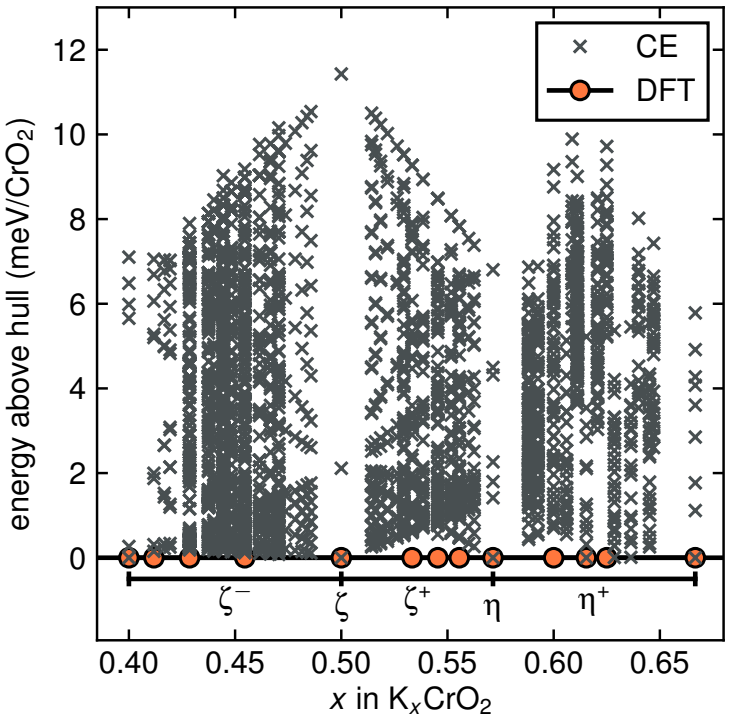

Figure 6.4: Energy above hull vs composition calculated from the cluster-expanded energies of many hierarchical orderings in P3. The compositions of DFT ground states in P3 are shown at a hull distance of zero. The compositions of important orderings and families of orderings are indicated.

porting Information [222]). Thus there are likely a continuum of (near) ground states in P3 that are responsible for the sloping voltage profile seen experimentally.

The other important family of ground state orderings are the M phases, which are stable for $3/4 \leq x \leq 7/8$. First predicted in K_xCoO_2 [126], the unique feature of the M phases is a mixture of octahedral and prismatic K coordination within the same layer. The relaxed structures of several representative M orderings are shown in Figure 6.5. These structures emerge when relaxing K-rich orderings in O3 that consist of rows of vacancies (also referred to as O′3 structures). The rows of K on either side of the vacant row relax toward each other to form two adjacent rows of distorted prismatic sites. The displacement of the K causes a periodic undulation of the adjacent CrO_2

layers. The M ground states shown in Figure 6.5 each contain two rows of prismatic K per unit cell, with varying amounts of octahedral K. The ground states at $x = 3/4$, $x = 4/5$, and $x = 5/6$ contain one, two, and three rows of octahedral K per unit cell, respectively. There are additional low-energy structures belonging to this family that interpolate the simpler structures. For example, the M structure at $x = 7/9$ (calculated to lie 0.03 meV/CrO_2 above the hull, which is within DFT error) interpolates the ground states at $x = 3/4$ and $x = 4/5$, alternating between one and two rows of octahedral K between pairs of prismatic K rows. Therefore, as with the P3 orderings, there is likely an infinite number of M phases with varying numbers of octahedral and prismatic K rows. A complete description of the M phases can be found in Reference [126]. We also find several metastable M phases below $x = 3/4$, which are qualitatively different from the row orderings seen above $x = 3/4$ (an example is shown in Figure S4, Supporting Information [222]). Such structures could potentially be accessed during conversion to P3.

6.3.3 Structural evolution

Our investigation of phase stability of K_xCrO_2 predicts a complex series of structural transitions upon K extraction that follows the sequence O3→M→P3→O3 and passes through a multitude of K-vacancy ordered phases when traversing the M and P3 hosts. Structural transitions often result in abrupt changes in lattice parameters that can have detrimental consequences during cycling of a battery [78, 225, 226]. Figure 6.6 shows the calculated lattice parameters of configurations on the hulls of each host structure. The lattice parameters of FM O3-$KCrO_2$ are predicted to be within 0.5% of the experimentally measured values. The removal of K from $KCrO_2$ leads to a contraction of the in-plane a and b lattice parameters (Figure 6.6(a)), which is consistent with the oxidation of

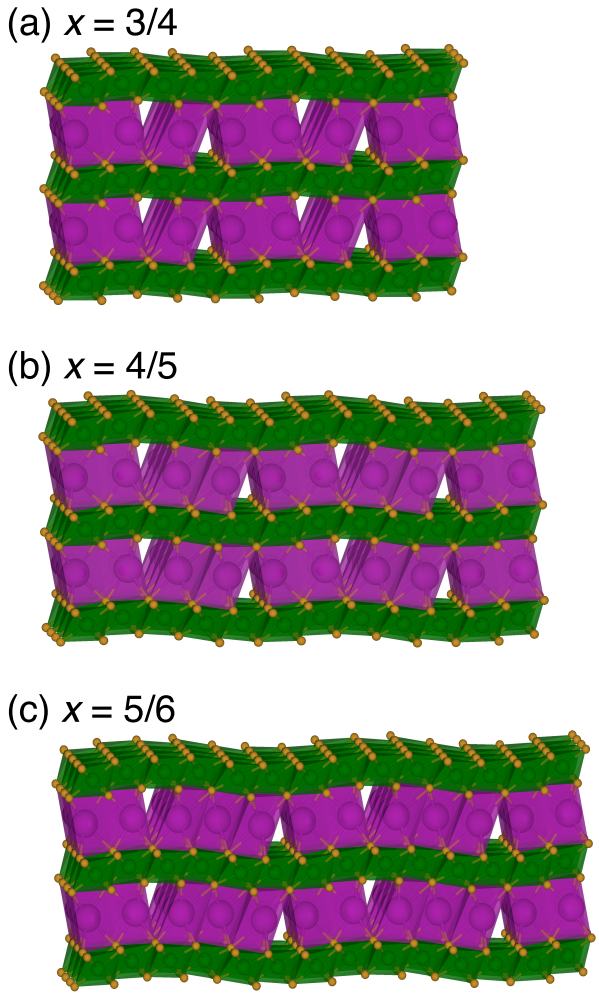

Figure 6.5: Relaxed structures of the ground state M phases at (a) $x = 3/4$, (b) $x = 4/5$, and (c) $x = 5/6$.

Cr^{3+} toward Cr^{4+}. A strong splitting of the a and b lattice parameters occurs in the M phases due to the monoclinic distortion that arises from the row ordering among K and vacancies that characterize the M phases. A similar but weaker splitting of the a and b lattice parameters also occurs in the P3 phases. The c lattice parameter increases upon deintercalation until $x = 1/3$ (Figure 6.6(b)), due to the well-known effect of a reduction in screening and an increase in the repulsion between adjacent O layers with the introduction of K vacancies [105].

We also simulated X-ray diffraction (XRD) patterns of the relaxed ground state structures to facilitate a direct comparison to the *in situ* XRD data reported by Kim et al. [195] (Figure 6.7). Note that slight quantitative differences in peak positions are expected due to discrepancies between the true and calculated lattice parameters. The positions of important peaks observed by Kim et al. are shown as dotted lines and labeled by letters, with an overall shift in composition of $\Delta x = -0.2$ (determined by adjusting the largest step in the *in situ* voltage curve until it coincides with $x = 1/2$, as in Figure 6.2(b)). This shift places the starting material at a composition of $x = 0.8$, which is within the composition interval in which the M phases are predicted to be stable. However, the presence of hexagonal O3 peaks near 13.7° and 18.0° (labeled a and b in Figure 6.7), which cannot be clearly attributed to any of our simulated M peaks, implies that the material may start as a metastable two-phase mixture of hexagonal O3 near $x = 1$ and M near $x = 0.8$. The three observed peaks labeled c, d, and e in Figure 6.7 were attributed to O′3 by Kim et al. but are close to simulated peaks in the M phases. The set of simulated M peaks near 16.0° is also consistent with experimentally observed peaks (labeled f), while the remaining M peaks are significantly less intense and may be difficult to resolve in practice. To test whether the M phases unambiguously provide the best agreement with experiment among the phases considered, we also simulated XRD patterns of the metastable configurations on the local hulls of O3 and P3 in the predicted M stability

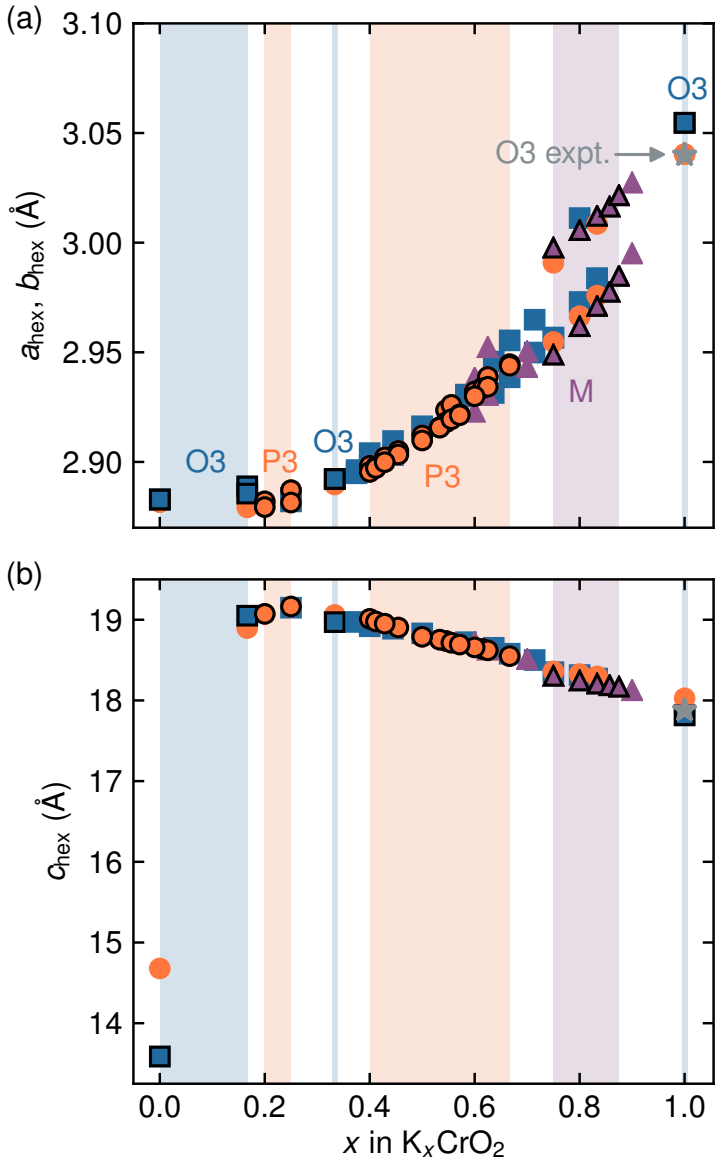

Figure 6.6: Relaxed lattice parameters (in terms of the hexagonal parent structures) vs composition for calculated configurations on the local hull of each host structure. Configurations on the global hull are outlined in black. Colored regions in the background indicate where each host structure is globally stable. Gray stars indicate the experimental lattice parameters of O3-$KCrO_2$ reported by Kim et al. [195]

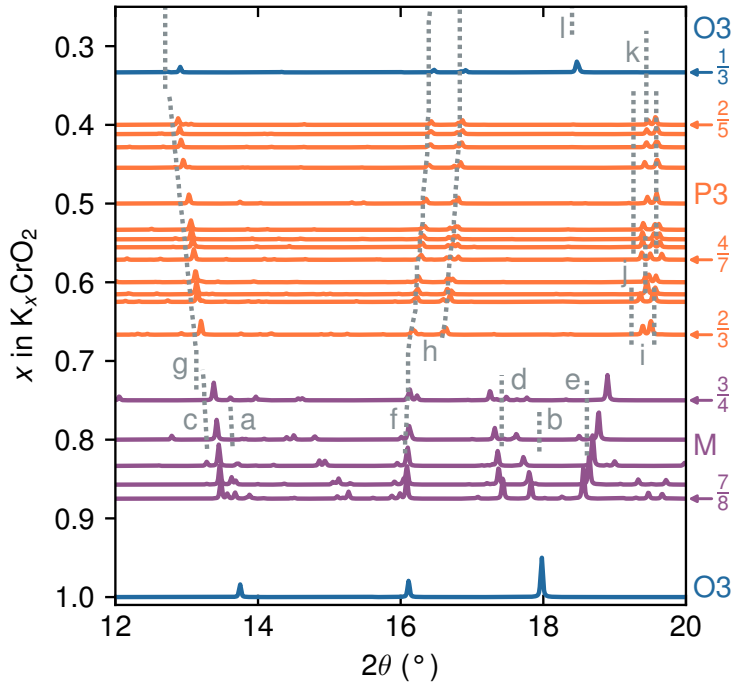

Figure 6.7: Simulated XRD patterns of configurations on the global hull. A wavelength of 0.71073 Å was used, corresponding to Mo Kα radiation. Generated using RIETAN-FP [227] within VESTA [71]. The compositions of certain configurations are indicated with arrows. Gray dotted lines with labels a–l indicate key peaks in the *in situ* XRD patterns from Kim et al. (Figure 4 from Reference [195]). The composition of the experimental data has been shifted by $\Delta x = -0.2$.

region (Figure S5, Supporting Information [222]). Neither set of simulated patterns for these metastable structures matches the experimentally observed peaks as closely as that of the M phases, most notably so for the peaks labeled d and e in Figure 6.7.

At compositions below $x = 3/4$, the series of observed peaks below 13.5° (labeled g in Figure 6.7) and near 16.5° (labeled h) match predictions well. The ground state ordering at $x = 2/3$ exhibits a pair of peaks near 19.5° that are consistent with the P′3 peaks reported by Kim et al. (labeled i). Upon reduction of the K composition, these peaks were observed to combine into a single hexagonal P3 peak before splitting again (labeled j), however, ground states predicted in this work show the emergence of a third peak in the same region that then disappears. This occurs near $x = 4/7$, the composition of the η ordering predicted to be a ground state. The η ordering has a hexagonal in-plane unit cell (Figure 6.3(d)) and may correspond to the experimentally observed hexagonal P3 structure. Below $x = 2/5$, Kim et al. again observe a single hexagonal P3 peak (labeled k), which could indicate that the K begin to disorder in this regime. Finally, a single hexagonal O3 peak was observed near $x = 0.3$ (labeled l) close to the O3 peaks of the ground state predicted to be stable at $x = 1/3$, though this phase may also be disordered. In summary, the simulated XRD patterns largely agree with experimental observations. While the available evidence does not definitively prove the formation of the M phases, it does with some plausibility suggest that their signatures in XRD may have been mistaken for those of O′3 phases.

6.4 Discussion

Our first-principles investigation of phase stability in layered K_xCrO_2 across the full K composition range has revealed the stability of a complex series of phases and K-vacancy orderings. The calculated voltage profile and simulated diffraction patterns are, upon

preliminary comparison, consistent with experimental observations, indicating that our description of phase stability in this system is plausible. Our study has produced two key results: A prediction of the stability of hierarchical ground state orderings in P3 that consist of well-ordered domains separated by anti-phase boundaries (APBs) and the prediction of the "M" phases, having mixed K coordination, as the stable structures at high K concentrations.

As with many layered transition-metal oxides, K_xCrO_2 prefers the P3 structure at intermediate K content, as the honeycomb network of trigonal prismatic sites in P3 enables a reduction in K-K repulsion in spite of the fact that those sites shares faces with Cr [7, 11]. We predict not just several ordered phases, but a continuum of ordered superstructures in P3 that belong to families that share common ordering tendencies (Figure 6.3). A favorable ordered motif, such as the ζ ordering shown in Figure 6.3(a), is preserved over a wide concentration interval, with variations in K concentration accommodated by the introduction of APBs as shown in Figure 6.3(b,c). The P3 orderings are examples of the "Devil's staircase" behavior [164, 165] found in many materials, including other layered intercalation compounds [8, 12, 126, 155] and metallic alloys [167–169]. The staircases of P3 orderings discussed here are not unique to K_xCrO_2, as they are also the predicted ground states in Na_xCoO_2 and K_xCoO_2 [12, 126]. The recurrence of these orderings suggests that they may appear in any P3 system in which electrostatic repulsions between alkali ions are the dominant interactions. It is therefore important to understand the K diffusion behavior within APB-based orderings. Though it is known that strong ordering tends to suppress diffusion [88, 228], the presence of APBs may give rise to unexpected, facile diffusion mechanisms. Future first-principles kinetic studies will explore this possibility. As for the evolution of the APB-based phases during cycling, they could display solid solution behavior in which transitions occur solely by the rearrangement of boundaries rather than by a nucleation and growth process.

The more surprising prediction of this study is the stability of the M phases — ground states with a mixture of octahedral and prismatic K in the same layer (Figure 6.5). These structures were first identified computationally in K_xCoO_2 [126], emerging from spontaneous relaxations of certain O3 structures. The unique stability of these undulating phases appears to originate from an in-layer rearrangement of K that allows them to spread out more than is possible in O3. The resulting reduction in K-K repulsion outweighs the strain penalty of warping the metal oxide layers [126]. In K_xCoO_2 the M phases are predicted to appear above the K compositions investigated electrochemically [124], and are likely not globally stable. As layered K_xCrO_2 is stable up to $x = 1$ [195], it is more likely to exhibit the M phases.

Our simulated XRD results (Figure 6.7) suggest that the M phases have diffraction patterns that are very similar to those assigned to monoclinic O′3 structures, to the point where it may be challenging to differentiate between the two. The energies of the M phases are significantly lower than the closest O3 or P3 configurations considered in this study, and the difference increases with x (Figure S2, Supporting Information [222]). For example, at $x = 3/4$ the M ground state lies 17 meV/CrO_2 below the O3 ground state and 5 meV/CrO_2 below the P3 ground state, while at $x = 5/6$ M lies 33 meV/CrO_2 below O3 and 35 meV/CrO_2 below P3. The sizable energetic preference for the M phases does not support the idea that O3 or P3 would form in their place. We have also confirmed that M phases provide a better match to the experimentally observed XRD data than the metastable O3 or P3 structures (Figure S5, Supporting Information [222]). We note that the formation of an M phase within an O3 or P3 electrode particle during cycling would result in coherency strain due to lattice mismatch and the warping of the CrO_2 layers. Such strain could potentially be quantified in XRD studies through analysis of peak broadening [229,230]. We also observe that the calculated lattice parameters of the M phases lie between those of the endpoint O3-$KCrO_2$ and P3-$K_{2/3}CrO_2$ phases and are

comparable to those of the most stable O3 and P3 structures in the M stability region (Figure S5, Supporting Information [222]). This observation, along with the presence of metastable M phases below $x = 3/4$ (Figure S4, Supporting Information [222]), suggests that the M phases could offer a continuous pathway for structural transformation from O3 to P3 as K is extracted.

If the M phases do indeed form, there would be important consequences for battery performance. The strain associated with forming the M phases upon charge could result in a significant overpotential, which may be part of the reason that the calculated voltage curve underpredicts experiment at high x (Figure 6.2(b)). The M phases may also explain the capacity loss observed experimentally, where K cannot be fully reinserted into the cathode at the end of first discharge. Kim et al. attributed this to slow kinetics in the O′3 phase [195], but it could be that the strongly ordered M phases suppress the transition back to the O3 phase altogether. It therefore may be favorable to make chemical substitutions that penalize the formation of the M phases or facilitate reversible transitions between M and O3, if possible. Layered cathode materials engineered to avoid such detrimental phase transitions while remaining stable at high K concentrations could allow for the low-voltage regime to be fully utilized.

6.5 Conclusion

This study investigated phase stability in layered K_xCrO_2, a promising cathode material for K-ion batteries. We found that O3 tends to be stable at extreme K concentrations, while P3 is stable at intermediate ones. A multitude of (near) ground state structures appear in P3, belonging to several families of hierarchical in-layer K orderings based on the stable $x = 1/2$ and $x = 4/7$ orderings. Antiphase boundaries between the ordered domains allow for smooth variations in composition with K (de)intercalation, but may

limit the speed and dimensionality of diffusion. We also predict the emergence of unusual "M" phases at high x ($3/4 \leq x \leq 7/8$) that contain mixed octahedral and prismatic K coordination within each intercalation layer. These phases display large distortions driven by K-K repulsion, and may lead to irreversiblities if they form during cycling. We find that the formation of the M phases is plausible, and that they may be difficult to distinguish from O′3 phases. Our calculated voltage profile and simulated XRD patterns are generally consistent with experimental observations, assuming a K-deficient starting material. These results should provide a foundation for understanding and optimizing layered oxide cathodes with near-maximal K content to unlock higher capacities in battery applications.

Chapter 7

Atomistic diffusion involving antiphase boundaries

7.1 Introduction

Na-ion batteries continue to attract interest as cost-effective alternatives to Li-ion batteries for select applications. In many reports, a layered transition-metal oxide intercalated with Na is used as an electrode [73, 79, 97, 231]. Such compounds have already been widely adopted as cathodes in Li-ion batteries due to their favorable electrochemical properties [78, 232, 233]. An important criterion for evaluating cathode materials is the ease with which ions diffuse through the crystal, as the ionic conductivity of the electrodes contributes to overall rate capability of the cell [4, 95]. Compared to Li, Na frequently induces more structural phase transitions and stronger ion-vacancy orderings [7, 8, 11, 81, 83, 84, 121, 234], which can significantly affect kinetics. Many issues associated with layered oxides for Na intercalation also apply to their K analogues for the emerging K-ion batteries [13, 126, 205, 235].

Layered oxides can adopt a variety of host crystal structures, each with distinct

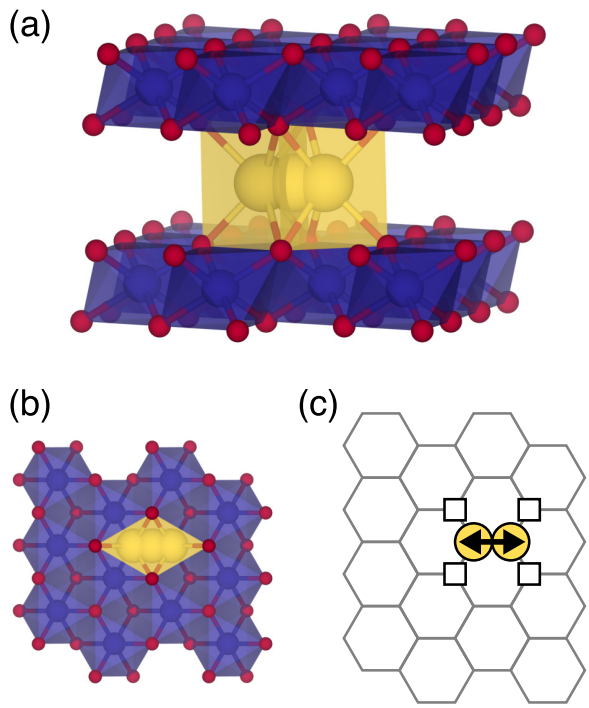

Figure 7.1: (a) Side view of P3-Na_xCoO_2, with Na shown hopping between nearest-neighbor trigonal prismatic sites in the Na layer. (b) Top view of the nearest-neighbor hop. (c) The same view as (b) shown on the honeycomb network of possible Na sites. Squares indicate sites that must be vacant in order for the hop to occur.

topologies of intercalant sites. The O3 structure [108], favored by many Li intercalation compounds such as Li_xCoO_2 [78, 234], hosts intercalating ions in octahedral sites that form two-dimensional triangular lattices. The related O1 structure [93] also hosts intercalating ions in octahedral sites. Hops between nearest-neighbor octahedral sites of layered intercalation compounds pass through intermediate tetrahedral sites. This leads to diffusion mechanisms that are mediated by divacancies, with important consequences for the concentration dependence of the diffusion coefficient [57, 93, 95].

While layered Na intercalation compounds such as Na_xCoO_2 also favor an O3 crystal structure at high concentrations, they usually transform to a P3 structure upon Na extraction through a change in stacking sequence of the two-dimensional transition-metal oxide building blocks [7, 108]. The P3 structure is shown in Figure 7.1(a) for Na_xCoO_2.

The Na ions of P3 occupy trigonal prismatic sites that form two-dimensional honeycomb networks. Elementary Na hops between nearest-neighbor prismatic sites in P3 pass through the shared face of their coordination prisms as illustrated in Figure 7.1. Simultaneous occupation of nearest-neighbor sites in P3 is highly unfavorable due to steric repulsion [8, 12]. The neighboring sites of the hop endpoints must therefore be vacant for a hop to occur as illustrated in Figure 7.1(c). Second-nearest-neighbor hops are also possible in P3 if the intermediate nearest-neighbor site is unstable (Figure S1, Supporting Information [236]). These crystallographic constraints lead to collective transport mechanisms that remain unexplored and poorly understood. It is generally believed that diffusion in P3 is faster than in O3 [154, 155, 234, 237, 238], but the mechanisms that are responsible for the enhanced ion mobility in P3 have not received much attention.

In this study, we investigate diffusion mechanisms in the P3 host structure from first principles, using P3-Na_xCoO_2 as a model. Since layered Na intercalation compounds exhibit stronger ordering tendencies than their Li counterparts [7,11], we focus in particular on the role of Na ordering on transport kinetics. Ordered phases introduce pronounced steps in the voltage profile and can impact kinetics, often reducing the mobility and/or dimensionality of transport [57,88]. Some Na and K intercalation compounds that adopt the P3 host, including Na_xCoO_2, are predicted to exhibit families of hierarchical phases consisting of well-ordered domains separated by a periodic array of antiphase boundaries (APBs) [11–13,126]. Our systematic study of diffusion in these ordered phases points to a transport mechanism that is mediated by APB motion, as opposed to mechanisms that rely on distinct vacancies or vacancy clusters. This would make diffusion in P3 structures fundamentally distinct from the more conventional diffusion mechanisms of O3 and O1 hosts [57, 93, 95].

7.2 Background

Select examples of the hierarchical orderings considered in this study are shown in Figure 7.2 alongside calculated and experimentally measured voltage curves for Na_xCoO_2 [12, 121]. Each step in the voltage curve corresponds to an in-layer Na ordering, with the large step at $x = 1/2$ corresponding to a particularly stable ground state that has been named ζ [12]. The local ordering is retained as the composition is decreased or increased from $x = 1/2$, with changes in composition accommodated by APBs between regions of the ζ ordering (shown as black lines in the insets of Figure 7.2). There are two types of APBs: One which introduces additional vacancies and one which introduces additional Na. The average spacing between APBs can be varied nearly continuously, giving rise to a "Devil's staircase" [164, 165] of orderings below and above $x = 1/2$. This description is consistent with the sloping, yet somewhat jagged structure of the measured voltage profile.

The family of orderings just below $x = 1/2$ (for $2/5 \leq x < 1/2$) is labeled ζ^-, while that just above $x = 1/2$ (for $1/2 < x \leq 4/7$) is labeled ζ^+ [12]. The average linear density of APBs is proportional to $1/2 - x$ and $x - 1/2$ for the ζ^- and ζ^+ orderings, respectively (derived in Section S1, Supporting Information [236]). The composition may equivalently be expressed in terms of the spacings between APBs, which provides a convenient way to label specific orderings within each family. For example, the $x = 5/11$ and $x = 6/11$ orderings shown in Figure 7.2 are labeled ζ_5^- and ζ_6^+, respectively [12].

The ζ^- and ζ^+ families of orderings were predicted to be stable at room temperature in Na_xCoO_2 [12]. These same intercalant orderings have also been predicted as ground states in K_xCoO_2 [126] and K_xCrO_2 [13], indicating that they are relevant in a wide range of related materials. It is therefore desirable to determine how intercalant migration occurs within such highly ordered phases. The continuous nature of these families of orderings

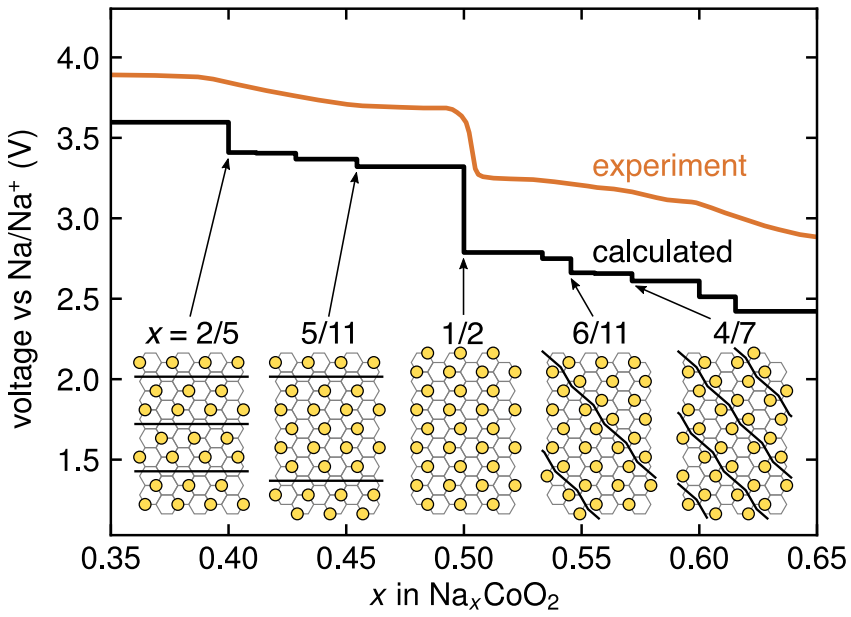

Figure 7.2: A section of the calculated voltage curve of Na_xCoO_2 from Reference [12]. Experimental voltage curve taken from Reference [121]. Insets show the in-layer Na orderings of calculated ground states at select compositions. Black lines in insets represent antiphase boundaries between regions of the $x = 1/2$ ordering.

suggests that transitions between individual phases during cycling may be accommodated by the collective motion of APBs through the crystal, but it is not immediately clear how this would occur. We seek to determine the viability of such a mechanism. We also wish to understand any differences in behavior between the "diluted" boundaries of the ζ^- orderings (those that introduce additional vacancies) and the "enriched" boundaries of the ζ^+ orderings (those that introduce additional Na). To study Na migration within these families of orderings, we chose one representative ordering from each, namely the ζ_5^- and ζ_6^+ orderings shown in Figure 7.2.

7.3 Methods

First-principles calculations were performed using large periodic supercells to calculate energies and migration barriers within the perfectly ordered regions of the ζ ordering and in the vicinity of APBs. Supercells of the representative ζ^- and ζ^+ orderings (ζ_5^- and ζ_6^+) were chosen such that Na sites that are equidistant from an APB are symmetrically equivalent, yielding three asymmetric Na sites in each case (Figure S3, Supporting Information [236]). The lowest energy stacking (under the described symmetry constraint) of each of the two primitive in-plane Na orderings was selected and tripled along the boundary direction. Finally, the c lattice vector of each supercell was adjusted to maximize the distance between each atom and its nearest periodic image in the next layer. The resulting supercells are shown in Figure S3 of the Supporting Information [236]. The minimum distances between periodic image atoms in our calculations are 8.54 Å and 9.75 Å for the ζ^- and ζ^+ supercells, respectively. CASM [10,68–70] was used to enumerate symmetrically distinct point defects and Na hops within the chosen supercells. For all hops considered, we required that the nearest-neighbor sites of the hop endpoint sites be unoccupied to avoid steric repulsion.

Energies were calculated using VASP [59–62] with a plane-wave energy cutoff of 530 eV and **k**-meshes of density 30 Å along each reciprocal lattice vector. The optB86b-vdW exchange-correlation functional [64–67] was employed to capture van der Waals interactions, as it has been shown to be effective in this system [12]. The representative ζ^- and ζ^+ structures were relaxed fully, but for all subsequent calculations the lattice was fixed to the relaxed lattice of either the ζ^- or ζ^+ structure and only the ions were allowed to relax. Migration energy pathways were calculated via the nudged elastic band method as implemented in VASP, using a minimum of seven images between endpoints. Static calculations using the linear tetrahedron method [63] were performed to obtain final energies of all relaxed structures.

7.4 Results

We investigate defect formation and Na migration barriers in the ζ_5^- ($x = 5/11$) and ζ_6^+ ($x = 6/11$) orderings of P3-Na_xCoO_2 to determine the mechanisms with which Na diffusion occurs in the families of APB-containing P3 orderings. For brevity, we will refer to the ζ_5^- and ζ_6^+ orderings as simply ζ^- and ζ^+, respectively. Our calculations indicate that the endpoints of many Na hops within the ζ^- and ζ^+ orderings are dynamically unstable: They either relax to a different configuration or are found to reside on a local maximum of the energy surface of the crystal as revealed with NEB calculations (some examples of the latter case are shown in Figure S4, Supporting Information [236]). We refer to these hops as "invalid" as their endpoints do not coincide with local minima in which the migrating Na ion can thermalize before performing a subsequent hop.

While the majority of simple nearest-neighbor hops in the ζ^- and ζ^+ orderings are found to be invalid, there are a number of allowed hops along the APBs. These valid hops are found to be crucial to Na transport as they enable a straightforward mechanism for

APB migration through kink formation and lateral expansion. Our calculations predict exceedingly low migration barriers for kink formation and expansion for the ζ^- APBs, and moderately low barriers for similar pathways in the ζ^+ ordering. We also compare the defect energies required for APB migration to vacancy formation energies and determine that additional vacancies are unlikely to play a significant role in Na transport within the well-ordered ζ^- and ζ^+ phases.

7.4.1 Na migration in the perfect ζ^- and ζ^+ orderings

We enumerated all distinct one-atom first-nearest-neighbor (1A1NN) hops within the perfect ζ^- and ζ^+ orderings. These are shown in Figure 7.3. Our calculations predict that almost all of these hops are invalid, indicated by open-face red arrows in Figure 7.3. There is only one allowed 1A1NN hop in the ζ^- ordering and it involves the Na closest to the APB hopping towards the APB (black arrow in Figure 7.3(a)). For the ζ^+ ordering, all 1A1NN hops were found to be invalid. There are also no valid one-atom second-nearest-neighbor hops in the ζ^+ ordering, as all of them would result in a simultaneous occupation of nearest-neighbor sites.

These results demonstrate the strong resilience of the ζ ordering at $x = 1/2$ with respect antisite disorder, as the Na in regions of perfect ζ ordering between APBs of ζ^- and ζ^+ are quite restricted in their mobility despite being surrounded by vacancies. In the apparent absence of simple Na migration mechanisms, we turn our attention to the possibility of collective APB migration in the ζ^- and ζ^+ orderings. This would allow for the local ζ ordering between APBs to be retained but also for vacancies/Na to move through the crystal with the APBs.

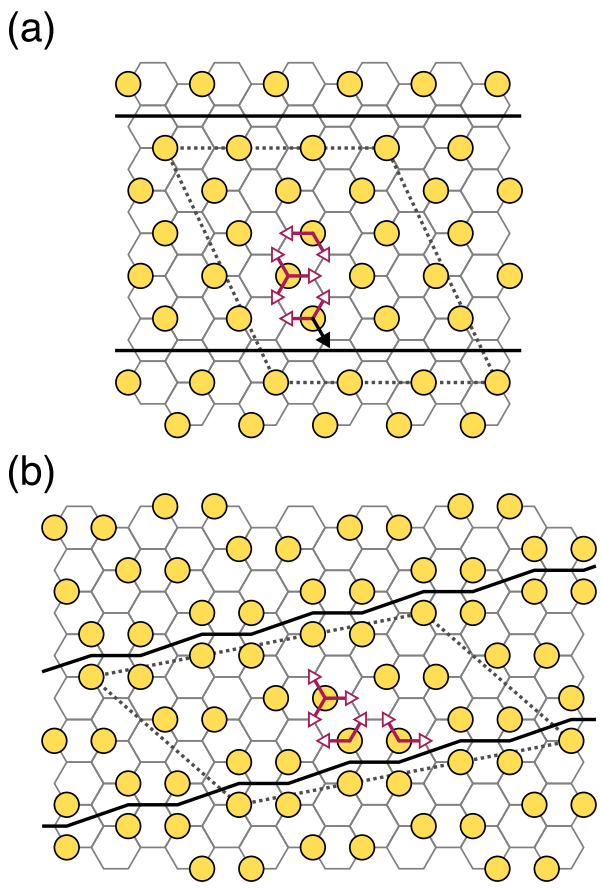

Figure 7.3: Symmetrically distinct one-atom nearest-neighbor Na hops in the representative (a) ζ^- and (b) ζ^+ orderings. Dotted lines indicate the in-plane supercell. Solid black lines indicate APBs. A filled-face black arrow indicates that the hop is valid, while an open-face red arrow indicates that the hop is invalid.

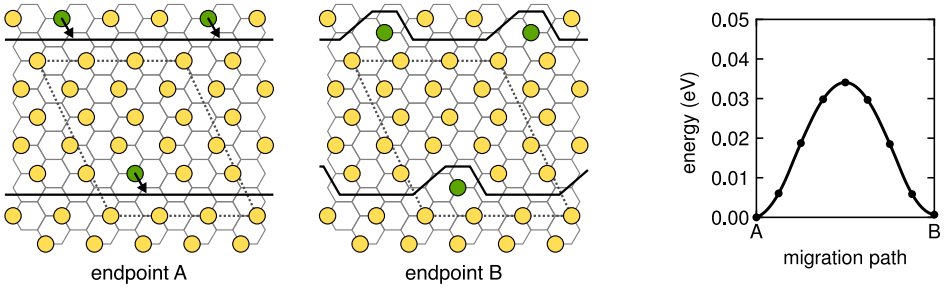

Figure 7.4: Migration energy for APB kink formation in the representative ζ^- ordering. Dotted lines indicate the in-plane supercell. Solid black lines indicate APBs. Green circles indicate the hopping Na and its periodic images, with the hop direction indicated by black arrows.

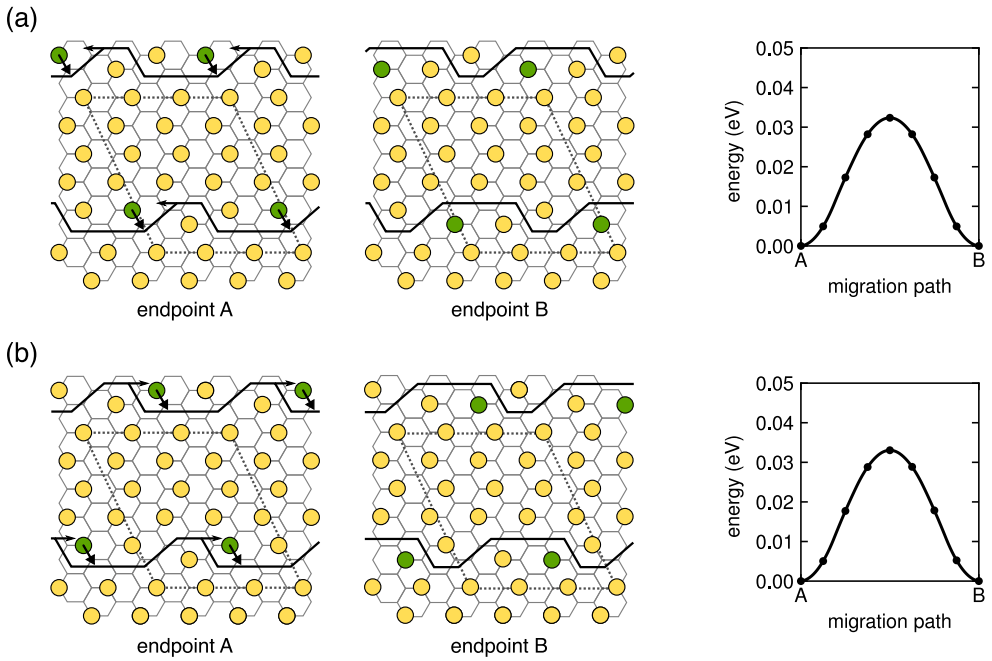

Figure 7.5: Migration energies for APB kink expansion in the representative ζ^- ordering. (a) and (b) show the two possible directions for expansion from an initial kink. Dotted lines indicate the in-plane supercell. Solid black lines indicate APBs. Green circles indicate the hopping Na and its periodic images, with the hop direction and kink expansion direction indicated by black arrows.

Boundary migration in the perfect ζ^- ordering

An examination of the lone valid 1A1NN hop in the ζ^- ordering suggests a simple mechanism for APB migration. As shown in Figure 7.4, this hop forms a kink in the APB, in which a section of the boundary is translated away from the rest of the boundary. The calculated migration barrier for this hop is just 0.03 eV. Furthermore, the end state of the hop has almost the same energy as the initial state, indicating that there is no defect energy associated with the kink (Figure 7.4). The remarkably low migration barrier implies that kinks may form readily in the ζ^--type APBs.

Once this kind of kink has formed, it can expand via subsequent 1A1NN hops involving the Na next to the kink. As shown in Figure 7.5, the kink may expand in either direction along the boundary with a migration barrier of 0.03 eV, the same as that of the initial kink formation. Note that while the kink expansion seems to introduce no additional defect energy, these hops are necessarily symmetric due to our particular choice of supercell (that is, endpoints A and B in Figure 7.5 are symmetrically equivalent). This symmetry also highlights that these events may be viewed as either expansion or contraction of a kink, depending on the orientation of the kink relative to the rest of the boundary.

From simple elementary hops, we have discovered a mechanism for APB migration in the ζ^- ordering. First a kink in the boundary is formed, and then the kink can expand such that the boundary as a whole translates. The individual migration barriers required for this mechanism are very low, comparable to thermal energy at room temperature.

Boundary migration in the perfect ζ^+ ordering

For the perfect ζ^+ ordering, we have identified a similar mechanism to that found in the ζ^- ordering, in which kinks in the APBs may form and then expand. Although there

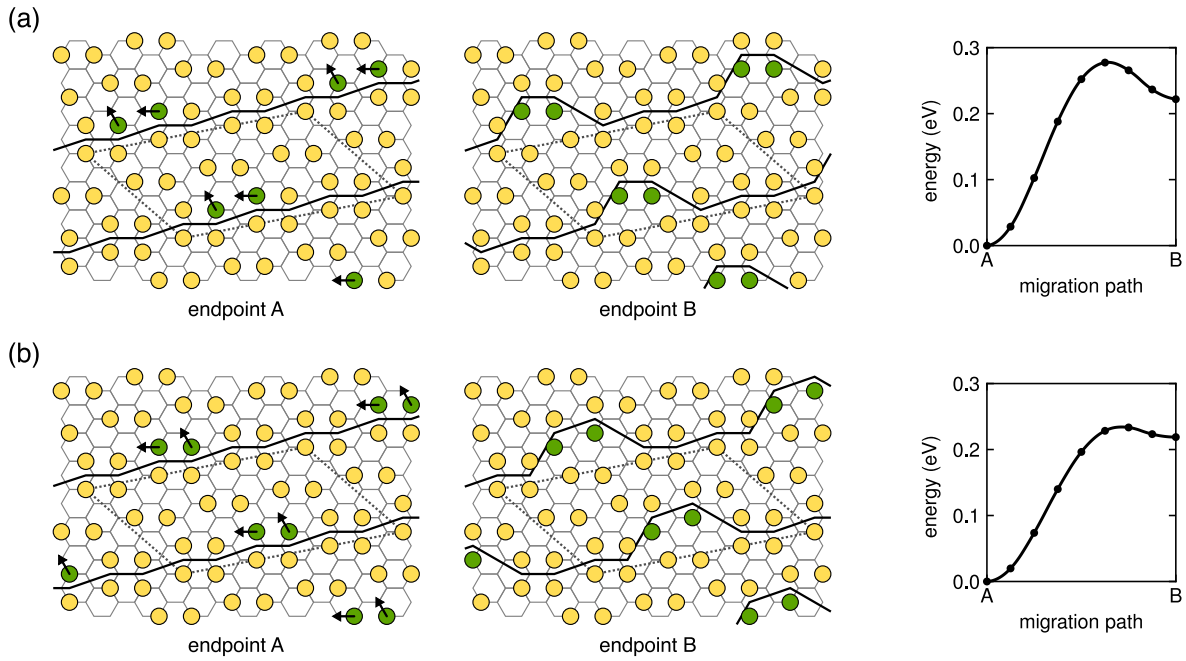

Figure 7.6: Migration energies for APB kink formation in the representative ζ^+ ordering. (a) and (b) show the two types of kinks that can form. These hops occur as simultaneous two-atom hops. Dotted lines indicate the in-plane supercell. Solid black lines indicate APBs. Green circles indicate the hopping Na and their periodic images, with the hop direction indicated by black arrows.

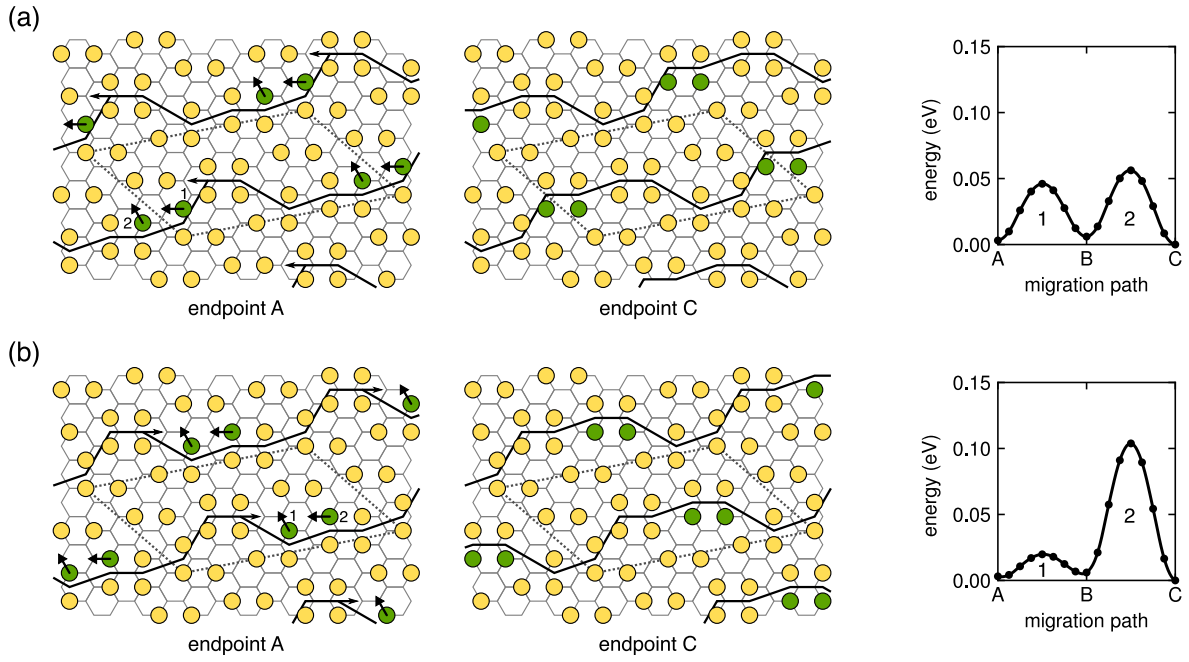

Figure 7.7: Migration energies for APB kink expansion in the representative ζ^+ ordering. (a) and (b) show the two possible directions for expansion from an initial kink. These hops occur as pairs of one-atom hops, with the numbers indicating their order. Dotted lines indicate the in-plane supercell. Solid black lines indicate APBs. Green circles indicate the hopping Na and their periodic images, with the hop direction and kink expansion direction indicated by black arrows.

is no 1A1NN hop possible in the perfect ζ^+ ordering, there are more complicated, two-atom hops that enable initial kink formation. Due to the orientation of the APBs, there are two distinct Na sites that lie at the boundary in the ζ^+ ordering, and there are two valid ways for these Na to collectively hop such that a kink is formed, as shown in Figure 7.6. These must occur as simultaneous hops, as decomposing them into pairs of valid 1A1NN hops is not possible (Figure 7.3). There are two distinct types of kinks, shown forming in Figure 7.6(a) and (b). The two types of kinks have the same defect energy of 0.22 eV, although the first type has a larger barrier to formation than the second (0.28 eV vs 0.23 eV). While these barriers are not as low as that of kink formation in the ζ^- ordering, they are still relatively low, suggesting that these kinks may readily form at room temperature.

As with the ζ^--type APBs, once a kink has formed in a ζ^+-type APB it may expand via hops involving the Na next to the kink. For example, the first type of kink (shown forming in Figure 7.6(a)) may expand in either direction through 1A1NN hops, as shown in Figure 7.7. Expansion in either direction requires pairs of 1A1NN hops that occur one after the other. For expansion in one direction (Figure 7.7(a)), the two hops have comparable barriers (0.04 eV and 0.05 eV), while for expansion in the other direction (Figure 7.7(b)), the first hop has a very low barrier and the second hop has a higher one (0.02 eV and 0.10 eV). Note that in our chosen supercell, the second type of kink (shown forming in Figure 7.6(b)), is equivalent to endpoint C in Figure 7.7, so that type of kink may expand by the reverse of the hops shown in Figure 7.7. For completeness, this is illustrated in Figure S5 of the Supporting Information [236].

For the ζ^+-type APBs, all barriers for kink expansion hops are less than half of the barriers for kink formation. The defect energy for kink expansion is also negligible, as the migration barriers shown in Figure 7.7 are close to symmetric. This suggests that for the ζ^+ ordering, kink formation is the limiting step in the APB migration mechanism, as once

a kink has formed its expansion is relatively facile. The fact that the individual migration barriers for 1A1NN ζ^+ kink expansion hops are nearly symmetric is consistent with the symmetry of the local environments of these hops under reversal of the hop direction, as shown in Figure S6 of the Supporting Information [236]. The same symmetry of the local environment does not exist for the equivalent 1A1NN hops occurring at perfect boundaries (i.e. one-atom kink formation hops), so in these cases one hop endpoint is preferred (Figure S6, Supporting Information [236]). This symmetrization of the local environment may explain why 1A1NN hops at perfect ζ^+ boundaries are invalid but become valid in the presence of a kink.

7.4.2 Vacancy formation

The ζ^- and ζ^+ orderings have compositions close to $x = 1/2$ and therefore contain high concentrations of vacancies. To assess the relevance of *additional* vacancies that may mediate diffusion processes that are distinct from those that lead to kink formation and expansion (in the absence of additional vacancies), we calculated vacancy formation energies in the ζ^- and ζ^+ orderings.

The vacancy formation energy in a particular ordered phase that is stable at a Na chemical potential μ is given by

$$E_{\mathrm{f,Va}} = E_{\mathrm{Va}} - E + \mu \tag{7.1}$$

where E_{Va} and E are the energies with and without a single point vacancy, respectively. Each type of vacancy defect has a vacancy formation energy that is a function of μ, since the ordering into which the vacancy is introduced is stable within a finite chemical potential (i.e. voltage) window. We consider the vacancy formation energies within the μ windows that stabilize the ζ_5^- and ζ_6^+ orderings. Note that this is likely an overestimation

of the actual stability window size, as there are likely intermediate phases on the Devil's staircase of orderings that have not been explicitly included [12].

The average formation energies of point vacancies on each of the three distinct Na sites in the ζ^- and ζ^+ orderings are listed in Figure 7.8, along with the energy window of each ordering. The size of the energy windows are small compared to the average vacancy formation energies, so we may use the averages as a convenient figure to discuss relative magnitudes. For the ζ^- ordering, where the boundaries are more dilute than the bulk ordering, vacancies prefer to lie away from the boundary (site 3). For the ζ^+ ordering, where the boundaries are more enriched than the bulk ordering, vacancies prefer to lie at the boundary (sites 1 and 2). This is consistent with the expectation that a homogeneous distribution of vacancies is preferred. The lowest average vacancy formation energy in the ζ^- ordering is 0.21 eV, while the lowest in the ζ^+ ordering is 0.52 eV.

We can compare these vacancy formation energies to the defect energies associated with APB migration in the ζ^- and ζ^+ orderings (Section 7.4.1) to assess whether additional vacancies are likely to contribute to Na diffusion. For the ζ^- ordering, the vacancy formation energy of 0.21 eV, while low, is not negligible. In contrast, the defect energy for APB kink formation in the ζ^- ordering is essentially zero. Hence, the concentration of APB kinks should be significantly higher than the concentration of additional vacancies at room temperature in the ζ^- orderings. For the ζ^+ ordering, the defect energy associated with APB kink formation of 0.22 eV (for both types of kinks) is not insignificant, however, it is still less than half of the lowest point vacancy formation energy of 0.52 eV. As with the ζ^- ordering, the formation of APB kinks is far more favorable than the formation of vacancies in the ζ^+ ordering. We also considered combined kink-vacancy defects for the ζ^+ ordering by enumerating all distinct point vacancies in supercells containing either of the two kinks shown in Figure 7.6. The lowest energy kink-vacancy defect has an average formation energy of 0.45 eV, which while lower than lowest point

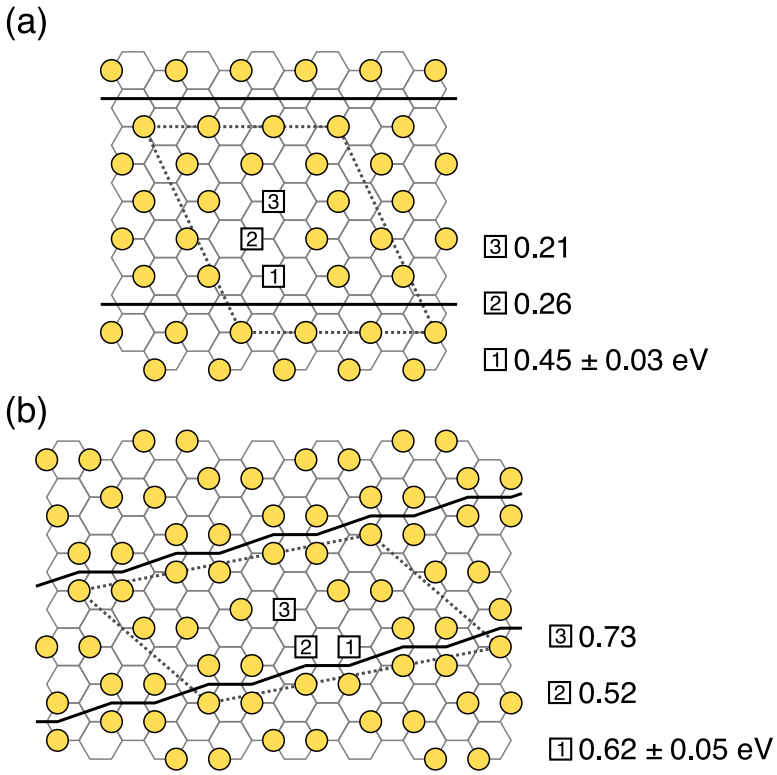

Figure 7.8: Calculated formation energy windows of symmetrically distinct point vacancies in the representative (a) ζ^- and (b) ζ^+ orderings. Dotted lines indicate the in-plane supercell. Solid black lines indicate APBs. Squares indicate point vacancies on different sites, labeled by site number.

vacancy formation energy in the perfect ordering, is still significantly higher than the APB kink formation energy without a point vacancy. These results imply that even though additional vacancies may increase the mobility of Na in the ζ^- and ζ^+ orderings, their contribution to macroscopic Na transport is likely to be negligible in comparison to that mediated by APB migration via kink formation and expansion.

7.5 Discussion

In this study, we have investigated Na diffusion mechanisms within highly ordered phases of P3-Na_xCoO_2. Two sets of hierarchical Na ordered phases were examined that are composed of regions of a single ordering (ζ) separated by one of two types of APBs. In the ζ^- orderings the boundaries incorporate extra vacancies, while in the ζ^+ orderings they incorporate extra Na. The APBs are not defects, but are instead crucial features of the equilibrium phases, with the equilibrium density of APBs set by the composition x. In the perfect orderings, diffusion via simple one-atom hops appears to be quite limited, as many endpoint configurations of these hops are unstable. There are, however, valid mechanisms in both the ζ^- and ζ^+ orderings that enable the APBs themselves to migrate. This can occur by the formation of a kink in the boundary followed by the continual expansion of the kink along the boundary (much like kink-mediated processes for grain boundary motion [239, 240] or surface step growth [241, 242]). Additional vacancies are not only not required for this mechanism to occur, but also have defect energies that are higher than those required for APB migration.

While both the the diluted APBs of the ζ^- orderings and the enriched APBs of the ζ^+ orderings allow for APB migration, the mechanisms and the energies of these processes are somewhat different. For the ζ^--type boundaries, kinks can form without incurring an energy penalty and can form and expand via one-atom hops with a minuscule barrier

of 0.03 eV. These hops are low enough in energy that the motion of Na at the boundaries could serve not only as a diffusion mechanism but also as a possible source of entropy, further lowering the free energy of ζ^- phases at finite temperature. We expect the true ζ^--type APBs to be rough and dynamically shifting, unlike the perfectly straight boundaries depicted in Figure 7.2. In contrast, kinks in the ζ^+-type boundaries must form via two-atom hops with barriers about an order of magnitude higher than those in the ζ^- case. Because there is also a significant kink defect energy for the ζ^+-type APBs, the reverse barriers are low, meaning it is likely that most kinks that form will subsequently be destroyed. However, kinks that persist can expand via one-atom hops that have more modest barriers than the initial kink formation. Based on these differences, we expect the ζ^+-type APBs to be both less rough (containing fewer kinks) and less mobile than the ζ^--type APBs.

In choosing a single representative from each family of APB-based orderings, we neglect any potential composition dependence of the migration barriers. To begin exploring the composition dependence of the migration barriers, we varied the c lattice parameter, which depends on composition and controls the spacing between CoO_2 slabs. The inter-slab spacing is known to affect intercalant migration barriers in layered oxide systems, with larger spacings yielding lower barriers [57, 93, 95, 202]. We recalculated formation barriers for each type of APB kink with the c lattice parameter fixed to that of the minimum or maximum composition of the corresponding family of orderings ($x = 2/5$ and $x = 1/2$ for ζ^-, $x = 1/2$ and $x = 4/7$ for ζ^+), using the relaxed c lattice parameters of the P3 ground state structures provided in Reference [12]. As shown in Figure S7 of the Supporting Information [236], the kink formation barriers decrease with increasing c lattice parameter, as expected. However, the variation in the barriers is not large, as none of them change by more than 0.01 eV over their respective c lattice parameter ranges. While the barriers for APB migration are not strongly affected by the c lattice param-

eter changes induced by varying composition, there are other factors, such as in-layer electrostatic effects, that could influence the barriers more significantly as one traverses each family of orderings.

While the results of this study indicate that APB migration is an important mechanism of Na transport in well-ordered P3 phases, we acknowledge that there could be additional mechanisms that are important to diffusion. It is possible that more complicated, coordinated multi-atom hops are allowed, beyond the one- and two-atom hops considered here. Such mechanisms would likely be difficult to identify by enumeration, but could perhaps be observed in molecular dynamics simulations [88, 243]. We did investigate whether the formation of APB kinks opens up any additional avenues for Na migration. For each type of APB kink, we calculated migration barriers of 1A1NN hops in the vicinity of a single kink (shown in Figure S8 of the Supporting Information [236], with the barriers of the valid hops listed in Table S1). As in the perfect orderings, most of the hops are invalid, but there are two valid hops for each type of kink besides the kink expansion/destruction hops discussed previously. For the ζ^- kinks, these hops have barriers that are more than double the barrier for kink expansion, while for the ζ^+ kinks, some of the additional hops have barriers comparable to those for kink expansion. This indicates that there may be additional relevant diffusion pathways in the ζ^+ orderings, but APB migration remains a significant mechanism for long-range diffusion.

Our results may have important implications for the performance of P3-Na_xCoO_2 and related electrode materials that adopt similar intercalant orderings. If APB migration is indeed the dominant diffusion mechanism, then long-range Na transport within a single crystal would be confined not just to the two-dimensional intercalation layers, but to a single dimension perpendicular to the APBs. We would also expect the Na mobility to increase with the density of APBs. This would result in a sharp drop in the diffusion coefficient as the APB density approaches zero, which occurs near $x = 1/2$. At this

composition, where the ζ ordering is stable, alternative mechanisms would take over, perhaps requiring vacancy defects.

Any predictions of this study will be difficult to test experimentally without understanding the macroscopic consequences of the APB migration mechanism. While we obtain low barriers for the elementary hops required for APB migration, these may not necessarily translate to fast bulk diffusion. Rapid localized hops may be highly correlated such that back-and-forth hopping dominates. The extent to which APB migration contributes to long-range diffusion must be determined through kinetic modeling, which could also provide estimates of effective Na diffusion coefficients and their composition dependence. However, our results reveal a subtle complication for modeling efforts in that many configurations are found to be mechanically unstable in P3. A general kinetic Monte Carlo approach using cluster expansion techniques [57, 93, 94, 244–246] will likely encounter difficulties, as the unstable configurations may be erroneously visited during simulations even if the cluster expansion assigns them high formation energies. The development of a more constrained kinetic model to investigate APB migration will be the focus of a future study.

7.6 Conclusion

We have examined diffusion mechanisms in the layered P3 crystal structure, which is adopted by many Na and K intercalation compounds at intermediate compositions. Using Na_xCoO_2 as a model system, we investigated Na migration mechanisms in phases comprised of ordered regions periodically separately by APBs. The Na in the ordered regions of these phases are largely immobile, however, atomic hops are possible along APBs, which lead to APB kink nucleation and propagation and thereby mediate Na diffusion through the crystal. This mechanism has low kinetic barriers and does not

require vacancy defects. The results of this study suggest that APB migration, though distinct from conventional vacancy-mediated diffusion, is an important, if not dominant diffusion mechanism in a variety of P3 layered intercalation compounds that host APB-based ordered phases.

Chapter 8

Macroscopic diffusion facilitated by antiphase boundaries

8.1 Introduction

Ionic mobility is a crucial property for functional materials in various device applications. As a prominent example, electrode materials for rechargeable batteries must allow sufficiently fast diffusion of the charge carrier ions so as not to limit the overall rate capability in an electrochemical cell [4]. Layered transition metal chalcogenides, such as $LiTiS_2$, $LiCoO_2$, $NaCoO_2$, and their analogues, have been explored extensively for battery applications due to their high cation diffusion coefficients and capacities [73, 78, 79, 97, 231–233]. Many transition metal chalcogenides also display interesting electronic phases that may be accessed or tuned electrochemically [6, 85, 194, 247–253]. Understanding the nature of ion diffusion through the two-dimensional intercalation layers of such materials is critical to engineering their performance, but is complicated by subtleties arising from the interplay of chemistry and crystal structure.

Diffusion mechanisms and rates can vary significantly with chemistry due to differ-

ing chalcogen anion stacking sequence preferences and the intercalant ion site topologies that result. For instance, layered Li intercalation compounds tend to only adopt structures with octahedral Li sites that form triangular lattices (e.g. O3 and O1, where O denotes octahedral coordination), while Na and K often stabilize additional structures with prismatic intercalant sites that form honeycomb networks (e.g. P3 and P2, where P denotes prismatic coordination) [7,11,78,108,234]. Furthermore, Na and K frequently assume intricate ion-vacancy orderings, especially in the P structures [7,8,11,13,81,83,84,121,126,205,234,235]. These structural variations lead to differences in the kinds of kinetic hops that are allowed as well as the mechanisms that enable long-range diffusion, which typically rely on the presence of specific defects such as vacancy clusters [95,171]. Largely due to the difficulty of ascertaining them experimentally, the mechanistic details of diffusion in many layered Na and K intercalation compounds have not been fully explored.

Recently, we conducted a study of Na migration mechanisms in P3-Na_xCoO_2, a canonical model system for understanding the behavior of layered Na intercalation compounds used as battery electrodes [14]. This material is predicted to adopt families of Na-vacancy orderings comprised of antiphase boundaries (APBs) that separate domains of a stable $x = 1/2$ ordering [12]. The phases directly below $x = 1/2$ contain APBs that add vacancies, while the phases directly above $x = 1/2$ contain APBs that add Na. By systematically considering various atomic hops, we found that the Na within the perfectly ordered regions between APBs are immobile, while those along APBs are very mobile and thereby facilitate the migration of APBs [14]. This mechanism, illustrated in Figure 8.1(a) for an APB that forms below $x = 1/2$, relies on the formation and expansion of kinks to facilitate APB motion. The limiting migration barriers, those of APB kink formation, were calculated to be relatively low (0.03 eV and 0.30 eV for $x < 1/2$ and $x > 1/2$, respectively). While our prior study and the present study focus on the Na

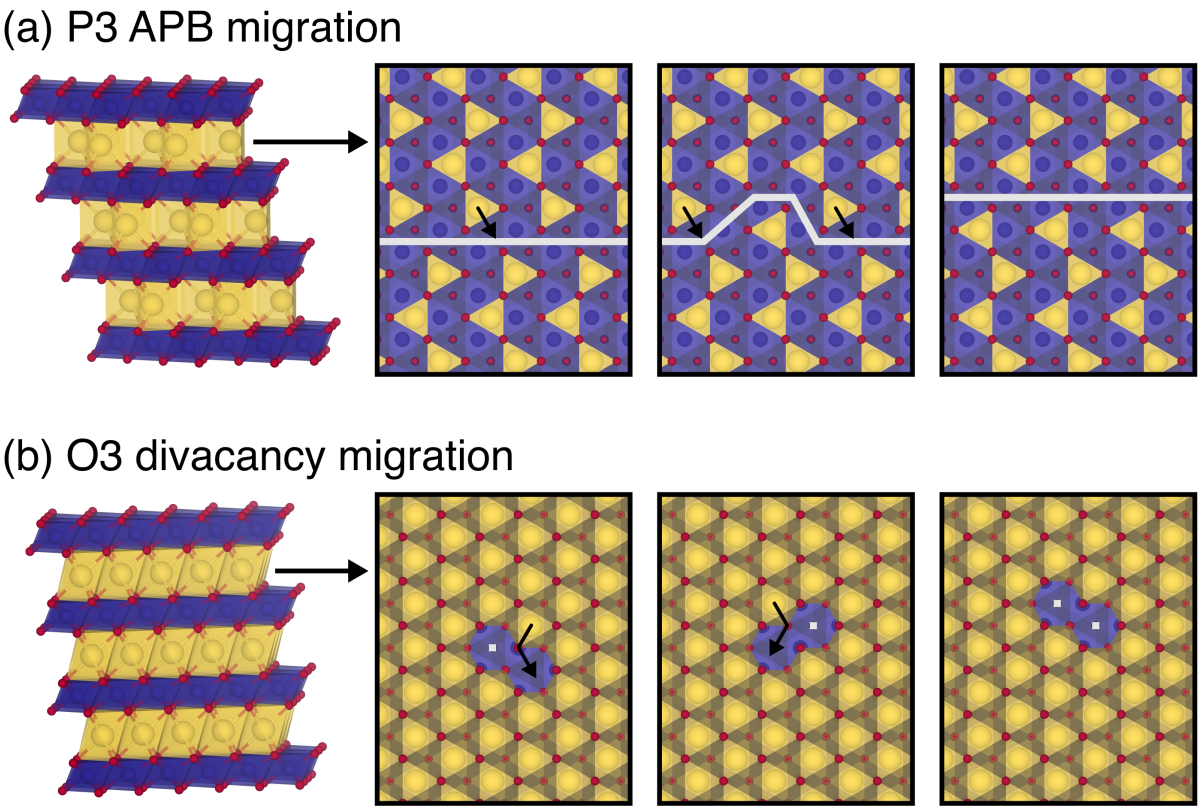

Figure 8.1: (a) Illustration of the kink-mediated APB migration mechanism in P3-Na_xCoO_2 at intermediate x, shown for a ζ^- APB ($x < 1/2$). (b) Illustration of divacancy migration via a cartwheel motion in O3-Na_xCoO_2 at high x.

material, we expect that our findings may apply to related K intercalation compounds, given that they tend to adopt similar APB-based ion-vacancy orderings [13, 126].

In this study, we use a specialized kinetic model to determine the extent to which the APB migration mechanism contributes to long-range diffusion in P3-Na_xCoO_2, as well as to understand the nature of the diffusion mathematically. The predicted behavior is consistent with Fickian diffusion in one dimension (perpendicular to the APBs), with a significant dependence of the diffusion coefficient on composition due to variations in the APB density and migration barriers. This work identifies APB migration as a key diffusion mechanism in the P3 structure that differs substantially from known mechanisms

in O3 and P2 materials, in that it allows for facile long-range ion transport in ordered phases without requiring vacancy cluster defects [57, 93, 95].

8.2 Background

The crystallographic constraints of the O and P layered structure types lead to different fundamental atomic hop mechanisms, as shown in Figure 8.2. In the P structures, Na can hop directly between neighboring prismatic sites (Figure 8.2(a)), yielding inherently lower migration barriers than in the O structures, where hops between neighboring octahedral sites must pass through a smaller intermediate tetrahedral site (Figure 8.2(b)) [57, 93, 234]. Beyond differences in migration barriers of individual hops, geometric and correlation effects play a critical role in determining diffusion mechanisms at non-dilute concentrations. The complex Na-vacancy orderings often hosted by the P structures can severely limit the rate of Na diffusion at particular stoichiometries. For example, in some ordered phases of P2-Na_xCoO_2, it was found that Na may only hop back and forth locally, and that vacancy defects must be present to allow any Na mobility [88].

Even in disordered phases, short-range ordering can significantly affect transport. Na diffusion in O3 relies on a well-known divacancy mechanism common to Li intercalation compounds [57, 93, 95], while similar multi-vacancy clusters are thought to be important in disordered phases in P2 [88, 171, 243]. The divacancy mechanism, shown in Figure 8.2(b), dominates diffusion in O3, as the divacancy configuration significantly lowers the migration barrier compared to the same hop without an additional vacancy next to the intermediate tetrahedral site [95]. The result is a tendency for isolated divacancies to remain intact and move via a "cartwheel" motion, as illustrated in Figure 8.1(b) [57]. Such mechanisms can result in highly correlated ion motion and a strong dependence of the diffusivity on the concentration of the vacancy clusters. Important mechanistic

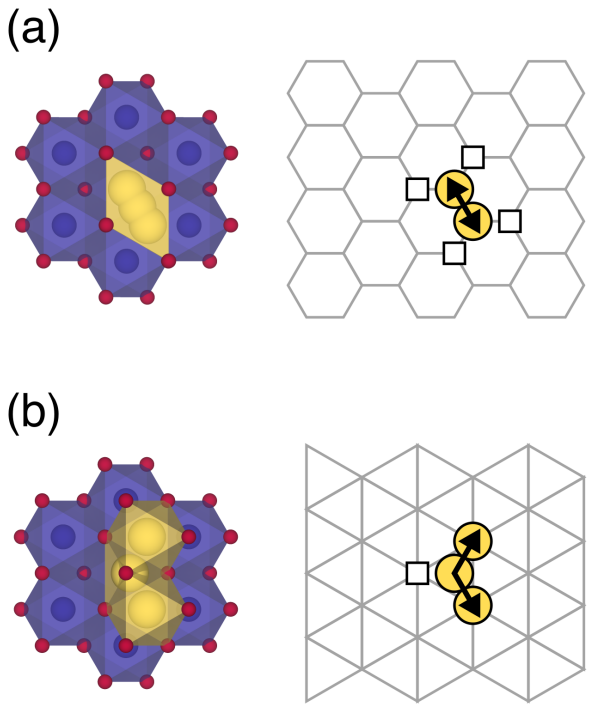

Figure 8.2: (a) Illustration of Na hopping between prismatic sites on a honeycomb network in a P structure. Squares indicate vacancies required for the hop endpoints to be stable. (b) Illustration of Na hopping between octahedral sites (via a tetrahedral site) on a triangular lattice in an O structure. Square indicates the additional vacancy that lowers the hop barrier within the divacancy mechanism.

details, as well as accurate rates of diffusion, can be exceedingly difficult to evaluate experimentally. It is generally accepted that diffusion in P2 is faster than in O3 [154, 155, 234, 237, 238], but little experimental data exists for the P3 structure specifically, despite its continued relevance for Na- and K-ion battery electrodes.

Also central to this study is the multitude of stable ion-vacancy orderings that naturally arise on the honeycomb networks of P3 intercalation compounds [8, 11, 12]. It is known that the geometry of the honeycomb network can lead to "Devil's staircases" of infinite ground state orderings that span a range of concentrations [165]. Intercalation compounds such as P3-Na_xCoO_2 and P3-Na_xTiS_2 are predicted to stabilize families of Na-vacancy orderings based on APBs [8, 12]. As shown in Figure 8.3 for P3-Na_xCoO_2, APBs separate translational variants of the stable $x = 1/2$ ordering (referred to as the ζ ordering) and introduce either more vacancies (ζ^- APBs) or more Na (ζ^+ APBs). These APBs can be thought of as extended defects in the ζ ordering, however, they appear as part of the predicted ground state orderings directly above and below $x = 1/2$ (not as configurational excitations). These orderings form two Devil's staircases, as the average density of APBs, which determines the composition, can vary essentially continuously. The same staircases of orderings have also been predicted in P3-K_xCoO_2 [126] and P3-K_xCrO_2 [13], so they are relevant to K intercalation compounds as well. Note that these orderings are distinct from those identified in P2-Na_xCoO_2 [160, 166], as the two triangular lattice sites of the honeycomb networks are inequivalent in P2, unlike in P3.

8.3 Methods

Kinetic Monte Carlo (KMC) simulations were used to simulate the diffusion behavior due to the migration of APBs. We constructed a model in which APB-based orderings on the honeycomb network are mapped onto two-dimensional grids (representing a single

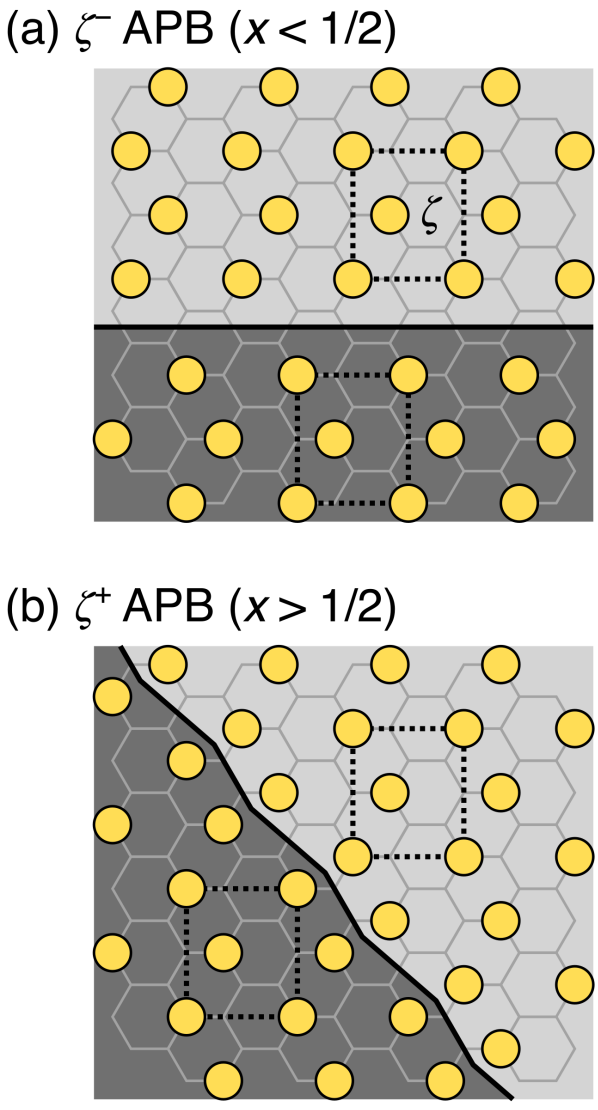

Figure 8.3: Examples of the (a) ζ^- and (b) ζ^+ APBs on the honeycomb network of P3. Black lines indicate the APBs, which separate translational variants of the ζ ($x = 1/2$) ordering (light and dark gray backgrounds). Dotted lines indicate the unit cell of the ζ ordering.

Na intercalation layer), with one dimension oriented along the length of the APBs and the other oriented perpendicular to the APBs. Each individual Na atom is mapped to one grid cell and assigned a phase (0 or 1) depending on the translational variant of the ζ ordering to which it belongs. The APBs are implicitly represented as the shared edges of grid cells with opposite phase. Examples of these phase grids for ζ^- and ζ^+ orderings are shown in Figure 8.4, where the light and dark gray regions of alternating phase correspond to those in Figure 8.3.

The phase grids can be converted into two-dimensional composition grids by first accounting for the space added or consumed by the APBs and then defining a local composition x over the model area. This procedure is illustrated in Figure 8.4. The regions between APBs are assigned a composition of $x = 1/2$ (the composition of the bulk ζ ordering), while the ζ^- and ζ^+ APBs are assigned compositions of $x = 0$ and $x = 1$, respectively. This scheme recovers the exact overall composition $\bar{x}$ of the original orderings upon averaging the local composition over the entire model area. The two-dimensional composition grids can then be averaged across the boundary length direction to obtain one-dimensional composition profiles. As shown in Figure 8.4, modulations in composition correspond to modulations in the linear density of APBs.

Abstracting the APB-based orderings into simple phase information enables KMC simulations in which configurations can only evolve via predefined kinetic events. Within our model, the allowed kinetic events are APB kink formation, destruction, and expansion, which all correspond to inverting the phase of cells adjacent to an APB. The cells in the bulk ζ regions between APBs are fixed, as the corresponding Na are predicted to be immobile [14]. The kinetic barriers calculated in Reference [14] are encoded into the KMC simulation and, along with a simple model for APB-APB repulsion, are used to calculate event rates (the vibrational prefactors [55] for all hops were taken to be identical). KMC simulations were run with periodic boundary conditions and at fixed composition

(conserving the total number of APBs). A custom KMC simulator was implemented in C++ using kmc-lotto, a simple library to perform event selection in arbitrary KMC simulations [254]. The Bortz-Kalos-Lebowitz algorithm was employed to select events and update the simulation time [58]. All simulations were run at a temperature of 300 K. Further details of the KMC simulations, including a link to our open-source KMC simulator code, are provided in Appendix E.

For simplicity in interpreting our simulation results, we report the physical quantities of time (t), wavenumber (k), and diffusivity (D) as dimensionless ratios in terms of corresponding scaling constants (t_0, k_0, D_0) defined as

$$t_0 = \frac{1}{\nu^*}, \quad k_0 = \frac{2\pi}{a}, \quad D_0 = a^2\nu^* \tag{8.1}$$

where ν^* is the vibrational prefactor of the kinetic hops [55], and a is the lattice constant of the honeycomb network.

8.4 Results

To probe the nature of macroscopic diffusion mediated by APBs in Na_xCoO_2, we investigated the relationship between the wavelength of composition modulations and their relaxation time. First, we imposed an initial sinusoidal one-dimensional composition profile resembling

$$x(s) = \bar{x} + A\cos(ks) \tag{8.2}$$

where $\bar{x}$ is the average composition and s is the position along the direction separating the APBs. The time evolution of the composition amplitude $A(t)$ was then extracted via a Fourier transform of the one-dimensional composition profile across simulation snapshots. In all cases, $A(t)$ was averaged over 100 independent simulation trajectories to obtain

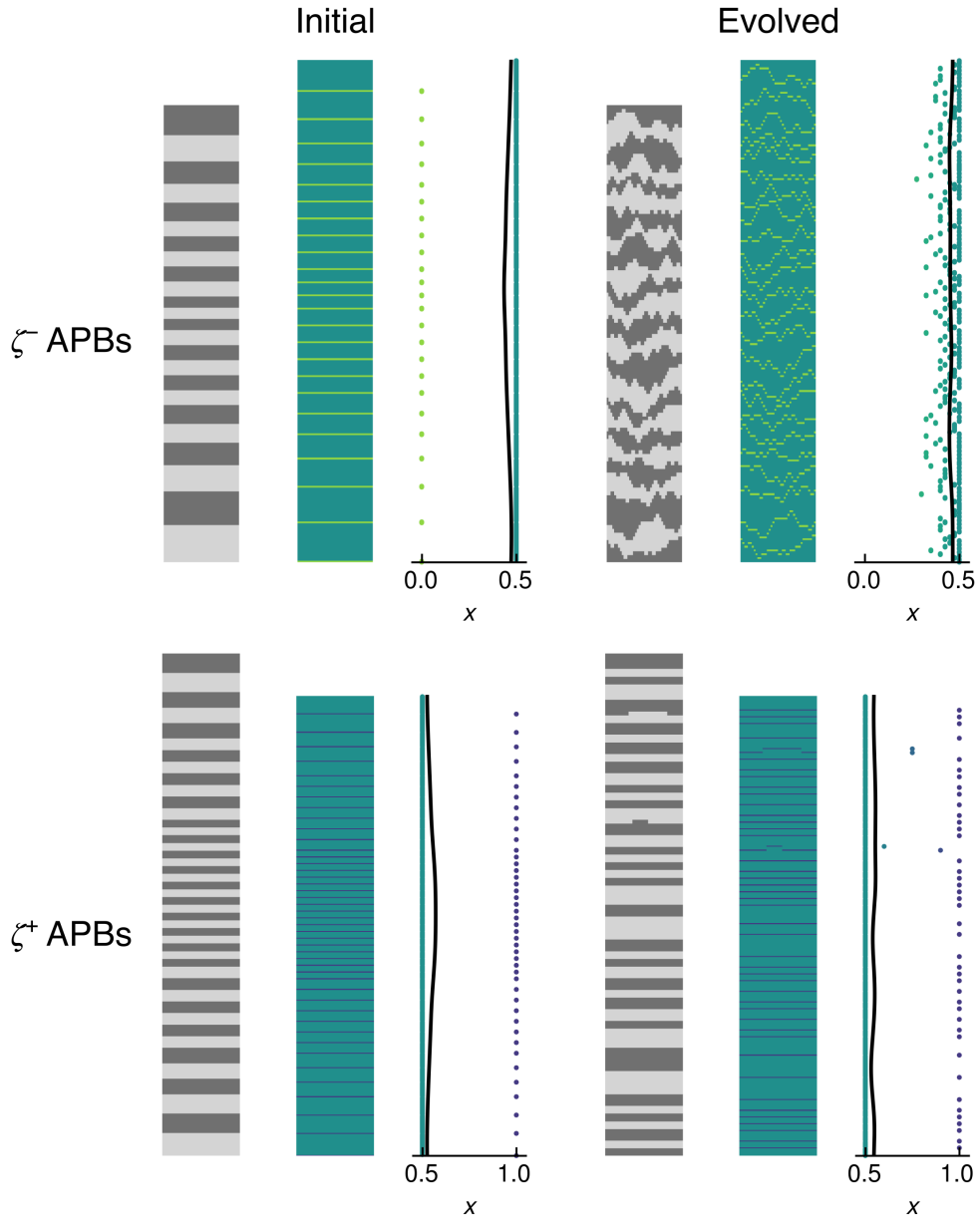

Figure 8.4: Phase grids, composition grids, and one-dimensional composition profiles (discrete and smoothed) for representative ζ^- and ζ^+ APB KMC simulations, showing initial and evolved states.

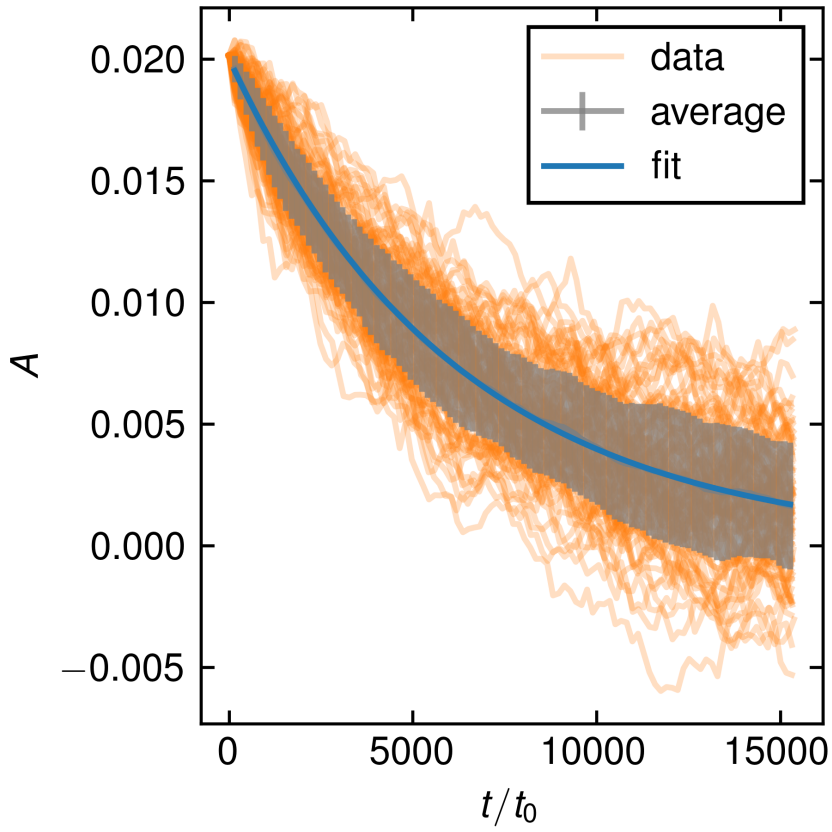

Figure 8.5: Composition amplitude A vs time t for a typical set of ζ^- APB KMC simulations, averaged and fit to a decaying exponential. Error bars represent one standard deviation.

ensemble-averaged amplitudes $\langle A(t) \rangle$ better representing the the true dynamics of the system (this also yields uncertainties for each amplitude value that were used to perform weighted fitting and error propagation). The ensemble-averaged amplitudes were fit to a decaying exponential

$$\langle A(t) \rangle = A_0 e^{-t/\tau} \tag{8.3}$$

where τ is the relaxation time. Figure 8.5 shows an example of one such fit for a set of simulations.

Following this procedure, we ran simulations in high aspect ratio supercells with

height (in the boundary separation direction) equal to the wavelength of the initial composition profile and width (in the boundary length direction) fixed at 20 grid cells. Initial and evolved snapshots from representative simulations are shown in Figure 8.4. Simulations were run at various wavelengths and close to fixed composition, with $\bar{x}$ taking on values between 0.4541 and 0.4554 for the ζ^- simulations and between 0.5465 and 0.5473 for the ζ^+ simulations. These compositions are close to the respective compositions of $x = 5/11$ and $x = 6/11$ at which the kinetic barriers were calculated [14]. The resulting dependence of τ^{-1} on the wavevector k is shown in Figure 8.6 for both APB types. For simple Fickian diffusion, one would expect

$$\tau^{-1} = Dk^2 \tag{8.4}$$

which can be obtained by Fourier transforming Fick's second law. If higher order derivatives were to enter into the underlying diffusion equation, for instance as in the Cahn–Hilliard equation [255], they would appear as terms involving higher powers of k on the right-hand side of Equation 8.4. Note that given our choice of scaling coefficients (Equation 8.1), Equation 8.4 is equivalent to

$$\left(\frac{\tau}{t_0}\right)^{-1} = 4\pi^2 \frac{D}{D_0} \left(\frac{k}{k_0}\right)^2 \tag{8.5}$$

As shown in Figure 8.6, the data are well described by Equation 8.4, particularly in the small k (large wavelength) limit, in both the ζ^- and ζ^+ cases. This indicates that the diffusion behavior resulting from APB migration is Fickian in nature. It is important to recognize that the diffusivity D we obtain is the *chemical* diffusion coefficient, as we are directly simulating a non-equilibrium process rather than using equilibrium simulations to obtain the self-diffusion coefficient and then multiplying with the thermodynamic

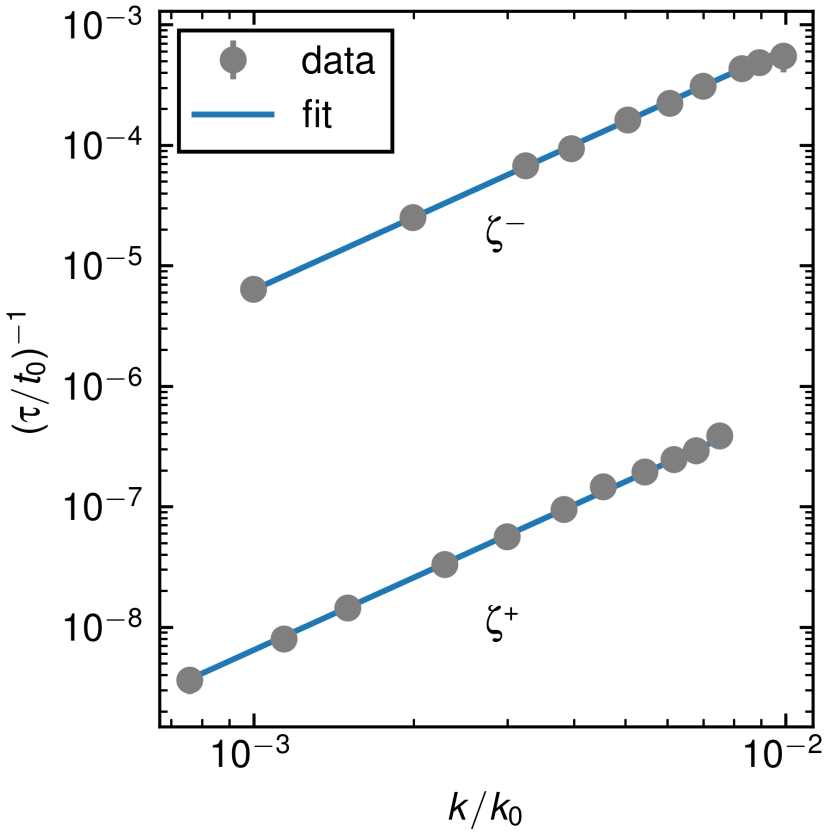

Figure 8.6: Inverse relaxation time τ^{-1} vs wavevector k fit to a Fickian relationship $\tau^{-1} = Dk^2$. Error bars (too small to be visible for most points) represent one standard deviation. Data is from simulations run at 300 K.

factor (the approach typically employed in KMC studies [57, 93, 94, 244, 246, 256]).

Assuming Fickian diffusion, we explored how the diffusivity arising from APB motion depends on average composition. Sets of simulations were run at various values of $\bar{x}$ (within the ranges in which each APB type is stable) and the resulting τ values were used to calculate D values via Equation 8.4. Figure 8.7 shows the dependence of D on $\bar{x}$. In both the ζ^- and ζ^+ regimes, the diffusivity drops significantly as the composition approaches $\bar{x} = 1/2$ and the corresponding density of APBs approaches zero. This result is intuitive, as the APB migration mechanism breaks down in the absence of APBs. Other, less facile transport mechanisms presumably take over near $\bar{x} = 1/2$,

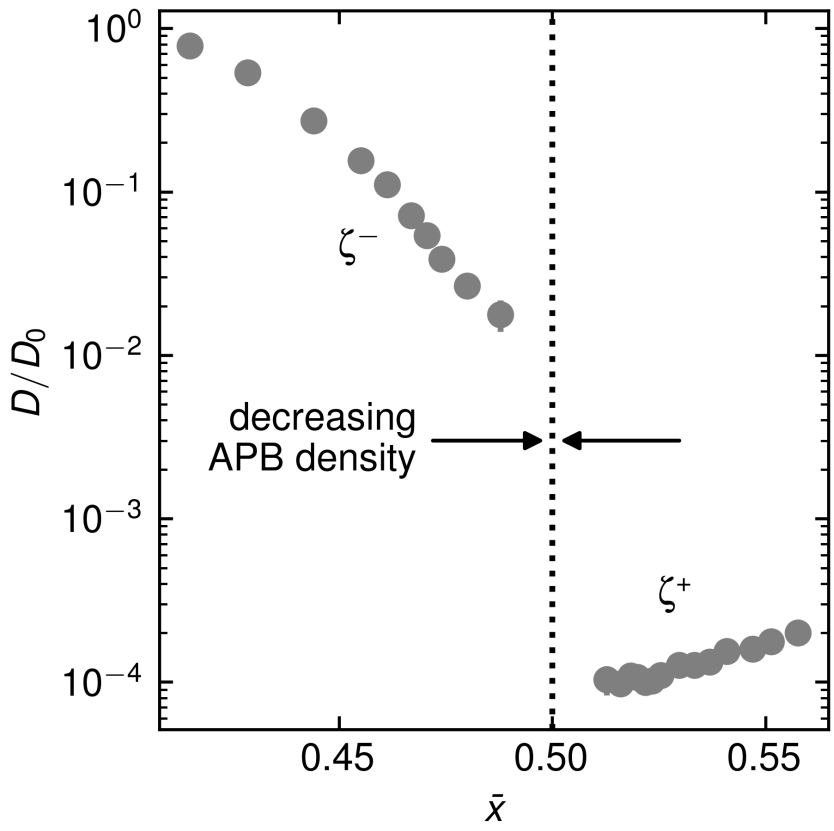

Figure 8.7: Diffusivity D vs average composition $\bar{x}$. Error bars (too small to be visible for most points) represent one standard deviation. Data is from simulations run at 300 K.

likely requiring vacancy defects in the ζ ordering, however our simplified model does not account for such mechanisms.

Away from $\bar{x} = 1/2$, the typical diffusivity for the ζ^- APBs is several orders of magnitude larger than that for the ζ^+ APBs. This is consistent with the predicted energetics of APB kink formation, which acts as a limiting step in the APB migration mechanism [14]. At 300 K, the predicted ratio of the hop rate of ζ^- kink formation to that of ζ^+ kink formation is more than 10^3 (assuming the same vibrational prefactor). Furthermore, the ζ^+ kinks introduce a significant defect energy while the ζ^- kinks do not, making it more likely for ζ^+ kinks to be destroyed rather than expand and facilitate APB

migration. This distinction is also qualitatively apparent from the phase grids resulting from our simulations. As illustrated by the evolved snapshots in Figure 8.4, the ζ^- APBs typically contain far more kinks than the ζ^+ APBs.

8.5 Discussion

In this study, we have examined macroscopic diffusion arising from a previously identified APB migration mechanism for layered intercalation compounds. The mechanism allows for the migration of APBs (which themselves contain either additional vacancies or additional ions relative to the rest of the structure) via the formation and subsequent expansion of kinks in the boundaries. Using P3-Na_xCoO_2 as a model system, we simulated APB kinetics in two regimes, above and below $x = 1/2$, to directly probe the relaxation of composition (APB density) modulations. The wavelength dependence of the relaxation time is consistent with Fick's laws, allowing us to extract one-dimensional chemical diffusion coefficients from our simulations. These diffusivity values depend strongly on composition, approaching zero as APB migration breaks down near $x = 1/2$ and reaching higher values for $x < 1/2$ than for $x > 1/2$ due to the higher mobility of APBs in that regime.

The results we have presented mostly illustrate qualitative diffusion behavior, due to the use of dimensionless quantities. To put our calculated diffusivity values into physical context, we may estimate the value of D_0 for the P3-Na_xCoO_2 system. We assume $a = 2.8$ Å, the calculated in-layer lattice constant of $Na_{1/2}CoO_2$ from Reference [12], and we assume $\nu^* = 10^{12}$–10^{13} Hz, the commonly assumed range of typical values for the vibrational prefactor. Substituting these values into Equation 8.1 yields a range of D_0 values of 8×10^{-4}–8×10^{-3} cm^2/s.

Room temperature Na diffusion coefficients of Na_xCoO_2 in the O3 and P2 structures

have been reported to be on the order of 10^{-10} cm^2/s [170], which is significantly lower than the typical values we obtain (Figure 8.7). However, a different, comprehensive study of P2-Na_xCoO_2 based on the potentiostatic intermittent titration technique reports chemical diffusion coefficients as high as 2×10^{-6} cm^2/s at certain compositions [228], which is more comparable to our calculated values for $x > 1/2$. The same study also found diverging minima in the diffusion coefficient at the compositions of certain ordered phases. To our knowledge, no analogous study of P3-Na_xCoO_2 has been reported in the literature, and there is generally limited experimental diffusion data available for any P3 materials. If APB migration is indeed the dominant Na diffusion mechanism in the P3 structure, it may be difficult to discern experimentally, as we predict the behavior to simply be Fickian in nature. One key indication would be if the composition dependence of the diffusion coefficient follows Figure 8.7, with a sharp drop at $x = 1/2$ and asymmetric slopes on either side of $x = 1/2$.

We acknowledge that the calculated diffusion rates (Figure 8.7), particularly for the ζ^- orderings below $x = 1/2$, are remarkably fast for a Na intercalation compound. These values could be overestimated due to idealizations in our KMC model, such as the assumption that APBs can only form certain kinds of kinks and cannot be broken. However, the calculated Na migration barriers for ζ^- APB motion are extremely low (0.03 eV) [14], so such rapid diffusion may be plausible. Molecular dynamics could perhaps be used as an alternate technique to verify the APB migration mechanism and the resulting speed of diffusion. *Ab initio* molecular dynamics simulations, however, are limited by the size of the simulation cell and the total simulation time, while standard molecular dynamics simulations require accurate interatomic potentials, which are often challenging to parameterize for compounds that undergo redox.

The mechanism considered here is fundamentally distinct from textbook atomistic descriptions of ion diffusion. Often, nondilute diffusion is facilitated by isolated defects,

such as single vacancies or small vacancy clusters [95]. By contrast, the APBs that facilitate diffusion in the APB migration mechanism are *extended* defects, which in the case of P3-Na_xCoO_2, are predicted to be abundant in the ground state orderings themselves (except near $x = 1/2$), with their density set by the composition. This difference may be key to avoiding the high correlation of atomic hops that can plague certain close-packed structures. In layered materials that rely on a divacancy mechanism for diffusion, isolated divacancies tend to simply rotate locally (Figure 8.1(b)), such that long-range ion migration is mediated by connected clusters of divacancies [57, 93]. Quite similarly, diffusion within the three-dimensional spinel crystal structure can, in some cases, depend overwhelmingly on triple-vacancy clusters [94], meaning that a percolating network of such clusters is necessary to avoid diffusion shutdown due to highly correlated hops [256]. The APB migration mechanism we describe does not seem to suffer from such extreme correlation effects, allowing for facile motion of APBs through the crystal.

Our results suggest the intriguing possibility of designing materials to exploit similar diffusion mechanisms. This need not be limited to layered materials, as three-dimensional structures could host similar extended defects (which could be planar rather than linear) to facilitate rapid transport. In battery applications, these principles could perhaps be extended beyond electrode materials towards achieving liquid-like diffusion in solid electrolyte materials as well.

8.6 Conclusion

This study reveals a seemingly unconventional APB-based Na diffusion mechanism in a layered intercalation compound that results in conventional Fickian diffusion in one dimension. The mechanism differs from the typical atomistic understanding of diffusion in that it involves the collective motion of boundaries, much like in theories of APB or

grain boundary motion in alloys. We emphasize that unlike in many systems, additional defects are not required to facilitate long-range diffusion, as the APBs that mediate Na transport are inherent to the stable ordered phases [12]. Furthermore, diffusion due to this mechanism does not appear to be limited by dramatic correlation effects that play a dominant role in determining the diffusion coefficients of layered and spinel intercalation compounds. We hope that these results encourage further kinetic studies of layered intercalation compounds as well as broader explorations of diffusion facilitated by extended defects.

Chapter 9

Conclusion

The field of beyond Li-ion batteries continues to grow, with researchers exploring a wide variety of possible technologies to help meet the world's pressing energy storage needs. Even as many practical advances are made, there is still much to be uncovered about fundamental thermodynamic and kinetic aspects of battery materials. This dissertation has investigated properties of common candidate electrode materials for Na- and K-ion batteries using first-principles statistical mechanics methods.

In Chapter 3 we summarized some general insights and trends gleaned from computation across intercalation compounds, focusing on ion ordering and stacking sequence transitions in layered structures. We examined these effects in detail for several layered oxide systems in Chapters 4, 5, and 6. Using density functional theory calculations and cluster expansion effective Hamiltonians, we predicted several families of hierarchical ion-vacancy orderings, each of which contains many ordered phases that are closely spaced in composition. These families include one based on rows of vacancies in the O3 structure of Na_xCoO_2 and Na_xCrO_2, one based on alternating regions of octahedral and prismatic K in K_xCrO_2 (dubbed the "M" phases), and several based on antiphase boundaries (APBs) in the P3 structure of all three systems. We predicted these phases to remain ordered

at room temperature, and found that they explain the multitude of small voltage steps observed experimentally. We also examined stacking sequence changes in these systems and their relationship to ion ordering, obtaining generally good agreement with reported structural evolution during cycling.

Building on our thermodynamic results, we considered the kinetic implications of our predicted P3 orderings in Chapter 7. We enumerated kinetic hops in APB-based ordered phases near $x = 1/2$, using Na_xCoO_2 as a model system. While the majority of hops were found to not be allowed, owing to the strong ordering tendencies of the system, we identified certain hops in the vicinity of APBs that are allowed. The nature of these hops suggested a mechanism for migration of the APBs themselves (which carry additional Na or vacancies) through the intercalation layers via the formation and expansion of kinks in the boundaries. We calculated relatively low migration barriers for this mechanism, and also concluded that it would likely dominate over mechanisms that require additional vacancies in the ordered phases. To determine the extent to which the APB migration mechanism contributes to long-range diffusion, we simulated APB motion in Chapter 8 using a simplified kinetic Monte Carlo model. By explicitly examining the relaxation of composition modulations (corresponding to modulations in APB density) at different wavelengths, we determined that the diffusion behavior is mostly Fickian, but with strong composition dependence of the diffusion coefficient. In regimes of greater APB density, we obtained extremely high diffusion rates for a Na intercalation material.

In this dissertation, we have revealed the rather intricate behavior displayed by some relatively simple systems. It is important to acknowledge that these particular materials represent a small subset of layered intercalation compounds, which themselves are just one class of candidate electrode materials for Na- and K-ion batteries. And continued improvements based on strategies such as chemical substitution can mitigate many of the problems related to ion ordering and structural phase transitions discussed here.

However, our results have broader qualitative implications for how we think about details of ordering and diffusion in materials. Our grouping of various orderings into families highlights the advantage of viewing ordered phases not in isolation, but in terms of common motifs that relate them. This concept holds relevance beyond battery materials, as similar staircases of hierarchical orderings have been found in other systems such as metallic alloys. Our demonstration of diffusion mediated by APBs shows how transport can rely on extended defects rather than isolated ones, and challenges the perception that ordered phases always exhibit sluggish diffusion. These ideas suggest new potential directions for research, such as the development of tools to identify and predict ordering patterns in a more systematic fashion and the engineering of materials in which diffusion is facilitated by the motion of extended defects. As computational techniques become more powerful, there is ample opportunity to further our understanding of ordering phenomena in materials for electrochemical applications and beyond.

Appendix A

Orbital occupation matrices

Orbital occupation matrices are obtained by projecting electronic wavefunctions onto particular reference orbitals, and offer a way to describe the electronic state at a given site. Their mathematical definition and use in simulating electronic ordering are detailed in Reference [6]. Here we describe the computational treatment of occupation matrices as implemented in CASM version 1.X [68].

Our goal is to efficiently represent occupation matrices and define how they transform under symmetry operations. First we must establish how orbitals (real spherical harmonics) themselves transform. The s orbitals are invariant under all operations, while p orbitals simply transform as the Cartesian coordinates. For d orbitals, we can represent a general orbital as

$$\mathbf{r}^\top M \mathbf{r}, \tag{A.1}$$

where M is a traceless, symmetric 3×3 matrix and $\mathbf{r} = (x, y, z)$. Applying a point symmetry operation S to the orbital transforms M as

$$M' = S M S^\top. \tag{A.2}$$

This is equivalent to the Kronecker product of S with itself acting on the vectorization $\mathbf{m} = \mathrm{vec}(M)$:

$$\mathbf{m}' = (S \otimes S)\, \mathbf{m}. \tag{A.3}$$

$\mathbf{m}$ has nine elements, only five of which are independent (because M is traceless and symmetric). We may therefore reduce $\mathbf{m}$ to a five-dimensional vector $\mathbf{d} = P\mathbf{m}$ via a 5×9 reduction matrix

$$P = \begin{pmatrix} 0 & 1/\sqrt{2} & 0 & 1/\sqrt{2} & 0 & 0 & 0 & 0 & 0 \\ 0 & 0 & 0 & 0 & 0 & 1/\sqrt{2} & 0 & 1/\sqrt{2} & 0 \\ -1/\sqrt{6} & 0 & 0 & 0 & -1/\sqrt{6} & 0 & 0 & 0 & \sqrt{2/3} \\ 0 & 0 & 1/\sqrt{2} & 0 & 0 & 0 & 1/\sqrt{2} & 0 & 0 \\ 1/\sqrt{2} & 0 & 0 & 0 & -1/\sqrt{2} & 0 & 0 & 0 & 0 \end{pmatrix}, \tag{A.4}$$

which reflects the following choice of reference orbitals: xy, yz, $3z^2 - r^2$, xz, $x^2 - y^2$. $\mathbf{d}$ then transforms as $\mathbf{d}' = G\mathbf{d}$, where

$$G = P\,(S \otimes S)\,P^{\top}. \tag{A.5}$$

An analogous procedure can be followed for f orbitals, but with M instead being a traceless, symmetric $3 \times 3 \times 3$ tensor. P in this case would be a 7×27 matrix acting on the 27-dimensional vectorization of M. The rest of this section will focus on d orbitals.

Let U be a d-orbital occupation matrix for a single spin channel. Applying S to U is equivalent to applying $S^{\top}$ to the reference orbitals, such that U transforms as

$$U' = G^{\top} U G, \tag{A.6}$$

and equivalently

$$\mathbf{u}' = \left(G^{\top} \otimes G^{\top}\right)\mathbf{u} \tag{A.7}$$

for $\mathbf{u} = \mathrm{vec}(U)$. U is a 5×5 symmetric matrix, meaning that the 25-dimensional vector $\mathbf{u}$ is confined to a 15-dimensional subspace. We obtain $\mathbf{v} = Q\mathbf{u}$ via a 15×25 reduction matrix

$$Q = \begin{pmatrix}
1 & 0 & 0 & 0 & 0 & 0 & 0 & 0 & 0 & 0 & 0 & 0 & 0 & 0 & 0 & 0 & 0 & 0 & 0 & 0 & 0 & 0 & 0 & 0 & 0 \\
0 & 0 & 0 & 0 & 0 & 0 & 1 & 0 & 0 & 0 & 0 & 0 & 0 & 0 & 0 & 0 & 0 & 0 & 0 & 0 & 0 & 0 & 0 & 0 & 0 \\
0 & 0 & 0 & 0 & 0 & 0 & 0 & 0 & 0 & 0 & 0 & 0 & 1 & 0 & 0 & 0 & 0 & 0 & 0 & 0 & 0 & 0 & 0 & 0 & 0 \\
0 & 0 & 0 & 0 & 0 & 0 & 0 & 0 & 0 & 0 & 0 & 0 & 0 & 0 & 0 & 0 & 0 & 0 & 1 & 0 & 0 & 0 & 0 & 0 & 0 \\
0 & 0 & 0 & 0 & 0 & 0 & 0 & 0 & 0 & 0 & 0 & 0 & 0 & 0 & 0 & 0 & 0 & 0 & 0 & 0 & 0 & 0 & 0 & 0 & 1 \\
0 & 0 & 0 & 0 & 0 & 0 & 0 & 0 & 0 & 0 & 0 & 0 & 0 & 0 & 0 & 0 & 0 & 0 & 0 & s & 0 & 0 & 0 & s & 0 \\
0 & 0 & 0 & 0 & 0 & 0 & 0 & 0 & 0 & 0 & 0 & 0 & 0 & 0 & s & 0 & 0 & 0 & 0 & 0 & 0 & 0 & s & 0 & 0 \\
0 & 0 & 0 & 0 & 0 & 0 & 0 & 0 & 0 & s & 0 & 0 & 0 & 0 & 0 & 0 & 0 & 0 & 0 & 0 & 0 & s & 0 & 0 & 0 \\
0 & 0 & 0 & 0 & s & 0 & 0 & 0 & 0 & 0 & 0 & 0 & 0 & 0 & 0 & 0 & 0 & 0 & 0 & 0 & s & 0 & 0 & 0 & 0 \\
0 & 0 & 0 & s & 0 & 0 & 0 & 0 & 0 & 0 & 0 & 0 & 0 & 0 & 0 & s & 0 & 0 & 0 & 0 & 0 & 0 & 0 & 0 & 0 \\
0 & 0 & s & 0 & 0 & 0 & 0 & 0 & 0 & 0 & s & 0 & 0 & 0 & 0 & 0 & 0 & 0 & 0 & 0 & 0 & 0 & 0 & 0 & 0 \\
0 & s & 0 & 0 & 0 & s & 0 & 0 & 0 & 0 & 0 & 0 & 0 & 0 & 0 & 0 & 0 & 0 & 0 & 0 & 0 & 0 & 0 & 0 & 0 \\
0 & 0 & 0 & 0 & 0 & 0 & 0 & s & 0 & 0 & 0 & s & 0 & 0 & 0 & 0 & 0 & 0 & 0 & 0 & 0 & 0 & 0 & 0 & 0 \\
0 & 0 & 0 & 0 & 0 & 0 & 0 & 0 & 0 & 0 & 0 & 0 & 0 & s & 0 & 0 & 0 & s & 0 & 0 & 0 & 0 & 0 & 0 & 0 \\
0 & 0 & 0 & 0 & 0 & 0 & 0 & 0 & s & 0 & 0 & 0 & 0 & 0 & 0 & 0 & s & 0 & 0 & 0 & 0 & 0 & 0 & 0 & 0
\end{pmatrix}, \tag{A.8}$$

where $s = 1/\sqrt{2}$, such that

$$\mathbf{v} = \begin{pmatrix} U_{1,1} \\ U_{2,2} \\ U_{3,3} \\ U_{4,4} \\ U_{5,5} \\ \sqrt{2}U_{4,5} \\ \sqrt{2}U_{3,5} \\ \sqrt{2}U_{2,5} \\ \sqrt{2}U_{1,5} \\ \sqrt{2}U_{1,4} \\ \sqrt{2}U_{1,3} \\ \sqrt{2}U_{1,2} \\ \sqrt{2}U_{2,3} \\ \sqrt{2}U_{3,4} \\ \sqrt{2}U_{2,4} \end{pmatrix}. \tag{A.9}$$

$\mathbf{v}$ therefore transforms as $\mathbf{v}' = H\mathbf{v}$, where

$$H = Q\left(G^\top \otimes G^\top\right) Q^\top \tag{A.10}$$

It is straightforward to account for time-reversal symmetry for two spin channels. Consider two occupation matrices $U_\uparrow$ and $U_\downarrow$ for the two spin channels, with corresponding reduced (15-dimensional) vectorizations $\mathbf{v}_\uparrow$ and $\mathbf{v}_\downarrow$. These can be concatenated to produce a single 30-dimensional vector

$$\mathbf{v}_{\uparrow\downarrow} = \begin{pmatrix} \mathbf{v}_\uparrow \\ \mathbf{v}_\downarrow \end{pmatrix} \tag{A.11}$$

that describes the occupations for both spin channels. Now consider the action of S along with possible time reversal. If there is no time reversal, the occupations transform as

$$\mathbf{v}'_{\uparrow\downarrow} = (I \otimes H)\,\mathbf{v}_{\uparrow\downarrow}, \tag{A.12}$$

where I is the 2×2 identity matrix. If there is time reversal, the occupations transform as

$$\mathbf{v}'_{\uparrow\downarrow} = (W \otimes H)\,\mathbf{v}_{\uparrow\downarrow}, \tag{A.13}$$

where

$$W = \begin{pmatrix} 0 & 1 \\ 1 & 0 \end{pmatrix} \tag{A.14}$$

is a permutation matrix that swaps the spin channels.

Appendix B

Calculation details for Chapter 3

Density of states and γ-surface calculations were performed using VASP [59–62]. The optB86b-vdW exchange-correlation functional [64] was selected to accurately capture van der Waals interactions. The density of states calculations employed a plane-wave energy cutoff of 550 eV and a **k**-point mesh of density 45 Å or higher along each reciprocal lattice vector.

The γ-surface calculations were set up using MULTISHIFTER, a CASM-powered [68] utility for calculating γ-surfaces and universal binding energy curves for arbitrary slip planes in crystals [257]. Supercells for the γ-surface calculations contained three layers with an in-plane size of one formula unit. This was found to be sufficient for isolating faults from their periodic images and converging stacking fault energies to within 2%. The γ-surfaces were calculated using 12 by 12 triangular grids of displacements over the unit cell. Only symmetrically distinct displacements on this grid were calculated. For the energy paths along the [110] direction shown in Figure 3.10, the number of samples was doubled. For each displacement, we varied the interlayer spacing around the fault plane from -0.1 Å to 0.4 Å in increments of 0.1 Å, relative to the original spacing. All ions were kept static, except for the one A ion in the fault plane (for $LiCoO_2$ and $NaCoO_2$), which relaxed until forces converged to within 0.2 eV/Å. To avoid local minimum trapping, we ran three separate calculations for each displacement and interlayer spacing in which we initialized the A ion from each of the three distinct triangular sublattices. The final energy versus interlayer spacing was fit to a parabola to determine the lowest energy for each displacement and initial A position (in some cases the fit yielded an R^2 value of less than 0.95 so we simply took the lowest value over the interlayer spacings), and the minimum of these was taken to be the stacking fault energy for each displacement.

The γ-surface calculations used a plane-wave energy cutoff of 700 eV and a **k**-point mesh of density 38 Å along each reciprocal lattice vector. Gaussian smearing of width 0.1 eV was used for the $LiCoO_2$ and $NaCoO_2$ relaxations, while static calculations using the linear tetrahedron method [63] were performed for CoO_2.

Appendix C

Details of hierarchical orderings in Na_xCoO_2

Here we describe the details of each family of hierarchical orderings in O3 and P3. We define a naming convention for specifying orderings within each family and provide composition formulas. Ground state orderings belonging to each P3 family are shown in Figure C.1.

C.1 The θ orderings in O3

The θ orderings in O3 can be viewed as rows of Na periodically separated by rows of vacancies (Figure 4.3). We denote a particular row ordering with a tuple S that is appended as a subscript to θ. Each element of the tuple corresponds to the number of filled Na rows between adjacent pairs of vacant rows within the super lattice of the ordering. As an example, consider the $\theta_{4,5}$ ordering shown in Figure 4.3(c). In this ordering 4 filled Na rows separate one pair of adacent vacant rows, while 5 filled Na rows separate the next pair of adjacent vacant rows. S for this ordering therefore contains $(4, 5)$. Due to the periodicity of the underlying triangular lattice, S may be reversed or cycled and still describe an equivalent ordering. The composition of a θ ordering is given by

$$x = \frac{\sum_{k \in S} k}{\sum_{k \in S} (k+1)} \tag{C.1}$$

where k corresponds to the number of filled rows between vacant rows as contained in S. For the $\theta_{4,5}$ ordering, this equation evaluates to

$$x = \frac{4+5}{(4+1)+(5+1)} = \frac{9}{11} \tag{C.2}$$

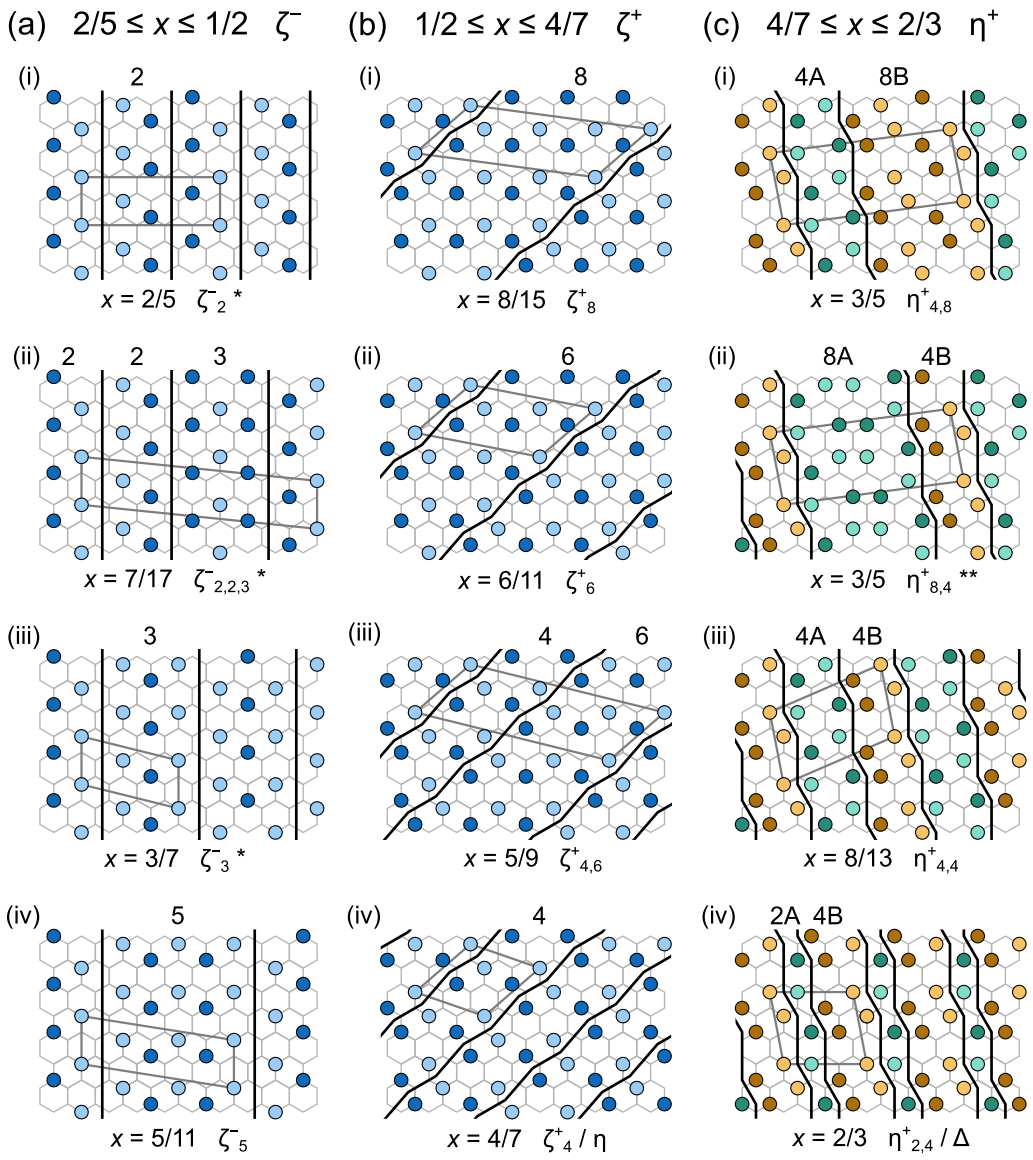

Figure C.1: Orderings belonging to the (a) ζ^-, (b) ζ^+, or (c) η^+ families on or near the local hull of P3. Regions of the ζ ordering are shown in blue, while green and orange represent two orientational variants of the η ordering η_A and η_B, respectively. Light and dark circles distinguish Na occupancy of the two distinct triangular sublattices. Black lines indicate APBs between different (a,b) translational variants of the ζ ordering or (c) orientational variants of the η ordering. Spacings between APBs are indicated above each ordering. Unit cells are shown as dark gray boxes. Single asterisks indicate that the ordering is above the global hull and double asterisks indicate that the ordering is also above the local hull but by less than 2.1 meV/CoO_2.

C.2 The ζ^- and ζ^+ orderings in P3

The ζ^- and ζ^+ orderings in P3 can both be viewed as regions of translational variants of the ζ ordering (Figure 4.6(a)(i)) periodically separately by one of two kinds of antiphase boundaries (APBs) (Figure 4.7(a,b)). We introduce a notation for these families that is similar to that used to describe the θ family. The spacing between two APBs is measured by the number of Na atoms in an unbroken zig-zag row of the ζ ordering, as shown in Figure C.1(a,b). We collect the repeated spacings for a given ordering in a tuple S which is used as a subscript in the label. The composition of the ζ^- orderings is then given by

$$x = \frac{\sum_{k\in S} k}{\sum_{k\in S} (2k+1)} \tag{C.3}$$

where k are the individual spacings between APBs contained in S. Note that we have not shown the ζ_4^- ordering at $x = 4/9$ in Figure C.1 because it requires a unit cell of 18 primitive cell volumes, just as the ζ_2^- ordering at $x = 2/5$ requires 10 primitive cell volumes rather than 5. This is because two APBs of this type separated by an even number of Na are not equivalent, as shown in Figure C.1(a)(i).

For the ζ^+ orderings, we still measure the spacing between APBs by the number of Na atoms in an unbroken zig-zag row of the ζ ordering, but spacings are restricted to even values due to the orientation of the APBs (Figure C.1(b)). The spacings are again collected as a tuple S and used as a subscript. The composition of the ζ^+ orderings is given by

$$x = \frac{\sum_{k\in S} k}{\sum_{k\in S} (2k-1)} \tag{C.4}$$

The composition approaches $x = 1/2$ as the spacings k between APBs go to infinity for both ζ^+ and ζ^-. Multiple sets of spacings can yield the same composition, for example $\zeta^-_{2,2,4}$ and $\zeta^-_{2,3,3}$ at $x = 8/19$ and ζ^+_8 and $\zeta^+_{6,10}$ at $x = 8/15$. While we did not calculate and compare the energies for any such pair of structures, they would likely be nearly degenerate in energy due to limited interactions between distant APBs.

C.3 The η^+ orderings in P3

The η^+ orderings in P3 can be viewed as alternating regions of two orientational variants of the η ordering, distinguished by the labels η_A and η_B (4.6(b)(i,ii)), periodically separately by APBs (Figure 4.7(c)). We present a naming convention for the η^+ family of orderings, similar to that used to describe the ζ^- and ζ^+ orderings. The spacing between two APBs is counted by the number of Na in the unit cell between them belonging to a region of either η_A or η_B, as shown in Figure C.1(c). Due to the geometry of the APBs, the η_B spacings are restricted to multiples of 4 and the η_A spacings are restricted to either 2 or multiples of 4.

We collect the repeated spacings for a given ordering in a tuple S which is used as a

subscript in the label. The spacings alternate between the η_A and η_B variants, and we arbitrarily choose that S begin with an η_A spacing. The composition of the η^+ orderings is then given by

$$x = \frac{\sum_{k\in S} k}{\sum_{k\in S} \left(\frac{3}{2}k + \lfloor \frac{k}{4} \rfloor - \frac{1}{2}\right)} \tag{C.5}$$

where k are the individual spacings between APBs contained in S. For the $\eta^+_{4,8}$ and $\eta^+_{8,4}$ orderings this equation evaluates to

$$x = \frac{4+8}{\left(6+1-\frac{1}{2}\right)+\left(12+2-\frac{1}{2}\right)} = \frac{12}{20} = \frac{3}{5} \tag{C.6}$$

and for the $\eta^+_{2,4}$ ordering it evaluates to

$$x = \frac{2+4}{\left(3+0-\frac{1}{2}\right)+\left(6+1-\frac{1}{2}\right)} = \frac{6}{9} = \frac{2}{3} \tag{C.7}$$

Figure C.1(c) shows ground states belonging to the η^+ family. The orderings $\eta^+_{2,8}$ at $x = 5/8$ and $\eta^+_{4,4,2,4}$ at $x = 7/11$ (not shown) have energies above the hull but by less than 0.5 meV/CoO_2 and are therefore considered as candidate ground states. As with the ζ^+ and ζ^- families, there are several η^+ structures having the same concentration that are essentially degenerate. For example, the two $x = 3/5$ orderings $\eta^+_{4,8}$ and $\eta^+_{8,4}$ shown in Figure C.1(c)(i,ii) have energies that are within 2 meV/CoO_2 of each other, with the first being on the hull.

Triplet clusters of Na on the same triangular sublattice form along the η^+-type APBs. When APBs are spaced such that the η_A regions are as narrow as possible ($k = 2$, as in the Δ ordering in Figure C.1(c)(iv)), two pairs of Na from adjacent triplet clusters form quadruplet clusters that actually resemble the third orientational variant η_C from Figure 4.6(b)(iii).

Appendix D

Supporting information for Chapter 5

D.1 Cluster expansions

The Clusters Approach to Statistical Mechanics (CASM) software package [10,68–70] was used to fit cluster expansion effective Hamiltonians for the O3 and P3 structures of Na_xCrO_2, based on energies calculated using density functional theory (DFT). Only ferromagnetic configurations were included, and any configurations that relaxed to a different host structure were excluded from the fits. For P3, we also excluded any configurations containing a nearest-neighbor Na-Na pair, as the mechanical instability of these structures made it impossible to obtain a reliable effective cluster interaction (ECI) for that pair cluster. We instead manually set that ECI to 3.33 eV/pair. The active cluster basis functions for each fit were selected from a large pool of pairs, triplets, and quadruplets using a genetic algorithm [50] based on a tenfold cross-validation score. The weighted root-mean-square error (WRMSE) was calculated using Boltzmann weighting based on the distance to the formation energy convex hull, with $kT = 0.035$ eV. Details of each fit are reported in Table D.1.

Table D.1: Number of distinct configurations trained on, clusters basis functions included, and WRMSE of each cluster expansion fit.

host structure	configurations trained on	clusters in fit	WRMSE (meV/CrO_2)
O3	228	34	4.3
P3	261	40	3.7

D.2 Monte Carlo simulations

Grand canonical Monte Carlo simulations were performed in CASM for the O3 and P3 structures using the fitted cluster expansions. Heating and cooling runs were performed between $T = 5$ K and 1000 K in 5 K increments at constant Na chemical potential μ. A grid of μ values was used with a spacing of 0.02 eV/Na. All Monte Carlo supercells contained six host layers, with at least 1200 CrO_2 per layer. Cooling runs were initialized from the final configurations of a single reference run at $T = 1000$ K sweeping from low to high μ. Separate heating runs were initialized from each ground state ordering of interest. We performed heating runs for the $x = 2/5$, $x = 3/5$, $x = 2/3$, $x = 3/4$, and $x = 4/5$ ground states in O3 and the $x = 2/5$, $x = 1/2$, $x = 4/7$, $x = 8/13$, and $x = 2/3$ ground states in P3. Thermodynamic integration [54,258] of our Monte Carlo results was carried out in order to calculate the grand potential $\Omega = U - TS - \mu N$ at each T and μ. Finally, equilibrium phase stability and voltage was computed at fixed T by minimizing Ω at each μ value over the collection of phases from heating and cooling runs.

Figure D.1 shows the resulting voltage curves and stability regions of each host structure at various temperatures from 200 K to 500 K, compared to the zero-temperature DFT voltage curve. At 200 K, the P3 stability window predicted from DFT ($1/2 \leq x \leq 4/7$) is preserved, while at 300 K only the $x = 1/2$ P3 ordering is stable relative to O3 (note, however, that we did not perform any heating runs for P3 ground states between $x = 1/2$ and $x = 4/7$). The O3 ground state at $x = 3/4$ is also found to remain mostly ordered at 300 K, although the corresponding voltage step is smoothed out slightly. By 500 K we find that P3 is completely overtaken by O3 at intermediate x. Figure D.2 shows the grand potential versus temperature obtained from heating and cooling runs in the P3 structure at $\mu = 0$, corresponding to an average composition of approximately $x = 1/2$. Due to hysteresis in the Monte Carlo simulations, the transition temperature upon heating is higher than that upon cooling. The true predicted transition temperature lies where the grand potentials from heating and cooling are equal, at around 475 K. Representative snapshots above and below this transition temperature show the disordering of the $x = 1/2$ ground state (insets in Figure D.2).

D.3 Additional figures

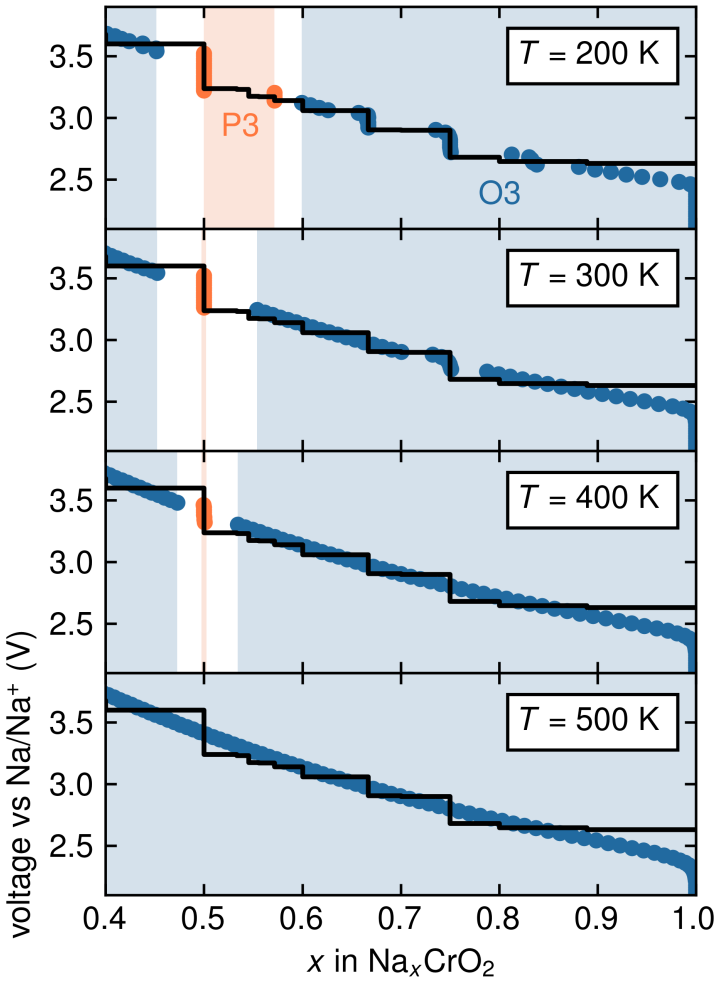

Figure D.1: Equilibrium voltage calculated from grand canonical Monte Carlo simulations at various temperatures (colored circles) compared to the voltage curve calculated from DFT (black lines). Shaded regions indicate where each host structure is globally stable.

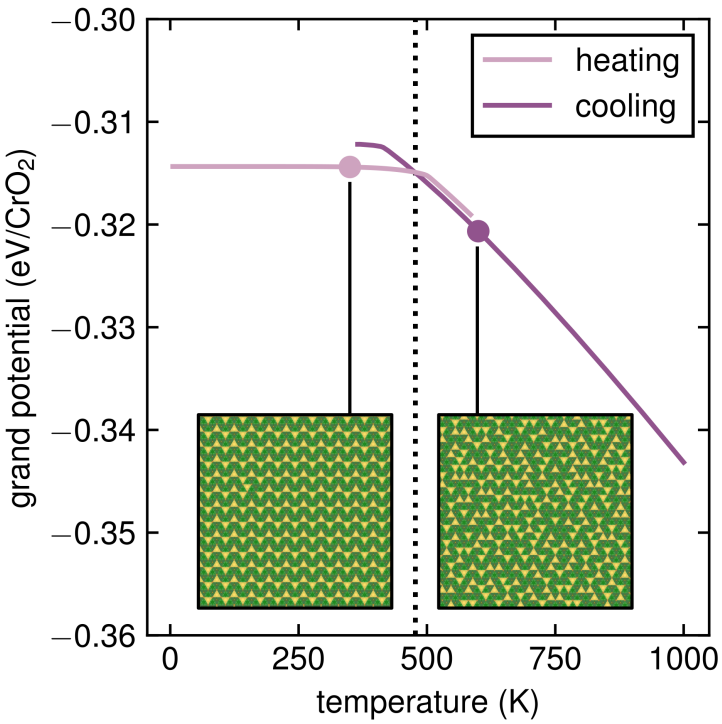

Figure D.2: Grand potential versus temperature for heating and cooling runs in P3 at $\mu = 0$. The transition temperature at which the two potential curves cross is indicated by a dotted line. Insets show Monte Carlo snapshots illustrating the disordering of the $x = 1/2$ ground state.

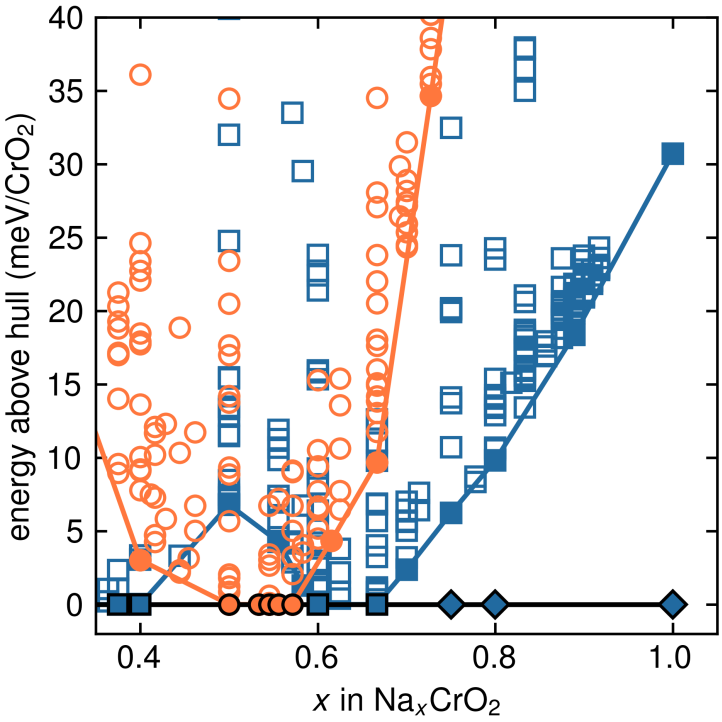

Figure D.3: Calculated energy above the global convex hull of O3 and P3 configurations versus composition. For O3, FM configurations are marked by squares while non-FM configurations are marked by diamonds. P3 configurations are marked as circles. Filled markers with lines connecting them indicate configurations on the local convex hull of each host structure (not accounting for magnetic ordering). Configurations on the global convex hull are outlined in black.

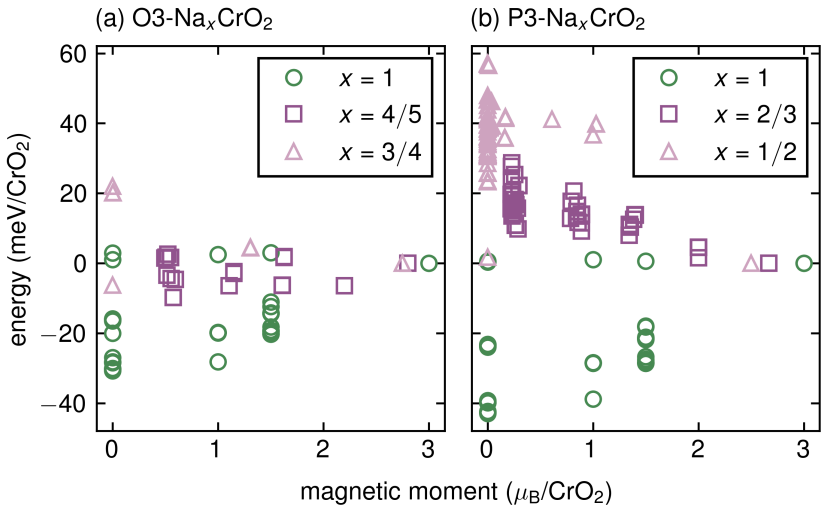

Figure D.4: Calculated energy versus magnetic moment for magnetic orderings within the predicted (a) O3 and (b) P3 Na_xCrO_2 ground state structures at various compositions. For each structure/composition, the energies are given relative to that of the FM state.

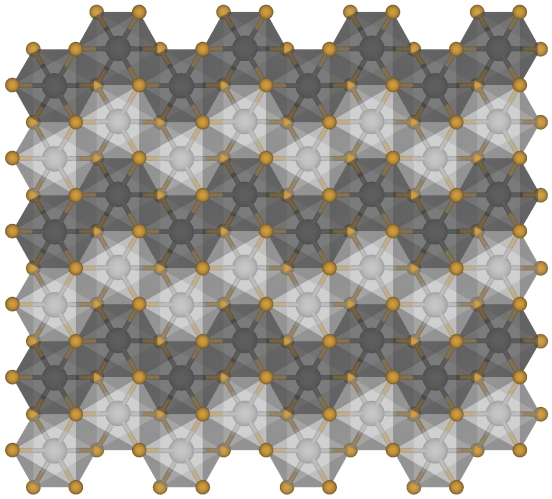

Figure D.5: Top view of the lowest energy in-layer AFM ordering found for both O3- and P3-$NaCrO_2$. Spin up/down Cr are shown as light/dark gray.

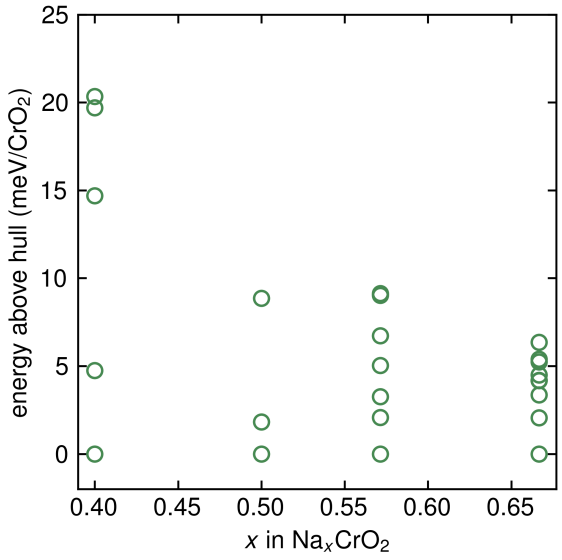

Figure D.6: Energy above the hull for different stackings of the P3 ground state orderings at select compositions.

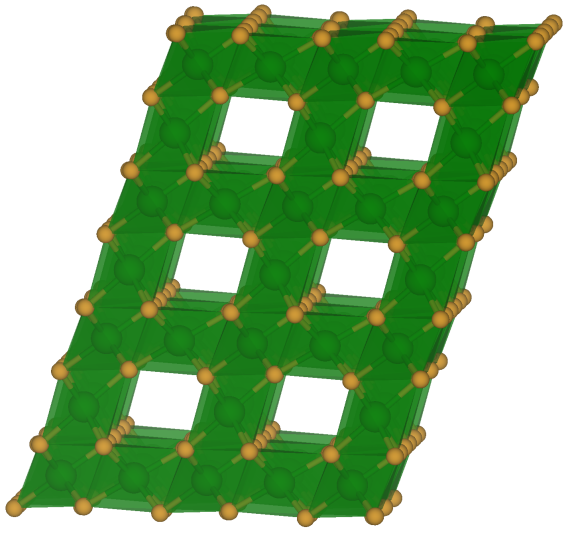

Figure D.7: CrO_2 in the spinel structure.

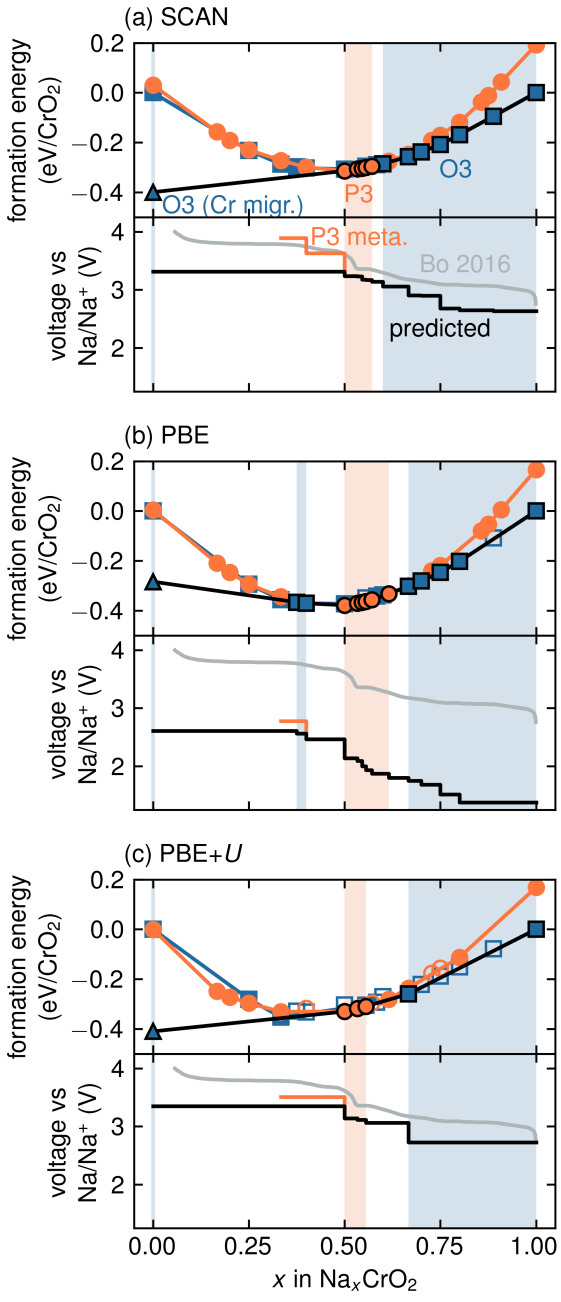

Figure D.8: Formation energies and voltages of FM configurations calculated with (a) SCAN, (b) PBE, and (c) PBE+U ($U = 3.5$ eV). Shaded regions indicate where each host structure is globally stable. Experimental voltage curve from Bo et al. [192] is shown for comparison.

Appendix E

Kinetic model of antiphase boundary migration

E.1 Simulation grid

E.1.1 Grid overview

Na-vacancy orderings consisting of regions of the ζ ordering separated by antiphase boundaries (APBs) may be mapped onto abstract two-dimensional grids, as shown in Figure E.1. In these grids, the l direction points along the length of the boundaries and the s direction points perpendicular, along the direction separating the boundaries. Each grid cell has dimensions u_l by u_s and contains exactly one Na. In the ζ^- case, the grid cells are staggered along the s direction, while in the ζ^+ case they are not. Each grid cell has a sublattice value (A or B) denoting the triangular sublattice of the honeycomb network on which its Na resides and a phase value (0 or 1) denoting the translational variant of the ζ ordering to which its Na belongs. APBs are implicitly represented by adjacent cells having opposite phase.

E.1.2 Space occupied by boundaries

As shown in Figure E.1, the ζ^- boundaries introduce some additional space between cells in the s direction, while the ζ^+ boundaries consume some space and cause the cells at boundaries to overlap slightly. These subtleties can be ignored in the grid representation but must be accounted for when mapping from the grid back to real space. Each ζ^- boundary adds a height $u_s/2$ in the s direction, which is said to be occupied by the boundary. Each ζ^+ boundary removes a height $u_s/4$ in the s direction and is said to occupy $u_s/4$ of the remaining height. The result is that the true, physical height (in the s direction) of a grid that is m cells tall with n boundaries is

$$\left(m + \frac{n}{2}\right) u_s \tag{E.1}$$

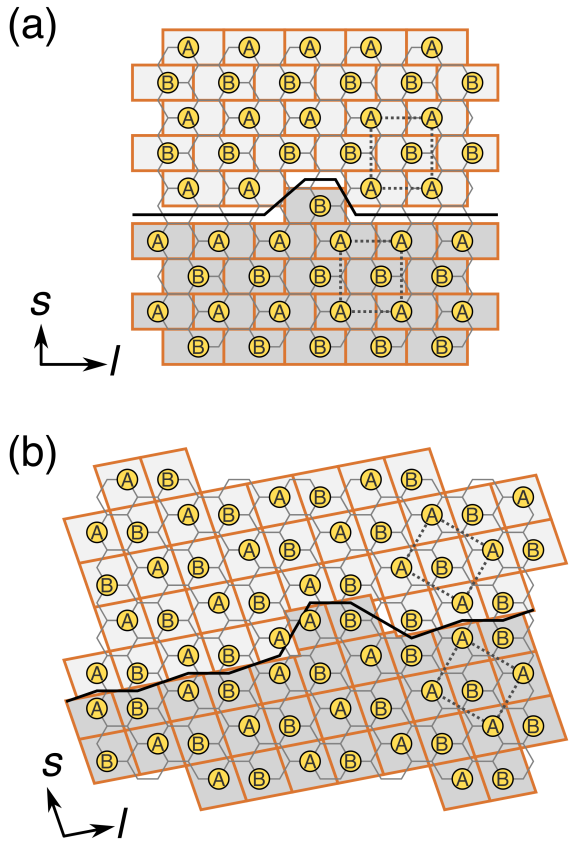

Figure E.1: Example (a) ζ^- and (b) ζ^+ configurations and their corresponding simulation grids. Dotted boxes indicate unit cells of the ζ ordering and black solid lines indicate antiphase boundaries. Na atoms (yellow circles) are labeled by sublattice (A or B). Grid cells are shaded according to their phase.

in the ζ^- case and

$$\left(m - \frac{n}{4}\right) u_s \tag{E.2}$$

in the ζ^+ case. Note that $u_s = a$ in the ζ^- case and $u_s = \frac{\sqrt{7}}{2}a$ in the ζ^+ case, where a is the lattice parameter of the underlying hexagonal lattice of the honeycomb network [14].

E.1.3 Local composition

After accounting for the space added/removed by APBs, a local composition may be defined over the model area. The space occupied by boundaries is assigned a local composition of $x = 0$ in the ζ^- case and $x = 1$ in the ζ^+ case. The remaining "bulk" regions of ζ ordering are assigned a local composition of $x = 1/2$. The resulting average composition of a grid that is m cells tall with n boundaries is

$$\bar{x} = \frac{\frac{m}{2} + 0}{m + \frac{n}{2}} = \frac{\frac{m}{n}}{2\frac{m}{n} + 1} \tag{E.3}$$

in the ζ^- case and

$$\bar{x} = \frac{\frac{m - \frac{n}{2}}{2} + \frac{n}{4}}{m - \frac{n}{4}} = \frac{2\frac{m}{n}}{4\frac{m}{n} - 1} \tag{E.4}$$

in the ζ^+ case. These expressions correspond exactly to the true average compositions given in Reference [12] in terms of the average spacing between boundaries, which is captured by the quantity m/n.

E.2 Kinetic events

E.2.1 Events considered

Kinetic events within the grid models equate to "flipping" one or more cells, that is, changing both the sublattice and phase values to their opposites. Candidate events we consider are flipping any one cell and, in the ζ^+ case only, flipping any pair of cells that are adjacent in the l direction. The rate of a given candidate event is determined by its local environment. Events that are invalid in the current configuration are assigned rates of zero. Valid events have rates based on the kinetic barriers for different types of hops considered (APB kink formation/destruction/evolution).

E.2.2 Event rate determination

Cardinal directions (N, S, E, W) will be used to refer to a cell's neighbors, where N corresponds to the s direction and E corresponds to the l direction.

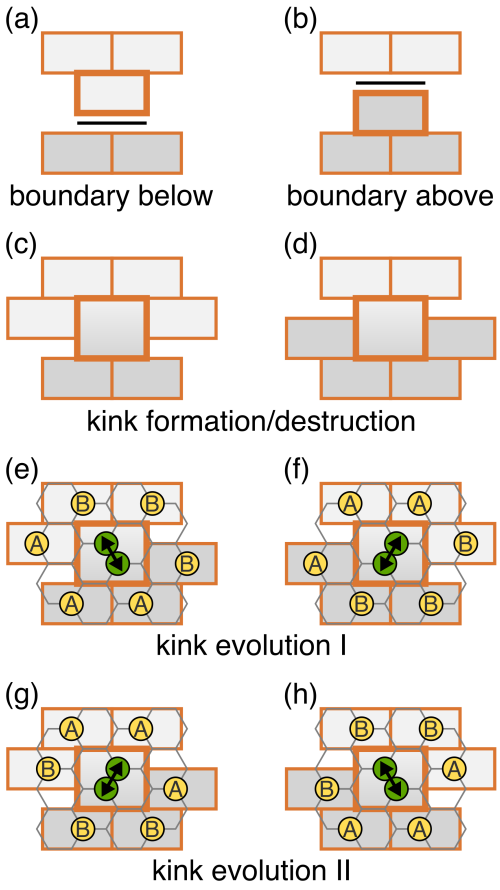

Figure E.2: (a,b) Local environments that determine whether a cell is at a valid boundary in the ζ^- model. (c-h) Local environments corresponding to distinct kinetic events in the ζ^- model, where the cells involved in each event are bolded.

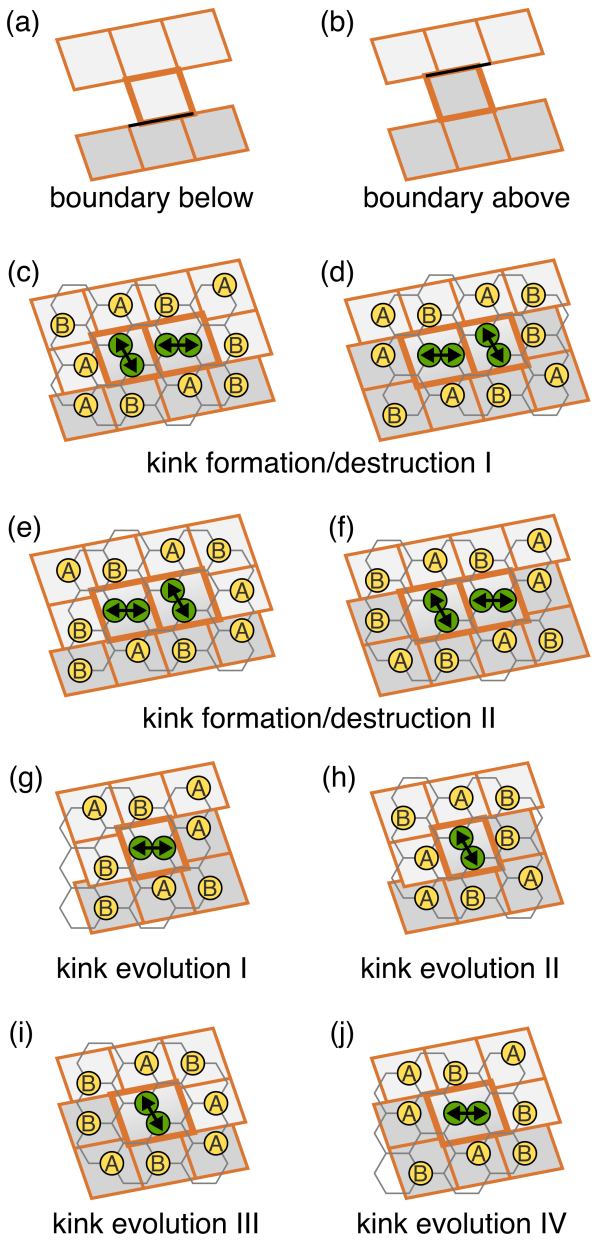

Figure E.3: (a,b) Local environments that determine whether a cell is at a valid boundary in the ζ^+ model. (c-j) Local environments corresponding to distinct kinetic events in the ζ^+ model, where the cells involved in each event are bolded.

Event validity determination The two main assumptions that determine the validity of an event are (1) only Na located at an APB can hop and (2) APBs cannot be created or destroyed (average composition is fixed). For an event to be valid, each cell involved must lie at a valid boundary, that is:

1. The cells above (NW/NE for ζ^-, NW/N/NE for ζ^+) have equal phase.
2. The cells below (SW/SE for ζ^-, SW/S/SE for ζ^+) have equal phase.
3. The cell's own phase is opposite either the above phase or the below phase but not both (this ensures that no flip will result in the merging/annihilation of two boundaries).

Examples of cells located at valid boundaries are shown in Figures E.2(a,b) and E.3(a,b).

For the ζ^+ model, there are some additional considerations due to the fact that kink formation/destruction can only occur via double Na hops. Events can only be valid in the following cases:

- One-cell events: W and E neighbors must have opposite phase (kink evolution, Figure E.3(g-j)).
- Two-cell events: The two cells must have equal phase, and W neighbor of W cell and E neighbor of E cell must have equal phase (kink formation/destruction, Figure E.3(c-f)).

Furthermore, no valid event can result in the formation of single Na kinks, as these are unstable. Therefore we also require:

- One-cell events: If phase of W (E) neighbor equals cell's own phase, phase of W neighbor of W (E neighbor of E) neighbor must also equal cell's own phase.
- Two-cell events: If W neighbor of W cell and E neighbor of E cell have phase equal to the cells' own phase (kink formation event), phase of W neighbor of W neighbor of W cell and phase of E neighbor of E neighbor of E cell must also equal cells' own phase.

Base barrier determination Each valid event may be categorized according to its local environment and assigned a base migration barrier $E_{\mathrm{a,base}}$ and endpoint energy change ΔE_{base}. The values of these quantities for each distinct hop considered in our model are listed in Table E.1, based on calculations from Reference [14].

For ζ^- events:

- If W neighbor phase is equal to E neighbor phase, event is either kink formation (W/E phase equals cell's own phase) or destruction (W/E phase is opposite cell's own phase). Figure E.2(c,d).

Table E.1: Base barriers and energy changes for different kinetic events in each model. A single barrier is listed for symmetric hops.

event	$E_{\mathrm{a,base}}$ (eV)	ΔE_{base} (eV)
ζ^- kink formation/destruction	0.03	0.00
ζ^- kink evolution I	0.03	0.00
ζ^- kink evolution II	0.03	0.00
ζ^+ kink formation I	0.28	0.22
ζ^+ kink destruction I	0.06	−0.22
ζ^+ kink formation II	0.23	0.22
ζ^+ kink destruction II	0.01	−0.22
ζ^+ kink evolution I	0.04	0.00
ζ^+ kink evolution II	0.05	0.00
ζ^+ kink evolution III	0.02	0.00
ζ^+ kink evolution IV	0.10	0.00

- If W neighbor phase is opposite E neighbor phase, event is kink evolution. Type I if W neighbor is sublattice A (Figure E.2e,f), type II if W neighbor is sublattice B (Figure E.2(g,h)).

For ζ^+ two-cell events (kink formation/destruction):

- If W neighbor of W cell and E neighbor of E cell have phase equal to (opposite) cells' own phase, event is kink formation (destruction). Type I if W neighbor is sublattice A (Figure E.3(c,d)), Type II if W neighbor is sublattice B (Figure E.3(e,f)).

For ζ^+ one-cell events (kink evolution):

- Type I: W neighbor sublattice is B and N neighbor sublattice is B (Figure E.3(g)).
- Type II: W neighbor sublattice is A and N neighbor sublattice is A (Figure E.3(h)).
- Type III: W neighbor sublattice is B and N neighbor sublattice is A (Figure E.3(i)).
- Type IV: W neighbor sublattice is A and N neighbor sublattice is B (Figure E.3(j)).

Boundary repulsion adjustment We also include a nearest-neighbor repulsion term for the APBs. The repulsion energy for each type of APB was calculated from density functional theory by constructing supercells containing two APBs and incrementally bringing them closer together, as shown in Figure E.4. These calculations were performed using VASP [59–62] with the same settings used in Reference [14]. In our model, we only add a penalty when two boundary segments are u_s (one cell) apart. The corresponding repulsion energy per unit of boundary length is 0.05 eV/u_l for both the ζ^- and ζ^+ boundaries. The ζ^- boundaries can actually be brought even closer together such that

no Na/cells separate them (Figure E.4(a)), which is forbidden in our model, but this has an energy more than four times that of one-cell separation and is therefore rather unlikely.

Each event's barrier is adjusted based on the change in boundary repulsion energy incurred, ΔE_{rep}. This is calculated by determining the change in the number of nearest-neighbor interactions between boundary segments in the s direction and multiplying with the nearest-neighbor repulsion energy per unit of boundary length. For each cell involved in an event:

- If phase of cell two cells N is opposite phase of N neighbor(s), there is another boundary N of the N neighbor(s):
  - If own phase equals N phase (boundary below), number of interactions increases by 1 (Figure E.5(a)).
  - If own phase opposite N phase (boundary above), number of interactions decreases by 1 (Figure E.5(b)).
- If phase of cell two cells S is opposite phase of S neighbor(s), there is another boundary S of the S neighbor(s):
  - If own phase equals N phase (boundary below), number of interactions decreases by 1 (Figure E.5(c)).
  - If own phase is oppose N phase (boundary above), number of interactions increases by 1 (Figure E.5(d)).

These cases are illustrated in Figure E.5 for the ζ^- model. The same procedure applies for the ζ^+ model.

Once ΔE_{rep} has been determined for an event, the adjusted migration barrier E_{a} is calculated as

$$E_{\text{a}} = E_{\text{a,base}} \tag{E.5}$$

if $\Delta E = \Delta E_{\text{base}} + \Delta E_{\text{rep}} < 0$ or

$$E_{\text{a}} = E_{\text{a,base}} + \Delta E_{\text{rep}} \tag{E.6}$$

otherwise. This procedure, illustrated in Figure E.6, preserves the base migration barrier of either the forward or reverse hop and ensures that no negative adjusted migration barriers are produced.

Rate calculation For a valid event with migration barrier E_{a}, its rate Γ is given by

$$\Gamma = \nu^* \exp \frac{-E_{\text{a}}}{k_{\text{B}} T} \tag{E.7}$$

where ν^* is a vibrational prefactor, k_{B} is the Boltzmann constant, and T is the temperature.

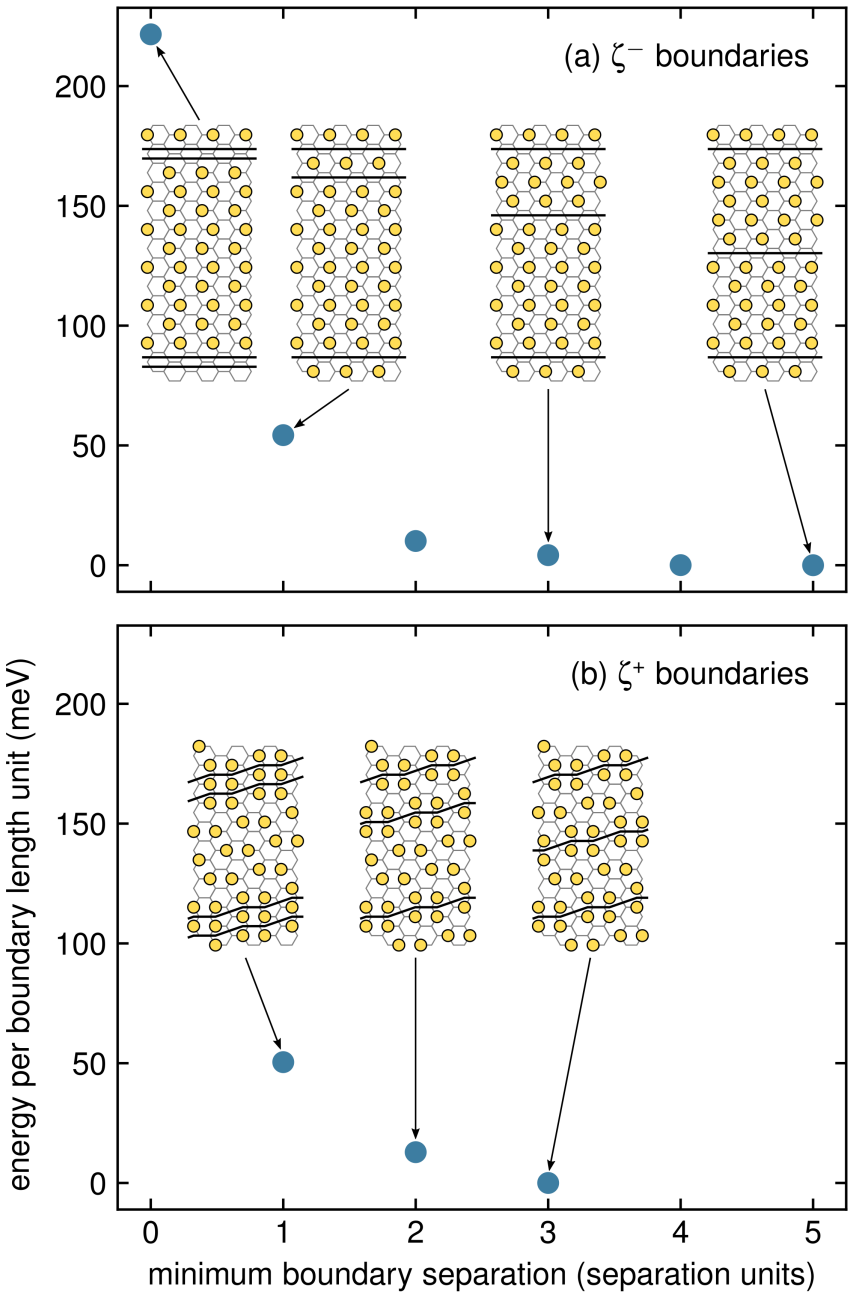

Figure E.4: Repulsion energy versus separation for (a) ζ^- and (b) ζ^+ boundaries. Insets show the configurations used to calculate certain points.

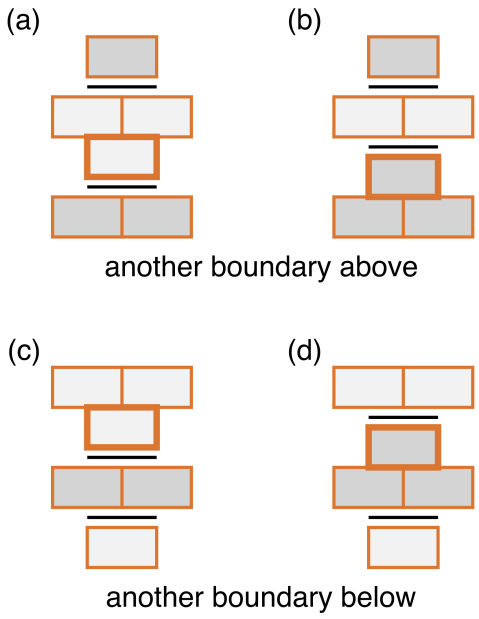

Figure E.5: Local environments containing two nearby boundary segments in the ζ^- model.

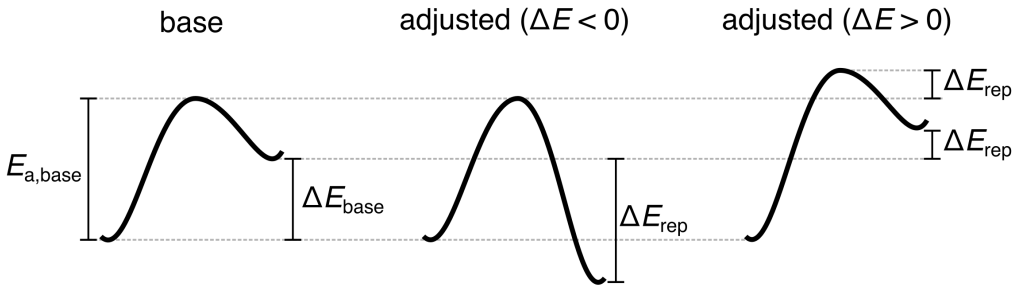

Figure E.6: Illustration of the procedure for adjusting the energy barrier of an kinetic event. If the total energy change ΔE is negative, the forward barrier is preserved. Otherwise, the reverse barrier is preserved.

E.3 Total energy

The total energy in our model, though not explicitly tracked, may be written as

$$U = n_{\text{cells}} u_0(\bar{x}) + n_{\text{kink}} u_{\text{kink}} + n_{\text{rep}} u_{\text{rep}} \tag{E.8}$$

where n_{cells} is the number of unit cells in the simulation supercell, $u_0(\bar{x})$ is an average reference energy per unit cell at the overall composition $\bar{x}$, n_{kink} is the number of APB kinks, u_{kink} is the defect energy per kink, n_{rep} is the number of nearest-neighbor APB segment pairs, and u_{rep} is the nearest-neighbor APB-APB repulsion energy per pair. With an appropriate expression for $u_0(\bar{x})$, one could in principle track U through KMC simulations at equilibrium in order to calculate the free energy resulting from our model at fixed composition.

E.4 Simulator code

Our custom KMC simulator code can be found at:
https://github.com/jonaskaufman/apb-kmc. It relies on the kmc-lotto library for event selection [254].

Bibliography

[1] N. Nitta, F. Wu, J. T. Lee, and G. Yushin, *Li-ion battery materials: present and future*, *Mater. Today* **18** (2015) 252–264.

[2] Y. Tian, G. Zeng, A. Rutt, T. Shi, H. Kim, J. Wang, J. Koettgen, Y. Sun, B. Ouyang, T. Chen, Z. Lun, Z. Rong, K. Persson, and G. Ceder, *Promises and Challenges of Next-Generation "Beyond Li-ion" Batteries for Electric Vehicles and Grid Decarbonization*, *Chem. Rev.* **121** (2021) 1623–1669.

[3] K. Kubota, M. Dahbi, T. Hosaka, S. Kumakura, and S. Komaba, *Towards K-Ion and Na-Ion Batteries as "Beyond Li-Ion"*, *Chem. Rec.* **18** (2018) 459–479.

[4] A. Van der Ven, Z. Deng, S. Banerjee, and S. P. Ong, *Rechargeable Alkali-Ion Battery Materials: Theory and Computation*, *Chem. Rev.* **120** (2020) 6977–7019.

[5] M. S. Islam and C. A. J. Fisher, *Lithium and sodium battery cathode materials: computational insights into voltage, diffusion and nanostructural properties*, *Chem. Soc. Rev.* **43** (2014) 185–204.

[6] M. D. Radin and A. Van der Ven, *Simulating Charge, Spin, and Orbital Ordering: Application to Jahn–Teller Distortions in Layered Transition-Metal Oxides*, *Chem. Mater.* **30** (2018) 607–618.

[7] M. D. Radin and A. Van der Ven, *Stability of Prismatic and Octahedral Coordination in Layered Oxides and Sulfides Intercalated with Alkali and Alkaline-Earth Metals*, *Chem. Mater.* **28** (2016) 7898–7904.

[8] J. Vinckevičiūtė, M. D. Radin, and A. Van der Ven, *Stacking-Sequence Changes and Na Ordering in Layered Intercalation Materials*, *Chem. Mater.* **28** (2016) 8640–8650.

[9] X. Chen, Y. Wang, Y. Wang, R. L. Dally, K. Wiaderek, T. Qiao, J. Liu, E. Hu, K. Burch, J. W. Lynn, and X. Li, *Dynamically preferred state with strong electronic fluctuations from electrochemical synthesis of sodium manganate*, *Matter* **5** (2022) 735–750.

[10] A. Van der Ven, J. C. Thomas, B. Puchala, and A. R. Natarajan, *First-Principles Statistical Mechanics of Multicomponent Crystals*, *Annu. Rev. Mater. Res.* **48** (2018) 27–55.

[11] J. L. Kaufman, J. Vinckevičiūtė, S. K. Kolli, J. G. Goiri, and A. Van der Ven, *Understanding intercalation compounds for sodium-ion batteries and beyond*, *Philos. Trans. R. Soc., A* **377** (2019) 20190020.

[12] J. L. Kaufman and A. Van der Ven, *Na_xCoO_2 phase stability and hierarchical orderings in the O3/P3 structure family*, *Phys. Rev. Mater.* **3** (2019) 015402.

[13] J. L. Kaufman and A. Van der Ven, *Ordering and Structural Transformations in Layered K_xCrO_2 for K-Ion Batteries*, *Chem. Mater.* **32** (2020) 6392–6400.

[14] J. L. Kaufman and A. Van der Ven, *Antiphase boundary migration as a diffusion mechanism in a P3 sodium layered oxide*, *Phys. Rev. Mater.* **5** (2021) 055401.

[15] J. L. Kaufman and A. Van der Ven, *Cation Diffusion Facilitated by Antiphase Boundaries in Layered Intercalation Compounds*, *Chem. Mater.* **34** (2022) 1889–1896.

[16] P. Hohenberg and W. Kohn, *Inhomogeneous Electron Gas*, *Phys. Rev.* **136** (1964) B864–B871.

[17] W. Kohn and L. J. Sham, *Self-Consistent Equations Including Exchange and Correlation Effects*, *Phys. Rev.* **140** (1965) A1133–A1138.

[18] R. M. Martin, *Electronic Structure: Basic Theory and Practical Methods*. Cambridge University Press, 2004.

[19] K. Burke, *The ABC of DFT*. Department of Chemistry, University of California, Irvine, 2007.

[20] D. Sholl and J. A. Steckel, *Density Functional Theory: A Practical Introduction*. John Wiley & Sons, 2009.

[21] W. Kohn, *Nobel Lecture: Electronic structure of matter—wave functions and density functionals*, *Rev. Mod. Phys.* **71** (1999) 1253–1266.

[22] E. Schrödinger, *An Undulatory Theory of the Mechanics of Atoms and Molecules*, *Phys. Rev.* **28** (1926) 1049–1070.

[23] M. Born and R. Oppenheimer, *Zur Quantentheorie der Molekeln*, *Ann. Phys.* **389** (1927) 457–484.

[24] J. P. Perdew and W. Yue, *Accurate and simple density functional for the electronic exchange energy: Generalized gradient approximation*, *Phys. Rev. B* **33** (1986) 8800–8802.

[25] J. P. Perdew, J. A. Chevary, S. H. Vosko, K. A. Jackson, M. R. Pederson, D. J. Singh, and C. Fiolhais, *Atoms, molecules, solids, and surfaces: Applications of the generalized gradient approximation for exchange and correlation*, *Phys. Rev. B* **46** (1992) 6671–6687.

[26] J. P. Perdew, K. Burke, and M. Ernzerhof, *Generalized Gradient Approximation Made Simple*, *Phys. Rev. Lett.* **77** (1996) 3865–3868.

[27] J. Tao, J. P. Perdew, V. N. Staroverov, and G. E. Scuseria, *Climbing the Density Functional Ladder: Nonempirical Meta–Generalized Gradient Approximation Designed for Molecules and Solids*, *Phys. Rev. Lett.* **91** (2003) 146401.

[28] J. P. Perdew, A. Ruzsinszky, G. I. Csonka, L. A. Constantin, and J. Sun, *Workhorse Semilocal Density Functional for Condensed Matter Physics and Quantum Chemistry*, *Phys. Rev. Lett.* **103** (2009) 026403.

[29] Y. Zhao and D. G. Truhlar, *A new local density functional for main-group thermochemistry, transition metal bonding, thermochemical kinetics, and noncovalent interactions*, *J. Chem. Phys.* **125** (2006) 194101.

[30] J. Sun, A. Ruzsinszky, and J. P. Perdew, *Strongly Constrained and Appropriately Normed Semilocal Density Functional*, *Phys. Rev. Lett.* **115** (2015) 036402.

[31] J. Sun, R. C. Remsing, Y. Zhang, Z. Sun, A. Ruzsinszky, H. Peng, Z. Yang, A. Paul, U. Waghmare, X. Wu, M. L. Klein, and J. P. Perdew, *Accurate first-principles structures and energies of diversely bonded systems from an efficient density functional*, *Nat. Chem.* **8** (2016) 831–836.

[32] J. P. Perdew and K. Schmidt, *Jacob's ladder of density functional approximations for the exchange-correlation energy*, *AIP Conf. Proc.* **577** (2001) 1–20.

[33] K. Burke, *Perspective on density functional theory*, *J. Chem. Phys.* **136** (2012) 150901.

[34] M. G. Medvedev, I. S. Bushmarinov, J. Sun, J. P. Perdew, and K. A. Lyssenko, *Density functional theory is straying from the path toward the exact functional*, *Science* **355** (2017) 49–52.

[35] S. L. Dudarev, G. A. Botton, S. Y. Savrasov, C. J. Humphreys, and A. P. Sutton, *Electron-energy-loss spectra and the structural stability of nickel oxide: An LSDA+U study*, *Phys. Rev. B* **57** (1998) 1505–1509.

[36] U. von Barth and L. Hedin, *A local exchange-correlation potential for the spin polarized case: I*, *J. Phys. C: Solid State Phys.* **5** (1972) 1629–1642.

[37] A. K. Rajagopal and J. Callaway, *Inhomogeneous Electron Gas*, *Phys. Rev. B* **7** (1973) 1912–1919.

[38] M. L. Cohen, *Pseudopotentials and Total Energy Calculations*, *Phys. Scr.* **T1** (1982) 5–10.

[39] D. R. Hamann, M. Schlüter, and C. Chiang, *Norm-Conserving Pseudopotentials*, *Phys. Rev. Lett.* **43** (1979) 1494–1497.

[40] D. Vanderbilt, *Soft self-consistent pseudopotentials in a generalized eigenvalue formalism*, *Phys. Rev. B* **41** (1990) 7892–7895.

[41] P. E. Blöchl, *Projector augmented-wave method*, *Phys. Rev. B* **50** (1994) 17953–17979.

[42] G. Kresse and D. Joubert, *From ultrasoft pseudopotentials to the projector augmented-wave method*, *Phys. Rev. B* **59** (1999) 1758–1775.

[43] H. J. Monkhorst and J. D. Pack, *Special points for Brillouin-zone integrations*, *Phys. Rev. B* **13** (1976) 5188–5192.

[44] J. M. Sanchez, F. Ducastelle, and D. Gratias, *Generalized cluster description of multicomponent systems*, *Physica A* **128** (1984) 334–350.

[45] D. De Fontaine, *Cluster Approach to Order-Disorder Transformations in Alloys*, in *Solid State Physics* (H. Ehrenreich and D. Turnbull, eds.), vol. 47, pp. 33–176. Academic Press, 1994.

[46] R. Drautz, *Atomic cluster expansion for accurate and transferable interatomic potentials*, *Phys. Rev. B* **99** (2019) 014104.

[47] R. Drautz, *Atomic cluster expansion of scalar, vectorial, and tensorial properties including magnetism and charge transfer*, *Phys. Rev. B* **102** (2020) 024104.

[48] A. E. Hoerl and R. W. Kennard, *Ridge Regression: Biased Estimation for Nonorthogonal Problems*, *Technometrics* **12** (1970) 55–67.

[49] R. Tibshirani, *Regression Shrinkage and Selection Via the Lasso*, *J. R. Stat. Soc. Ser. B* **58** (1996) 267–288.

[50] G. L. W. Hart, V. Blum, M. J. Walorski, and A. Zunger, *Evolutionary approach for determining first-principles hamiltonians*, *Nat. Mater.* **4** (2005) 391–394.

[51] J. Kristensen and N. J. Zabaras, *Bayesian uncertainty quantification in the evaluation of alloy properties with the cluster expansion method*, *Comput. Phys. Commun.* **185** (2014) 2885–2892.

[52] N. Metropolis, A. W. Rosenbluth, M. N. Rosenbluth, A. H. Teller, and E. Teller, *Equation of State Calculations by Fast Computing Machines*, *J. Chem. Phys.* **21** (1953) 1087–1092.

[53] W. K. Hastings, *Monte Carlo sampling methods using Markov chains and their applications*, *Biometrika* **57** (1970) 97–109.

[54] A. van de Walle and M. Asta, *Self-driven lattice-model Monte Carlo simulations of alloy thermodynamic properties and phase diagrams*, *Modell. Simul. Mater. Sci. Eng.* **10** (2002) 521–538.

[55] G. H. Vineyard, *Frequency factors and isotope effects in solid state rate processes*, *J. Phys. Chem. Solids* **3** (1957) 121–127.

[56] H. Jónsson, G. Mills, and K. W. Jacobsen, *Nudged elastic band method for finding minimum energy paths of transitions*, in *Classical and Quantum Dynamics in Condensed Phase Simulations*, pp. 385–404. World Scientific, 1998.

[57] A. Van der Ven, G. Ceder, M. Asta, and P. D. Tepesch, *First-principles theory of ionic diffusion with nondilute carriers*, *Phys. Rev. B* **64** (2001) 184307.

[58] A. B. Bortz, M. H. Kalos, and J. L. Lebowitz, *A new algorithm for Monte Carlo simulation of Ising spin systems*, *J. Comput. Phys.* **17** (1975) 10–18.

[59] G. Kresse and J. Hafner, *Ab initio molecular dynamics for liquid metals*, *Phys. Rev. B* **47** (1993) 558–561.

[60] G. Kresse and J. Hafner, *Ab initio molecular-dynamics simulation of the liquid-metal–amorphous-semiconductor transition in germanium*, *Phys. Rev. B* **49** (1994) 14251–14269.

[61] G. Kresse and J. Furthmüller, *Efficiency of ab-initio total energy calculations for metals and semiconductors using a plane-wave basis set*, *Comput. Mater. Sci.* **6** (1996) 15–50.

[62] G. Kresse and J. Furthmüller, *Efficient iterative schemes for ab initio total-energy calculations using a plane-wave basis set*, *Phys. Rev. B* **54** (1996) 11169–11186.

[63] P. E. Blöchl, O. Jepsen, and O. K. Andersen, *Improved tetrahedron method for Brillouin-zone integrations*, *Phys. Rev. B* **49** (1994) 16223–16233.

[64] J. Klimeš, D. R. Bowler, and A. Michaelides, *Chemical accuracy for the van der Waals density functional*, *J. Phys.: Condens. Matter* **22** (2010) 022201.

[65] J. Klimeš, D. R. Bowler, and A. Michaelides, *Van der Waals density functionals applied to solids*, *Phys. Rev. B* **83** (2011) 195131.

[66] M. Dion, H. Rydberg, E. Schröder, D. C. Langreth, and B. I. Lundqvist, *Van der Waals Density Functional for General Geometries*, *Phys. Rev. Lett.* **92** (2004) 246401.

[67] G. Román-Pérez and J. M. Soler, *Efficient Implementation of a van der Waals Density Functional: Application to Double-Wall Carbon Nanotubes*, *Phys. Rev. Lett.* **103** (2009) 096102.

[68] "CASM: A Clusters Approach to Statistical Mechanics." https://github.com/prisms-center/CASMcode, 2022.

[69] J. C. Thomas and A. Van der Ven, *Finite-temperature properties of strongly anharmonic and mechanically unstable crystal phases from first principles*, *Phys. Rev. B* **88** (2013) 214111.

[70] B. Puchala and A. Van der Ven, *Thermodynamics of the Zr-O system from first-principles calculations*, *Phys. Rev. B* **88** (2013) 094108.

[71] K. Momma and F. Izumi, *VESTA 3 for three-dimensional visualization of crystal, volumetric and morphology data*, *J. Appl. Crystallogr.* **44** (2011) 1272–1276.

[72] J. B. Goodenough and K.-S. Park, *The Li-Ion Rechargeable Battery: A Perspective*, *J. Am. Chem. Soc.* **135** (2013) 1167–1176.

[73] C. Delmas, *Sodium and Sodium-Ion Batteries: 50 Years of Research*, *Adv. Energy Mater.* **8** (2018) 1703137.

[74] J.-Y. Hwang, S.-T. Myung, and Y.-K. Sun, *Recent Progress in Rechargeable Potassium Batteries*, *Adv. Funct. Mater.* **28** (2018) 1802938.

[75] H. D. Yoo, I. Shterenberg, Y. Gofer, G. Gershinsky, N. Pour, and D. Aurbach, *Mg rechargeable batteries: an on-going challenge*, *Energy Environ. Sci.* **6** (2013) 2265–2279.

[76] A. Ponrouch, C. Frontera, F. Bardé, and M. R. Palacín, *Towards a calcium-based rechargeable battery*, *Nat. Mater.* **15** (2016) 169–172.

[77] K. Mizushima, P. C. Jones, P. J. Wiseman, and J. B. Goodenough, *Li_xCoO_2 ($0 < x \leq 1$): A new cathode material for batteries of high energy density*, *Mater. Res. Bull.* **15** (1980) 783–789.

[78] M. D. Radin, S. Hy, M. Sina, C. Fang, H. Liu, J. Vinckeviciute, M. Zhang, M. S. Whittingham, Y. S. Meng, and A. Van der Ven, *Narrowing the Gap between Theoretical and Practical Capacities in Li-Ion Layered Oxide Cathode Materials*, *Adv. Energy Mater.* **7** (2017) 1602888.

[79] M. H. Han, E. Gonzalo, G. Singh, and T. Rojo, *A comprehensive review of sodium layered oxides: powerful cathodes for Na-ion batteries*, *Energy Environ. Sci.* **8** (2015) 81–102.

[80] S. Mariyappan, Q. Wang, and J. M. Tarascon, *Will Sodium Layered Oxides Ever Be Competitive for Sodium Ion Battery Applications?*, *J. Electrochem. Soc.* **165** (2018) A3714.

[81] R. Berthelot, D. Carlier, and C. Delmas, *Electrochemical investigation of the P2–Na_xCoO_2 phase diagram*, *Nat. Mater.* **10** (2011) 74–80.

[82] K. Kubota, I. Ikeuchi, T. Nakayama, C. Takei, N. Yabuuchi, H. Shiiba, M. Nakayama, and S. Komaba, *New Insight into Structural Evolution in Layered $NaCrO_2$ during Electrochemical Sodium Extraction*, *J. Phys. Chem. C* **119** (2015) 166–175.

[83] C. Didier, M. Guignard, M. R. Suchomel, D. Carlier, J. Darriet, and C. Delmas, *Thermally and Electrochemically Driven Topotactical Transformations in Sodium Layered Oxides Na_xVO_2*, *Chem. Mater.* **28** (2016) 1462–1471.

[84] M. D. Radin, J. Alvarado, Y. S. Meng, and A. Van der Ven, *Role of Crystal Symmetry in the Reversibility of Stacking-Sequence Changes in Layered Intercalation Electrodes*, *Nano Lett.* **17** (2017) 7789–7795.

[85] X. Li, X. Ma, D. Su, L. Liu, R. Chisnell, S. P. Ong, H. Chen, A. Toumar, J.-C. Idrobo, Y. Lei, J. Bai, F. Wang, J. W. Lynn, Y. S. Lee, and G. Ceder, *Direct visualization of the Jahn–Teller effect coupled to Na ordering in $Na_{5/8}MnO_2$*, *Nat. Mater.* **13** (2014) 586–592.

[86] P. Vassilaras, D.-H. Kwon, S. T. Dacek, T. Shi, D.-H. Seo, G. Ceder, and J. C. Kim, *Electrochemical properties and structural evolution of O3-type layered sodium mixed transition metal oxides with trivalent nickel*, *J. Mater. Chem. A* **5** (2017) 4596–4606.

[87] R. J. Clément, P. G. Bruce, and C. P. Grey, *Review—Manganese-Based P2-Type Transition Metal Oxides as Sodium-Ion Battery Cathode Materials*, *J. Electrochem. Soc.* **162** (2015) A2589.

[88] T. J. Willis, D. G. Porter, D. J. Voneshen, S. Uthayakumar, F. Demmel, M. J. Gutmann, M. Roger, K. Refson, and J. P. Goff, *Diffusion mechanism in the sodium-ion battery material sodium cobaltate*, *Sci. Rep.* **8** (2018) 1–10.

[89] M. Liu, Z. Rong, R. Malik, P. Canepa, A. Jain, G. Ceder, and K. A. Persson, *Spinel compounds as multivalent battery cathodes: a systematic evaluation based on ab initio calculations*, *Energy Environ. Sci.* **8** (2015) 964–974.

[90] J. R. Kim and G. G. Amatucci, *Structural and Electrochemical Investigation of Na^+ Insertion into High-Voltage Spinel Electrodes*, *Chem. Mater.* **27** (2015) 2546–2556.

[91] X. Sun, P. Bonnick, V. Duffort, M. Liu, Z. Rong, K. A. Persson, G. Ceder, and L. F. Nazar, *A high capacity thiospinel cathode for Mg batteries*, *Energy Environ. Sci.* **9** (2016) 2273–2277.

[92] S. K. Kolli and A. Van der Ven, *Controlling the Electrochemical Properties of Spinel Intercalation Compounds*, *ACS Appl. Energy Mater.* **1** (2018) 6833–6839.

[93] A. Van der Ven, J. C. Thomas, Q. Xu, B. Swoboda, and D. Morgan, *Nondilute diffusion from first principles: Li diffusion in* Li_xTiS_2, *Phys. Rev. B* **78** (2008) 104306.

[94] J. Bhattacharya and A. Van der Ven, *First-principles study of competing mechanisms of nondilute Li diffusion in spinel* Li_xTiS_2, *Phys. Rev. B* **83** (2011) 144302.

[95] A. Van der Ven, J. Bhattacharya, and A. A. Belak, *Understanding Li Diffusion in Li-Intercalation Compounds*, *Acc. Chem. Res.* **46** (2013) 1216–1225.

[96] E. Levi, Y. Gofer, and D. Aurbach, *On the Way to Rechargeable Mg Batteries: The Challenge of New Cathode Materials*, *Chem. Mater.* **22** (2010) 860–868.

[97] N. Yabuuchi, K. Kubota, M. Dahbi, and S. Komaba, *Research Development on Sodium-Ion Batteries*, *Chem. Rev.* **114** (2014) 11636–11682.

[98] A. Luntz, *Beyond Lithium Ion Batteries*, *J. Phys. Chem. Lett.* **6** (2015) 300–301.

[99] R. C. Massé, E. Uchaker, and G. Cao, *Beyond Li-ion: electrode materials for sodium- and magnesium-ion batteries*, *Sci. China Mater.* **58** (2015) 715–766.

[100] D. Kundu, E. Talaie, V. Duffort, and L. F. Nazar, *The Emerging Chemistry of Sodium Ion Batteries for Electrochemical Energy Storage*, *Angew. Chem., Int. Ed.* **54** (2015) 3431–3448.

[101] O. Sapunkov, V. Pande, A. Khetan, C. Choomwattana, and V. Viswanathan, *Quantifying the promise of 'beyond' Li–ion batteries*, *Transl. Mater. Res.* **2** (2015) 045002.

[102] J. W. Choi and D. Aurbach, *Promise and reality of post-lithium-ion batteries with high energy densities*, *Nat. Rev. Mater.* **1** (2016) 1–16.

[103] A. M. Skundin, T. L. Kulova, and A. B. Yaroslavtsev, *Sodium-Ion Batteries (a Review)*, *Russ. J. Electrochem.* **54** (2018) 113–152.

[104] D. Cherns and G. P. Ngo, *Electron microscope studies of sodium and lithium intercalation in* TiS_2, *J. Solid State Chem.* **50** (1983) 7–19.

[105] A. Van der Ven, M. K. Aydinol, G. Ceder, G. Kresse, and J. Hafner, *First-principles investigation of phase stability in Li_xCoO_2*, *Phys. Rev. B* **58** (1998) 2975–2987.

[106] J. Reed and G. Ceder, *Role of Electronic Structure in the Susceptibility of Metastable Transition-Metal Oxide Structures to Transformation*, *Chem. Rev.* **104** (2004) 4513–4534.

[107] S. Kim, X. Ma, S. P. Ong, and G. Ceder, *A comparison of destabilization mechanisms of the layered Na_xMO_2 and Li_xMO_2 compounds upon alkali de-intercalation*, *Phys. Chem. Chem. Phys.* **14** (2012) 15571–15578.

[108] C. Delmas, J.-J. Braconnier, C. Fouassier, and P. Hagenmuller, *Electrochemical intercalation of sodium in Na_xCoO_2 bronzes*, *Solid State Ionics* **3–4** (1981) 165–169.

[109] K. Kubota, N. Yabuuchi, H. Yoshida, M. Dahbi, and S. Komaba, *Layered oxides as positive electrode materials for Na-ion batteries*, *MRS Bull.* **39** (2014) 416–422.

[110] P.-F. Wang, Y. You, Y.-X. Yin, Y.-S. Wang, L.-J. Wan, L. Gu, and Y.-G. Guo, *Suppressing the P2–O2 Phase Transition of $Na_{0.67}Mn_{0.67}Ni_{0.33}O_2$ by Magnesium Substitution for Improved Sodium-Ion Batteries*, *Angew. Chem., Int. Ed.* **55** (2016) 7445–7449.

[111] Y. Wang, Y. Ding, and J. Ni, *Ground-state phase diagram of Na_xCoO_2: correlation of Na ordering with CoO_2 stacking sequences*, *J. Phys.: Condens. Matter* **21** (2009) 035401.

[112] Y. Lei, X. Li, L. Liu, and G. Ceder, *Synthesis and Stoichiometry of Different Layered Sodium Cobalt Oxides*, *Chem. Mater.* **26** (2014) 5288–5296.

[113] R. D. Shannon, *Revised effective ionic radii and systematic studies of interatomic distances in halides and chalcogenides*, *Acta Crystallogr., Sect. A* **32** (1976) 751–767.

[114] M. S. Dresselhaus, G. Dresselhaus, and A. Jorio, *Group Theory: Application to the Physics of Condensed Matter*. Springer, 2008.

[115] E. Pavarini, E. Koch, F. Anders, and M. Jarrell, *Correlated electrons: from models to materials*, tech. rep., Forschungszentrum Jülich GmbH Zenralbibliothek, Verlag Jülich, 2012.

[116] L. Croguennec, C. Pouillerie, A. N. Mansour, and C. Delmas, *Structural characterisation of the highly deintercalated $Li_xNi_{1.02}O_2$ phases (with $x \leq 0.30$)*, *J. Mater. Chem.* **11** (2001) 131–141.

[117] S. K. Kolli and A. Van der Ven, *First-Principles Study of Spinel $MgTiS_2$ as a Cathode Material*, *Chem. Mater.* **30** (2018) 2436–2442.

[118] A. Emly and A. Van der Ven, *Mg Intercalation in Layered and Spinel Host Crystal Structures for Mg Batteries*, *Inorg. Chem.* **54** (2015) 4394–4402.

[119] A. H. Thompson, *Electrochemical Potential Spectroscopy: A New Electrochemical Measurement*, *J. Electrochem. Soc.* **126** (1979) 608.

[120] D. A. Winn, J. M. Shemilt, and B. C. H. Steele, *Titanium disulphide: A solid solution electrode for sodium and lithium*, *Mater. Res. Bull.* **11** (1976) 559–566.

[121] K. Kubota, T. Asari, H. Yoshida, N. Yaabuuchi, H. Shiiba, M. Nakayama, and S. Komaba, *Understanding the Structural Evolution and Redox Mechanism of a $NaFeO_2$–$NaCoO_2$ Solid Solution for Sodium-Ion Batteries*, *Adv. Funct. Mater.* **26** (2016) 6047–6059.

[122] P. Bonnick, X. Sun, K.-C. Lau, C. Liao, and L. F. Nazar, *Monovalent versus Divalent Cation Diffusion in Thiospinel Ti_2S_4*, *J. Phys. Chem. Lett.* **8** (2017) 2253–2257.

[123] M. Aykol, S. Kim, and C. Wolverton, *van der Waals Interactions in Layered Lithium Cobalt Oxides*, *J. Phys. Chem. C* **119** (2015) 19053–19058.

[124] Y. Hironaka, K. Kubota, and S. Komaba, *P2- and P3-K_xCoO_2 as an electrochemical potassium intercalation host*, *Chem. Commun.* **53** (2017) 3693–3696.

[125] J.-Y. Hwang, J. Kim, T.-Y. Yu, S.-T. Myung, and Y.-K. Sun, *Development of P3-$K_{0.69}CrO_2$ as an ultra-high-performance cathode material for K-ion batteries*, *Energy Environ. Sci.* **11** (2018) 2821–2827.

[126] M. Y. Toriyama, J. L. Kaufman, and A. Van der Ven, *Potassium ordering and structural phase stability in layered K_xCoO_2*, *ACS Appl. Energy Mater.* **2** (2019) 2629–2636.

[127] A. Maazaz, C. Delmas, and P. Hagenmuller, *A study of the Na_xTiO_2 system by electrochemical deintercalation*, *J. Inclusion Phenom.* **1** (1983) 45–51.

[128] D. Wu, X. Li, B. Xu, N. Twu, L. Liu, and G. Ceder, *$NaTiO_2$: a layered anode material for sodium-ion batteries*, *Energy Environ. Sci.* **8** (2015) 195–202.

[129] Q. Huang, M. L. Foo, J. W. Lynn, H. W. Zandbergen, G. Lawes, Y. Wang, B. H. Toby, A. P. Ramirez, N. P. Ong, and R. J. Cava, *Low temperature phase transitions and crystal structure of $Na_{0.5}CoO_2$*, *J. Phys.: Condens. Matter* **16** (2004) 5803–5814.

[130] M. Guignard, C. Didier, J. Darriet, P. Bordet, E. Elkaïm, and C. Delmas, *P2-Na_xVO_2 system as electrodes for batteries and electron-correlated materials*, *Nat. Mater.* **12** (2013) 74–80.

[131] N. Yabuuchi, I. Ikeuchi, K. Kubota, and S. Komaba, *Thermal Stability of Na_xCrO_2 for Rechargeable Sodium Batteries; Studies by High-Temperature Synchrotron X-ray Diffraction*, *ACS Appl. Mater. Interfaces* **8** (2016) 32292–32299.

[132] V. Vítek, *Intrinsic stacking faults in body-centred cubic crystals*, *Philos. Mag.* **18** (1968) 773–786.

[133] J. W. Christian and V. Vítek, *Dislocations and stacking faults*, *Rep. Prog. Phys.* **33** (1970) 307–411.

[134] M. Yamaguchi and Y. Umakoshi, *The deformation behaviour of intermetallic superlattice compounds*, *Prog. Mater. Sci.* **34** (1990) 1–148.

[135] G. Lu, N. Kioussis, V. V. Bulatov, and E. Kaxiras, *Generalized-stacking-fault energy surface and dislocation properties of aluminum*, *Phys. Rev. B* **62** (2000) 3099–3108.

[136] H. Van Swygenhoven, P. M. Derlet, and A. G. Frøseth, *Stacking fault energies and slip in nanocrystalline metals*, *Nat. Mater.* **3** (2004) 399–403.

[137] S. Kibey, J. B. Liu, D. D. Johnson, and H. Sehitoglu, *Predicting twinning stress in fcc metals: Linking twin-energy pathways to twin nucleation*, *Acta Mater.* **55** (2007) 6843–6851.

[138] D. Hull and D. J. Bacon, *Introduction to Dislocations*. Elsevier, 2011.

[139] H. Gabrisch, R. Yazami, and B. Fultz, *The Character of Dislocations in $LiCoO_2$*, *Electrochem. Solid-State Lett.* **5** (2002) A111.

[140] M. Dresselhaus and G. Dresselhaus, *Intercalation compounds of graphite*, *Adv. Phys.* **30** (1981) 139–326.

[141] M. Remškar, A. Popović, and H. I. Starnberg, *Stacking transformation and defect creation in Cs intercalated TiS_2 single crystals*, *Surf. Sci.* **430** (1999) 199–205.

[142] A. Ulvestad, A. Singer, J. N. Clark, H. M. Cho, J. W. Kim, R. Harder, J. Maser, Y. S. Meng, and O. G. Shpyrko, *Topological defect dynamics in operando battery nanoparticles*, *Science* **348** (2015) 1344–1347.

[143] R. J. Clément, D. S. Middlemiss, I. D. Seymour, A. J. Ilott, and C. P. Grey, *Insights into the Nature and Evolution upon Electrochemical Cycling of Planar Defects in the β-$NaMnO_2$ Na-Ion Battery Cathode: An NMR and First-Principles Density Functional Theory Approach*, *Chem. Mater.* **28** (2016) 8228–8239.

[144] Q. Li, Z. Yao, J. Wu, S. Mitra, S. Hao, T. S. Sahu, Y. Li, C. Wolverton, and V. P. Dravid, *Intermediate phases in sodium intercalation into MoS_2 nanosheets and their implications for sodium-ion batteries*, *Nano Energy* **38** (2017) 342–349.

[145] X. Bai, M. Sathiya, B. Mendoza-Sánchez, A. Iadecola, J. Vergnet, R. Dedryvère, M. Saubanère, A. M. Abakumov, P. Rozier, and J.-M. Tarascon, *Anionic Redox Activity in a Newly Zn-Doped Sodium Layered Oxide P2-$Na_{2/3}Mn_{1-y}Zn_yO_2$ (0 < y < 0.23)*, *Adv. Energy Mater.* **8** (2018) 1802379.

[146] M. Sathiya, Q. Jacquet, M.-L. Doublet, O. M. Karakulina, J. Hadermann, and J.-M. Tarascon, *A Chemical Approach to Raise Cell Voltage and Suppress Phase Transition in O3 Sodium Layered Oxide Electrodes*, *Adv. Energy Mater.* **8** (2018) 1702599.

[147] X. Ma, H. Chen, and G. Ceder, *Electrochemical Properties of Monoclinic $NaMnO_2$*, *J. Electrochem. Soc.* **158** (2011) A1307.

[148] P. Vassilaras, X. Ma, X. Li, and G. Ceder, *Electrochemical Properties of Monoclinic $NaNiO_2$*, *J. Electrochem. Soc.* **160** (2012) A207.

[149] D. H. Lee, J. Xu, and Y. S. Meng, *An advanced cathode for Na-ion batteries with high rate and excellent structural stability*, *Phys. Chem. Chem. Phys.* **15** (2013) 3304–3312.

[150] X. Li, D. Wu, Y.-N. Zhou, L. Liu, X.-Q. Yang, and G. Ceder, *O3-type $Na(Mn_{0.25}Fe_{0.25}Co_{0.25}Ni_{0.25})O_2$: A quaternary layered cathode compound for rechargeable Na ion batteries*, *Electrochem. Commun.* **49** (2014) 51–54.

[151] B. Mortemard de Boisse, D. Carlier, M. Guignard, L. Bourgeois, and C. Delmas, *P2-$Na_xMn_{1/2}Fe_{1/2}O_2$ Phase Used as Positive Electrode in Na Batteries: Structural Changes Induced by the Electrochemical (De)intercalation Process*, *Inorg. Chem.* **53** (2014) 11197–11205.

[152] P. Vassilaras, A. J. Toumar, and G. Ceder, *Electrochemical properties of $NaNi_{1/3}Co_{1/3}Fe_{1/3}O_2$ as a cathode material for Na-ion batteries*, *Electrochem. Commun.* **38** (2014) 79–81.

[153] H. Liu, J. Xu, C. Ma, and Y. S. Meng, *A new O3-type layered oxide cathode with high energy/power density for rechargeable Na batteries*, *Chem. Commun.* **51** (2015) 4693–4696.

[154] B. Mortemard de Boisse, J.-H. Cheng, D. Carlier, M. Guignard, C.-J. Pan, S. Bordère, D. Filimonov, C. Drathen, E. Suard, B.-J. Hwang, A. Wattiaux, and C. Delmas, *O3–$Na_xMn_{1/3}Fe_{2/3}O_2$ as a positive electrode material for Na-ion batteries: structural evolutions and redox mechanisms upon Na^+ (de)intercalation*, *J. Mater. Chem. A* **3** (2015) 10976–10989.

[155] L. Vitoux, M. Guignard, M. R. Suchomel, J. C. Pramudita, N. Sharma, and C. Delmas, *The Na_xMoO_2 Phase Diagram (1/2 ≤ x < 1): An Electrochemical Devil's Staircase*, *Chem. Mater.* **29** (2017) 7243–7254.

[156] L. Vitoux, M. Guignard, J. Darriet, and C. Delmas, *Exploration of the Na_xMoO_2 phase diagram for low sodium contents ($x \leq 0.5$)*, *J. Mater. Chem. A* **6** (2018) 14651–14662.

[157] T. Wang, D. Su, D. Shanmukaraj, T. Rojo, M. Armand, and G. Wang, *Electrode Materials for Sodium-Ion Batteries: Considerations on Crystal Structures and Sodium Storage Mechanisms*, *Electrochem. Energ. Rev.* **1** (2018) 200–237.

[158] Q. Bai, L. Yang, H. Chen, and Y. Mo, *Computational Studies of Electrode Materials in Sodium-Ion Batteries*, *Adv. Energy Mater.* **8** (2018) 1702998.

[159] A. J. Toumar, S. P. Ong, W. D. Richards, S. Dacek, and G. Ceder, *Vacancy Ordering in O3-Type Layered Metal Oxide Sodium-Ion Battery Cathodes*, *Phys. Rev. Applied* **4** (2015) 064002.

[160] Y. Hinuma, Y. S. Meng, and G. Ceder, *Temperature-concentration phase diagram of P2-Na_xCoO_2 from first-principles calculations*, *Phys. Rev. B* **77** (2008) 224111.

[161] C. Wolverton and A. Zunger, *First-Principles Prediction of Vacancy Order-Disorder and Intercalation Battery Voltages in Li_xCoO_2*, *Phys. Rev. Lett.* **81** (1998) 606–609.

[162] V. L. Chevrier, S. P. Ong, R. Armiento, M. K. Y. Chan, and G. Ceder, *Hybrid density functional calculations of redox potentials and formation energies of transition metal compounds*, *Phys. Rev. B* **82** (2010) 075122.

[163] "Supporting Information for: Na_xCoO_2 phase stability and hierarchical orderings in the O3/P3 structure family." http://link.aps.org/supplemental/10.1103/PhysRevMaterials.3.015402, 2019.

[164] P. Bak and J. von Boehm, *Ising model with solitons, phasons, and "the devil's staircase"*, *Phys. Rev. B* **21** (1980) 5297–5308.

[165] J. Kanamori, *Infinite Series of Ground States of the Ising Model on the Honeycomb Lattice*, *J. Phys. Soc. Jpn.* **53** (1984) 250–260.

[166] Y. S. Meng, Y. Hinuma, and G. Ceder, *An investigation of the sodium patterning in Na_xCoO_2 ($0.5 \leq x \leq 1$) by density functional theory methods*, *J. Chem. Phys.* **128** (2008) 104708.

[167] A. R. Natarajan, E. L. S. Solomon, B. Puchala, E. A. Marquis, and A. Van der Ven, *On the early stages of precipitation in dilute Mg–Nd alloys*, *Acta Mater.* **108** (2016) 367–379.

[168] E. Decolvenaere, M. J. Gordon, and A. Van der Ven, *Testing predictions from density functional theory at finite temperatures: β_2-like ground states in Co-Pt*, *Phys. Rev. B* **92** (2015) 085119.

[169] J. G. Goiri and A. Van der Ven, *Phase and structural stability in Ni-Al systems from first principles*, *Phys. Rev. B* **94** (2016) 094111.

[170] T. Shibata, Y. Fukuzumi, W. Kobayashi, and Y. Moritomo, *Fast discharge process of layered cobalt oxides due to high Na^+ diffusion*, *Sci. Rep.* **5** (2015) 9006.

[171] S. Guo, Y. Sun, J. Yi, K. Zhu, P. Liu, Y. Zhu, G.-z. Zhu, M. Chen, M. Ishida, and H. Zhou, *Understanding sodium-ion diffusion in layered P2 and P3 oxides via experiments and first-principles calculations: a bridge between crystal structure and electrochemical performance*, *NPG Asia Mater.* **8** (2016) e266–e266.

[172] M. E. Arroyo y de Dompablo, C. Marianetti, A. Van der Ven, and G. Ceder, *Jahn-Teller mediated ordering in layered Li_xMO_2 compounds*, *Phys. Rev. B* **63** (2001) 144107.

[173] C. Didier, M. Guignard, C. Denage, O. Szajwaj, S. Ito, I. Saadoune, J. Darriet, and C. Delmas, *Electrochemical Na-Deintercalation from $NaVO_2$*, *Electrochem. Solid-State Lett.* **14** (2011) A75.

[174] J. J. Braconnier, C. Delmas, and P. Hagenmuller, *Etude par desintercalation electrochimique des systemes Na_xCrO_2 et Na_xNiO_2*, *Mater. Res. Bull.* **17** (1982) 993–1000.

[175] S. Miyazaki, S. Kikkawa, and M. Koizumi, *Chemical and electrochemical deintercalations of the layered compounds $LiMO_2$ (M = Cr, Co) and $NaM'O2$ (M' = Cr, Fe, Co, Ni)*, *Synth. Met.* **6** (1983) 211–217.

[176] S. Komaba, C. Takei, T. Nakayama, A. Ogata, and N. Yabuuchi, *Electrochemical intercalation activity of layered $NaCrO_2$ vs. $LiCrO_2$*, *Electrochem. Commun.* **12** (2010) 355–358.

[177] A. Mendiboure, C. Delmas, and P. Hagenmuller, *Electrochemical intercalation and deintercalation of Na_xMnO_2 bronzes*, *J. Solid State Chem.* **57** (1985) 323–331.

[178] Y. Takeda, K. Nakahara, M. Nishijima, N. Imanishi, O. Yamamoto, M. Takano, and R. Kanno, *Sodium deintercalation from sodium iron oxide*, *Mater. Res. Bull.* **29** (1994) 659–666.

[179] N. Yabuuchi, H. Yoshida, and S. Komaba, *Crystal Structures and Electrode Performance of Alpha-$NaFeO_2$ for Rechargeable Sodium Batteries*, *Electrochemistry* **80** (2012) 716–719.

[180] S. Kikkawa, S. Miyazaki, and M. Koizumi, *Deintercalated NaCoO2 and LiCoO2*, *Journal of Solid State Chemistry* **62** (1986) 35–39.

[181] S. Komaba, T. Nakayama, A. Ogata, T. Shimizu, C. Takei, S. Takada, A. Hokura, and I. Nakai, *Electrochemically Reversible Sodium Intercalation of Layered $NaNi_{0.5}Mn_{0.5}O_2$ and $NaCrO_2$*, *ECS Trans.* **16** (2009) 43.

[182] H. Yoshida, N. Yabuuchi, and S. Komaba, *$NaFe_{0.5}Co_{0.5}O_2$ as high energy and power positive electrode for Na-ion batteries*, *Electrochem. Commun.* **34** (2013) 60–63.

[183] C.-Y. Yu, J.-S. Park, H.-G. Jung, K.-Y. Chung, D. Aurbach, Y.-K. Sun, and S.-T. Myung, *$NaCrO_2$ cathode for high-rate sodium-ion batteries*, *Energy Environ. Sci.* **8** (2015) 2019–2026.

[184] X. Xia and J. R. Dahn, *$NaCrO_2$ is a Fundamentally Safe Positive Electrode Material for Sodium-Ion Batteries with Liquid Electrolytes*, *Electrochem. Solid-State Lett.* **15** (2011) A1.

[185] P. R. Elliston, F. Habbal, N. Saleh, G. E. Watson, K. W. Blazey, and H. Rohrer, *Magnetic and optical study of $NaCrO_2$*, *J. Phys. Chem. Solids* **36** (1975) 877–881.

[186] A. Olariu, P. Mendels, F. Bert, B. G. Ueland, P. Schiffer, R. F. Berger, and R. J. Cava, *Unconventional Dynamics in Triangular Heisenberg Antiferromagnet $NaCrO_2$*, *Phys. Rev. Lett.* **97** (2006) 167203.

[187] D. Hsieh, D. Qian, R. F. Berger, R. J. Cava, J. W. Lynn, Q. Huang, and M. Z. Hasan, *Unconventional spin order in the triangular lattice system $NaCrO_2$: A neutron scattering study*, *Physica B* **403** (2008) 1341–1343.

[188] D. Hsieh, D. Qian, R. F. Berger, R. J. Cava, J. W. Lynn, Q. Huang, and M. Z. Hasan, *Magnetic excitations in triangular lattice $NaCrO_2$*, *J. Phys. Chem. Solids* **69** (2008) 3174–3175.

[189] M. Hemmida, H.-A. Krug von Nidda, N. Büttgen, A. Loidl, L. K. Alexander, R. Nath, A. V. Mahajan, R. F. Berger, R. J. Cava, Y. Singh, and D. C. Johnston, *Vortex dynamics and frustration in two-dimensional triangular chromium lattices*, *Phys. Rev. B* **80** (2009) 054406.

[190] K. Somesh, Y. Furukawa, G. Simutis, F. Bert, M. Prinz-Zwick, N. Büttgen, A. Zorko, A. A. Tsirlin, P. Mendels, and R. Nath, *Universal fluctuating regime in triangular chromate antiferromagnets*, *Phys. Rev. B* **104** (2021) 104422.

[191] Y.-N. Zhou, J.-J. Ding, K.-W. Nam, X. Yu, S.-M. Bak, E. Hu, J. Liu, J. Bai, H. Li, Z.-W. Fu, and X.-Q. Yang, *Phase transition behavior of $NaCrO_2$ during sodium extraction studied by synchrotron-based X-ray diffraction and absorption spectroscopy*, *J. Mater. Chem. A* **1** (2013) 11130–11134.

[192] S.-H. Bo, X. Li, A. J. Toumar, and G. Ceder, *Layered-to-Rock-Salt Transformation in Desodiated Na_xCrO_2 (x 0.4)*, *Chem. Mater.* **28** (2016) 1419–1429.

[193] C. L. Jakobsen, M. Brighi, B. P. Andersen, G. Ducrest, R. Černý, and D. B. Ravnsbæk, *Expanded solid-solution behavior and charge-discharge asymmetry in Na_xCrO_2 Na-ion battery electrodes*, *J. Power Sources* **535** (2022) 231317.

[194] X. Chen, H. Tang, Y. Wang, and X. Li, *Balancing orbital effects and on-site Coulomb repulsion through Na modulations in Na_xVO_2*, *Phys. Rev. Materials* **5** (2021) 084402.

[195] H. Kim, D.-H. Seo, A. Urban, J. Lee, D.-H. Kwon, S.-H. Bo, T. Shi, J. K. Papp, B. D. McCloskey, and G. Ceder, *Stoichiometric Layered Potassium Transition Metal Oxide for Rechargeable Potassium Batteries*, *Chem. Mater.* **30** (2018) 6532–6539.

[196] A. Chakraborty, M. Dixit, D. Aurbach, and D. T. Major, *Predicting accurate cathode properties of layered oxide materials using the SCAN meta-GGA density functional*, *npj Comput. Mater.* **4** (2018) 1–9.

[197] D. A. Kitchaev, H. Peng, Y. Liu, J. Sun, J. P. Perdew, and G. Ceder, *Energetics of MnO_2 polymorphs in density functional theory*, *Phys. Rev. B* **93** (2016) 045132.

[198] J. H. Yang, D. A. Kitchaev, and G. Ceder, *Rationalizing accurate structure prediction in the meta-GGA SCAN functional*, *Phys. Rev. B* **100** (2019) 035132.

[199] D. A. Kitchaev, J. Vinckeviciute, and A. Van der Ven, *Delocalized Metal–Oxygen π-Redox Is the Origin of Anomalous Nonhysteretic Capacity in Li-Ion and Na-Ion Cathode Materials*, *J. Am. Chem. Soc.* **143** (2021) 1908–1916.

[200] J. Vinckeviciute, D. A. Kitchaev, and A. Van der Ven, *A Two-Step Oxidation Mechanism Controlled by Mn Migration Explains the First-Cycle Activation Behavior of Li_2MnO_3-Based Li-Excess Materials*, *Chem. Mater.* **33** (2021) 1625–1636.

[201] A. R. Natarajan and A. Van der Ven, *Toward an Understanding of Deformation Mechanisms in Metallic Lithium and Sodium from First-Principles*, *Chem. Mater.* **31** (2019) 8222–8229.

[202] X. Li, Y. Wang, D. Wu, L. Liu, S.-H. Bo, and G. Ceder, *Jahn–Teller Assisted Na Diffusion for High Performance Na Ion Batteries*, *Chem. Mater.* **28** (2016) 6575–6583.

[203] K. Dennis, K. Colburn, and J. Lazar, *Environmentally beneficial electrification: The dawn of 'emissions efficiency'*, *Electr. J.* **29** (2016) 52–58.

[204] E. A. Olivetti, G. Ceder, G. G. Gaustad, and X. Fu, *Lithium-Ion Battery Supply Chain Considerations: Analysis of Potential Bottlenecks in Critical Metals*, *Joule* **1** (2017) 229–243.

[205] T. Hosaka, K. Kubota, A. S. Hameed, and S. Komaba, *Research Development on K-Ion Batteries*, *Chem. Rev.* **120** (2020) 6358–6466.

[206] S. Komaba, T. Hasegawa, M. Dahbi, and K. Kubota, *Potassium intercalation into graphite to realize high-voltage/high-power potassium-ion batteries and potassium-ion capacitors*, *Electrochem. Commun.* **60** (2015) 172–175.

[207] M. Sha, L. Liu, H. Zhao, and Y. Lei, *Review on Recent Advances of Cathode Materials for Potassium-ion Batteries*, *Energy Environ. Mater.* **0** (2020) 1–11.

[208] R. Rajagopalan, Y. Tang, X. Ji, C. Jia, and H. Wang, *Advancements and Challenges in Potassium Ion Batteries: A Comprehensive Review*, *Adv. Funct. Mater.* **30** (2020) 1909486.

[209] C. Vaalma, G. A. Giffin, D. Buchholz, and S. Passerini, *Non-Aqueous K-Ion Battery Based on Layered $K_{0.3}MnO_2$ and Hard Carbon/Carbon Black*, *J. Electrochem. Soc.* **163** (2016) A1295.

[210] H. Kim, J. C. Kim, S.-H. Bo, T. Shi, D.-H. Kwon, and G. Ceder, *K-Ion Batteries Based on a P2-Type $K_{0.6}CoO_2$ Cathode*, *Adv. Energy Mater.* **7** (2017) 1700098.

[211] H. Kim, D.-H. Seo, J. C. Kim, S.-H. Bo, L. Liu, T. Shi, and G. Ceder, *Investigation of Potassium Storage in Layered P3-Type $K_{0.5}MnO_2$ Cathode*, *Adv. Mater.* **29** (2017) 1702480.

[212] C. Liu, S. Luo, H. Huang, Z. Wang, A. Hao, Y. Zhai, and Z. Wang, *$K_{0.67}Ni_{0.17}Co_{0.17}Mn_{0.66}O_2$: A cathode material for potassium-ion battery*, *Electrochem. Commun.* **82** (2017) 150–154.

[213] X. Wang, X. Xu, C. Niu, J. Meng, M. Huang, X. Liu, Z. Liu, and L. Mai, *Earth Abundant Fe/Mn-Based Layered Oxide Interconnected Nanowires for Advanced K-Ion Full Batteries*, *Nano Lett.* **17** (2017) 544–550.

[214] M. G. T. Nathan, N. Naveen, W. B. Park, K.-S. Sohn, and M. Pyo, *Fast chargeable P2–K-$_{2/3}$[$Ni_{1/3}Mn_{2/3}$]O_2 for potassium ion battery cathodes*, *J. Power Sources* **438** (2019) 226992.

[215] H. Zhang, K. Xi, K. Jiang, X. Zhang, Z. Liu, S. Guo, and H. Zhou, *Enhanced K-ion kinetics in a layered cathode for potassium ion batteries*, *Chem. Commun.* **55** (2019) 7910–7913.

[216] Q. Zhang, C. Didier, W. K. Pang, Y. Liu, Z. Wang, S. Li, V. K. Peterson, J. Mao, and Z. Guo, *Structural Insight into Layer Gliding and Lattice Distortion in Layered Manganese Oxide Electrodes for Potassium-Ion Batteries*, *Adv. Energy Mater.* **9** (2019) 1900568.

[217] A. Gao, M. Li, N. Guo, D. Qiu, Y. Li, S. Wang, X. Lu, F. Wang, and R. Yang, *K-Birnessite Electrode Obtained by Ion Exchange for Potassium-Ion Batteries: Insight into the Concerted Ionic Diffusion and K Storage Mechanism*, *Adv. Energy Mater.* **9** (2019) 1802739.

[218] J. U. Choi, Y. Ji Park, J. H. Jo, Y. H. Jung, D.-C. Ahn, T.-Y. Jeon, K.-S. Lee, H. Kim, S. Lee, J. Kim, and S.-T. Myung, *An optimized approach toward high energy density cathode material for K-ion batteries*, *Energy Storage Mater.* **27** (2020) 342–351.

[219] C. Delmas, M. Devalette, C. Fouassier, and P. Hagenmuller, *Les phases K_xCrO_2 ($x \leqslant 1$)*, *Mater. Res. Bull.* **10** (1975) 393–398.

[220] C. Fouassier, C. Delmas, and P. Hagenmuller, *Evolution structurale et proprietes physiques des phases A_xMO_2 (A = Na, K; M = Cr, Mn, Co) ($x \leqslant 1$)*, *Mater. Res. Bull.* **10** (1975) 443–449.

[221] N. Naveen, S. C. Han, S. P. Singh, D. Ahn, K.-S. Sohn, and M. Pyo, *Highly stable P′3-$K_{0.8}CrO_2$ cathode with limited dimensional changes for potassium ion batteries*, *J. Power Sources* **430** (2019) 137–144.

[222] "Supporting Information for: Ordering and Structural Transformations in Layered K_xCrO_2 for K-Ion Batteries." https://pubs.acs.org/doi/10.1021/acs.chemmater.0c01460, 2020.

[223] C. Delmas, G. Le Flem, C. Fouassier, and P. Hagenmuller, *Etude comparative des proprietes magnetiques des oxydes lamellaires $ACrO_2$ (A = Li, Na, K)—II: Calcul des integrales d'echange*, *J. Phys. Chem. Solids* **39** (1978) 55–57.

[224] J. L. Soubeyroux, D. Fruchart, C. Delmas, and G. Le Flem, *Neutron powder diffraction studies of two-dimensional magnetic oxides*, *J. Magn. Magn. Mater.* **14** (1979) 159–162.

[225] W. H. Woodford, W. Craig Carter, and Y.-M. Chiang, *Design criteria for electrochemical shock resistant battery electrodes*, *Energy Environ. Sci.* **5** (2012) 8014–8024.

[226] H. Liu, M. Wolf, K. Karki, Y.-S. Yu, E. A. Stach, J. Cabana, K. W. Chapman, and P. J. Chupas, *Intergranular Cracking as a Major Cause of Long-Term Capacity Fading of Layered Cathodes*, *Nano Lett.* **17** (2017) 3452–3457.

[227] F. Izumi and K. Momma, *Three-dimensional visualization in powder diffraction*, *Solid State Phenom.* **130** (2007) 15–20.

[228] G. J. Shu and F. C. Chou, *Sodium-ion diffusion and ordering in single-crystal P2-Na_xCoO_2*, *Phys. Rev. B* **78** (2008) 052101.

[229] G. K. Williamson and W. H. Hall, *X-ray line broadening from filed aluminium and wolfram*, *Acta Metall.* **1** (1953) 22–31.

[230] C. R. Fell, M. Chi, Y. S. Meng, and J. L. Jones, *In situ X-ray diffraction study of the lithium excess layered oxide compound $Li[Li_{0.2}Ni_{0.2}Mn_{0.6}]O_2$ during electrochemical cycling*, *Solid State Ionics* **207** (2012) 44–49.

[231] E. Goikolea, V. Palomares, S. Wang, I. R. de Larramendi, X. Guo, G. Wang, and T. Rojo, *Na-Ion Batteries—Approaching Old and New Challenges*, *Adv. Energy Mater.* **10** (2020) 2002055.

[232] M. S. Whittingham, *Lithium Batteries and Cathode Materials*, *Chem. Rev.* **104** (2004) 4271–4302.

[233] M. S. Whittingham, *Ultimate Limits to Intercalation Reactions for Lithium Batteries*, *Chem. Rev.* **114** (2014) 11414–11443.

[234] C. Delmas, D. Carlier, and M. Guignard, *The Layered Oxides in Lithium and Sodium-Ion Batteries: A Solid-State Chemistry Approach*, *Adv. Energy Mater.* **11** (2020) 2001201.

[235] H. Kim, J. C. Kim, M. Bianchini, D.-H. Seo, J. Rodriguez-Garcia, and G. Ceder, *Recent Progress and Perspective in Electrode Materials for K-Ion Batteries*, *Adv. Energy Mater.* **8** (2018) 1702384.

[236] "Supporting Information for: Antiphase boundary migration as a diffusion mechanism in a P3 sodium layered oxide." http://link.aps.org/supplemental/10.1103/PhysRevMaterials.5.055401, 2021.

[237] C. Delmas, A. Maazaz, C. Fouassier, J.-M. Réau, and P. Hagenmuller, *Influence de l'environnement de l'ion alcalin sur sa mobilite dans les structures a feuillets $A_x(L_xM_{1-x})O_2$*, *Mater. Res. Bull.* **14** (1979) 329–335.

[238] E. Lee, J. Lu, Y. Ren, X. Luo, X. Zhang, J. Wen, D. Miller, A. DeWahl, S. Hackney, B. Key, D. Kim, M. D. Slater, and C. S. Johnson, *Layered P2/O3 Intergrowth Cathode: Toward High Power Na-Ion Batteries*, *Adv. Energy Mater.* **4** (2014) 1400458.

[239] H. Gleiter, *Theory of grain boundary migration rate*, *Acta Metall.* **17** (1969) 853–862.

[240] E. Annevelink, E. Ertekin, and H. T. Johnson, *Grain boundary structure and migration in graphene via the displacement shift complete lattice*, *Acta Mater.* **166** (2019) 67–74.

[241] W. K. Burton, N. Cabrera, F. C. Frank, and N. F. Mott, *The growth of crystals and the equilibrium structure of their surfaces*, *Philos. Trans. R. Soc., A* **243** (1951) 299–358.

[242] H.-C. Jeong and E. D. Williams, *Steps on surfaces: experiment and theory*, *Surf. Sci. Rep.* **34** (1999) 171–294.

[243] Y. Mo, S. P. Ong, and G. Ceder, *Insights into Diffusion Mechanisms in P2 Layered Oxide Materials by First-Principles Calculations*, *Chem. Mater.* **26** (2014) 5208–5214.

[244] J. Bhattacharya and A. Van der Ven, *Phase stability and nondilute Li diffusion in spinel* $Li_{1+x}Ti_2O_4$, *Phys. Rev. B* **81** (2010) 104304.

[245] M. Aldegunde, N. Zabaras, and J. Kristensen, *Quantifying uncertainties in first-principles alloy thermodynamics using cluster expansions*, *J. Comput. Phys.* **323** (2016) 17–44.

[246] J. G. Goiri, S. K. Kolli, and A. Van der Ven, *Role of short- and long-range ordering on diffusion in Ni-Al alloys*, *Phys. Rev. Mater.* **3** (2019) 093402.

[247] C. Delmas, J. P. Pérès, A. Rougier, A. Demourgues, F. Weill, A. Chadwick, M. Broussely, F. Perton, P. Biensan, and P. Willmann, *On the behavior of the* Li_xNiO_2 *system: an electrochemical and structural overview*, *J. Power Sources* **68** (1997) 120–125.

[248] S. J. Clarke, A. J. Fowkes, A. Harrison, R. M. Ibberson, and M. J. Rosseinsky, *Synthesis, Structure, and Magnetic Properties of* $NaTiO_2$, *Chem. Mater.* **10** (1998) 372–384.

[249] E. Chappel, M. D. Núñez-Regueiro, G. Chouteau, O. Isnard, and C. Darie, *Study of the ferrodistorsive orbital ordering in* $NaNiO_2$ *by neutron diffraction and submillimeter wave ESR*, *Eur. Phys. J. B* **17** (2000) 615–622.

[250] W. Tian, M. F. Chisholm, P. G. Khalifah, R. Jin, B. C. Sales, S. E. Nagler, and D. Mandrus, *Single crystal growth and characterization of nearly stoichiometric $LiVO_2$*, *Mater. Res. Bull.* **39** (2004) 1319–1328.

[251] Q. Huang, M. L. Foo, R. A. Pascal, J. W. Lynn, B. H. Toby, T. He, H. W. Zandbergen, and R. J. Cava, *Coupling between electronic and structural degrees of freedom in the triangular lattice conductor Na_xCoO_2*, *Phys. Rev. B* **70** (2004) 184110.

[252] M. Giot, L. C. Chapon, J. Androulakis, M. A. Green, P. G. Radaelli, and A. Lappas, *Magnetoelastic Coupling and Symmetry Breaking in the Frustrated Antiferromagnet α-$NaMnO_2$*, *Phys. Rev. Lett.* **99** (2007) 247211.

[253] L. Vitoux, M. Guignard, N. Penin, D. Carlier, J. Darriet, and C. Delmas, *$NaMoO_2$: a Layered Oxide with Molybdenum Clusters*, *Inorg. Chem.* **59** (2020) 4015–4023.

[254] J. L. Kaufman, "kmc-lotto." https://github.com/jonaskaufman/kmc-lotto, 2021.

[255] J. W. Cahn and J. E. Hilliard, *Free Energy of a Nonuniform System. I. Interfacial Free Energy*, *J. Chem. Phys.* **28** (1958) 258–267.

[256] S. K. Kolli and A. Van der Ven, *Elucidating the Factors That Cause Cation Diffusion Shutdown in Spinel-Based Electrodes*, *Chem. Mater.* **33** (2021) 6421–6432.

[257] J. G. Goiri and A. Van der Ven, *MultiShifter: Software to generate structural models of extended two-dimensional defects in 3D and 2D crystals*, *Comput. Mater. Sci.* **191** (2021) 110310.

[258] A. S. Dalton, A. A. Belak, and A. Van der Ven, *Thermodynamics of Lithium in TiO_2(B) from First Principles*, *Chem. Mater.* **24** (2012) 1568–1574.